DEVELOPMENT AND APPLICATION OF MODELS FOR STUDY OF EMERGENT AND PRE-EMERGENT CORONAVIRUSES

Kenneth Harold Dinnon III

A dissertation submitted to the faculty at the University of North Carolina at Chapel Hill in partial fulfillment of the requirements for the degree of Doctor in Philosophy in the Department of Microbiology and Immunology in the School of Medicine.

Chapel Hill
2021

Approved by:

Ralph S. Baric

Mark T. Heise

Helen M. Lazear

Stanley M. Lemon

Nathaniel J. Moorman

Timothy P. Sheahan

ABSTRACT

Kenneth Harold Dinnon III: Development and application of models for study of emergent and pre-emergent coronaviruses
(Under the direction of Ralph S. Baric)

RNA viruses pose a serious global health threat as evidenced by the emergence of SARS-CoV-2 and the COVID-19 pandemic. Three coronaviruses (CoVs) have jumped into the human population over the past two decades: SARS-CoV in 2002, MERS-CoV in 2012, and SARS-CoV-2 in 2019. The potential for future CoV emergence is underappreciated. Bats serve as a reservoir for diverse coronaviruses that may spill over into humans, but it is unclear what fraction of these viruses are capable of infecting humans. Prior to the COVID-19 pandemic, there were no specific antivirals or vaccines for human CoVs, and due to antigenic diversity of bat CoVs, it is unclear if COVID-19 vaccines will prevent future outbreaks. Here we develop models to understand pre-emergent CoVs and recently emergent SARS-CoV-2.

We investigated the potential for a bat reservoir MERS-CoV-like virus, PDF-2180, for human emergence. CoV entry into host cells is dependent on interaction with cellular surface receptors and CoV spike protein processing by host proteases. Traditionally the host range restriction for CoVs has been thought to be limited to spike-receptor interactions. Initially not predicted to infect human cells, we identified that PDF-2180 could infect human cells but required exogenous trypsin protease, independently of the MERS-CoV receptor, DPP4. This showed that with adaptation for efficient protease processing, PDF-2180 has the potential for human infection.

COVID-19 revealed the need for laboratory models to understand SARS-CoV-2 and develop medical countermeasures. Unlike SARS-CoV, early clinical isolates of SARS-CoV-2

could not infect mice due to incompatibilities with the mouse ortholog of the receptor, ACE2. Here, we developed two mouse-adapted strains of SARS-CoV-2: ‘MA’ and ‘MA10’. SARS-CoV-2 MA10 is a highly pathogenic strain that very closely resembles COVID-19 seen in humans. We use these models to understand SARS-CoV-2 infection and pathogenesis, as well as preclinically test numerous monoclonal antibody therapies, antivirals, and vaccines including Moderna’s mRNA-1273. We also elucidate the mechanisms of long term sequelae in mice to understand ‘long-COVID’ or ‘post-acute sequelae of COVID-19’ seen in human COVID-19 survivors. Altogether, these models will continue to answer unknowns of COVID-19 and develop medical countermeasures for ongoing and future CoV pandemics.

ACKNOWLEDGEMENTS

I have so many people to thank for helping me throughout my graduate school career. Firstly, I want to thank my mentor Ralph Baric, who has been extremely supportive and generous throughout my time in the lab. I feel extremely lucky to have been able to pursue so many different scientific pursuits, and always have the support from Ralph. He has always allowed me to follow random tangetial thoughts and ideas, just to satisfy my curiosity. And of course, he has also supported me to follow his random tangential thoughts and ideas for those “quick and easy papers”. I also need to thank the many many members of the Baric Lab who have also been extremely supportive and a great team to work with over the entirety of my time in the lab, but especially so in surviving the past 18 months. Special thanks to Sarah, Ethan, Tim, Lisa, Emily, Amy, and Vineet for always being there for scientific discussion, advice, and for being great people to work with on so many projects.

I also want to thank all of my family and friends who have been supportive throughout graduate school. My mom and sister have been particularly supportive. Spending time with my friends made during graduate school, and keeping in touch with friends from college and high school has made my time here so much fun, even if some of them may say I spend too much time in lab… I will miss my time here at UNC, but I am excited for the next steps. And I look forward to staying in touch with my wonderful friends and colleagues during all those next steps.

TABLE OF CONTENTS

LIST OF FIGURES

LIST OF TABLES

LIST OF ABBREVIATIONS

AAV	Adeno-associated virus
ACE2	Angiotensin converting enzyme 2
AdV	Adenovirus
Ager	Advanced glycosylation end-product specific receptor
ALI	Acute lung injury
ANOVA	Analysis of variance
APN	Aminopeptidase N
ARDS	Acute respiratory distress syndrome
AT1	Alveolar type 1 cell
AT2	Alveolar type 2 cell
ATS	American Thoracic Society
BCoV	Bovine coronavirus
BMBL	Biosafety in Microbiological and Biomedical Laboratories
BSL2	Biosafety level 2
BSL3	Biosafety level 3
CCSP	Clara cell phospholipid-binding protein

CD26	Cluster of differentiation 26
CD4	Cluster of differentiation 4
CD8	Cluster of differentiation 8
CDC	Centers of Disease Control and Prevention
Col1a1	Collagen type 1 alpha 1 chain
CoV	Coronavirus
COVID-19	Coronavirus disease 2019
CT	Computed tomography
DAD	Diffuse alveolar damage
DAPI	4′,6-diamidino-2-phenylindole
DATP	Damage associated transient progenitor
DMEM	Dulbecco’s Modified Eagle Medium
DMV	Double membrane vesicle
dpi	days post infection
DPP4	Dipeptidyl-peptidase 4
DSP	Digital spatial profiling
EF50	Mid-tidal expiratory flow

EHS	Environmental Health and Safety
Fbn1	Fibrillin 1
FDA	Food and Drug Authority
Fn1	Fibronectin 1
FoxJ1	Forkhead box J1
GFP	Green fluorescent protein
H&E	Hematoxylin and eosin
hACE2	human ACE2
HAE	Human airway epithelial cells
HBE	Human bronchiolar epithelial cells
HCoV	Human coronavirus
IBC	Institutional Biosafety Committee
IBV	Infectious bronchitis virus
IFN	Interferon
IFN-α	Interferon alpha
IFN-γ	Interferon gamma
IFN-λ	Interferon lambda

IFN-λ1a	Interferon lambda 1a
IFNR DKO	Interferon alpha/beta receptor, interferon lambda receptor double knock out mice
IHC	Immunohistochemistry
IL	Interleukin
IPF	Idiopathic pulmonary fibrosis
ISG	Interferon stimulated gene
ISH	*In situ* hybridization
LAMP3	Lysosomal associated membrane protein 3
LOD	Limit of detection
M	Membrane protein
MA	Mouse adapted
MA10	Mouse adapted after passage 10
mACE2	Mouse ACE2
MEM	Modified Eagle's Medium
MERS	Middle East respiratory syndrome
MERS-CoV	Middle East respiratory syndrome coronavirus

MHV	Murine hepatitis virus
MOI	Multiplicity of infection
N	Nucleocapsid protein
NHP	Non-human primate
NIAID	National Institute of Allergy and Infectious Diseases
NIH	National Institutes of Health
nLUC	Nanoluciferase
nsp	Non-structural protein
ORF	Open reading frame
OSN	Olfactory sensory neuron
PASC	Post-acute sequelae of SARS-CoV-2 infection
PATS	pre-AT1 transitional state
PBS	Phosphate buffered saline
PBST	Phosphate buffered saline with Tween-20
PCA	Principal component analysis
PDCoV	Porcine deltacoronavirus
PEDV	Porcine epidemic diarrhea virus

PEG-IFN-λ1a	Pegylated interferon lambda 1a
PenH	Enhanced pause
PFU	Plaque forming unit
RBD	Receptor binding domain
RDS	Respiratory distress syndrome
RDV	Remdesivir
RLU	Relative light units
RNA	Ribonucleic acid
ROI	Region of interest
Rpef	Ratio of peak expiratory flow to total expiratory time
S	Spike protein
SADS-CoV	Swine acute diarrhea syndrome coronavirus
SARS	Severe acute respiratory syndrome
SARS-CoV	Severe acute respiratory syndrome coronavirus
SARS-CoV-2	Severe acute respiratory syndrome coronavirus 2
Scgb1a1	Secretoglobin family 1A member 1
scRNAseq	Single cell RNA sequencing

Sftpb	Surfactant protein B
Sftpc	Surfactant protein C
SMA	Smooth muscle actin
SOP	Standard operating procedure
SPP1	Secreted phosphoprotein 1
TGEV	Transmissible gastroenteritis virus
TGF-β1	Transforming growth factor beta 1
Tgfb1	Transforming growth factor beta 1
Th1	Type 1 T-helper cell
Th2	Type 2 T-helper cell
TMPRSS2	Transmembrane serine protease 2
TNF-α	Tumor necrosis factor alpha
Uchl1	Ubiquitin C-terminal hydrolase L1
UNC-CH	University of North Carolina at Chapel Hill
USAMRIID	United States Army Medical Research Institute of Infectious Diseases
UTR	Untranslated Region
VEEV	Venezuelan equine encephalitis virus

VRP	Virus replicon particle
WBP	Whole body plethysmography
WHO	World Health Organization
WT	Wild type

CHAPTER 1 – INTRODUCTION

1.1 Emerging viruses pose a threat to human health

In the past two decades, we have seen the emergence of several RNA viruses into naïve human populations. Mosquito-transmitted chikungunya and Zika viruses were introduced into the Caribbean and South America in 2013 and 2015, respectively[1,2]. The 2009 H1N1 influenza pandemic caused an estimated 60 million infections in the United States before becoming a circulating seasonal influenza strain[3]. Severe acute respiratory syndrome coronavirus (SARS-CoV) and Middle East respiratory syndrome coronavirus (MERS-CoV) caused severe, but limited outbreaks mainly in China and the Middle East or traveler-associated cases in Canada and South Korea[4-6]. Together, these emergent viruses have caused severe economic and public health burdens.

Most notably, the emergence of SARS-CoV-2 in 2019 has caused the ongoing COVID-19 pandemic, resulting in drastic disruption of normal life, economic strain, nearly 180 million confirmed infections and nearly 4 million deaths as of July 2021[7]. Despite the terrible toll the COVID-19 pandemic has had globally, the scientific and medical community has adapted rapidly to employ diverse expertise towards a common goal of curbing the pandemic. With rapid community focus and collaboration, several COVID-19 vaccines reached World Health Organization (WHO) and United States Food and Drug Administration (FDA) emergency use authorization in record speed and have noticeably helped to fight the spread of SARS-CoV-2 globally.

With global warming, increased global range of viral vectors such as mosquitos and ticks, the increase in human population, density, land use changes, expanding agricultural space, global travel, and destruction of natural habitats, the emergence frequency of zoonotic pathogens is only likely to increase[8].

1.2 Human coronaviruses and disease

Prior to the emergence of SARS-CoV in 2002, there were only two known human CoVs (HCoV-229E and HCoV-OC43)[9,10]. After the SARS-CoV epidemic, molecular surveillance for coronaviruses (CoVs) increased and two additional HCoVs were identified (HCoV-NL63 and HKU1)[11,12]. These endemic human CoVs are most often associated with mild upper respiratory illness in the young and elderly, causing roughly 20-30% of common colds[10,13-18]. Like recent emerging CoVs (SARS-CoV, MERS-CoV, SARS-CoV-2), the human endemic CoVs are also thought to have arisen due to zoonotic events[19-21]. Phylogenetic analysis reveals HCoV-229E and HCoV-NL63 likely originated in bats before their introduction and fixation in human populations roughly 200 and 900 years ago, respectively[20-22]. Due to high similarity to bovine coronavirus (BCoV), HCoV-OC43 is thought to have originated from cattle roughly 120 years ago[19]. HKU1 is thought to have arisen from rodents in the mid 1950s[23,24]. These HCoVs were not considered to be highly pathogenic or of high concern but are vastly understudied. It was not until the SARS-CoV epidemic that the human pathogenic potential of coronaviruses was fully recognized.

Severe acute respiratory syndrome (SARS) CoV emerged in China in 2002-2003 and caused a limited outbreak resulting in roughly 8,000 cases and 10% mortality. SARS-CoV patients developed flu-like symptoms, with the most severe cases developing severe acute respiratory distress syndrome (ARDS) and respiratory failure[25-29]. While the respiratory tract is the primary site of SARS-CoV infection, some patients had infection of peripheral organs such as the gastrointestinal tract, liver, and kidneys[30,31]. SARS-CoV-induced disease is mostly immune

mediated as the virus is often cleared or controlled before the peak of symptoms, with the immune system continuing to cause damage to the lungs causing acute lung injury (ALI) and diffuse alveolar damage (DAD)[29]. This prolonged immune response is often more severe in the elderly and those with comorbidities. SARS-CoV ultimately caused reported cases in 32 countries globally. Due to the lack of specific antivirals or vaccines, the SARS-CoV outbreak was controlled through extensive public health measures.

In 2012, Middle East respiratory syndrome (MERS) CoV emerged in the Kingdom of Saudi Arabia[32]. MERS-CoV continues to circulate in dromedary camels as an intermediate reservoir host, causing sporadic infections in humans. To date, roughly 2,500 confirmed cases have been reported with a 35% mortality rate, though these numbers are likely skewed by lack of detection of asymptomatic or mild cases[33]. MERS-CoV is less efficient in human-to-human spread than other CoVs, which may account for the relatively limited cases. Like SARS-CoV, disease is mostly immune mediated following the clearance of virus, though features are not as well understood due to limited clinical samples and autopsy reports.

In late 2019, SARS-CoV-2 emerged in Wuhan, China causing a rapid outbreak that was designated a global pandemic by the WHO in March of 2020[7]. The precise zoonotic source of SARS-CoV-2 remains unknown, but phylogenetic analysis suggests a common ancestor in bats with the possibility of an intermediate host[34,35]. SARS-CoV-2 is the causative agent of coronavirus disease 19 (COVID-19), which can manifest similar to SARS, but shows increased transmissibility and roughly 40-45% of those infected are asymptomatic[36]. Symptoms are often present within and persist 2-14 days after virus exposure. COVID-19 patients report varying combinations of anosmia (loss of the ability to sense smell), malaise, fever, unproductive cough, body aches, shortness of breath, nausea or vomiting, and diarrhea[37,38]. The elderly and those with comorbidities such as diabetes, obesity, immune compromising conditions, and pre-existing chronic lung diseases often have more severe COVID-19 symptoms and prognoses. For those that recover from acute SARS-CoV-2 infection, up to 50% of patients report long-term sequelae,

termed ‘long COVID’ or ‘post-acute sequelae of SARS-CoV-2 infection’ (PASC), characterized by prolonged fatigue, muscle weakness, difficulty breathing, anxiety, sleep disruptions, chest pain, chronic kidney disease, or hair loss[39-42]. These manifestations of PASC occur long after clearance of SARS-CoV-2 and are likely the result of the damage caused by the viral infection and subsequent host immune response; however, the exact mechanisms of these long-term manifestations are unknown.

Prior to the COVID-19 pandemic, no HCoV vaccines or antivirals were available. Studies by the Baric laboratory and others had identified preclinical candidates, such as Remdesivir, as a broad-spectrum antiviral effective against SARS-CoV, MERS-CoV, HCoVs, and zoonotic CoVs[43-47]. However, these preclinical candidates had not yet been tested in clinical trials. However, with the emergence of SARS-CoV-2, Remdesivir and several vaccine candidates were rapidly tested in clinical trials, leading to the availability of several emergency use monoclonal antibody, vaccines, and antiviral therapies.

1.3 Livestock and animal coronaviruses

In addition to endemic and emergent human CoVs, we have seen the emergence of several animal coronaviruses associated with the increase in global industrial farming and increased animal housing density. In most cases, these livestock coronaviruses cause gastrointestinal infections and are transmitted via the fecal-oral route. For example, transmissible gastroenteritis virus (TGEV)[48], porcine epidemic diarrhea virus (PEDV)[49], porcine deltacoronavirus (PDCoV)[50], and swine acute diarrhea syndrome coronavirus (SADS-CoV)[51,52] are all enteric coronaviruses that have near 100% mortality in suckling piglets. TGEV has caused outbreaks for most of the 20th century, with particularly severe economic losses in the 1990s, highlighting the importance of CoVs on livestock and human food supply. PEDV caused sporadic outbreaks globally dating back to the 1970s, until it was introduced into China in 2010 and the United States in 2013, causing severe damage to the swine industry[53]. In 2012, a distinct virus,

PDCoV, was identified in Hong Kong and spread to the United States in 2014 and similarly caused outbreaks on pig farms[50]. Most recently in China, SADS-CoV emerged in swine herds, but has not yet spread globally. Like porcine enteric viruses, bovine coronavirus (BCoV) is associated with severe diarrhea in calves. Some coronaviruses such as avian infectious bronchitis virus (IBV) can cause respiratory disease and have severe impacts on poultry farming. Additionally, coronaviruses such as such as canine and feline coronaviruses are common pathogens of companion animals. Unlike HCoVs, there are live attenuated vaccines for several of these animal coronaviruses, often from viruses isolated after serial passage in cell culture and accumulation of attenuating mutations, but these vaccines vary in efficacy based on circulating strain diversity and antigenicity[54].

Domesticated animal coronaviruses also have the potential for spillover into human populations. As mentioned above, HCoV-OC43 is thought to have been a spillover of BCoV into humans roughly 120 years ago[19]. Recently there have been reported cases of PDCoV infecting children in Haiti[55]. Similarly, a novel canine-feline recombinant coronavirus was detected in eight patients in Malaysia during a pneumonia outbreak in 2017-2018[56,57]. Additionally, SADS-CoV is able to effectively replicate in primary human airway epithelial cells, indicating that SADS-CoV may also be capable of infecting humans[58].

1.4 Zoonotic reservoirs of coronaviruses

Since the discoveries of SARS-CoV in 2002 and MERS-CoV in 2012, metagenomic surveying of bat and other animal reservoir coronaviruses has revealed an extremely diverse pool of coronaviruses[21,24,59-66]. The coronavirus family consists of four genera: *Alphacoronavirus*, *Betacoronavirus*, *Gammacoronavirus*, and *Deltacoronavirus*. Alphacoronaviruses and betacoronaviruses infect mammals, with large diversity in bats. Gammacoronaviruses and deltacoronaviruses predominantly infect birds, though some

viruses can also infect mammals. There are roughly 1,200 species of bats globally, each predicted to harbor an average of 2-3 species of CoV for a total predicted bat-reservoir CoV richness of 3,204 CoV species[62]. A large majority of these viruses have not been described, sequenced, or isolated. Thus, their potential for cross-species transmission is largely unknown.

SARS-CoV was detected in masked palm civets in live animal markets during the SARS-CoV epidemic and identified as a potential intermediate host. However, it is unclear if civets served as the direct source of human infections or if they supported replication during the outbreak after exposure to a different zoonotic source. MERS-CoV has been isolated from camels in the Middle East and molecular clock analysis suggests MERS-CoV has been circulating in camels for several decades[67]. Due to the endemic nature of MERS-CoV in camels and the close cultural association of humans and camels in the Middle East, sporadic spill-over events are likely to continue to occur.

Through phylogenetic analysis and protein molecular modeling, some of SARS-CoV-like viruses were predicted to be able to infect human cells utilizing the same receptor as SARS-CoV, angiotensin converting enzyme 2 (ACE2)[60,61,63,68]. Previous work in the Baric lab identified viruses WIV1 and SHC014 as possible pre-emergent coronaviruses due to their capacity to infect primary human airway cells[60,61]. WIV1 and SHC014 are 92 and 90% identical to SARS-CoV, respectively, with divergence in the receptor binding domain (RBD) of the spike protein which is responsible for host receptor recognition and attachment[60,61]. This divergence in the RBDs of WIV1 and SHC014 also revealed that existing monoclonal antibodies from SARS-CoV survivors and SARS-CoV vaccine candidates only had limited efficacy in neutralizing these viruses or protecting

mice from infection[60,61]. These findings suggested that these zoonotic viruses are capable of infecting human cells, but that existing intervention strategies developed for SARS-CoV would likely not be effective.

After the emergence of SARS-CoV-2 and an increase in surveillance, a plethora of additional animal betacoronaviruses have been reported from bats and many other animal hosts such as pangolins[35,69]. Pseudotyped virus entry and binding assays have revealed some of these zoonotic are capable of using human ACE2 as a receptor, suggesting additional reservoir viruses are capable of emergence[68].

In addition to many SARS-CoV-like viruses identified, a smaller number of MERS-CoV-like viruses have also been identified, though few have been analyzed for ability to infect human cells[62,70-72]. HKU4 and HKU5 are both MERS-CoV-like bat viruses that have identified through deep sequencing and metagenomics. pseudotyped virus experiments reveal HKU4 is capable of utilizing the same receptor as MERS-CoV, DPP4[73,74]. However, HKU5 is not able to utilize DPP4 as a receptor, though it remains unknown if HKU5 can utilize a different human protein receptor[74]. Another MERS-CoV-like bat virus, PDF-2180, was identified in Uganda with 80% similarity to MERS-CoV across a majority of the genome, but with only 50% similarity in the S1 subdomain of the spike protein, making PDF-2180 the closest known bat virus relative of MERS-CoV[70]. In Chapter 2 of this dissertation, we further characterize the ability of PDF-2180 to infect human cells[71].

1.5 Coronavirus cellular entry mechanisms

All coronaviruses encode a spike glycoprotein that mediates binding to host cellular receptors and mediates membrane fusion and viral entry. The compatibility of the viral spike protein and host receptor is a key determinant of host range capability and cellular tropism. The

spike is comprised of two main domains: S1 and S2. The S1 domain is further divided into the N-terminal domain (NTD) and C-terminal domain (CTD)[75]. For betacoronaviruses, the CTD also functions as the receptor binding domain (RBD) that directly contacts the host receptor. Upon binding of the RBD to the host receptor, the S undergoes a conformational change that exposes a hydrophobic core of the S2 domain that mediates lipid membrane fusion and delivery of the viral genome into the cytoplasm of the host cell[75]. For HCoVs, the receptors are known: angiotensin-converting enzyme 2 (ACE2) for SARS-CoV, SARS-CoV-2, and HCoV-NL63[7,68,76-80]; dipeptidyl peptidase 4 (DPP4, CD26) for MERS-CoV[81-83], aminopeptidase N (APN, CD13) for HCoV-229E[84], and 9-*O*-acetylated sialic acid for HCoV-OC43 and HKU1[85-88]. Interestingly, porcine APN is the receptor for TGEV and PDCoV[89,90], and debated to be the receptor for PEDV[91,92], highlighting a convergent host target for coronavirus entry.

In addition to RBD-receptor interactions, the spike protein must also be proteolytically processed by host proteases at the S1/S2 junction to allow for proper conformational changes and infection[93-97]. For SARS-CoV and SARS-CoV, endosomal serine proteases such as TMPRSS2 cleave the spike following endosomal uptake of receptor bound virions, allowing for maturation of the spike into a fusinogenic form. The Golgi localized serine protease, furin, is capable of facilitating infection of MERS-CoV and SARS-CoV-2[98-100]. Culturing of several porcine coronaviruses such as PEDV and PDCoV *in vitro* requires the use of exogenous trypsin or pancreatin (a gastrointestinal mix of proteases, lipases, and amylases), recapitulating the extracellular protease environment of the gastrointestinal tract[101-103]. Exogenous trypsin treatment of SARS-CoV and HCoV-229E augments viral replication and can induce cellular syncytia formation[104-106].

Upon efficient spike protein and receptor interaction, protease processing, and membrane fusion, the positive-sense coronavirus genome is deposited into the host cytoplasm where it can be directly translated into viral nonstructural and replicase proteins to initiate virus replication[107]. Due to the uniquely large genomes of coronaviruses compared to other RNA viruses, they often

encode multiple redundant host modulators allowing for replication in numerous cell types from a variety of hosts[108]. Thus, spike protein, host receptor, and host protease compatibility is often the determining step in host range[109,110]; though additional intracellular restrictions may also apply as we do not observe ubiquitous coronavirus replication in tissues with robust receptor expression.

1.6 Coronavirus mouse models

When SARS-CoV-2 emerged in December of 2019, it was quickly identified to utilize the same human receptor as SARS-CoV, ACE2[7,68]. However, early circulating strains of SARS-CoV-2 were incapable of infecting laboratory mice due to incompatibilities with murine ACE2. While several non-human primate (NHP)[111-113], hamster[114,115], ferret[116], and transgenic mouse models were rapidly developed[61,117-121], these models are not widely accessible, and these non-murine animal systems often lack genetic tools and immunological reagents for downstream analysis. Nonhuman primates (NHPs) such as Rhesus macaques, Cynomolgus macaques, and African green monkeys support SARS-CoV-2 infection and display high similarity to human COVID-19 disease[122], but experiments using NHPs are limited by costs, animal availability, and complex husbandry. Hamster and ferret models are permissive to SARS-CoV-2 but fail to display severe disease as seen in humans[114-116], and genetic and immunological tools are lacking.

Early SARS-CoV-2 isolates were unable to utilize mouse ACE2 as a receptor, thus standard laboratory mice were non-permissive to infection. However, following the SARS-CoV epidemic several transgenic mouse lines expressing human ACE2 were generated, and these lines allow for replication of SARS-CoV and SARS-CoV-2[61,117-121]. However, these transgenic mouse models only develop mild respiratory disease and often die from

neurological disease due to SARS-CoV and SARS-CoV-2 infection of the central nervous system, which is not reflective of the human disease. Due to limited availability and high demand of these transgenic mouse models, several groups developed adenovirus- or adeno-associated virus-vector transduced mice expressing human ACE2, allowing for infection of standard laboratory strains or knockout mice[123-125]. Similar to the transgenic human ACE2 mice, these models develop limited clinical disease. Nonetheless, these transgenic and transduced mouse models are still extremely effective for testing medical countermeasures such as antivirals, vaccines, and monoclonal antibodies using viral replication as a measurement. However, to understand the mechanisms of SARS-CoV-2 pathogenesis, these models may be inappropriate due to artificial tropism due to transgenic promoter choice or tropism of transduction viral vector and immune responses derived from the viral vector. Groups have developed humanized ACE2 mice that natively express human ACE2 under the murine ACE2 locus, but these mice are also limited in their availability and only display mild disease signs.

An alternative approach is to adapt SARS-CoV-2 to utilize murine ACE2 as a receptor. Several groups have been able to isolate SARS-CoV-2 variants from rare quasispecies in clinical samples that are capable of infecting wildtype mice[126-130]. These initially isolated viruses often have few mutations across their genomes, all containing a mutation in the RBD that allows for murine ACE2 binding. These variants, while able to infect widely available wildtype mice, only cause limited disease. We herein utilized reverse genetics to alter the SARS-CoV-2 RBD based on our knowledge of SARS-CoV, WIV1, and SHC014 models to allow infection of wildtype mice by generating a mouse-adapted ‘SARS-CoV-2 MA’ strain[119]. This SARS-CoV-2 MA strain efficiently replicates in

wildtype mice, but also causes only limited respiratory disease. However, we and others serially passaged these mouse-adapted variants in mice to allow *in vivo* evolution of SARS-CoV-2 to accumulate additional mutations to increase fitness and pathogenesis in wildtype mice[129,131]. We generated 'SARS-CoV-2 MA10' after ten serial passages in mice to generate a highly representative model of COVID-19 disease in mice[132]. While these models utilize viruses with additional mutations relative to human isolates that may theoretically disrupt efficacy of humoral vaccine responses, they are highly relevant in understanding the mechanisms of SARS-CoV-2 pathogenesis. This work will be further discussed in Chapters 3-6 of this dissertation.

As the COVID-19 pandemic continues, new variants have emerged in the human population that have increased transmissibility or evade humoral immunity[133]. Of note, one of the dominant mutations that arises in many of these highly prevalent variants is substitution N501Y in the S protein, which coincidentally is also the mutation identified by two independent groups via wildtype mouse quasispecies selection[128,134]. Thus, many of the currently circulating SARS-CoV-2 strains are capable of infecting wildtype mice[135-137]. However, without further serial passage, they only cause mild respiratory disease.

1.7 Objectives of this dissertation

Emergent and pre-emergent coronaviruses pose a serious risk to human health. As demonstrated by the COVID-19 pandemic, rapid responses and medical countermeasure development are dependent on robust and representative *in vitro* and *in vivo* models. Here we investigate the human emergence potential of MERS-CoV-like PDF-2180 and the protease requirements for culturing the virus *in vitro*. Additionally, we employed our extensive knowledge of coronavirus replication, host tropism, and animal

models to develop multiple COVID-19 mouse models and implement their use in medical countermeasure development. Finally, we employ our highly pathogenic COVID-19 mouse model to identify the temporal and spatial changes during in surviving mice to understand the mechanisms of post-acute COVID-19 syndrome (PASC). These findings will allow for therapeutic targeting of host immune and repair pathways to ameliorate chronic sequelae following SARS-CoV-2 infection.

REFERENCES

1 Pyke, A. T., Moore, P. R. & McMahon, J. New insights into chikungunya virus emergence and spread from Southeast Asia. *Emerging Microbes & Infections* **7**, 1-3, doi:10.1038/s41426-018-0024-2 (2018).

2 Pierson, T. C. & Diamond, M. S. The emergence of Zika virus and its new clinical syndromes. *Nature* **560**, 573-581, doi:10.1038/s41586-018-0446-y (2018).

3 Girard, M. P., Tam, J. S., Assossou, O. M. & Kieny, M. P. The 2009 A (H1N1) influenza virus pandemic: A review. *Vaccine* **28**, 4895-4902, doi:10.1016/j.vaccine.2010.05.031 (2010).

4 Docea, A. *et al.* A new threat from an old enemy: Re-emergence of coronavirus (Review). *International Journal of Molecular Medicine*, doi:10.3892/ijmm.2020.4555 (2020).

5 Oh, M.-D. *et al.* Middle East respiratory syndrome: what we learned from the 2015 outbreak in the Republic of Korea. *The Korean Journal of Internal Medicine* **33**, 233-246, doi:10.3904/kjim.2018.031 (2018).

6 Borgundvaag, B. SARS outbreak in the Greater Toronto Area: the emergency department experience. *Canadian Medical Association Journal* **171**, 1342-1344, doi:10.1503/cmaj.1031580 (2004).

7 Zhou, P. *et al.* A pneumonia outbreak associated with a new coronavirus of probable bat origin. *Nature* **579**, 270-273, doi:10.1038/s41586-020-2012-7 (2020).

8 Kreuder Johnson, C. *et al.* Spillover and pandemic properties of zoonotic viruses with high host plasticity. *Scientific Reports* **5**, 14830, doi:10.1038/srep14830 (2015).

9 McIntosh, K., Dees, J. H., Becker, W. B., Kapikian, A. Z. & Chanock, R. M. Recovery in tracheal organ cultures of novel viruses from patients with respiratory disease. *Proc Natl Acad Sci U S A* **57**, 933-940, doi:10.1073/pnas.57.4.933 (1967).

10 Bradburne, A. F., Bynoe, M. L. & Tyrrell, D. A. Effects of a "new" human respiratory virus in volunteers. *Br Med J* **3**, 767-769, doi:10.1136/bmj.3.5568.767 (1967).

11 van der Hoek, L. *et al.* Identification of a new human coronavirus. *Nat Med* **10**, 368-373, doi:10.1038/nm1024 (2004).

12 Woo, P. C. *et al.* Characterization and complete genome sequence of a novel coronavirus, coronavirus HKU1, from patients with pneumonia. *J Virol* **79**, 884-895, doi:10.1128/JVI.79.2.884-895.2005 (2005).

13 Perlman, S. & Netland, J. Coronaviruses post-SARS: update on replication and pathogenesis. *Nat Rev Microbiol* **7**, 439-450, doi:10.1038/nrmicro2147 (2009).

14 Weiss, S. R. & Navas-Martin, S. Coronavirus pathogenesis and the emerging pathogen severe acute respiratory syndrome coronavirus. *Microbiol Mol Biol Rev* **69**, 635-664, doi:10.1128/MMBR.69.4.635-664.2005 (2005).

15 Falsey, A. R. *et al.* The "common cold" in frail older persons: impact of rhinovirus and coronavirus in a senior daycare center. *J Am Geriatr Soc* **45**, 706-711, doi:10.1111/j.1532-5415.1997.tb01474.x (1997).

16 Kraaijeveld, C. A., Reed, S. E. & Macnaughton, M. R. Enzyme-linked immunosorbent assay for detection of antibody in volunteers experimentally infected with human coronavirus strain 229 E. *J Clin Microbiol* **12**, 493-497, doi:10.1128/jcm.12.4.493-497.1980 (1980).

17 Macnaughton, M. R., Hasony, H. J., Madge, M. H. & Reed, S. E. Antibody to virus components in volunteers experimentally infected with human coronavirus 229E group viruses. *Infect Immun* **31**, 845-849, doi:10.1128/iai.31.3.845-849.1981 (1981).

18 Reed, S. E. The behaviour of recent isolates of human respiratory coronavirus in vitro and in volunteers: evidence of heterogeneity among 229E-related strains. *J Med Virol* **13**, 179-192, doi:10.1002/jmv.1890130208 (1984).

19 Vijgen, L. *et al.* Complete Genomic Sequence of Human Coronavirus OC43: Molecular Clock Analysis Suggests a Relatively Recent Zoonotic Coronavirus Transmission Event. *Journal of Virology* **79**, 1595-1604, doi:10.1128/jvi.79.3.1595-1604.2005 (2005).

20 Huynh, J. *et al.* Evidence supporting a zoonotic origin of human coronavirus strain NL63. *J Virol* **86**, 12816-12825, doi:10.1128/JVI.00906-12 (2012).

21 Hu, B., Ge, X., Wang, L.-F. & Shi, Z. Bat origin of human coronaviruses. *Virology Journal* **12**, doi:10.1186/s12985-015-0422-1 (2015).

22 Pfefferle, S. *et al.* Distant relatives of severe acute respiratory syndrome coronavirus and close relatives of human coronavirus 229E in bats, Ghana. *Emerg Infect Dis* **15**, 1377-1384, doi:10.3201/eid1509.090224 (2009).

23 Lau, S. K. P. *et al.* Discovery of a Novel Coronavirus, China Rattus Coronavirus HKU24, from Norway Rats Supports the Murine Origin of Betacoronavirus 1 and Has Implications for the Ancestor of Betacoronavirus Lineage A. *Journal of Virology* **89**, 3076-3092, doi:10.1128/jvi.02420-14 (2015).

24 Cui, J., Li, F. & Shi, Z.-L. Origin and evolution of pathogenic coronaviruses. *Nature Reviews Microbiology* **17**, 181-192, doi:10.1038/s41579-018-0118-9 (2019).

25 Drosten, C. *et al.* Identification of a Novel Coronavirus in Patients with Severe Acute Respiratory Syndrome. *New England Journal of Medicine* **348**, 1967-1976, doi:10.1056/nejmoa030747 (2003).

26 Ksiazek, T. G. *et al.* A Novel Coronavirus Associated with Severe Acute Respiratory Syndrome. *New England Journal of Medicine* **348**, 1953-1966, doi:10.1056/nejmoa030781 (2003).

27 Kuiken, T. *et al.* Newly discovered coronavirus as the primary cause of severe acute respiratory syndrome. *Lancet* **362**, 263-270, doi:10.1016/S0140-6736(03)13967-0 (2003).

28 Peiris, J. S. *et al.* Coronavirus as a possible cause of severe acute respiratory syndrome. *Lancet* **361**, 1319-1325, doi:10.1016/s0140-6736(03)13077-2 (2003).

29 Zhong, N. *et al.* Epidemiology and cause of severe acute respiratory syndrome (SARS) in Guangdong, People's Republic of China, in February, 2003. *The Lancet* **362**, 1353-1358, doi:10.1016/s0140-6736(03)14630-2 (2003).

30 Humar, A., McGilvray, I., Phillips, M. J. & Levy, G. A. Severe acute respiratory syndrome and the liver. *Hepatology* **39**, 291-294, doi:10.1002/hep.20069 (2004).

31 Chu, K. H. *et al.* Acute renal impairment in coronavirus-associated severe acute respiratory syndrome. *Kidney International* **67**, 698-705, doi:10.1111/j.1523-1755.2005.67130.x (2005).

32 Zaki, A. M., van Boheemen, S., Bestebroer, T. M., Osterhaus, A. D. & Fouchier, R. A. Isolation of a novel coronavirus from a man with pneumonia in Saudi Arabia. *N Engl J Med* **367**, 1814-1820, doi:10.1056/NEJMoa1211721 (2012).

33 Müller, M. A. *et al.* Presence of Middle East respiratory syndrome coronavirus antibodies in Saudi Arabia: a nationwide, cross-sectional, serological study. *The Lancet Infectious Diseases* **15**, 559-564, doi:10.1016/s1473-3099(15)70090-3 (2015).

34 Lam, T. T.-Y. *et al.* Identifying SARS-CoV-2-related coronaviruses in Malayan pangolins. *Nature* **583**, 282-285, doi:10.1038/s41586-020-2169-0 (2020).

35 Xiao, K. *et al.* Isolation of SARS-CoV-2-related coronavirus from Malayan pangolins. *Nature* **583**, 286-289, doi:10.1038/s41586-020-2313-x (2020).

36 Oran, D. P. & Topol, E. J. Prevalence of Asymptomatic SARS-CoV-2 Infection. *Annals of Internal Medicine* **173**, 362-367, doi:10.7326/m20-3012 (2020).

37 Rothan, H. A. & Byrareddy, S. N. The epidemiology and pathogenesis of coronavirus disease (COVID-19) outbreak. *J Autoimmun* **109**, 102433, doi:10.1016/j.jaut.2020.102433 (2020).

38 Wang, D. *et al.* Clinical Characteristics of 138 Hospitalized Patients With 2019 Novel Coronavirus-Infected Pneumonia in Wuhan, China. *JAMA* **323**, 1061-1069, doi:10.1001/jama.2020.1585 (2020).

39 Carfi, A., Bernabei, R., Landi, F. & Gemelli Against, C.-P.-A. C. S. G. Persistent Symptoms in Patients After Acute COVID-19. *JAMA* **324**, 603-605, doi:10.1001/jama.2020.12603 (2020).

40 Tenforde, M. W. *et al.* Symptom Duration and Risk Factors for Delayed Return to Usual Health Among Outpatients with COVID-19 in a Multistate Health Care Systems Network - United States, March-June 2020. *MMWR Morb Mortal Wkly Rep* **69**, 993-998, doi:10.15585/mmwr.mm6930e1 (2020).

41 Huang, C. *et al.* 6-month consequences of COVID-19 in patients discharged from hospital: a cohort study. *Lancet* **397**, 220-232, doi:10.1016/S0140-6736(20)32656-8 (2021).

42 Nalbandian, A. *et al.* Post-acute COVID-19 syndrome. *Nature Medicine* **27**, 601-615, doi:10.1038/s41591-021-01283-z (2021).

43 Brown, A. J. *et al.* Broad spectrum antiviral remdesivir inhibits human endemic and zoonotic deltacoronaviruses with a highly divergent RNA dependent RNA polymerase. *Antiviral Research* **169**, 104541, doi:10.1016/j.antiviral.2019.104541 (2019).

44 Sheahan, T. P. *et al.* Broad-spectrum antiviral GS-5734 inhibits both epidemic and zoonotic coronaviruses. *Sci Transl Med* **9**, doi:10.1126/scitranslmed.aal3653 (2017).

45 Sheahan, T. P. *et al.* Comparative therapeutic efficacy of remdesivir and combination lopinavir, ritonavir, and interferon beta against MERS-CoV. *Nat Commun* **11**, 222, doi:10.1038/s41467-019-13940-6 (2020).

46 Sheahan, T. P. *et al.* An orally bioavailable broad-spectrum antiviral inhibits SARS-CoV-2 in human airway epithelial cell cultures and multiple coronaviruses in mice. *Sci Transl Med* **12**, doi:10.1126/scitranslmed.abb5883 (2020).

47 Pruijssers, A. J. *et al.* Remdesivir Inhibits SARS-CoV-2 in Human Lung Cells and Chimeric SARS-CoV Expressing the SARS-CoV-2 RNA Polymerase in Mice. *Cell Reports* **32**, 107940, doi:10.1016/j.celrep.2020.107940 (2020).

48 Garwes, D. J. Transmissible gastroenteritis. *Vet Rec* **122**, 462-463, doi:10.1136/vr.122.19.462 (1988).

49 Jung, K., Saif, L. J. & Wang, Q. Porcine epidemic diarrhea virus (PEDV): An update on etiology, transmission, pathogenesis, and prevention and control. *Virus Res* **286**, 198045, doi:10.1016/j.virusres.2020.198045 (2020).

50 Jung, K., Hu, H. & Saif, L. J. Porcine deltacoronavirus infection: Etiology, cell culture for virus isolation and propagation, molecular epidemiology and pathogenesis. *Virus Res* **226**, 50-59, doi:10.1016/j.virusres.2016.04.009 (2016).

51 Zhou, P. *et al.* Fatal swine acute diarrhoea syndrome caused by an HKU2-related coronavirus of bat origin. *Nature* **556**, 255-258, doi:10.1038/s41586-018-0010-9 (2018).

52 Zhou, L. *et al.* The re-emerging of SADS-CoV infection in pig herds in Southern China. *Transboundary and Emerging Diseases* **66**, 2180-2183, doi:10.1111/tbed.13270 (2019).

53 Schulz, L. L. & Tonsor, G. T. Assessment of the economic impacts of porcine epidemic diarrhea virus in the United States. *Journal of Animal Science* **93**, 5111-5118, doi:10.2527/jas.2015-9136 (2015).

54 Saif, L. J. Animal coronavirus vaccines: lessons for SARS. *Dev Biol (Basel)* **119**, 129-140 (2004).

55 Lednicky, J. A. *et al. Emergence of porcine delta-coronavirus pathogenic infections among children in Haiti through independent zoonoses and convergent evolution* (Cold Spring Harbor Laboratory, 2021).

56 Vlasova, A. N. *et al.* Novel Canine Coronavirus Isolated from a Hospitalized Pneumonia Patient, East Malaysia. *Clinical Infectious Diseases*, doi:10.1093/cid/ciab456 (2021).

57 Saif, L. J. Bovine respiratory coronavirus. *Vet Clin North Am Food Anim Pract* **26**, 349-364, doi:10.1016/j.cvfa.2010.04.005 (2010).

58 Edwards, C. E. *et al.* Swine acute diarrhea syndrome coronavirus replication in primary human cells reveals potential susceptibility to infection. *Proceedings of the National Academy of Sciences* **117**, 26915-26925, doi:10.1073/pnas.2001046117 (2020).

59 Fan, Y., Zhao, K., Shi, Z.-L. & Zhou, P. Bat Coronaviruses in China. *Viruses* **11**, 210, doi:10.3390/v11030210 (2019).

60 Menachery, V. D. *et al.* A SARS-like cluster of circulating bat coronaviruses shows potential for human emergence. *Nat Med* **21**, 1508-1513, doi:10.1038/nm.3985 (2015).

61 Menachery, V. D. *et al.* SARS-like WIV1-CoV poised for human emergence. *Proc Natl Acad Sci U S A* **113**, 3048-3053, doi:10.1073/pnas.1517719113 (2016).

62 Anthony, S. J. *et al.* Global patterns in coronavirus diversity. *Virus Evolution* **3**, doi:10.1093/ve/vex012 (2017).

63 Ge, X. Y. *et al.* Isolation and characterization of a bat SARS-like coronavirus that uses the ACE2 receptor. *Nature* **503**, 535-538, doi:10.1038/nature12711 (2013).

64 Hu, B. *et al.* Discovery of a rich gene pool of bat SARS-related coronaviruses provides new insights into the origin of SARS coronavirus. *PLOS Pathogens* **13**, e1006698, doi:10.1371/journal.ppat.1006698 (2017).

65 Latinne, A. *et al. Origin and cross-species transmission of bat coronaviruses in China* (Cold Spring Harbor Laboratory, 2020).

66 Morse, S. S. *et al.* Prediction and prevention of the next pandemic zoonosis. *Lancet* **380**, 1956-1965, doi:10.1016/S0140-6736(12)61684-5 (2012).

67 Müller, M. A. *et al.* MERS Coronavirus Neutralizing Antibodies in Camels, Eastern Africa, 1983–1997. *Emerging Infectious Diseases* **20**, doi:10.3201/eid2012.141026 (2014).

68 Letko, M., Marzi, A. & Munster, V. Functional assessment of cell entry and receptor usage for SARS-CoV-2 and other lineage B betacoronaviruses. *Nature Microbiology* **5**, 562-569, doi:10.1038/s41564-020-0688-y (2020).

69 Zhang, T., Wu, Q. & Zhang, Z. Probable Pangolin Origin of SARS-CoV-2 Associated with the COVID-19 Outbreak. *Current Biology* **30**, 1346-1351.e1342, doi:10.1016/j.cub.2020.03.022 (2020).

70 Anthony, S. J. *et al.* Further Evidence for Bats as the Evolutionary Source of Middle East Respiratory Syndrome Coronavirus. *mBio* **8**, doi:10.1128/mBio.00373-17 (2017).

71 Menachery, V. D. *et al.* Trypsin Treatment Unlocks Barrier for Zoonotic Bat Coronavirus Infection. *J Virol* **94**, doi:10.1128/JVI.01774-19 (2020).

72 Hassan, M. M. *et al.* NeoCoV Is Closer to MERS-CoV than SARS-CoV. *Infectious Diseases: Research and Treatment* **13**, 117863372093071, doi:10.1177/1178633720930711 (2020).

73 Wang, Q. *et al.* Bat Origins of MERS-CoV Supported by Bat Coronavirus HKU4 Usage of Human Receptor CD26. *Cell Host & Microbe* **16**, 328-337, doi:10.1016/j.chom.2014.08.009 (2014).

74 Yang, Y. *et al.* Receptor usage and cell entry of bat coronavirus HKU4 provide insight into bat-to-human transmission of MERS coronavirus. *Proc Natl Acad Sci U S A* **111**, 12516-12521, doi:10.1073/pnas.1405889111 (2014).

75 Li, F. Structure, Function, and Evolution of Coronavirus Spike Proteins. *Annual Review of Virology* **3**, 237-261, doi:10.1146/annurev-virology-110615-042301 (2016).

76 Li, W. *et al.* Angiotensin-converting enzyme 2 is a functional receptor for the SARS coronavirus. *Nature* **426**, 450-454, doi:10.1038/nature02145 (2003).

77 Li, F., Li, W., Farzan, M. & Harrison, S. C. Structure of SARS coronavirus spike receptor-binding domain complexed with receptor. *Science* **309**, 1864-1868, doi:10.1126/science.1116480 (2005).

78 Hofmann, H. *et al.* Human coronavirus NL63 employs the severe acute respiratory syndrome coronavirus receptor for cellular entry. *Proceedings of the National Academy of Sciences* **102**, 7988-7993, doi:10.1073/pnas.0409465102 (2005).

79 Lan, J. *et al.* Structure of the SARS-CoV-2 spike receptor-binding domain bound to the ACE2 receptor. *Nature* **581**, 215-220, doi:10.1038/s41586-020-2180-5 (2020).

80 Shang, J. *et al.* Structural basis of receptor recognition by SARS-CoV-2. *Nature* **581**, 221-224, doi:10.1038/s41586-020-2179-y (2020).

81 Raj, V. S. *et al.* Dipeptidyl peptidase 4 is a functional receptor for the emerging human coronavirus-EMC. *Nature* **495**, 251-254, doi:10.1038/nature12005 (2013).

82 Wang, N. *et al.* Structure of MERS-CoV spike receptor-binding domain complexed with human receptor DPP4. *Cell Research* **23**, 986-993, doi:10.1038/cr.2013.92 (2013).

83 Park, Y.-J. *et al.* Structures of MERS-CoV spike glycoprotein in complex with sialoside attachment receptors. *Nature Structural & Molecular Biology* **26**, 1151-1157, doi:10.1038/s41594-019-0334-7 (2019).

84 Yeager, C. L. *et al.* Human aminopeptidase N is a receptor for human coronavirus 229E. *Nature* **357**, 420-422, doi:10.1038/357420a0 (1992).

85 Hulswit, R. J. G. *et al.* Human coronaviruses OC43 and HKU1 bind to 9-O-acetylated sialic acids via a conserved receptor-binding site in spike protein domain A. *Proceedings of the National Academy of Sciences* **116**, 2681-2690, doi:10.1073/pnas.1809667116 (2019).

86 Huang, X. *et al.* Human Coronavirus HKU1 Spike Protein UsesO-Acetylated Sialic Acid as an Attachment Receptor Determinant and Employs Hemagglutinin-Esterase Protein as a Receptor-Destroying Enzyme. *Journal of Virology* **89**, 7202-7213, doi:10.1128/jvi.00854-15 (2015).

87 Matrosovich, M., Herrler, G. & Klenk, H. D. 1-28 (Springer International Publishing, 2013).

88 Schultze, B. & Herrler, G. Bovine coronavirus uses N-acetyl-9-O-acetylneuraminic acid as a receptor determinant to initiate the infection of cultured cells. *Journal of General Virology* **73**, 901-906, doi:10.1099/0022-1317-73-4-901 (1992).

89 Delmas, B. *et al.* Aminopeptidase N is a major receptor for the enteropathogenic coronavirus TGEV. *Nature* **357**, 417-420, doi:10.1038/357417a0 (1992).

90 Wang, B. *et al.* Porcine Deltacoronavirus Engages the Transmissible Gastroenteritis Virus Functional Receptor Porcine Aminopeptidase N for Infectious Cellular Entry. *Journal of Virology* **92**, JVI.00318-00318, doi:10.1128/jvi.00318-18 (2018).

91 Shirato, K. *et al.* Porcine aminopeptidase N is not a cellular receptor of porcine epidemic diarrhea virus, but promotes its infectivity via aminopeptidase activity. *Journal of General Virology* **97**, 2528-2539, doi:10.1099/jgv.0.000563 (2016).

92 Li, W., van Kuppeveld, F. J. M., He, Q., Rottier, P. J. M. & Bosch, B. J. Cellular entry of the porcine epidemic diarrhea virus. *Virus Res* **226**, 117-127, doi:10.1016/j.virusres.2016.05.031 (2016).

93 Simmons, G., Zmora, P., Gierer, S., Heurich, A. & Pohlmann, S. Proteolytic activation of the SARS-coronavirus spike protein: cutting enzymes at the cutting edge of antiviral research. *Antiviral Res* **100**, 605-614, doi:10.1016/j.antiviral.2013.09.028 (2013).

94 Hoffmann, M., Hofmann-Winkler, H. & Pöhlmann, S. 71-98 (Springer International Publishing, 2018).

95 Belouzard, S., Chu, V. C. & Whittaker, G. R. Activation of the SARS coronavirus spike protein via sequential proteolytic cleavage at two distinct sites. *Proceedings of the National Academy of Sciences* **106**, 5871-5876, doi:10.1073/pnas.0809524106 (2009).

96 Shulla, A. *et al.* A Transmembrane Serine Protease Is Linked to the Severe Acute Respiratory Syndrome Coronavirus Receptor and Activates Virus Entry. *Journal of Virology* **85**, 873-882, doi:10.1128/jvi.02062-10 (2011).

97 Park, J. E. *et al.* Proteolytic processing of Middle East respiratory syndrome coronavirus spikes expands virus tropism. *Proc Natl Acad Sci U S A* **113**, 12262-12267, doi:10.1073/pnas.1608147113 (2016).

98 Johnson, B. A. *et al.* Loss of furin cleavage site attenuates SARS-CoV-2 pathogenesis. *Nature* **591**, 293-299, doi:10.1038/s41586-021-03237-4 (2021).

99 Kleine-Weber, H., Elzayat, M. T., Hoffmann, M. & Pohlmann, S. Functional analysis of potential cleavage sites in the MERS-coronavirus spike protein. *Sci Rep* **8**, 16597, doi:10.1038/s41598-018-34859-w (2018).

100 Millet, J. K. & Whittaker, G. R. Host cell entry of Middle East respiratory syndrome coronavirus after two-step, furin-mediated activation of the spike protein. *Proceedings of the National Academy of Sciences* **111**, 15214-15219, doi:10.1073/pnas.1407087111 (2014).

101 Hofmann, M. & Wyler, R. Propagation of the virus of porcine epidemic diarrhea in cell culture. *J Clin Microbiol* **26**, 2235-2239, doi:10.1128/jcm.26.11.2235-2239.1988 (1988).

102 Hu, H. *et al.* Isolation and characterization of porcine deltacoronavirus from pigs with diarrhea in the United States. *J Clin Microbiol* **53**, 1537-1548, doi:10.1128/JCM.00031-15 (2015).

103 Wicht, O. *et al.* Proteolytic activation of the porcine epidemic diarrhea coronavirus spike fusion protein by trypsin in cell culture. *J Virol* **88**, 7952-7961, doi:10.1128/JVI.00297-14 (2014).

104 Matsuyama, S., Ujike, M., Morikawa, S., Tashiro, M. & Taguchi, F. Protease-mediated enhancement of severe acute respiratory syndrome coronavirus infection. *Proc Natl Acad Sci U S A* **102**, 12543-12547, doi:10.1073/pnas.0503203102 (2005).

105 Kawase, M., Shirato, K., Matsuyama, S. & Taguchi, F. Protease-Mediated Entry via the Endosome of Human Coronavirus 229E. *Journal of Virology* **83**, 712-721, doi:10.1128/jvi.01933-08 (2009).

106 Bonnin, A., Danneels, A., Dubuisson, J., Goffard, A. & Belouzard, S. HCoV-229E spike protein fusion activation by trypsin-like serine proteases is mediated by proteolytic processing in the S2′ region. *Journal of General Virology* **99**, 908-912, doi:10.1099/jgv.0.001074 (2018).

107 V'Kovski, P., Kratzel, A., Steiner, S., Stalder, H. & Thiel, V. Coronavirus biology and replication: implications for SARS-CoV-2. *Nature Reviews Microbiology* **19**, 155-170, doi:10.1038/s41579-020-00468-6 (2021).

108 Kasuga, Y., Zhu, B., Jang, K.-J. & Yoo, J.-S. Innate immune sensing of coronavirus and viral evasion strategies. *Experimental & Molecular Medicine* **53**, 723-736, doi:10.1038/s12276-021-00602-1 (2021).

109 Park, J.-E. *et al.* Proteolytic processing of Middle East respiratory syndrome coronavirus spikes expands virus tropism. *Proceedings of the National Academy of Sciences* **113**, 12262-12267, doi:10.1073/pnas.1608147113 (2016).

110 Zheng, Y. *et al.* Lysosomal Proteases Are a Determinant of Coronavirus Tropism. *J Virol* **92**, doi:10.1128/JVI.01504-18 (2018).

111 Rockx, B. *et al.* Comparative pathogenesis of COVID-19, MERS, and SARS in a nonhuman primate model. *Science* **368**, 1012-1015, doi:10.1126/science.abb7314 (2020).

112 Yu, P. *et al.* Age-related rhesus macaque models of COVID-19. *Animal Model Exp Med* **3**, 93-97, doi:10.1002/ame2.12108 (2020).

113 Munster, V. J. *et al.* Respiratory disease in rhesus macaques inoculated with SARS-CoV-2. *Nature* **585**, 268-272, doi:10.1038/s41586-020-2324-7 (2020).

114 Imai, M. *et al.* Syrian hamsters as a small animal model for SARS-CoV-2 infection and countermeasure development. *Proc Natl Acad Sci U S A* **117**, 16587-16595, doi:10.1073/pnas.2009799117 (2020).

115 Sia, S. F. *et al.* Pathogenesis and transmission of SARS-CoV-2 in golden hamsters. *Nature* **583**, 834-838, doi:10.1038/s41586-020-2342-5 (2020).

116 Kim, Y. I. *et al.* Infection and Rapid Transmission of SARS-CoV-2 in Ferrets. *Cell Host Microbe* **27**, 704-709 e702, doi:10.1016/j.chom.2020.03.023 (2020).

117 Sun, S. H. *et al.* A Mouse Model of SARS-CoV-2 Infection and Pathogenesis. *Cell Host Microbe* **28**, 124-133 e124, doi:10.1016/j.chom.2020.05.020 (2020).

118 Bao, L. *et al.* The pathogenicity of SARS-CoV-2 in hACE2 transgenic mice. *Nature* **583**, 830-833, doi:10.1038/s41586-020-2312-y (2020).

119 Dinnon, K. H., 3rd *et al.* A mouse-adapted model of SARS-CoV-2 to test COVID-19 countermeasures. *Nature* **586**, 560-566, doi:10.1038/s41586-020-2708-8 (2020).

120 Zheng, J. *et al.* COVID-19 treatments and pathogenesis including anosmia in K18-hACE2 mice. *Nature* **589**, 603-607, doi:10.1038/s41586-020-2943-z (2021).

121 Yinda, C. K. *et al.* K18-hACE2 mice develop respiratory disease resembling severe COVID-19. *PLOS Pathogens* **17**, e1009195, doi:10.1371/journal.ppat.1009195 (2021).

122 Muñoz-Fontela, C. *et al.* Animal models for COVID-19. *Nature* **586**, 509-515, doi:10.1038/s41586-020-2787-6 (2020).

123 Sun, J. *et al.* Generation of a Broadly Useful Model for COVID-19 Pathogenesis, Vaccination, and Treatment. *Cell* **182**, 734-743 e735, doi:10.1016/j.cell.2020.06.010 (2020).

124 Israelow, B. *et al.* Mouse model of SARS-CoV-2 reveals inflammatory role of type I interferon signaling. *J Exp Med* **217**, doi:10.1084/jem.20201241 (2020).

125 Hassan, A. O. *et al.* A SARS-CoV-2 Infection Model in Mice Demonstrates Protection by Neutralizing Antibodies. *Cell* **182**, 744-753 e744, doi:10.1016/j.cell.2020.06.011 (2020).

126 Wang, J. *et al.* Mouse-adapted SARS-CoV-2 replicates efficiently in the upper and lower respiratory tract of BALB/c and C57BL/6J mice. *Protein Cell* **11**, 776-782, doi:10.1007/s13238-020-00767-x (2020).

127 Gu, H. *et al.* Adaptation of SARS-CoV-2 in BALB/c mice for testing vaccine efficacy. *Science* **369**, 1603-1607, doi:10.1126/science.abc4730 (2020).

128 Rathnasinghe, R. *et al. The N501Y mutation in SARS-CoV-2 spike leads to morbidity in obese and aged mice and is neutralized by convalescent and post-vaccination human sera* (Cold Spring Harbor Laboratory, 2021).

129 Roy Wong, L.-Y. *et al. Eicosanoid signaling as a therapeutic target in middle-aged mice with severe COVID-19* (Cold Spring Harbor Laboratory, 2021).

130 Muruato, A. *et al. Mouse Adapted SARS-CoV-2 protects animals from lethal SARS-CoV challenge* (Cold Spring Harbor Laboratory, 2021).

131 Roberts, A. *et al.* A mouse-adapted SARS-coronavirus causes disease and mortality in BALB/c mice. *PLoS Pathog* **3**, e5, doi:10.1371/journal.ppat.0030005 (2007).

132 Leist, S. R. *et al.* A Mouse-Adapted SARS-CoV-2 Induces Acute Lung Injury and Mortality in Standard Laboratory Mice. *Cell* **183**, 1070-1085 e1012, doi:10.1016/j.cell.2020.09.050 (2020).

133 Harvey, W. T. *et al.* SARS-CoV-2 variants, spike mutations and immune escape. *Nature Reviews Microbiology* **19**, 409-424, doi:10.1038/s41579-021-00573-0 (2021).

134 Gu, H. *et al.* Adaptation of SARS-CoV-2 in BALB/c mice for testing vaccine efficacy. *Science* **369**, 1603-1607, doi:10.1126/science.abc4730 (2020).

135 Montagutelli, X. *et al. The B1.351 and P.1 variants extend SARS-CoV-2 host range to mice* (Cold Spring Harbor Laboratory, 2021).

136 Martinez, D. R. *et al. A broadly neutralizing antibody protects against SARS-CoV, pre-emergent bat CoVs, and SARS-CoV-2 variants in mice* (Cold Spring Harbor Laboratory, 2021).

137 Martinez, D. R. *et al.* Chimeric spike mRNA vaccines protect against Sarbecovirus challenge in mice. *Science*, eabi4506, doi:10.1126/science.abi4506 (2021).

CHAPTER 2 – TRYPSIN TREATMENT UNLOCKS BARRIER FOR ZOONOTIC BAT CORONAVIRUS INFECTION[1]

2.1 Introduction

Since the beginning of the 21st century, public health infrastructures have been required to periodically respond to new and reemerging zoonotic viral diseases, including influenza, Ebola, and Zika virus outbreaks[1]. Severe acute respiratory syndrome coronavirus (SARS-CoV), the first major outbreak of the century, highlighted the global impact of a newly emerging virus in the context of expanding development, increased globalization, and poor public health infrastructures[2-4]. A decade later, the emergence and continued outbreaks of the Middle East respiratory syndrome corona- virus (MERS-CoV) further illustrate the ongoing threat posed by circulating zoonotic viruses[5]. Together, the outbreaks of the early part of this century argue that continued preparations and vigilance are needed to maintain global public health.

Despite their spontaneous emergence, several research approaches to rapidly respond and even predict outbreak strains already exist. During the MERS-CoV outbreak, our group and others were able to leverage reagents generated against related group 2C coronaviruses, namely, HKU4-CoV and HKU5-CoV[6,7]. These reagents, created independent of viable virus replication, provided valuable insights and models for testing serologic responses during the early stages of the MERS-CoV outbreak. Similarly, reverse genetics systems permitted the exploration of

[1]First published as: Menachery, V.D.[**], Dinnon III, K.H.[**], Yount, B.L., Jr., McAnarney, E.T., Gralinski, L.E., Hale, A., Graham, R.L., Scobey, T., Anthony, S.J., Wang, L., et al. (2020). Trypsin Treatment Unlocks Barrier for Zoonotic Bat Coronavirus Infection. J Virol 94. 10.1128/JVI.01774-19. [**]=co-first authors.

zoonotic coronaviruses[8]; using the known SARS-CoV spike/ACE2 receptor interaction, chimeric viruses containing the backbones of bat CoVs were generated to evaluate the efficacy of both vaccines and therapeutics[9-12]. The inverse approach placed the zoonotic spike proteins in the context of the epidemic SARS-CoV backbone[13,14]. These studies provided insight into potential threats circulating in bats as well as the efficacy of current therapeutic treatments[15]. While far from comprehensive, the results indicated that these approaches, reagents, and predictions may prove useful in preparations for future CoV outbreaks.

In this study, we extend the examination of zoonotic viruses to a novel MERS-like CoV strain isolated from a Ugandan bat, namely, PDF-2180 CoV (MERS-Uganda). Our initial attempt to cultivate a chimeric MERS-CoV containing the Ugandan MERS-like spike produced viral subgenomic transcripts but failed to result in infectious virus after electroporation[16]. However, in the current study, we demonstrate that exogenous trypsin treatment produced high-titer virus capable of plaque formation and continued replication. These results are consistent with the recovery of enteric CoVs like porcine epidemic diarrhea virus[17] but have not previously been described as a major barrier for bat derived CoVs. The chimeric Ugandan MERS-like spike virus could replicate efficiently in both Vero and Huh7 cells in the context of trypsin-containing media but failed to produce infection of either continuous or primary human respiratory cell cultures. Importantly, the MERS-Uganda chimeric virus successfully infected cells of the human digestive tract, potentially identifying another route for cross-species transmission and emergence. Notably, blockade of human DPP4, the receptor for MERS-CoV, had no significant impact on replication of the chimeric MERS-Uganda virus, suggesting the use of an alternative receptor. Similarly, the addition of trypsin also rescued replication of full-length HKU5-CoV, a related group 2C bat CoV, and showed no replication defect during DPP4 blockade. Together, the results indicate that proteolytic activation of the spike protein is a potent constraint to infection for zoonotic CoVs and expand the correlates for CoV emergence beyond receptor binding alone.

2.2 Results

Utilizing the MERS-CoV infectious clone[18], we previously attempted to evaluate the potential of PDF-2180 CoV to emerge from zoonotic populations. Replacing the wild-type MERS-CoV spike with the PDF-2180 spike produced a virus capable of generating viral transcripts in cell culture, but not sustained replication[16]. These results suggested that the significant amino acid differences observed within the receptor- binding domain precluded infection of Vero cells. However, amino acid changes were not confined only to the receptor-binding domain (RBD); highlighting changes be- tween the Uganda spike on the MERS-CoV trimer revealed significant differences throughout the S1 region of spike **(Figure 2.1A and B)**. While the S2 remained highly conserved **(Figure 2.1C)**, changes in the C- and N-terminal domains of S1, in addition to the RBD, may also influence entry and infection compatibility. Notably, recent reports had also indicated differential protease cleavage of wild-type MERS-CoV based on cell types, suggesting that spike processing influences docking and entry of pseudotyped virus[19]. To explore if spike cleavage impaired infectivity, we evaluated MERS-Uganda virus replication in the presence of trypsin-containing media. The addition of trypsin to the chimeric virus resulted in cytopathic effect, fusion of the Vero monolayer, formation of plaques under a trypsin-containing overlay, and collection of high-titer infectious virus stock **(Figure 2.1D)**. Utilizing the trypsin-treated stock, we subsequently examined the MERS-Uganda spike by Western blotting, finding that increasing amounts of trypsin produced more robust spike expression and cleavage **(Figure 2.1E)**. Together, these data indicate that the PDF-2180 spike can mediate infection of Vero cells in a trypsin-dependent manner.

The requirement for trypsin complicated our studies due to cell toxicity; to overcome this issue, we utilized both trypsin-adapted Vero cells and a MERS-Uganda chimera encoding RFP in place of open reading frame 5 (ORF5), similar to a previously generated MERS-CoV reporter virus[18]. Following MERS-Uganda infection, cultures with trypsin-containing medium showed evidence for replication of viral genomic RNA **(Figure 2.2A)**. Similarly, the nucleocapsid protein

was observed only in the presence of exogenous trypsin following infection with the MERS-Uganda chimera **(Figure 2.2B**). Notably, wild-type MERS-CoV expressing RFP was also augmented in the presence of trypsin with increased genomic RNA and nucleocapsid protein relative to no trypsin control **(Figure 2.2A-B)**. Examination of RFP signal confirmed these RNA and protein results **(Figure 2.2C)**, as RFP was only observed in MERS-Uganda chimeric infection in the presence of trypsin.

2.2.1 MERS-Uganda spike replicates in human cells.

Having demonstrated infection and replication, we next sought to determine the capacity of MERS-Uganda chimeric virus to grow in human cells. Previously, MERS-CoV had been shown to replicate efficiently in Huh7 cells[20]. In the Huh7 hepatocyte line, infection with MERS-Uganda RFP chimeric virus resulted in RFP-positive cells and cell fusion **(Figure 2.3A)**. In contrast, while a few RFP-positive cells were observed in the non-trypsin-treated group, neither expanding RFP expression nor cytopathic effect were seen in the absence of trypsin. Our observation may have been the result of residual trypsin activity from the undiluted virus stock, resulting in low-level infection. Exploring further, N protein analysis by Western blotting indicated that the PDF-2180 spike chimera could produce significant viral proteins in the presence of trypsin **(Figure 2.3B)**; only low levels of viral protein were observed in the control-treated infection. While replication of the MERS-Uganda chimera was not equivalent to that of wild-type MERS-CoV, the results clearly demonstrate the capacity of the PDF-2180 spike to mediate infection of human cells in the presence of trypsin.

We next examined the capacity of the MERS-Uganda spike to infect human respiratory cells, the primary targets of SARS-CoV, MERS-CoV, and common cold-causing human CoVs. Using Calu3 cells, a human lung epithelial cell line, we observed robust replication of wild-type MERS-CoV based on RFP expression, consistent with previous studies[18]. However, no evidence of infection was noted in MERS-Uganda-infected Calu3 cells in the presence or absence of

trypsin. We subsequently explored infection of primary human airway epithelial (HAE) cultures. Grown on an air-liquid interface, HAE cultures have a propensity to facilitate improved infections of several human CoVs, so we tested whether they were more permissive for infection with the PDF-2180 spike chimera[21]. To infect, PDF-2180 chimeric virus grown in the presence of trypsin was inoculated onto the apical surface of the HAE culture; cultures were subsequently washed with phosphate-buffered saline (PBS) containing 5 μg/ml trypsin at 0, 18, 24, and 48 hours post infection for 10 minutes and then removed. Following infection, no evidence of RFP expression was observed even after trypsin washes of the apical surface **(Figure 2.3C)**. Similarly, we found no evidence for accumulation of viral genomic RNA by qRT-PCR, indicating no evidence for replication in HAE cultures **(Figure 2.3D)**. In contrast, wild-type MERS-CoV efficiently infects these HAE cultures, as demonstrated by both RFP expression and viral genomic RNA accumulation. Together, the Calu3 and HAE results suggest that the PDF-2180 spike is unable to infect human respiratory cells in humans, even in the presence of exogenous trypsin.

We next evaluated the capacity of the PDF-2180 chimera to infect cells of the digestive tract. While uncommon in humans, several animal CoVs have been shown to cause severe disease via the enteric pathway[22,23]. In addition, most bat CoV sequences, including PDF-2180-CoV, were isolated from bat guano samples, suggesting an enteric tropism. Importantly, the presence of trypsin and other soluble host proteases in the digestive tract could facilitate infection with the PDF-2180 spike in humans. To test this question, we infected Caco-2 cells, a human epithelial colorectal adenocarcinoma cell line, with wild-type MERS-CoV and MERS-Uganda spike chimera in the presence or absence of trypsin **(Figure 2.3E)**. For MERS-CoV, infection of Caco-2 cells resulted in robust infection and spread with or without trypsin in the media. For the MERS- Uganda chimera, the addition of trypsin facilitated infection producing many RFP-positive Caco-2 cells; however, infection was not as robust as with the wild-type MERS-CoV. Examination of N protein by Western blotting indicated that the MERS- Uganda spike could produce infection in Caco-2 cells but confirmed replication at levels lower than that with wild-type MERS-CoV

(Figure 2.3F). Together, the results indicate that human cells, including gut cells, can support infection with the MERS-Uganda chimera in the presence of trypsin.

2.2.2 MERS-Uganda spike does not use DPP4 for entry.

The absence of infection of human respiratory cells coupled with significant changes in the RBD suggested that MERS-Uganda does not utilize the MERS-CoV receptor human DPP4 for entry[16]. To explore this question, we utilized antibodies to block DPP4 in Vero cells to determine the effect on MERS-Uganda chimeric virus replication. As expected, the anti-DPP4 antibody successfully ablated replication of wild-type MERS-CoV in both the presence and the absence of trypsin treatment, as measured by both RFP and N protein expression **(Figure 2.4A-B)**. In contrast, the human DPP4-blocking antibody had no impact on infection with the MERS-Uganda chimera virus in the presence of trypsin, confirming that the MERS-CoV receptor is not required to mediate infection with the PDF-2180 spike. Together, these results indicate that while the MERS-Uganda spike infects human cells, it does not require human DPP4 to mediate infection.

2.2.3 MERS-CoV therapeutics are ineffective against MERS-Uganda spike.

Having established replication capacity in human cells, we next sought to determine if therapeutics developed against the MERS-CoV spike could disrupt infection with the MERS-Uganda spike chimera. Several monoclonal antibodies have been identified as possible therapeutic options for the treatment of MERS-CoV, including LCA60 and G4. We first evaluated LCA60, a potent antibody that binds adjacent to the spike RBD of MERS-CoV[24]. However, the major changes in the RBD region of the MERS-Uganda spike predicted a lack of efficacy **(Figure 2.5A)**. LCA60 potently neutralized wild-type MERS-CoV grown in both the presence and the absence of trypsin **(Figure 2.5B)**. However, consistent with expectations, the LCA60 antibody had no impact on infection with the MERS-Uganda chimera, failing to neutralize the bat spike-

expressing virus **(Figure 2.5B)**. We subsequently examined a second monoclonal antibody, G4, which had previously mapped to a conserved portion of the S2 region of the MERS-spike **(Figure 2.5A)**[25]. With the epitope relatively conserved in the MERS-Uganda spike, we tested the efficacy against the zoonotic spike chimera. However, the results demonstrate no neutralization of MERS-Uganda spike virus by the S2-targeted antibody **(Figure 2.5C)**. Notably, G4 also failed to neutralize wild-type MERS-CoV grown in the presence of exogenous trypsin **(Figure 2.5C)**. Together, the results indicate that both group 2C CoV spikes could escape neutralization by the S2-targeted antibody in the presence of exogenous trypsin. Overall, these experiments suggest that antibodies targeted against MERS-CoV, even to regions in the highly conserved S2 domain, may not have utility against viruses expressing the PDF-2180 spike.

2.2.4 Trypsin treatment rescues the replication of zoonotic HKU5-CoV.

Based on the MERS-Uganda chimera virus, we wondered if a similar barrier prevented replication of other zoonotic CoVs. Previously, our group had generated a full-length infectious clone for HKU5-CoV, another group 2C coronavirus sequence isolated from bats. Similar to the MERS-Uganda chimera, the infectious clone of HKU5-CoV produced subgenomic transcripts but failed to achieve productive infection[6]. Revisiting the full-length recombinant virus, we sought to determine if trypsin treatment could also rescue HKU5-CoV. Following HKU5-CoV infection, the addition of trypsin to the media resulted in cytopathic effect and cell fusion. In contrast, cultures lacking trypsin showed no signs of viral infection. Exploring viral genomic RNA, trypsin in the culture media permitted robust infection with HKU5-CoV that increased over time and was absent in cells not treated with trypsin **(Figure 2.6A)**. Similarly, trypsin in the media also permitted the accumulation and proteolytic cleavage of the HKU5 spike protein in a dose- and time-dependent manner **(Figure 2.6B)**. Importantly, the addition of the anti-DPP4 antibody had no impact on HKU5-CoV infection, suggesting the use of a different receptor than that used by wild-type MERS-CoV, similar to the findings with the MERS-Uganda spike **(Figure 2.6C)**. Together, these results

demonstrate that protease cleavage is also the primary barrier to infection of Vero cells with HKU5-CoV. Examining further, we compared the predicted cleavage at S1/S2 border, S2', and the endosomal cysteine protease site across MERS, PDF2180, and HKU5 spikes **(Figure 2.6D)**[25]. For the S1/S2 site, MERS, Uganda, and HKU5 maintain the RXXR cleavage motif, although the different interior amino acids may alter efficiency. For the S2' sequence, MERS and HKU5 also retain the RXXR motif; however, the Uganda spike lacks the first arginine (SNAR), potentially impacting cleavage. Finally, all three spikes maintain an aromatic residue at position two in the endosomal cysteine protease (ECP) site[26]. However, the HKU5 spike maintains N at position 1 which is similar to a MERS mutant previously shown to inactivate cathepsin L activation[27]. Together, the results suggest that potential sequence changes in the protease cleavage sites may contribute to the trypsin dependency of MERS-Uganda and HKU5 spike-mediated infections.

2.3 Discussion

In this study, we expanded our examination of circulating zoonotic viruses and identified protease cleavage as an important barrier to emergence of some group 2C zoonotic CoVs. The chimeric virus containing the spike protein from PDF-2180 was capable of replication in Vero cells and human cells (Huh7 and Caco-2) if treated with exogenous trypsin. However, neither continuous nor primary human airway cultures were susceptible to infection, in contrast to wild-type MERS-CoV. The MERS-Uganda chimera also maintained replication despite treatment with antibodies blocking human DPP4, suggesting use of either an alternative receptor or a different entry mechanism for infection. Importantly, current therapeutics targeting the MERS spike protein showed no efficacy against the MERS-Uganda chimera, highlighting a potential public health vulnerability to this and related group 2C CoVs. Finally, the trypsin-mediated rescue of a second zoonotic group 2C CoV, HKU5-CoV, validates findings that suggested that protease cleavage may represent a critical barrier to zoonotic CoV infection in new hosts[28,29]. Together, the results highlight the importance of spike processing in CoV infection, expand the correlates associated

with emergence beyond receptor binding alone, and provide a platform strategy to recover previously non-cultivatable zoonotic CoVs.

With the ongoing threat posed by circulating zoonotic viruses, understanding the barriers for viral emergence represents a critical area of research. For CoVs, receptor binding has been believed to be the primary constraint to infection in new host populations. Following the SARS-CoV outbreak, emergence in humans was attributed to mutations within the receptor-binding domain that distinguished the epidemic strain from progenitor viruses harbored in bats and civets[30]. Yet, work by our group and others has indicated that zoonotic SARS-like viruses circulating in Southeast Asian bats are capable of infecting human cells by binding to the known human ACE2 receptor without adaptation[13,14,31]. Similarly, pseudotyped virus studies have identified zoonotic strains HKU4-CoV and NL140422-CoV as capable of binding to human DPP4 without mutations to the spike[29,32]. In this study, we demonstrate that both PDF-2180 and HKU5-CoV spikes are capable of binding to and infecting human cells if primed by trypsin cleavage. Together, the results argue that several circulating zoonotic CoV strains have the capacity to bind to human cells without adaption and that receptor binding may not be the only barrier to CoV emergence.

Data from this study implicate the processing of the spike protein as a critical factor for CoV infection. In the absence of trypsin, the MERS-Uganda and HKU5-CoV spikes were unable to mediate infection and initially suggested a lack of receptor compatibility[6,16]. However, exogenous trypsin treatment produced robust infection, indicating that despite binding to human cells, CoVs cannot overcome incomplete spike processing. As such, evaluating zoonotic virus populations for emergence threats must also consider the capacity for CoV spike activation in addition to receptor binding. While exogenous processing of the spike has been well described as necessary for enteric CoVs[17], spike processing has not been considered a primary barrier for bat CoVs despite their enteric origins. In this new paradigm for bat CoVs, the combination of receptor binding and proteolytic activation by endogenous proteases permits zoonotic CoV

infection, as with MERS-CoV and SARS-CoV **(Figure 2.7)**. The absence of receptor binding **(Figure 2.7A)** or compatible host protease activity **(Figure 2.7B)** restricts infection with certain zoonotic strains like PDF-2180 or HKU5-CoV. These barriers can be overcome with the addition of exogenous proteases, disrupting the need for host proteases, and permitting receptor-dependent or receptor-independent entry **(Figure 2.7C)**.

Overall, the new paradigm argues that both receptor binding and protease activation barriers must be overcome for successful zoonotic CoV infection of a new host. The requirement for exogenous trypsin treatment is not unique to MERS-Uganda or HKU5-CoV. Influenza strains are well known to require trypsin treatment to facilitate their release in cell culture[33]. In addition, highly pathogenic avian influenza strains have been linked to mutations that improve cleavage by ubiquitous host proteases, augmenting their tissue tropism and virulence[34]. Similarly, a wealth of enteric viruses, including poliovirus, cowpox, and rotaviruses, depend on trypsin to prime, modulate, and/or expand infection[35,36]. Even within the CoV family, enteric viruses, including porcine epidemic diarrhea virus (PEDV), porcine delta CoV, and swine acute diarrhea syndrome (SADS) CoV require trypsin for replication in cell culture[37-39]. Together, these prior studies illustrate the importance of protease activation in virus infections. However, the protease barrier to PDF-2180 and HKU5-CoV spike-mediated infection may also reflect on the emergence of SARS-CoV and MERS-CoV. While initial studies argued that receptor binding was the primary barrier, the existence of zoonotic strains capable of efficiently using the same human entry receptors does not support that model[13,14]. It is possible that emergence of epidemic CoV strains also requires modifying protease cleavage in either humans or an intermediate host, such as camels or civets, in addition to increased receptor-binding affinity. Consistent with this idea, reports have detailed differential infection with MERS-CoV based on host protease expression[19]. Similarly, mouse adaptation of MERS-CoV resulted in spike modifications that alter protease activation and entry *in vivo*[40]. Coupled with the augmented replication and protein production of wild-type MERS-CoV in the presence of trypsin, the results suggest that the proteolytic cleavage

epidemic MERS-CoV could still be enhanced, potentially by augmenting the cell surface entry mechanism, as previously described for SARS-CoV[41]. While group 2B bat CoV strains (WIV1-CoV, WIV16-CoV, and SHC014-CoV) do not require trypsin for infection[9,13,14,42], differences in protease activation may contribute to infection changes relative to the epidemic SARS-CoV. In this context, our findings expand the importance of protease cleavage as a criterion to consider for zoonotic virus emergence in a new host population.

In evaluating the threat to humans posed by PDF-2180 and HKU5-CoV, the results demonstrate a pathway to emergence. Neither CoV spike uses human DPP4 for entry, and the PDF-2180 chimera failed to replicate in human respiratory models, even in the presence of trypsin. As many different proteases can promote CoV entry, future studies must determine if other protease treatments or other components can promote virus replication in HAE cultures[28,43,44]. However, replication in Huh7 and Caco-2 cells indicates human infection compatibility and may portend differential tropism, possibly in the alimentary or biliary tracts, as has been described for several mammalian CoVs[37-39]. MERS-Uganda or HKU5-CoV could utilize this same trypsin-rich environment in the gut to emerge as an enteric pathogen in humans, although its pathology and virulence would be hard to predict. Evidence from both SARS-CoV and MERS-CoV outbreaks suggests the involvement of enteric pathways during infection[45,46]. Replication in the gut might select for mutations that expand spike processing/tropism and allow replication in other tissues, including the lung, and lead to virulent disease in the new host population, as seen with porcine respiratory coronavirus[47]. In examining the threat posed by PDF-2180 and HKU5-CoV, we must consider the emergence of these CoVs in tissues other than the lung and that they harbor distinct pathologies compared with epidemic SARS and MERS-CoV.

The receptor dynamics of MERS-Uganda and HKU5-CoV also remain unclear in the context of this study. In the presence of trypsin, neither spike protein requires the MERS-CoV receptor DPP4 for entry, which is consistent with the differences between the receptor-binding domains of the bat and epidemic strains. Therefore, it was not surprising that antibodies that target

the RBD of the MERS-CoV spike were ineffective in blocking infection of the PDF-2180 chimera. However, the S2-targeted antibody G4 also had no efficacy against MERS-Uganda, despite a relatively conserved binding epitope. This result is possibly explained by differing amino acid sequences between MERS-CoV and PDF-2180 at the G4 epitope, specifically residue 1175, which is associated with G4 escape mutants in MERS-CoV[48]. Alternatively, the G4 antibody also failed to neutralize wild-type MERS-CoV grown in the presence of trypsin, indicating that entry is still possible, despite treatment with antibody binding the S2 domain. These results suggest that trypsin treatment may permit a conformational change either masking the G4 epitope or facilitating fusion/entry prior to antibody binding. Conversely, the presence of trypsin may prime a receptor-independent entry for the MERS-Uganda chimera, similar to the JHVM strain of MHV[49]. Yet, this result would contrast with that of PEDV, which requires receptor binding prior to trypsin activation to facilitate infection[38]. Importantly, the lack of infection in respiratory cells suggests that some receptor or attachment factor is necessary to mediate entry with the PDF-2180 spike. Recent work with MERS-CoV binding sialic acid supports this idea[50] and indicates that the PDF-2180 spike may not have a similar binding motif. Overall, further experimental studies are required to fully understand the receptor dynamics of the PDF-2180 spike.

This study provides a new strategy to recover zoonotic CoVs, and highlights proteolytic cleavage of the spike as a major barrier to group 2C zoonotic CoV infection. For both MERS-Uganda and HKU5-CoV, the addition of exogenous trypsin rescues infection, indicating that spike cleavage, not receptor binding, limits these strains in new hosts and tissues. The adaptation of the protease cleavage sites or infection of tissues with robust host protease expression could permit these two zoonotic CoV strains to emerge and may pose a threat to public health due to the absence of effective spike-based therapeutics. In considering cross-species transmission, our results using reconstructed bat group 2C CoVs confirm spike processing as a correlate associated with emergence. Adding spike processing to receptor binding as primary barriers offers a new framework to evaluate the threat of emergence for zoonotic CoV strains.

2.4 Materials and Methods

2.4.1 Cells, viruses, cell culture infection, and plaque assays.

Vero cells were grown in Dulbecco's modified Eagle medium (DMEM; Gibco, CA) supplemented with 5% FetalClone II (HyClone, UT) and antibiotic/antimycotic (anti/anti) (Gibco). Huh7 cells were grown in DMEM supplemented with 10% FetalClone II and anti/anti. Caco-2 cells were grown in MEM (Gibco) supplemented with 20% fetal bovine serum (HyClone) and anti/anti. Human airway epithelial cell (HAE) cultures were obtained from the University of North Carolina (UNC) Cystic Fibrosis (CF) Center Tissue Procurement and Cell Culture Core from human lungs procured under University of North Carolina at Chapel Hill Institutional Review Board-approved protocols. Wild-type MERS-CoV, chimeric MERS-Uganda, and HKU5-CoV were cultured on Vero cells in Opti-MEM (Gibco) supplemented with anti/anti. For indicated experiments, trypsin (Gibco) was added at 0.5 μg/ml unless otherwise indicated.

Generation of wild-type MERS-CoV, MERS-Uganda, and HKU5-CoV viruses utilized reverse genetics and have been previously described[6,16,18]. For MERS-Uganda chimera expressing RFP, we utilized the MERS-CoV backbone, replacing ORF5 with RFP as previously described[18]. Synthetic constructions of chimeric mutant and full-length MERS-Uganda and HKU5-CoV were approved by the University of North Carolina Institutional Biosafety Committee.

Replication in Vero, Calu-3 2B4, Caco-2, Huh7, and HAE cells was performed as previously described[12,51-53]. Briefly, cells were washed with PBS and inoculated with virus or mock diluted in Opti-MEM for 60 minutes at 37°C. Following inoculation, cells were washed three times, and fresh medium with or without trypsin was added to signify time zero. Three or more biological replicates were harvested at each described time point. For HAE cultures, apical surfaces were washed with PBS containing 5 μg/ml trypsin at 0, 8, 18, 24, and 48 hours post infection. Sample

collections were not conducted in a blind manner nor were samples randomized. Microscopy photos were captured via a Keyence BZ-X700 microscope.

For antibody neutralization assays, MERS-CoV and MERS-Uganda stocks were grown in Opti-MEM both with and without trypsin. All stocks were quantified via plaque assay by overlaying cells with 0.8% agarose in Opti-MEM supplemented with 0.5 μg/ml trypsin and anti/anti. MERS-Uganda stocks grown without trypsin had low titers but were sufficient for neutralization assays.

For anti-DPP4 blocking experiments, Vero cells were preincubated with serum-free Opti-MEM containing 5 μg/ml anti-human DPP4 antibody (R&D systems, MN) for 1 hour. Medium was removed, and cells were infected for 1 hour with virus or mock inoculum at a multiplicity of infection of 0.1. The inoculum was removed, cells were washed three times with PBS, and medium was replaced.

2.4.2 RNA isolation and quantification.

RNA was isolated via TRIzol reagent (Invitrogen, CA) and Direct-zol RNA miniprep kit (Zymo Research, CA) according to the manufacturer's protocol. MERS-CoV and MERS-Uganda genomic RNA (gRNA) was quantified via TaqMan fast virus 1-step master mix (Applied Biosystems, CA) using previously reported primers and probes targeting ORF1ab[53] and normalized to host 18S rRNA (Applied Biosystems). HKU5-CoV RNA was first reverse transcribed using SuperScript III (Invitrogen) and was then assayed using SsoFast EvaGreen supermix (Bio-Rad, CA) and scaled to host glyceraldehyde-3-phosphate dehydrogenase (GAPDH) transcript levels. HKU5 gRNA was amplified with the following primers: forward, 5=-CTCTCTCTCGTTCTCTTGCAGAAC-3=; and reverse, 5=-GTTGAGCTCTGCT CTATACTTGCC-3=. GAPDH RNA was amplified with the following primers: forward, 5=-AGCCACATCGCT GAGACA-3=; and reverse, 5=-GCCCAATACGACCAAATCC-3=. Fold change was calculated

using the threshold cycle (ΔΔ*CT*) method and was scaled to RNA present at 0 hours post infection.

2.4.3 Generation of VRP, polyclonal mouse antisera, and Western blot analysis.

Virus replicon particles (VRPs) expressing the MERS-CoV nucleocapsid, MERS-Uganda spike, or HKU5-5 CoV spike were con- structed using a non-select agent biosafety level 2 (BSL2) Venezuelan equine encephalitis virus (VEEV) strain 3546 replicon system, as previously described[54]. Briefly, RNA containing the nonstructural genes of VEEV and either MERS-CoV nucleocapsid or HKU5-5 CoV spike was packaged using helper RNAs encoding VEEV structural proteins as described previously[55]. Six-week-old female BALB/c mice were primed and boosted with VRPs to generate mouse antisera toward either MERS-CoV nucleocapsid or HKU5-5 CoV spike. Following vaccination, mouse polyclonal sera were collected as described previously[56]. For Western blotting, lysates from infected cells were prepared as described before in detail[57], and these blots were probed using the indicated mouse polyclonal sera. MERS-CoV N sera was able to detect to HKU5-CoV N protein via Western blot as previously described[7].

2.4.4 Virus neutralization assays.

Plaque reduction neutralization titer assays were performed with previously characterized antibodies against MERS-CoV, as previously described[24,48]. Briefly, antibodies were serially diluted 6- to 8-fold and incubated with 80 PFU of the indicated viruses for 1 h at 37°C. The virus and antibodies were then added to a 6-well plate of confluent Vero cells in triplicate. After a 1 hour incubation at 37°C, cells were overlaid with 3 ml of 0.8% agarose in Opti-MEM supplemented with 0.5 μg/ml trypsin and anti/anti. Plates were incubated for 2 or 3 days at 37°C for MERS-CoV or MERS- Uganda, respectively, and were then stained with neutral red for 3 h, and plaques were counted. The percentage of plaque reduction was calculated as (1 – [number of plaques with antibody/number of plaques without antibody]) * 100.

2.4.5 Biosafety and biosecurity.

Reported studies were initiated after the University of North Carolina Institutional Biosafety Committee approved the experimental protocols. All work for these studies was performed with approved standard operating procedures (SOPs) and safety conditions for MERS-CoV and other related CoVs. Our institutional CoV BSL3 facilities have been designed to conform to the safety requirements recommended by Biosafety in Microbiological and Biomedical Laboratories (BMBL), the U.S. Department of Health and Human Services, the Public Health Service, the Centers for Disease Control and Prevention (CDC), and the National Institutes of Health (NIH). Laboratory safety plans have been submitted, and the facility has been approved for use by the UNC Department of Environmental Health and Safety (EHS) and the CDC.

2.4.6 Accession number

The nearly complete genome sequence for MERS-CoV EMC (GenBank accession number JX869059) and PREDICT/PDF-2180 (GenBank accession number KX574227) were previously deposited in GenBank[16,58].

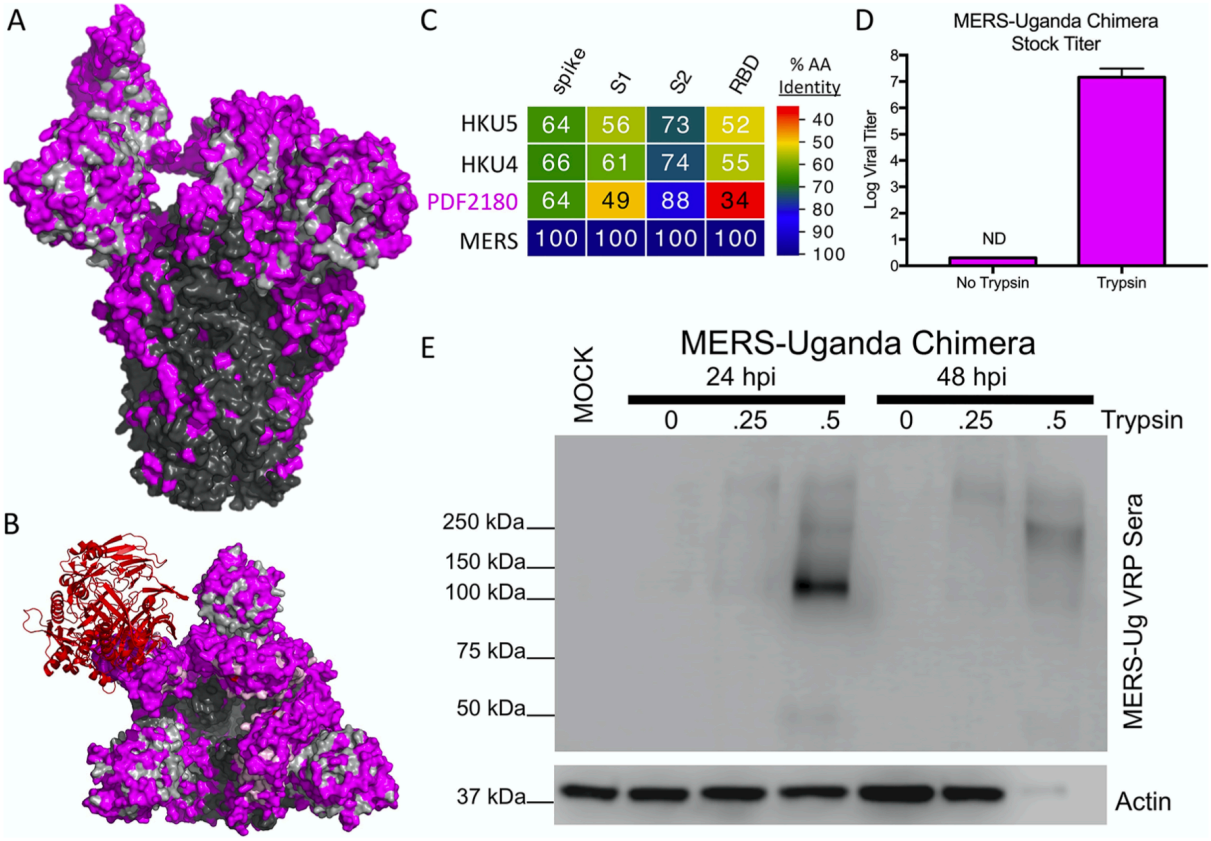

Figure 2.1. Exogenous trypsin rescues MERS-Uganda spike replication.

Exogenous trypsin rescues MERS-Uganda spike replication. (A and B) Structure of the MERS-CoV spike trimer in complex with the receptor human DPP4 (red) from the side (A) and top (B). Consensus amino acids are outlined for the S1 (gray) and S2 (black) domains, with PDF-2180 differences noted in magenta. (C) Spike protein sequences of the indicated viruses were aligned according to the bounds of total spike, S1, S2, and receptor-binding domain (RBD). Sequence identities were extracted from the alignments, and a heatmap of sequence identity was constructed using EvolView (www.evolgenius.info/evolview) with MERS-CoV as the reference sequence. (D) MERS-Uganda chimera stocks were grown in the presence or absence of trypsin and were quantitated by plaque assay with a trypsin-containing overlay (n = 2). (E) Protein expression of MERS-Uganda spike (S) and actin 24 and 48 hours post infection of Vero cells in the presence of increasing amounts of trypsin (none, 0.25 μg/ml, and 0.5 μg/ml) in the media.

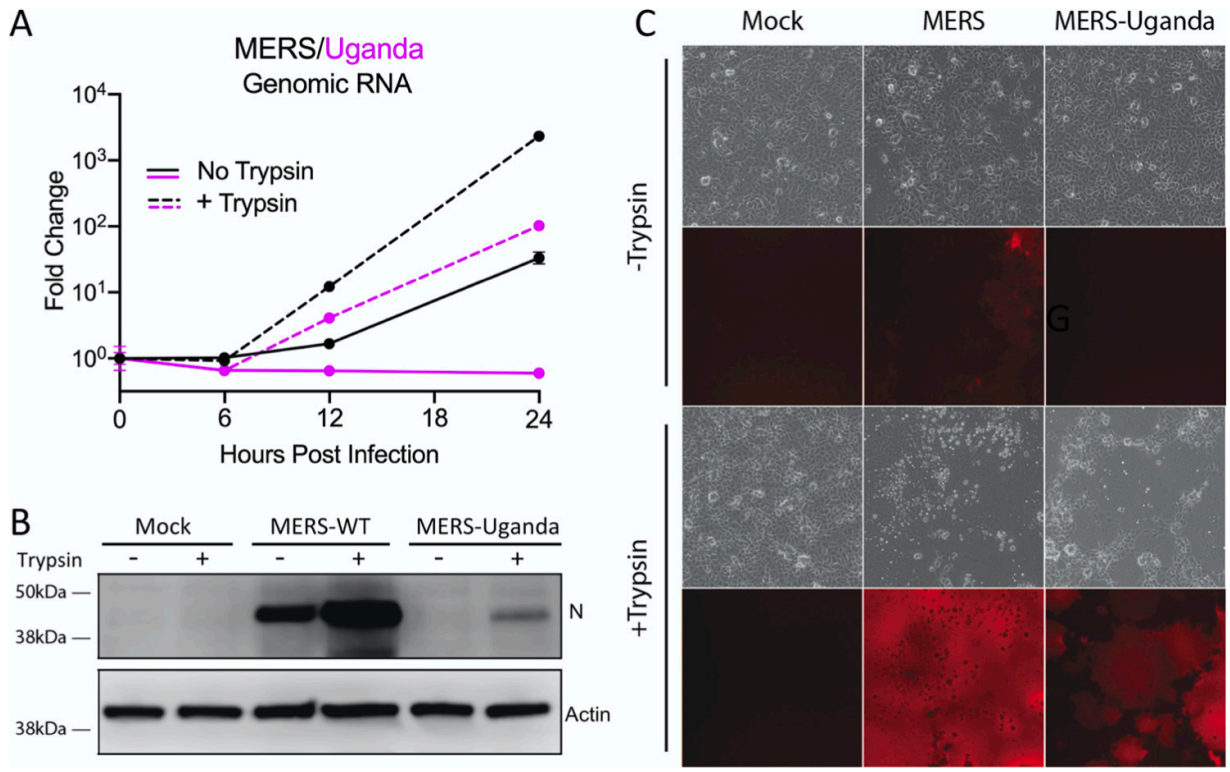

Figure 2.2. Trypsin treatment facilitates MERS-Uganda replication in Vero cells

(A) Trypsin-resistant Vero cells were infected with MERS-CoV (black) or MERS-Uganda chimera (magenta) and were monitored for expression of genomic RNA in the presence or absence of trypsin (*n* = 3 for each time point). (B) Protein expression of MERS-CoV nucleocapsid (N) and actin 18 hours post infection of Vero cells in the presence or absence of trypsin in the media. (C) RFP expression microscopy in Vero cells infected with MERS-CoV, MERS-Uganda spike chimera, or mock in the presence or absence of trypsin.

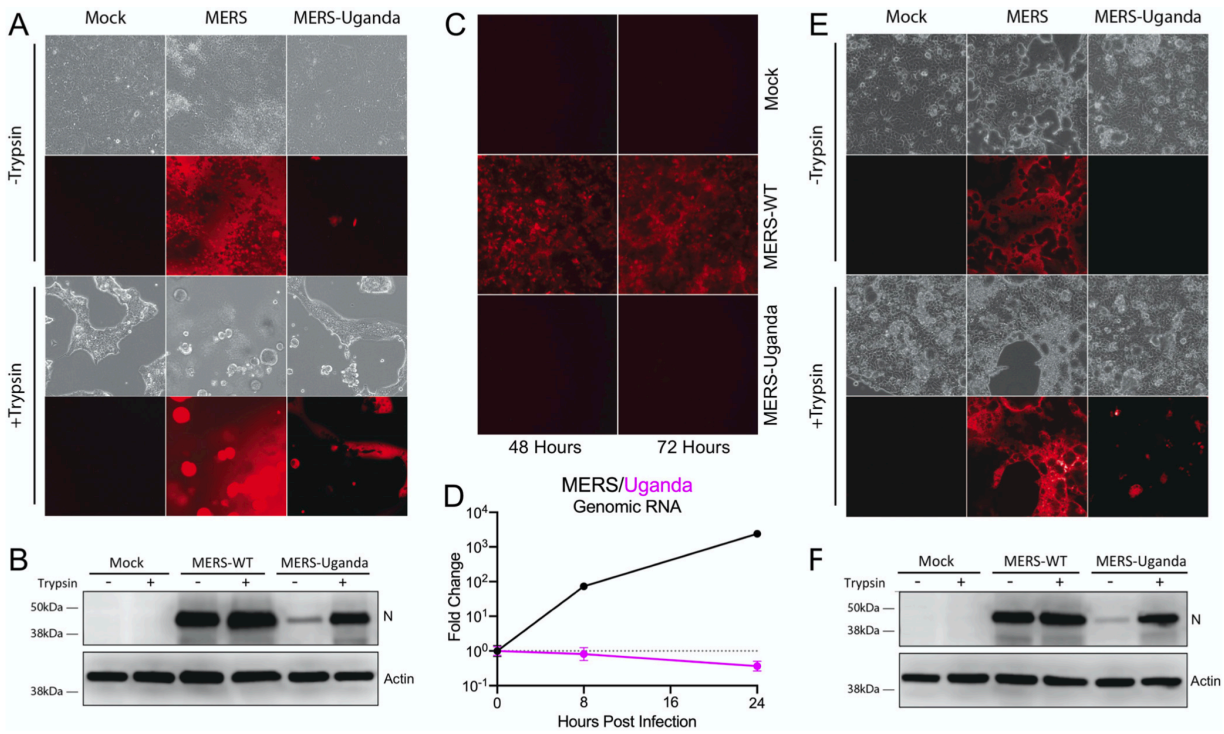

Figure 2.3. MERS-Uganda spike chimera replicates in human cells

(A and B) Huh7 cells were infected with MERS-CoV or MERS-Uganda chimeric viruses, showing microscopy images of cell monolayer and RFP expression with and without trypsin treatment (A) and N protein expression following infection of Huh7 cells in the presence or absence of trypsin (B). (C and D) Primary HAE cultures were infected with MERS-CoV or MERS-Uganda chimera, showing RFP expression (C) and genomic viral RNA following infection (D) (*n* = 3 for 8 and 24 hours post infection [hpi]). (E and F) Caco-2 cells were infected with MERS-CoV or MERS-Uganda chimeric viruses expressing RFP, showing microscopy images of cell monolayer and RFP expression with and without trypsin treatment (E) and N protein expression following infection of Caco-2 cells in the presence or absence of trypsin (F).

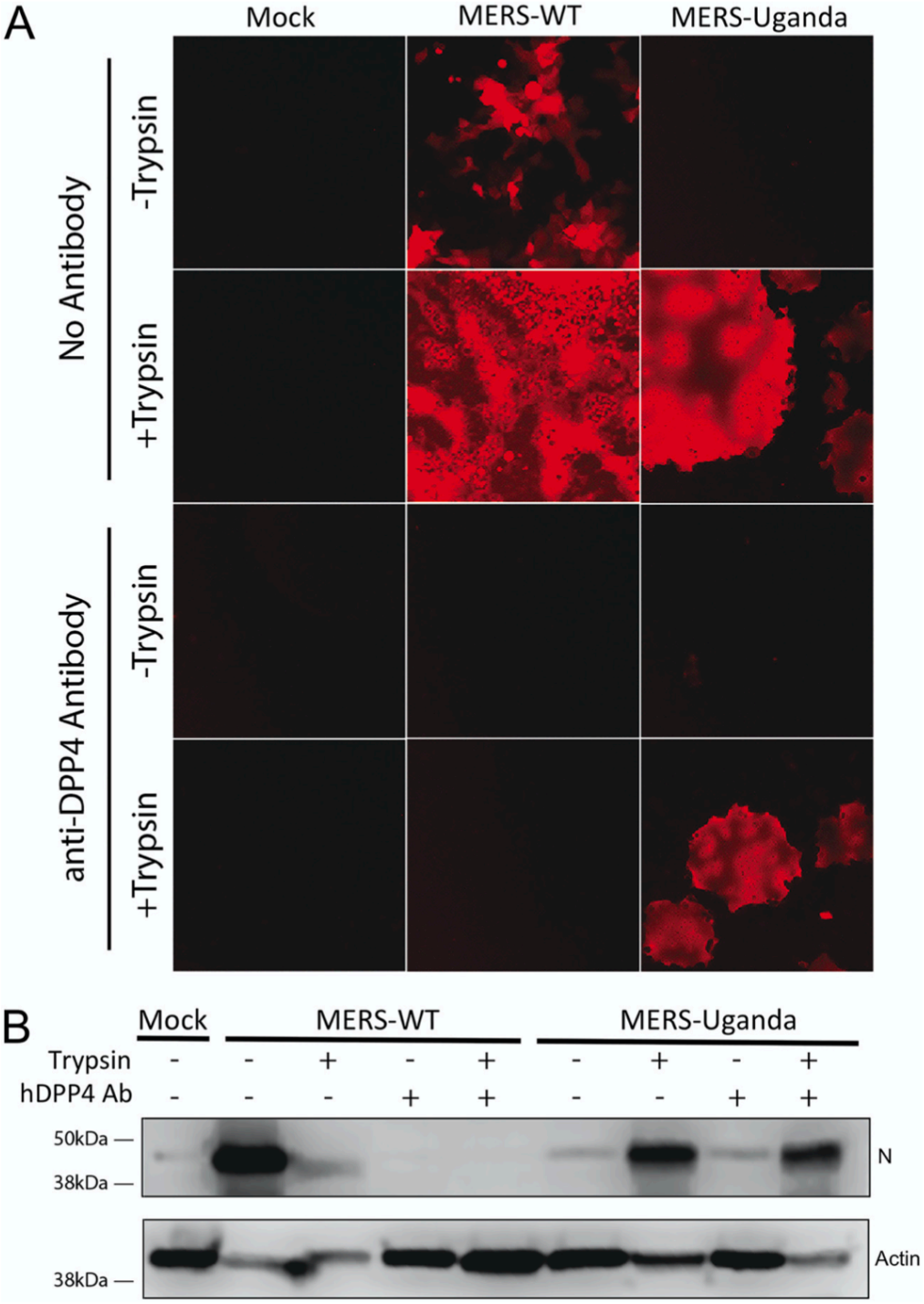

Figure 2.4. MERS-Uganda spike does not utilize DPP4 for infection.

(A and B) Vero cells were infected with MERS-CoV or MERS-Uganda chimeric virus in the presence or absence of trypsin and a blocking antibody against human DPP4. (A) Fluorescent microscopy showing RFP expression 24 hours post infection for each treatment group. (B) Western blot of N protein and actin 24 hours post infection.

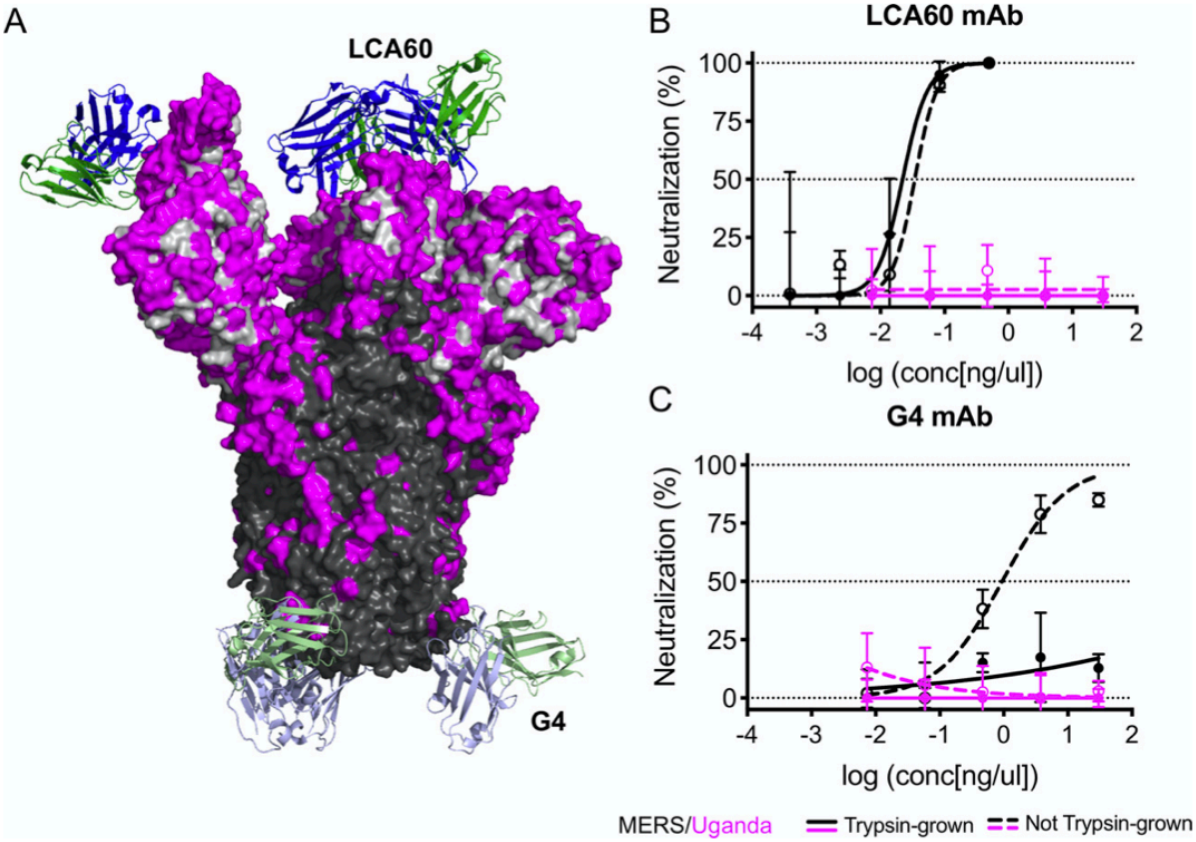

Figure 2.5. Antibodies against MERS-CoV fail to neutralize MERS-Uganda chimera.

(A) Structure of the MERS-CoV spike trimer with therapeutic antibody LCA60 bound adjacent to the receptor-binding domain and the antibody G4 bound to the S2 portion. Consensus amino acids are outlined for the S1 (gray) and S2 (black) domains, with PDF-2180 differences noted in magenta. (B and C) Plaque neutralization curves for LCA60 (B) and G4 (C) with (solid) and without (dotted) trypsin treatment for MERS-CoV (black) and MERS-Uganda chimera (magenta) (*n* = 3 per concentration).

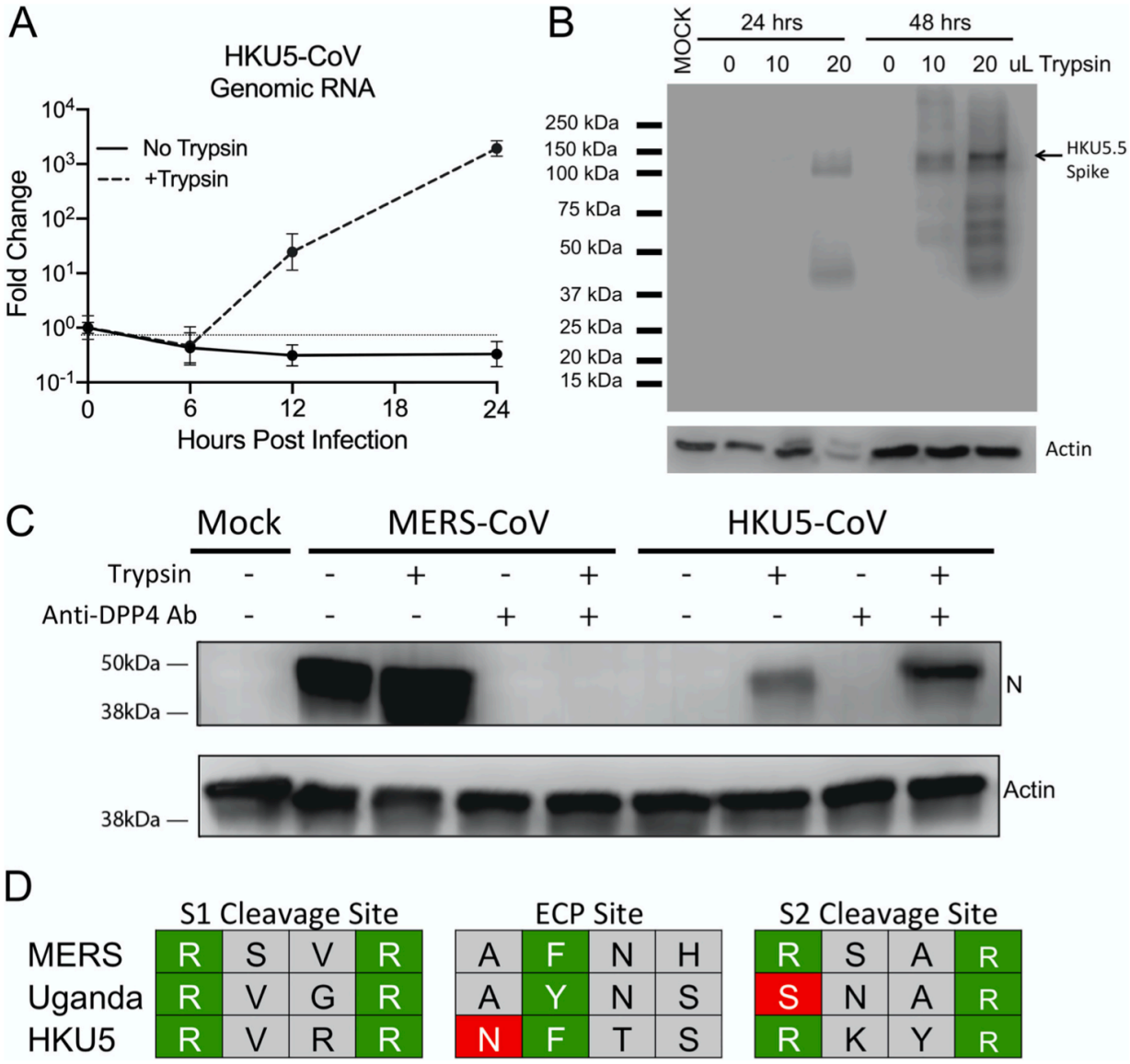

Figure 2.6. Exogenous trypsin rescues replication of HKU5-CoV.

Vero cells were infected with full-length HKU5-CoV in the presence or absence of trypsin. (A) Expression (reverse transcription-quantitative PCR [qRT-PCR]) of HKU5-CoV viral genome in the presence or absence of trypsin (*n* = 3). (B) Immunoblotting of HKU5 spike protein and cellular actin 24 and 48 hours post infection with various concentrations of trypsin in the media. (C) Immunoblotting for MERS N protein and cellular actin following infection in the presence or absence of trypsin and human DPP4 antibody. (D) Alignment of amino acid sequence from the S1/S2, endosomal cysteine protease (ECP), and the S2 cleavage sites. Green boxes represent key residues conserved, and red boxes outline amino acid changes that potentially impact cleavage.

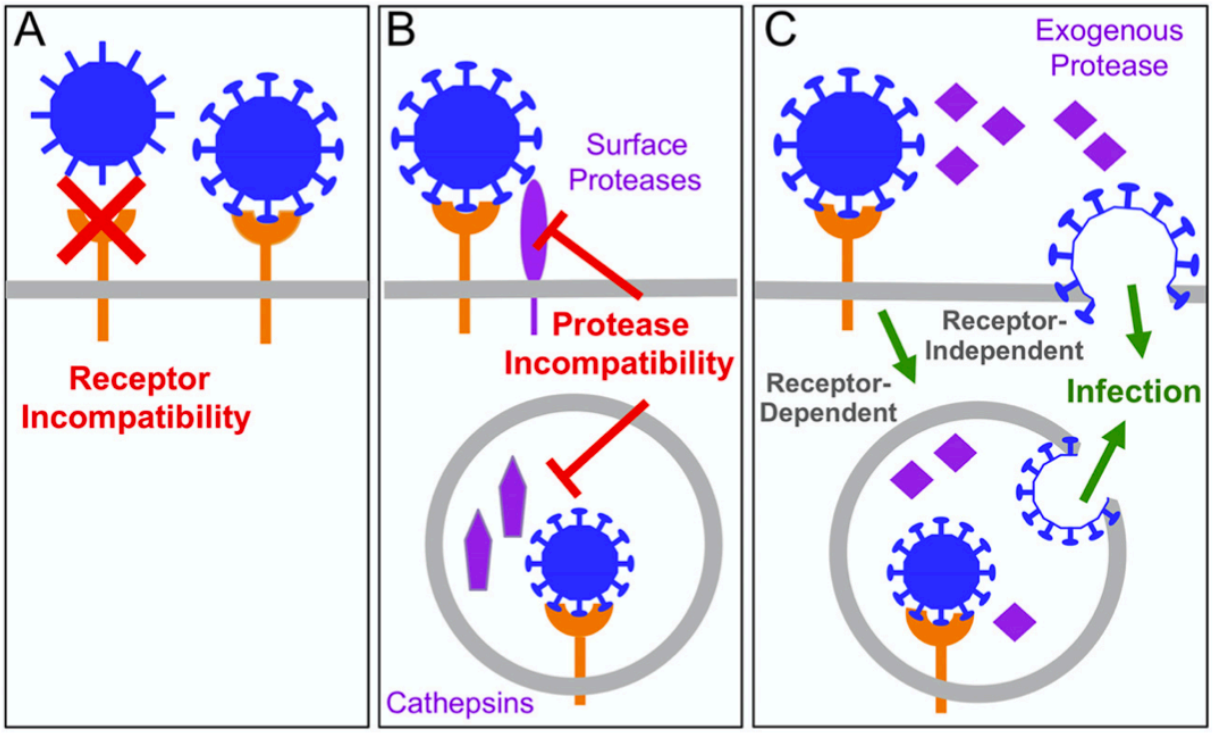

Figure 2.7. Barriers to zoonotic coronavirus emergence

Both receptor binding and protease activation are key correlates that govern zoonotic coronavirus emergence. (A) A lack of receptor binding with zoonotic CoVs precludes the infection of new host cells. (B) Despite receptor binding, the absence of compatible host proteases for spike cleavage restricts infection in new hosts. (C) The addition of exogenous protease overcomes the host protease barriers and may or may not require receptor binding.

REFERENCES

1 Reperant, L. A. & Osterhaus, A. AIDS, Avian flu, SARS, MERS, Ebola, Zika... what next? *Vaccine* **35**, 4470-4474, doi:10.1016/j.vaccine.2017.04.082 (2017).

2 Perlman, S. & Netland, J. Coronaviruses post-SARS: update on replication and pathogenesis. *Nat Rev Microbiol* **7**, 439-450, doi:10.1038/nrmicro2147 (2009).

3 Morse, S. S. *et al.* Prediction and prevention of the next pandemic zoonosis. *Lancet* **380**, 1956-1965, doi:10.1016/S0140-6736(12)61684-5 (2012).

4 Cunningham, A. A., Daszak, P. & Wood, J. L. N. One Health, emerging infectious diseases and wildlife: two decades of progress? *Philos Trans R Soc Lond B Biol Sci* **372**, doi:10.1098/rstb.2016.0167 (2017).

5 Chafekar, A. & Fielding, B. C. MERS-CoV: Understanding the Latest Human Coronavirus Threat. *Viruses* **10**, doi:10.3390/v10020093 (2018).

6 Agnihothram, S. *et al.* A mouse model for Betacoronavirus subgroup 2c using a bat coronavirus strain HKU5 variant. *mBio* **5**, e00047-00014, doi:10.1128/mBio.00047-14 (2014).

7 Agnihothram, S. *et al.* Evaluation of serologic and antigenic relationships between middle eastern respiratory syndrome coronavirus and other coronaviruses to develop vaccine platforms for the rapid response to emerging coronaviruses. *J Infect Dis* **209**, 995-1006, doi:10.1093/infdis/jit609 (2014).

8 Johnson, B. A., Graham, R. L. & Menachery, V. D. Viral metagenomics, protein structure, and reverse genetics: Key strategies for investigating coronaviruses. *Virology* **517**, 30-37, doi:10.1016/j.virol.2017.12.009 (2018).

9 Becker, M. M. *et al.* Synthetic recombinant bat SARS-like coronavirus is infectious in cultured cells and in mice. *Proc Natl Acad Sci U S A* **105**, 19944-19949, doi:10.1073/pnas.0808116105 (2008).

10 Rockx, B. *et al.* Early upregulation of acute respiratory distress syndrome-associated cytokines promotes lethal disease in an aged-mouse model of severe acute respiratory syndrome coronavirus infection. *J Virol* **83**, 7062-7074, doi:10.1128/JVI.00127-09 (2009).

11 Sheahan, T. *et al.* Mechanisms of zoonotic severe acute respiratory syndrome coronavirus host range expansion in human airway epithelium. *J Virol* **82**, 2274-2285, doi:10.1128/JVI.02041-07 (2008).

12 Sheahan, T., Rockx, B., Donaldson, E., Corti, D. & Baric, R. Pathways of cross-species transmission of synthetically reconstructed zoonotic severe acute respiratory syndrome coronavirus. *J Virol* **82**, 8721-8732, doi:10.1128/JVI.00818-08 (2008).

13 Menachery, V. D. *et al.* SARS-like WIV1-CoV poised for human emergence. *Proc Natl Acad Sci U S A* **113**, 3048-3053, doi:10.1073/pnas.1517719113 (2016).

14 Menachery, V. D. *et al.* A SARS-like cluster of circulating bat coronaviruses shows potential for human emergence. *Nat Med* **21**, 1508-1513, doi:10.1038/nm.3985 (2015).

15 Sheahan, T. P. *et al.* Broad-spectrum antiviral GS-5734 inhibits both epidemic and zoonotic coronaviruses. *Sci Transl Med* **9**, doi:10.1126/scitranslmed.aal3653 (2017).

16 Anthony, S. J. *et al.* Further Evidence for Bats as the Evolutionary Source of Middle East Respiratory Syndrome Coronavirus. *mBio* **8**, doi:10.1128/mBio.00373-17 (2017).

17 Hofmann, M. & Wyler, R. Propagation of the virus of porcine epidemic diarrhea in cell culture. *J Clin Microbiol* **26**, 2235-2239, doi:10.1128/jcm.26.11.2235-2239.1988 (1988).

18 Scobey, T. *et al.* Reverse genetics with a full-length infectious cDNA of the Middle East respiratory syndrome coronavirus. *Proc Natl Acad Sci U S A* **110**, 16157-16162, doi:10.1073/pnas.1311542110 (2013).

19 Park, J. E. *et al.* Proteolytic processing of Middle East respiratory syndrome coronavirus spikes expands virus tropism. *Proc Natl Acad Sci U S A* **113**, 12262-12267, doi:10.1073/pnas.1608147113 (2016).

20 de Wilde, A. H. *et al.* MERS-coronavirus replication induces severe in vitro cytopathology and is strongly inhibited by cyclosporin A or interferon-alpha treatment. *J Gen Virol* **94**, 1749-1760, doi:10.1099/vir.0.052910-0 (2013).

21 B, S. B. *et al.* Human airway epithelial cell culture to identify new respiratory viruses: coronavirus NL63 as a model. *J Virol Methods* **156**, 19-26, doi:10.1016/j.jviromet.2008.10.022 (2009).

22 Tekes, G. & Thiel, H. J. Feline Coronaviruses: Pathogenesis of Feline Infectious Peritonitis. *Adv Virus Res* **96**, 193-218, doi:10.1016/bs.aivir.2016.08.002 (2016).

23 Song, D. & Park, B. Porcine epidemic diarrhoea virus: a comprehensive review of molecular epidemiology, diagnosis, and vaccines. *Virus Genes* **44**, 167-175, doi:10.1007/s11262-012-0713-1 (2012).

24 Corti, D. *et al.* Prophylactic and postexposure efficacy of a potent human monoclonal antibody against MERS coronavirus. *Proc Natl Acad Sci U S A* **112**, 10473-10478, doi:10.1073/pnas.1510199112 (2015).

25 Kleine-Weber, H., Elzayat, M. T., Hoffmann, M. & Pohlmann, S. Functional analysis of potential cleavage sites in the MERS-coronavirus spike protein. *Sci Rep* **8**, 16597, doi:10.1038/s41598-018-34859-w (2018).

26 Biniossek, M. L., Nagler, D. K., Becker-Pauly, C. & Schilling, O. Proteomic identification of protease cleavage sites characterizes prime and non-prime specificity of cysteine cathepsins B, L, and S. *J Proteome Res* **10**, 5363-5373, doi:10.1021/pr200621z (2011).

27 Yang, Y. *et al.* Two Mutations Were Critical for Bat-to-Human Transmission of Middle East Respiratory Syndrome Coronavirus. *J Virol* **89**, 9119-9123, doi:10.1128/JVI.01279-15 (2015).

28 Zheng, Y. *et al.* Lysosomal Proteases Are a Determinant of Coronavirus Tropism. *J Virol* **92**, doi:10.1128/JVI.01504-18 (2018).

29 Yang, Y. *et al.* Receptor usage and cell entry of bat coronavirus HKU4 provide insight into bat-to-human transmission of MERS coronavirus. *Proc Natl Acad Sci U S A* **111**, 12516-12521, doi:10.1073/pnas.1405889111 (2014).

30 Graham, R. L. & Baric, R. S. Recombination, reservoirs, and the modular spike: mechanisms of coronavirus cross-species transmission. *J Virol* **84**, 3134-3146, doi:10.1128/JVI.01394-09 (2010).

31 Ge, X. Y. *et al.* Isolation and characterization of a bat SARS-like coronavirus that uses the ACE2 receptor. *Nature* **503**, 535-538, doi:10.1038/nature12711 (2013).

32 Luo, C. M. *et al.* Discovery of Novel Bat Coronaviruses in South China That Use the Same Receptor as Middle East Respiratory Syndrome Coronavirus. *J Virol* **92**, doi:10.1128/JVI.00116-18 (2018).

33 Klenk, H. D., Rott, R., Orlich, M. & Blodorn, J. Activation of influenza A viruses by trypsin treatment. *Virology* **68**, 426-439, doi:10.1016/0042-6822(75)90284-6 (1975).

34 Luczo, J. M., Stambas, J., Durr, P. A., Michalski, W. P. & Bingham, J. Molecular pathogenesis of H5 highly pathogenic avian influenza: the role of the haemagglutinin cleavage site motif. *Rev Med Virol* **25**, 406-430, doi:10.1002/rmv.1846 (2015).

35 Clark, S. M., Roth, J. R., Clark, M. L., Barnett, B. B. & Spendlove, R. S. Trypsin enhancement of rotavirus infectivity: mechanism of enhancement. *J Virol* **39**, 816-822, doi:10.1128/JVI.39.3.816-822.1981 (1981).

36 Roivainen, M. & Hovi, T. Intestinal trypsin can significantly modify antigenic properties of polioviruses: implications for the use of inactivated poliovirus vaccine. *J Virol* **61**, 3749-3753, doi:10.1128/JVI.61.12.3749-3753.1987 (1987).

37 Hu, H. *et al.* Isolation and characterization of porcine deltacoronavirus from pigs with diarrhea in the United States. *J Clin Microbiol* **53**, 1537-1548, doi:10.1128/JCM.00031-15 (2015).

38 Wicht, O. *et al.* Proteolytic activation of the porcine epidemic diarrhea coronavirus spike fusion protein by trypsin in cell culture. *J Virol* **88**, 7952-7961, doi:10.1128/JVI.00297-14 (2014).

39 Zhou, P. *et al.* Fatal swine acute diarrhoea syndrome caused by an HKU2-related coronavirus of bat origin. *Nature* **556**, 255-258, doi:10.1038/s41586-018-0010-9 (2018).

40 Li, K. *et al.* Mouse-adapted MERS coronavirus causes lethal lung disease in human DPP4 knockin mice. *Proc Natl Acad Sci U S A* **114**, E3119-E3128, doi:10.1073/pnas.1619109114 (2017).

41 Matsuyama, S., Ujike, M., Morikawa, S., Tashiro, M. & Taguchi, F. Protease-mediated enhancement of severe acute respiratory syndrome coronavirus infection. *Proc Natl Acad Sci U S A* **102**, 12543-12547, doi:10.1073/pnas.0503203102 (2005).

42 Zeng, L. P. *et al.* Bat Severe Acute Respiratory Syndrome-Like Coronavirus WIV1 Encodes an Extra Accessory Protein, ORFX, Involved in Modulation of the Host Immune Response. *J Virol* **90**, 6573-6582, doi:10.1128/JVI.03079-15 (2016).

43 Millet, J. K. & Whittaker, G. R. Host cell proteases: Critical determinants of coronavirus tropism and pathogenesis. *Virus Res* **202**, 120-134, doi:10.1016/j.virusres.2014.11.021 (2015).

44 Earnest, J. T. *et al.* The tetraspanin CD9 facilitates MERS-coronavirus entry by scaffolding host cell receptors and proteases. *PLoS Pathog* **13**, e1006546, doi:10.1371/journal.ppat.1006546 (2017).

45 Zhou, J. *et al.* Human intestinal tract serves as an alternative infection route for Middle East respiratory syndrome coronavirus. *Science Advances* **3**, eaao4966, doi:10.1126/sciadv.aao4966 (2017).

46 Ding, Y. *et al.* Organ distribution of severe acute respiratory syndrome (SARS) associated coronavirus (SARS-CoV) in SARS patients: implications for pathogenesis and virus transmission pathways. *J Pathol* **203**, 622-630, doi:10.1002/path.1560 (2004).

47 Zhang, X. *et al.* Complete genomic sequences, a key residue in the spike protein and deletions in nonstructural protein 3b of US strains of the virulent and attenuated coronaviruses, transmissible gastroenteritis virus and porcine respiratory coronavirus. *Virology* **358**, 424-435, doi:10.1016/j.virol.2006.08.051 (2007).

48 Pallesen, J. *et al.* Immunogenicity and structures of a rationally designed prefusion MERS-CoV spike antigen. *Proc Natl Acad Sci U S A* **114**, E7348-E7357, doi:10.1073/pnas.1707304114 (2017).

49 Gallagher, T. M., Buchmeier, M. J. & Perlman, S. Cell receptor-independent infection by a neurotropic murine coronavirus. *Virology* **191**, 517-522, doi:10.1016/0042-6822(92)90223-c (1992).

50 Li, W. *et al.* Identification of sialic acid-binding function for the Middle East respiratory syndrome coronavirus spike glycoprotein. *Proc Natl Acad Sci U S A* **114**, E8508-E8517, doi:10.1073/pnas.1712592114 (2017).

51 Sims, A. C., Burkett, S. E., Yount, B. & Pickles, R. J. SARS-CoV replication and pathogenesis in an in vitro model of the human conducting airway epithelium. *Virus Res* **133**, 33-44, doi:10.1016/j.virusres.2007.03.013 (2008).

52 Sims, A. C. *et al.* Release of severe acute respiratory syndrome coronavirus nuclear import block enhances host transcription in human lung cells. *J Virol* **87**, 3885-3902, doi:10.1128/JVI.02520-12 (2013).

53 Almazan, F. *et al.* Engineering a replication-competent, propagation-defective Middle East respiratory syndrome coronavirus as a vaccine candidate. *mBio* **4**, e00650-00613, doi:10.1128/mBio.00650-13 (2013).

54 Agnihothram, S. *et al.* Development of a Broadly Accessible Venezuelan Equine Encephalitis Virus Replicon Particle Vaccine Platform. *J Virol* **92**, doi:10.1128/JVI.00027-18 (2018).

55 Bolles, M. *et al.* A double-inactivated severe acute respiratory syndrome coronavirus vaccine provides incomplete protection in mice and induces increased eosinophilic proinflammatory pulmonary response upon challenge. *J Virol* **85**, 12201-12215, doi:10.1128/JVI.06048-11 (2011).

56 Sheahan, T. *et al.* Successful vaccination strategies that protect aged mice from lethal challenge from influenza virus and heterologous severe acute respiratory syndrome coronavirus. *J Virol* **85**, 217-230, doi:10.1128/JVI.01805-10 (2011).

57 Huynh, J. *et al.* Evidence supporting a zoonotic origin of human coronavirus strain NL63. *J Virol* **86**, 12816-12825, doi:10.1128/JVI.00906-12 (2012).

58 Zaki, A. M., van Boheemen, S., Bestebroer, T. M., Osterhaus, A. D. & Fouchier, R. A. Isolation of a novel coronavirus from a man with pneumonia in Saudi Arabia. *N Engl J Med* **367**, 1814-1820, doi:10.1056/NEJMoa1211721 (2012).

CHAPTER 3 – A MOUSE-ADAPTED MODEL OF SARS-COV-2 TO TEST COVID-19 COUNTERMEASURES[2]

3.1 Introduction

Zoonotic coronaviruses are readily transmitted to new host species, as demonstrated by the emergence of SARS-CoV in 2002 and 2003, Middle East respiratory syndrome coronavirus (MERS-CoV) in 2012 and SARS-CoV-2, the causative agent of the COVID-19 pandemic. SARS-CoV-2 has caused nearly 200 million infections and over 4 million deaths worldwide. As there is only one antiviral agent approved[1] for emergency use against SARS-CoV-2, small animal model systems are vital to improve understanding of disease mechanisms of COVID-19 and to evaluate medical countermeasures for improved global health. Mouse models can provide key insights into the pathogenic mechanisms of coronavirus disease and can serve as high-throughput preclinical evaluation platforms to identify highly performing antiviral agents and vaccines[2,3]. SARS-CoV-2 enters host cells by binding the cellular receptor ACE2. However, standard laboratory mice do not support infection with SARS-CoV-2 owing to incompatibility of the spike (S) protein with mouse ACE2, complicating model development[4].

[2]First published as: Dinnon III, K.H.[**], Leist, S.R.[**], Schäfer, A., Edwards, C.E., Martinez, D.R., Montgomery, S.A., West, A., Yount Jr, B.L., Hou, Y.J., Adams, L.E., Gully, K.L., Brown, A.J., Huang, E., Bryant, M.D., Choong, I.C., Glenn, J.S., Gralinski, L.E., Sheahan, T.P., Baric, R.S. A Mouse-Adapted Model of SARS-CoV-2 to Test COVID-19 Countermeasures. *Nature* 586, no. 7830 (2020): 560–66. [**]=co-first authors

3.2 Results

3.2.1 Infection of *Hfh4-ACE2* transgenic mice

Animal models will be critical for development of medical countermeasures to the COVID-19 pandemic. Laboratory mice infected with mouse-adapted strains of SARS-CoV and MERS-CoV have informed our understanding of viral pathogenesis and intervention strategies. Several animal models for SARS-CoV-2 have been reported, with varying degrees of viral replication and clinical disease, including *ACE2* transgenic mice[5-7] and virally transduced *ACE2* mice which express human ACE2[3,8,9], ferrets[10], hamsters[11,12] and non-human primates[13-15]. To determine the utility of mice overexpressing human ACE2 under the control of the *Hfh4* (also known as *Foxj1*) promoter as a model for SARS-CoV-2 disease, we infected with *Hfh4-ACE2* mice with SARS-CoV-2[5,16,17]. The *Hfh4* promoter drives expression of human ACE2 in ciliated cells of respiratory tract epithelium and in the central nervous system[18,19]. *Hfh4-ACE2* mice infected with SARS-CoV-2 showed little weight loss, but only 60% survived at 5 days post-infection (dpi) **(Figure 3.5a, b)**. Virus was detected in the lung at 2 and 5 dpi **(Figure 3.5c)**. Similar to previous reports of SARS-CoV and SARS-CoV-2 infection in *Hfh4-ACE2* mice, SARS-CoV-2 virus was detected in the brains of mice that succumbed to infection, suggesting that mortality was driven by viral invasion of the brain **(Figure 3.5d)**[5,17]. Next, we used whole-body plethysmography to monitor pulmonary function in mice infected with SARS-CoV-2[20]. We evaluated several complementary metrics of pulmonary obstruction and bronchoconstriction, including enhanced pause (PenH) and the fraction of expiration time at which the peak occurs (Rpef), which remained at normal levels for the duration of these studies, further indicating that respiratory infection was probably not a major driver of mortality **(Figure 3.5f, g)**. Thus, although *ACE2* expression driven by the *Hfh4* promoter facilitates SARS-CoV-2 infection of mice, the observed pathogenesis does not accurately model the more severe disease manifestations observed in humans.

3.2.2 Remodeling the SARS-CoV-2–ACE2 interface

Next, instead of genetically altering the host, we sought to remodel the SARS-CoV-2 S receptor-binding domain (RBD) to facilitate efficient binding to mouse ACE2. We compared the ACE2-contacting residues in the RBDs of S proteins from several group 2B coronaviruses capable of infecting mice with those of SARS-CoV-2 **(Figure 3.1a, Figure 3.6)**[17,21,22]. There were variations in this region in S proteins from SARS-CoV, WIV1 and SHC014 at a few amino acid positions, but residue 498 of SARS-CoV-2 was uniquely divergent, suggesting incompatibility of SARS-CoV-2 Q498 with mouse ACE2. In addition, molecular modelling of the SARS-CoV-2 S RBD–receptor interface predicted a loss of the interaction between Q498 of SARS-CoV-2 S protein and Q42 of human ACE2 with mouse ACE2 **(Figure 3.1b, c)**, which may diminish binding efficiency. Thus, substitution of residue Q498 and the adjacent P499 with Y and T, respectively, from WIV1 and SARS-CoV might restore the interaction with Q42 of mouse ACE2 while preserving the interaction with human ACE2 **(Figure 3.1d, e)**. Using reverse genetics[18], we engineered Q498Y/P499T into the SARS-CoV-2 *S* gene and recovered the recombinant virus (SARS-CoV-2 MA). Notably, SARS-CoV-2 MA replicated with slightly lower titers compared with parental wild-type virus in Vero E6 cells **(Figure 3.1f)** and primary differentiated bronchiolar human airway epithelial (HAE) cells **(Figure 3.1g)**. In contrast to wild-type SARS-CoV-2, SARS-CoV-2 MA RNA could be detected in cells expressing mouse ACE2 by 24 h after infection **(Figure 3.1h)**.

3.2.3 SARS-CoV-2 MA replicates in mouse airways

After demonstrating SARS-CoV-2 MA could use mouse ACE2 for entry into cells, we sought to determine whether this virus could infect young adult wild-type mice. Although overt clinical signs of infection such as weight loss were not observed in young adult BALB/c mice infected with 10^5 plaque-forming units (PFU) SARS-CoV-2 MA **(Figure 3.2a)**, high-titer virus replication was observed in lung tissue at 2 dpi, but was cleared by 4 dpi **(Figure 3.2b)**. Under

identical conditions, replication of wild-type SARS-CoV-2 was not detected. Using whole-body plethysmography, we found that young adult mice infected with SARS-CoV-2 MA showed a small but significant change in PenH **(Figure 3.2d)** and a significant decrease in Rpef **(Figure 3.2e)** at 2 dpi, indicative of impaired lung function. Histological analysis of mice infected with SARS-CoV-2 MA revealed interstitial congestion, epithelial damage, inflammatory infiltrate and peribronchiolar lymphocytic inflammation surrounding airways at 2 dpi; viral antigen staining revealed these to be the main sites of viral replication **(Figure 3.2f)**. At 4 dpi, histological analysis showed increased inflammation and hemorrhage in the lung **(Figure 3.2g)**. Concordant with infectious titer data demonstrating virus clearance by 4 dpi, viral antigen was not detected in lung tissue sections at this time **(Figure 3.2b, g)**. Similar to observations of SARS-CoV-2 in humans, SARS-CoV-2 MA was observed in the upper airway and viral antigen was present in nasal turbinate epithelium at 2 dpi **(Figure 3.2c, h)**. Thus, similar to SARS-CoV-2 infection in humans, SARS-CoV-2 MA infection in young adult mice resulted in efficient virus replication in the upper and lower airways and limited replication in the parenchyma, and was associated with mild-to-moderate disease.

3.2.4 Age effect on SARS-CoV-2 disease in mice

Higher morbidity and mortality rates have been consistently observed in older human individuals throughout the COVID-19 pandemic[23]. Similarly, wild-type and mouse-adapted SARS-CoV show highly age-dependent disease phenotypes in humans and mice, respectively[24,25]. To determine whether the infection of aged mice with SARS-CoV-2 MA would recapitulate the age-dependent increase in disease severity observed in humans with COVID-19, we infected one-year-old BALB/c mice with SARS-CoV-2 MA. In contrast to young adult mice, aged BALB/c mice exhibited a transient but significant decrease in body weight at 3–4 dpi compared with mock-infected mice **(Figure 3.3a)** (old versus young, $P < 0.0001$ (3 dpi) and $P < 0.0040$ (4 dpi)). Similar to young adult mice, aged mice had high viral titer in the lung at 2 dpi, but in contrast to young

adult mice, viral clearance in the aged mice was delayed, as indicated by detectable virus at 4 dpi **(Figure 3.3b)**. Similarly, replication in the upper airway persisted in half of the aged mice at 4 dpi **(Figure 3.3c)**. The loss of pulmonary function was more pronounced in aged animals, as shown by significant differences in PenH and Rpef among mock-infected and SARS-CoV-2 MA-infected mice **(Figure 3.3d, e)**. PenH was significantly higher in aged mice infected with SARS-CoV-2 MA at 2 dpi compared with young mice infected with SARS-CoV-2 MA (P = 0.0457). Rpef was significantly lower in aged, infected mice at 2 dpi (P = 0.0264) and 4 dpi (P = 0.0280). Compared to young mice, aged mice infected with SARS-CoV-2 MA displayed increased epithelial damage, peribronchiolar lymphocytic inflammation, hemorrhage, and edema in the lung at 2 dpi and 4 dpi, and viral antigen was found in conducting airway epithelium, interstitium and nasal epithelium, with minimal antigen staining at 4 dpi, concordant with detection of viral titer **(Figure 3.3b, f–h)**. Additionally, levels of several proinflammatory cytokines were increased in the lung but not in the serum at 2 dpi, indicative of a localized cytokine and chemokine response **(Figure 3.7)**.

3.2.5 Vectored vaccine and IFN-λ1a efficacy

As demonstrated with mouse-adapted strains of SARS-CoV[21], the replication-competent SARS-CoV-2 MA strain facilitates the identification of virus and host factors that guide pathogenesis and disease severity and enables rapid testing of intervention strategies in standard laboratory mice. Using a virus replicon particle (VRP) system, we vaccinated ten-week-old BALB/c mice against SARS-CoV-2 S and nucleocapsid (N), with GFP as a control, with a boost after three weeks, and challenged them four weeks after the boost with SARS-CoV-2 MA. Three weeks after the boost, serum from mice vaccinated with S—but not from mice vaccinated with GFP or N—potently neutralized SARS-CoV-2 reporter virus expressing nanoluciferase (nLUC) **(Figure 3.4a)**. Upon challenge with SARS-CoV-2 MA, only mice vaccinated with VRP expressing S exhibited significantly diminished viral titer in the lungs and nasal turbinate **(Figure 3.4b, c)**.

IFN-λ (type III interferon) signals through a receptor expressed mainly on epithelial cells, including those in the lungs[26,27]. Treatment with IFNs has been used as panviral treatment for several viral infections, including in trials for the treatment of SARS-CoV and MERS-CoV infections. Pegylated human interferon lambda-1 (PEG-IFN-λ1) is a phase-3-ready treatment for hepatitis delta virus infection and has been proposed as a treatment for patients with COVID-19[28]. Thus, we sought to determine whether PEG-IFN-λ1 would initiate an antiviral response capable of inhibiting productive infection of HAE cell cultures by SARS-CoV-2. Pretreatment of HAE cells with PEG-IFN-λ1 provided a potent dose-dependent reduction in production of infectious SARS-CoV-2 **(Figure 3.4d)**.

To determine whether the in vitro antiviral effect of peg-IFN-λ1 translates to in vivo efficacy, we performed prophylactic and therapeutic efficacy studies in one-year old BALB/c mice. We subcutaneously administered 2 μg PEG-IFN-λ1 18 h before or 12 h after infection of mice with 10^5 PFU SARS-CoV-2 MA. Both prophylactic and therapeutic administration of PEG-IFN-λ1 significantly reduced weight loss at 2 and 3 dpi **(Figure 3.4e)** and diminished SARS-CoV-2 MA replication in the lung at 2 dpi **(Figure 3.4f)**. PEG-IFN-λ1 had minimal effects on viral titer in nasal turbinate, although the accuracy of these readings was probably limited by the low limit of detection (LOD) **(Figure 3.4g)**. Both prophylactic and therapeutic PEG-IFN-λ1 protected mice from pulmonary dysfunction, as measured by PenH and Rpef **(Figure 3.4h, i)**. PEG-IFN-λ1 also reduced the SARS-CoV-2 MA titer in the lungs of treated young mice at 2 dpi **(Figure 3.8a, b)**. When tested in *Hfh4-ACE2* mice, PEG-IFN-λ1 reduced viral titer in the lungs at 2 dpi, but had no effect at 5 dpi **(Figure 3.8c–e)**, possibly owing to decreased potency by 5 dpi. Together, these data demonstrate the utility of these models for rapid evaluation of vaccines and therapeutic drug efficacy in standard laboratory mice. In addition, they demonstrate that PEG-IFN-λ1 exerts potent antiviral activity against SARS-CoV-2 in vitro and can diminish virus replication in vivo even when given therapeutically.

3.3 Discussion

Structural studies have identified the residues in SARS-CoV and SARS-CoV-2 S-protein RBD that bind human ACE2[29,30]. Using molecular modelling and reverse genetics[18], we altered the SARS-CoV-2 RBD to enable viral entry via mouse ACE2, highlighting the precision of the structure-based predictions. Unlike parental wild-type virus, the resultant recombinant virus (SARS-CoV-2 MA) is able to use mouse ACE2 to infect cells in vitro. Recombinant SARS-CoV-2 MA did not grow more efficiently than wild-type virus in primary HAE or Vero cells, suggesting that the fitness of the virus is not increased in human cells. SARS-CoV-2 MA replicated in both the upper and lower airways of BALB/c mice, and resulted in more severe disease in aged mice, reproducing the age-related increase in disease severity observed in humans. SARS-CoV-2 MA infection is cleared by 4 dpi in young but not in aged adult mice, probably owing to control by IFNs and the innate immune system[8,31], and is exemplified by sensitivity to PEG-IFN- λ1.

SARS-CoV-2 is a pandemic pathogen of concern and the risk potential of experiments to intentionally alter host range was reviewed for potential pandemic pathogen care and oversight (P3C0) concerns before the research was started. By current US review standards, SARS-CoV-2 MA was not considered dual-use research of concern, which is limited to a subset of pathogens. Before the start of the studies, appropriate discussion and documentation of proposed experiments and protocols were reviewed and approvals were obtained by institutional and external review. We recommend that SARS-CoV-2 MA and its derivatives are maintained in a biosafety level 3 laboratory.

We show the utility of the SARS-CoV-2 MA model for screening medical countermeasures through vaccine challenge studies and the evaluation of a clinical candidate, PEG-IFN-λ1. PEG-IFN-λ1 is a phase-3-ready drug in clinical development for hepatitis delta virus infection. It has been given to more than 3,000 patients in the context of 19 clinical trials as a weekly subcutaneous injection, often for 24–48 weeks, to treat patients with chronic viral hepatitis[32,33]. PEG-IFN-λ1 is a promising therapy for the treatment of SARS-CoV-2 infection[34,35], and blocks

porcine coronavirus replication in gut cells in vitro[36] and SARS-CoV replication in human airway cells[37]. Our results, which demonstrate reduction in SARS-CoV-2 infection in primary human cells and in mice, support further multiple-investigator sponsored studies currently underway to evaluate PEG-IFN-λ1 for prevention and treatment of SARS-CoV-2 infection (Clinicaltrials. gov identifiers: NCT04331899, NCT04343976, NCT04344600 and NCT04354259).

Although the mutations in the SARS-CoV-2 MA S-protein RBD may attenuate the function of some human monoclonal antibodies or vaccines in mice, this phenotype was not observed with mouse-adapted strains of SARS-CoV[38-40] and the mutations did not alter the potent neutralizing activity of two human monoclonal antibodies that target the SARS-CoV-2 S-protein RBD[41]. We also demonstrate that the *Hfh4-ACE2* transgenic mouse model[17] supports efficient SARS-CoV-2 replication and pathogenesis in vivo. Thus, this transgenic mouse model offers an alternative model of replication and disease that uses wild-type SARS-CoV-2 and is appropriate for evaluating therapeutic antibodies and other countermeasures that target RBD epitopes that are altered in SARS-CoV-2 MA.

Similar to SARS-CoV infection, SARS-CoV-2 infection of *Hfh4-ACE2* transgenic mice results in mild bronchiolitis in young mice and about 40% mortality; this mortality is associated with viral invasion of the central nervous system[5,17,42]. A recent study used a mouse *Ace2* promoter to drive overexpression of *ACE2*, and infected 6- to 11-month-old mice, resulting in mild weight loss and pulmonary inflammation[6]. The discrepancy in weight loss between that study and the *Hfh4-ACE2* model presented here may be a result of differences in the age of mice used or differences in distribution of *ACE2* expression. Models using viral delivery to overexpress human ACE2 in mice have also been reported[3,8]. Although these systems allow for rapid studies in commercially available mice, including knockout mice, the cellular distribution of human ACE2 may not faithfully recapitulate endogenously expressed ACE2 and proper SARS-CoV-2 tropism.

Our SARS-CoV-2 MA model captures multiple aspects of SARS-CoV-2 pathogenesis in young and aged BALB/c mice and provides an urgently needed high-throughput in vivo system

to evaluate medical countermeasures during this devastating pandemic. As the model uses standard immune-competent laboratory mice, its accessibility, ease of use, availability of reagents, cost and utility are more favorable than for other *ACE2* transgenic mice, ferret, hamster, and non-human primate models. The model also provides a key first step in the serial adaptation of SARS-CoV-2 in mice[21], which could potentially select for variants that develop more severe pathogenic manifestations of acute respiratory distress syndrome, coagulopathies and other human disease outcomes. In addition, the SARS-CoV-2 MA model can be used to evaluate the role of host genetics and antiviral defense genes in viral pathogenesis using transgenic and knockout mice. Together, these data describe two new animal models with distinct features for testing of different medical countermeasures.

3.4 Methods & Materials

3.4.1 Ethics and biosafety

The generation of recombinant SARS-CoV-2 MA was approved for use under BSL3 conditions by the University of North Carolina at Chapel Hill Institutional Review Board (UNC-CH IBC) and by a Potential Pandemic Pathogen Care and Oversight committee at the National Institute of Allergy and Infectious Diseases (NIAID). All animal work was approved by Institutional Animal Care and Use Committee at University of North Carolina at Chapel Hill according to guidelines outlined by the Association for the Assessment and Accreditation of Laboratory Animal Care and the US Department of Agriculture. All work was performed with approved standard operating procedures and safety conditions for SARS-CoV-2. Our institutional BSL3 facilities have been designed to conform to the safety requirements recommended by Biosafety in Microbiological and Biomedical Laboratories (BMBL), the US Department of Health and Human Services, the Public Health Service, the Centers for Disease Control and Prevention (CDC), and

the National Institutes of Health (NIH). Laboratory safety plans have been approved, and the facility has been approved for use by the UNC Department of Environmental Health and Safety (EHS) and the CDC.

3.4.2 SARS-CoV-2 S RBD and ACE2 analysis and modelling

Group 2B coronavirus S and ACE2 amino acid sequences were aligned using Geneious Prime (v.2020.0.5). Accession numbers used were: SARS-CoV Urbani (AY278741), WIV1 (KF367457), SHC014 (KC881005), SARS-CoV-2 (MN985325.1), human ACE2 (BAB40370) and mouse ACE2 (NP_081562). Protein similarity scores were calculated using BLOSUM62 matrix. Contact residues previously identified by crystal structures[29,30,43] Structure modelling was performed using Modeller (v.9.20) and visualized using PyMOL (v.1.8.6.0).

3.4.3 Viruses, cells, and transfections

All viruses used were derived from an infectious clone of SARS-CoV-2, which was designed using similar strategies for SARS-CoV and MERS-CoV[18,44,45]. The Q498Y/P499T substitutions were generated by site-directed mutagenesis using the following primers: forward: 5′-ATATGGTTTCTACACG ACTAATGGTGTTGGTTACCAACC-3′, reverse: 5′-TAGTCGTGTAGAAACCAT ATGATTGTAAAGGAAAGTAACAATT AAAACCTTC-3′. Viruses were derived following systematic cDNA assembly of the infectious clone, followed by in vitro transcription and electroporation into Vero E6 cells. Virus stocks were passaged once on Vero E6 cells and titrated via plaque assay. In brief, virus was serial diluted and inoculated onto confluent monolayers of Vero E6 cells, followed by agarose overlay. Plaques were visualized at 2 dpi by staining with neutral red dye.

Vero E6 cells were obtained from USAMRIID in 2003 (ATCC CRL-1586) and were maintained in Dulbecco's modified Eagle's medium (DMEM; Gibco), 5% Fetal Clone II serum (FCII, Hyclone), and 1x antibiotic–antimycotic (Gibco). DBT-9 cells were previously clonally

derived in our laboratory, maintained in DMEM, 10% FCII, and 1x antibiotic–antimycotic. Cells were confirmed to be negative for mycoplasma contamination.

For the Vero E6 single step growth curve, cells were infected at a multiplicity of infection (MOI) of 0.5 for 1 h. Inoculum was removed and monolayer was washed twice with PBS and replaced with medium. For the HAE cell growth curve, cells were infected at an MOI of 0.5 for 2 h. Inoculum was removed and cells were washed three times with PBS. At designated time points, Vero E6 supernatant was removed without replacement or HAE cells were washed apically with 200 µl 1× PBS for 10 min and stored at −80 °C until titrated by plaque assay as described above.

For ACE2 receptor usage, non-permissive DBT-9 cells were transfected with pcDNA3.1 empty vector, pcDNA3.1-hACE2 or pcDNA3.1-mACE2 using Lipofectamine 2000 (Invitrogen). At 24 h after transfection, cells were infected at an MOI of 0.5 for 1 h, removed and washed twice with PBS. At 24 h after infection, medium was removed, and total cellular RNA was collected via TRIzol (Invitrogen) and extracted using Direct-Zol RNA MiniPrep kit (Zymo Research). Viral RNA was quantified via qRT–PCR using TaqMan Fast Virus 1-Step Master Mix (Thermo Fisher Scientific) on a QuantStudio 3 (Applied Biosystems). SARS-CoV-2 RNA was quantified using US Centers of Disease Control and Prevention diagnostic N1 assay with the primers: forward: 5′-GACCCCAAAATCAGCGAAAT-3′, probe: 5′-FAM-ACCCCGCATTACGTTTGGTGGAC C-BHQ1-3′, reverse: 5′-TCTGGTTACTGCCAGTTGAATCTG-3′. Host 18S rRNA was used as housekeeping control (Invitrogen, product number 4319413E). Viral RNA was analyzed using the ΔΔ*C*t method and fold change over viral RNA in cell transfected with empty vector.

3.4.4 In vivo Infections

Hfh4-ACE2-overexpressing mice were bred and maintained at University of North Carolina at Chapel Hill. BALB/c mice were obtained from Envigo (strain 047). Mice were infected with 10^5 PFU intranasally under ketamine–xylazine anesthesia. Body weight was monitored daily and whole-body plethysmography (WBP) was performed as indicated. In brief, mice were allowed

to equilibrate in WBP chambers (DSI Buxco respiratory solutions, DSI) for 30 min before a 5 min data acquisition period using FinePointe software. At indicated time points, a subset of mice were euthanized by isoflurane overdose and tissue samples were collected for titer and histopathology analysis. A subset of mice for nasal turbinate histopathology were perfused with 10% phosphate buffered formalin before tissue collection. The right caudal lung lobe was taken for titration and stored at −80 °C until homogenized in 1 ml PBS and titrated by plaque assay as described above. The left lung lobe was taken for histopathology and were fixed in 10% phosphate buffered formalin for 7 days before paraffin embedding and sectioning.

3.4.5 Histopathology and antigen staining

Lungs were fixed for 7 days in 10% phosphate buffered formalin, paraffin embedded, and sectioned at 4 μm. Serial sections were stained with hematoxylin and eosin, and stained for immunohistochemistry for SARS-CoV-2 N using a monoclonal anti-SARS-CoV N antibody (1:250, NB100-56576, Novus Biologicals) on deparaffinized sections on the Ventana Discovery Ultra platform (Roche). Photomicrographs were captured on an Olympus BX43 light microscope at 200× magnification with a DP27 camera using cellSens Entry software.

3.4.6 Vaccination studies

Non-select BSL2 Venezuelan equine encephalitis virus strain 3526 based replicon particles (VRPs) were generated to express GFP, SARS-CoV-2 S or N as previously described[18,46]. Mice were vaccinated via hind footpad infection with 10^3 VRP in 10 μl, boosted identically at 3 weeks post prime, and bled via submandibular bleed at 3 weeks to confirm presence of neutralizing antibodies. Neutralizing antibody levels were assessed via neutralization assay using wild-type SARS-CoV-2 expressing nanoluciferase (nLUC) in place of ORF7a. In brief, the *ORF7a* gene of SARS-CoV-2 was removed from the molecular clone and nLUC inserted downstream of the ORF7a transcription regulatory sequence. Recombinant viruses encoding

nLUC (SARS-CoV-2 nLUC) were recovered, titrated and serial dilutions of sera were incubated with virus for 1 h at 37 °C, then added to monolayers of Vero E6 cells. Forty-eight hours after infection, viral infection was quantified using nLUC activity via Nano-Glo Luciferase Assay System (Promega). IC_{50} values were calculated from full dilution curves.

Mice were challenged 4 weeks post boost with 10^5 PFU intranasally under ketamine–xylazine anesthesia. Body weight was monitored daily. On day 2 after infection, mice were euthanized by isoflurane overdose and tissue samples were collected for titer analysis as described above.

3.4.7 PEG-IFN-λ1 treatment in vitro and in vivo

PEG-IFN-λ1 was obtained from Eiger BioPharmaceuticals by MTA in GMP prefilled syringes, 0.18 mg per syringe (0.4 mg ml^{-1}). Primary HAE cell cultures were obtained from the Tissue Procurement and Cell Culture Core Laboratory in the Marsico Lung Institute/Cystic Fibrosis Research Center at UNC. Human tracheobronchial epithelial cells provided by S. Randell were obtained under University of North Carolina Institutional Review Board-approved protocols (no. 03-1396) by the Cystic Fibrosis Center Tissue Culture Core from airway specimens resected from patients undergoing surgery. Primary cells were expanded to generate passage 1 cells and passage 2 cells were plated at a density of 250,000 cells per well on Transwell-COL (12-mm diameter) supports (Corning). HAE cell cultures were generated by differentiation at an air-liquid interface for 6 to 8 weeks to form well-differentiated, polarized cultures that resembled in vivo pseudostratified mucociliary epithelium[47]. HAE cells were treated with a range of PEG-IFN-λ1 doses basolaterally for 24 h before infection. Remdesivir (1 μM) was obtained from Gilead Sciences by MTA and was used as a positive control. Cultures were infected at an MOI of 0.5 for 2 h. Inoculum was removed and culture was washed three times with PBS. At 48 h after infection, apical washes were taken to measure viral replication via plaque assays as described above. This study was repeated in cells from two separate human donors.

One-year-old or 10-week-old BALB/c, or 4- to 7-week old *Hfh4-ACE2* mice were subcutaneously treated with a single 2 μg dose of PEG-IFN-λ1 prophylactically at 18 h before infection, therapeutically at 12 h after infection[48], or PBS-vehicle-treated, and infected with 10^5 PFU of SARS-CoV-2 MA intranasally under ketamine–xylazine anesthesia. *Hfh4-ACE2* mice at 4 to 7 weeks of age were treated as above and infected with 10^5 PFU of SARS-CoV-2 MA. Body weight was monitored daily. WBP was performed as indicated. On days indicated, mice were euthanized by isoflurane overdose and tissue samples were collected for titer analysis as described above.

3.4.8 Data analysis and presentation

All data were visualized and analyzed in Prism (v.8.4.2). Non-parametric tests were performed as described in figure legends. Figures were arranged in Adobe Illustrator (v.24.1).

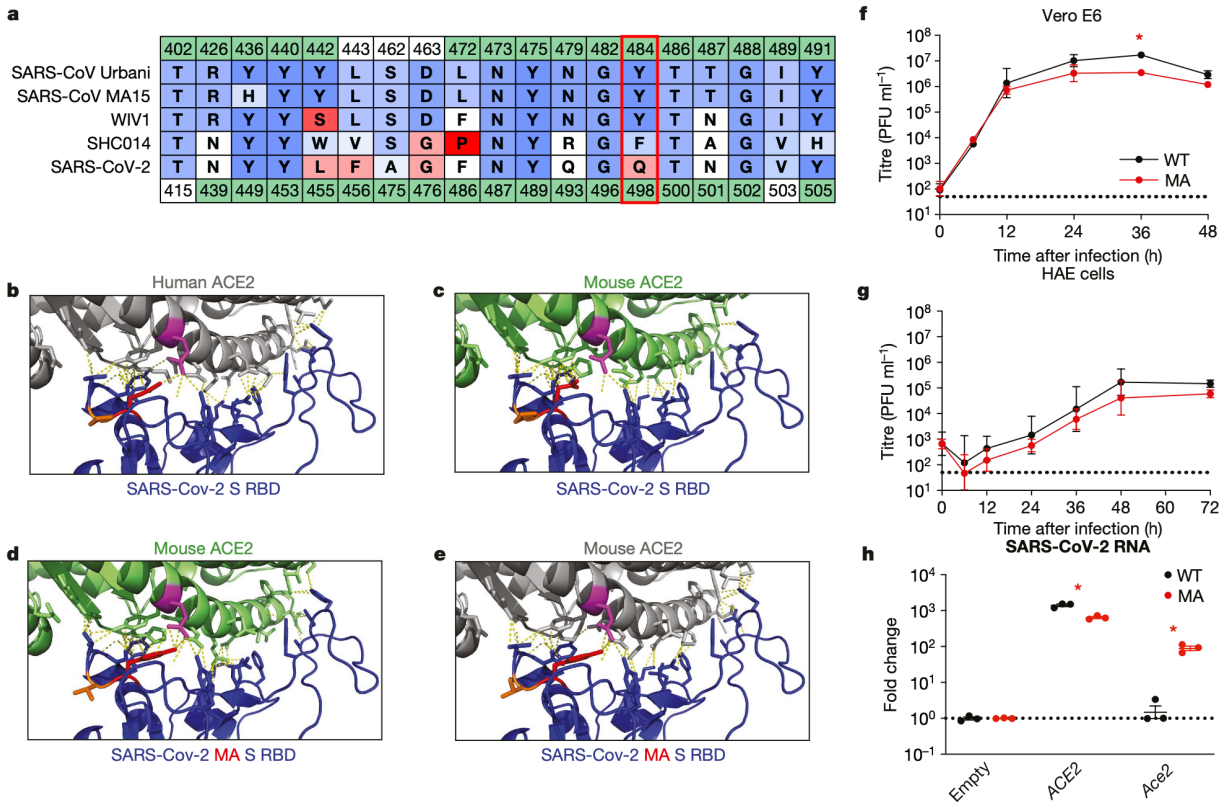

Figure 3.1. Generation of SARS-CoV-2 MA.

a, Table of group 2B S RBD–ACE2 interacting residues. Amino acid positions are numbered relative to SARS-CoV (top row) and SARS-CoV-2 (bottom row). Green shading indicates contacts as determined by published crystal structures. Amino acids are colored by BLOSUM62 conservation score relative to S protein from SARS-CoV Urbani (red, least conserved; blue, most conserved). SARS-CoV Urbani, SARS-CoV MA15, WIV1 and SHC014 S proteins can use mouse ACE2 as a functional receptor, whereas SARS-CoV-2 S cannot. The red outline indicates Q498 in SARS-CoV-2 S, which makes contact with human ACE2 in both SARS-CoV S and is divergent in SARS-CoV-2. **b**, SARS-CoV-2 S RBD–human ACE2 interface (PDB: 6M0J). SARS-CoV-2 S Q498 (red) interacts with Q42 (magenta) of human ACE2. **c**, Modelling of SARS-CoV-2 S RBD and mouse ACE2. SARS-CoV-2 S Q498 does not interact with Q42 of mouse ACE2. **d**, Modelling of SARS-CoV-2 S(Q498Y/P499T) (orange) shows restored interaction with Q42 of mouse ACE2. **e**, Modelling of SARS-CoV-2 S(Q498Y/P499T) showing interaction with Q42 of human ACE2. **f**, **g**, Single-step growth curve of SARS-CoV-2 (WT) and SARS-CoV-2 MA (MA) in Vero E6 (**f**) and HAE (**g**) cells. The dotted line represents LOD. The log-transformed data were analyzed by two-way analysis of variance (ANOVA) followed by Sidak's multiple comparisons. In **f**, $*P = 0.0053$ (36 h). **h**, Non-permissive DBT-9 cells were transfected to express human *ACE2* or mouse *Ace2* and infected with SARS-CoV-2 or SARS-CoV-2 MA. Viral RNA was quantified by quantitative PCR with reverse transcription (RT–qPCR) 24 h after infection and normalized expression in cells transfected with empty vector. The log-transformed data were analyzed by two-way ANOVA followed by Dunnett's multiple comparisons. $*P = 0.0322$ (*ACE2*), $*P < 0.0001$ (*Ace2*). In **f**–**h**, $n = 3$ technical replicates for each group, representative of 2 independent experiments. Data are mean ± s.d.

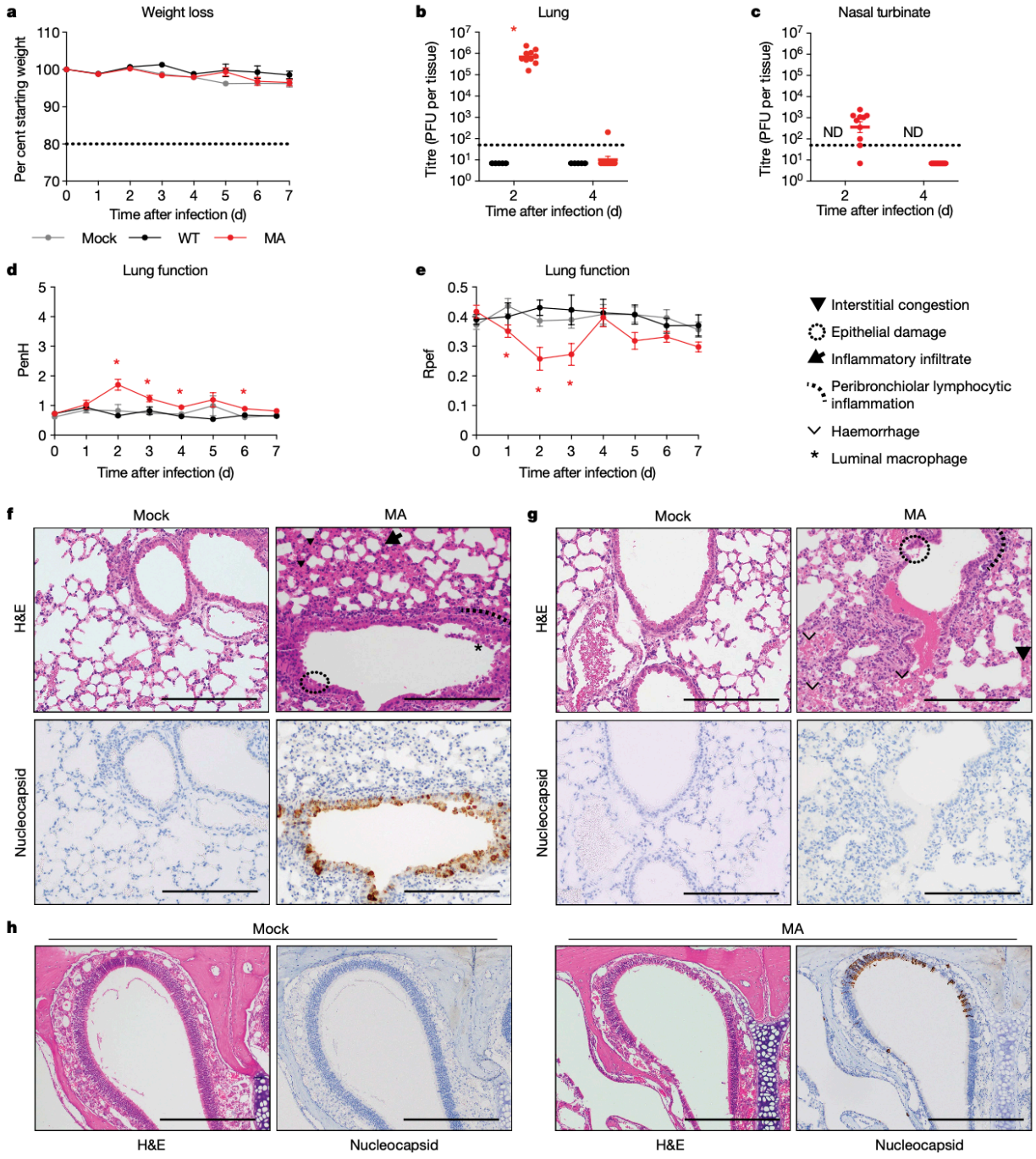

Figure 3.2. SARS-CoV-2 MA replicates in young BALB/c mice.

a–**h**, Twelve-week- old female BALB/c mice were mock-infected (grey) (**a**, **d**, **e**) or infected with 10^5 PFU wild-type SARS-CoV-2 (black) or SARS-CoV-2 MA (red) (**a**–**e**). Combined data from two independent experiments. **a**, Weight loss. The dotted line represents weight-loss criteria for humane euthanasia. Data were analyzed using mixed-effects analysis followed by Dunnett's multiple comparisons. **b**, **c**, Viral lung (**b**) and nasal turbinate (**c**) titer (2 dpi: *n* = 5 (WT), *n* = 10 (MA); 4 dpi: *n* = 5 (WT), *n* = 9 (MA)). The dotted line represents LOD. Undetected samples are plotted at half the LOD. The log-transformed data were analyzed by two-way ANOVA followed by

Sidak's multiple comparisons. ND, not determined. In **b**, *$P \leq 0.0001$. **d**, **e**, Whole-body plethysmography assessing pulmonary function for PenH (**d**) and Rpef (**e**). Data were analyzed by two-way ANOVA followed by Dunnett's multiple comparisons. Data are mean ± s.e.m. In **d**, *$P = 0.012$ (2 dpi), 0.0025 (3 dpi), 0.0030 (4 dpi), 0.0018 (6 dpi). In **e**, *$P = 0.0426$ (1 dpi), 0.0194 (2 dpi), 0.0442 (3 dpi). **f**–**h**, Lung sections at 2 dpi (**f**) and 4 dpi (**g**), and nasal turbinates at 2 dpi (**h**). Hematoxylin and eosin (H&E) staining and immunohistochemistry staining for SARS-CoV-2 N protein, counterstained with hematoxylin. Scale bars, 200 μm. Images representative of two independent experiments.

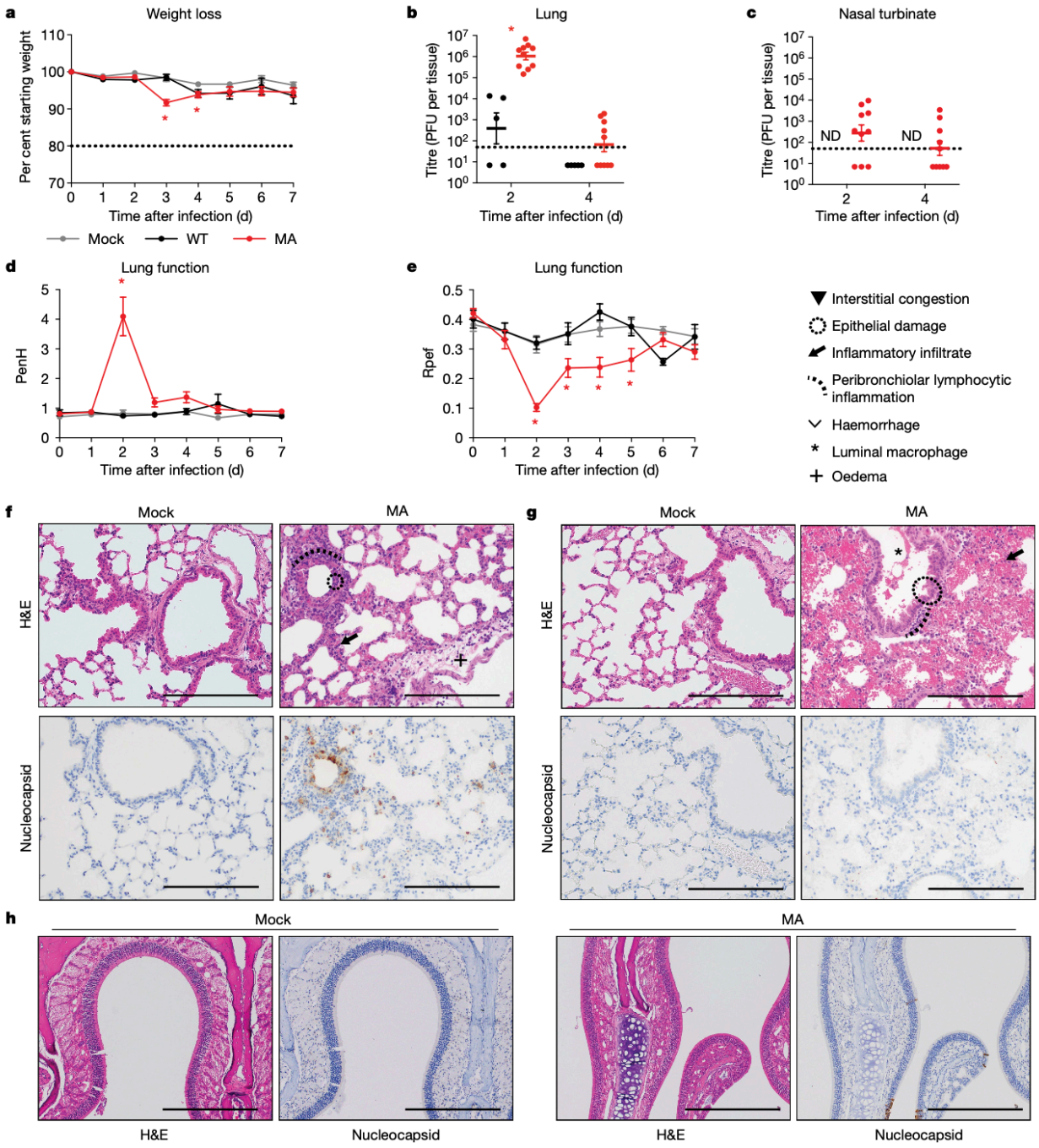

Figure 3.3. SARS-CoV-2 MA replicates in old BALB/c mice with minor disease.

a–**h**, One-year-old female BALB/c were mock-infected (grey) or infected with 10^5 PFU SARS-CoV-2 (black) or SARS-CoV-2 MA (red). Combined data from two independent experiments. **a**, Weight loss. The dotted line represents weight-loss criteria for humane euthanasia. Data were analyzed by mixed-effects analysis followed by Dunnett's multiple comparisons. *$P \leq 0.0001$ (3 dpi), 0.0305 (4 dpi). **b**, **c**, Viral lung (**b**) and nasal turbinate (**c**) titers. $n = 5$ (WT), $n = 10$ (MA). The dotted line represents LOD. Undetected samples are plotted at half the LOD. The log-transformed data were analyzed by two-way ANOVA followed by Sidak's multiple comparisons. In **b**, *$P \leq$

0.0001. **d**, **e**, Whole-body plethysmography assessing pulmonary function for PenH (**d**) and Rpef (**e**). Data were analyzed by two-way ANOVA followed by Dunnett's multiple comparisons. Data are mean ± s.e.m. In **d**, $*P = 0.0014$ (2 dpi). In **e**, $*P \leq 0.0001$ (2 dpi), 0.0242 (3 dpi), 0.0130 (4 dpi), 0.0481 (5 dpi). **f**–**h**, Lung sections at 2 dpi (**f**) and 4 dpi (**g**), and nasal turbinates at 2 dpi (**h**). H&E staining and immunohistochemistry staining for SARS-CoV-2 N protein, counterstained with hematoxylin. Scale bars, 200 μm. Images representative of two independent experiments.

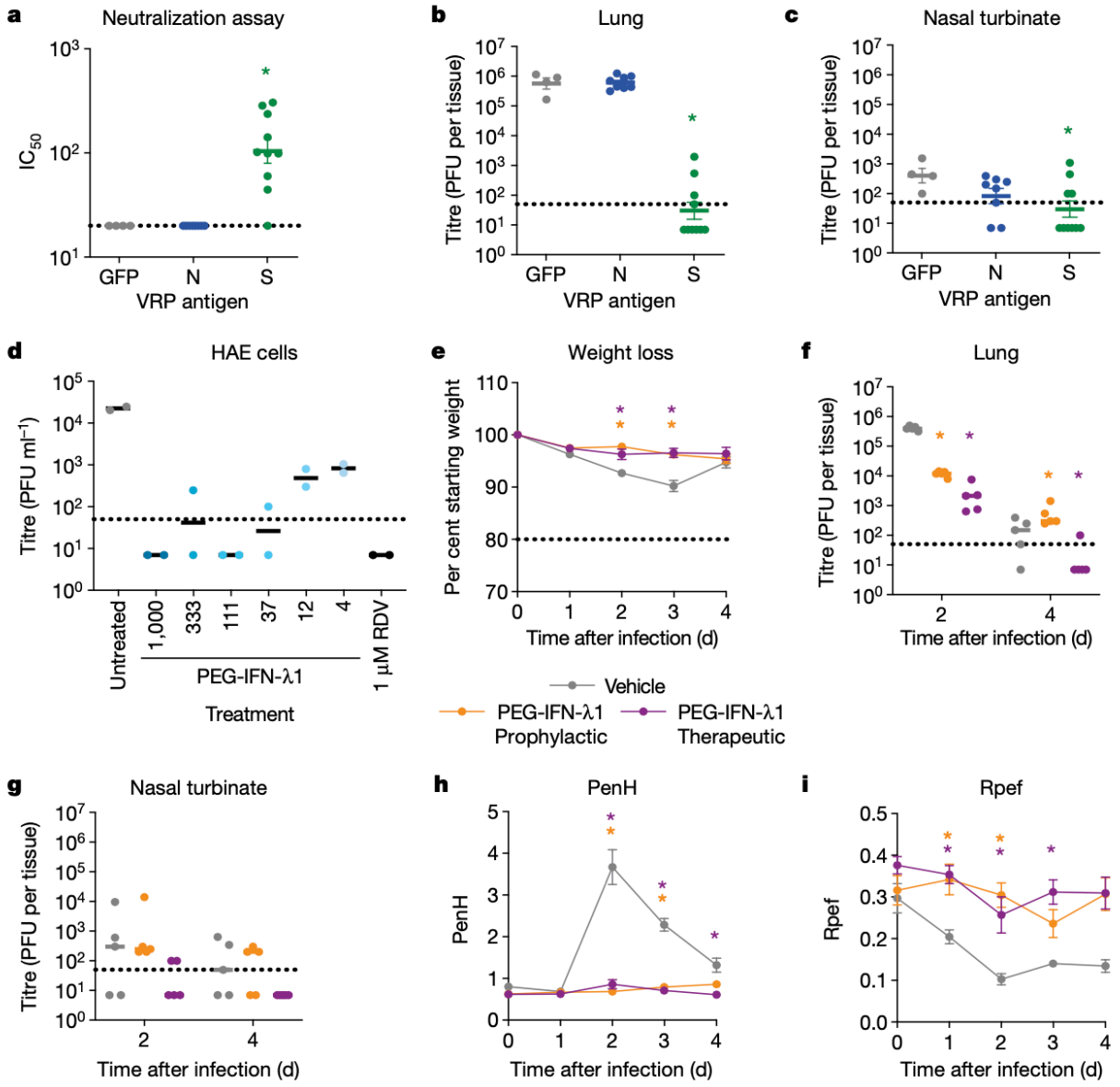

Figure 3.4. Evaluation of prevention and intervention strategies against SARS-CoV-2 MA infection in mice.

a–**c**, Groups of 10-week-old female BALB/c mice were vaccinated with VRPs expressing wild-type S (n = 10), N (n = 8) or GFP (n = 4). **a**, Half-maximal inhibitory concentration (IC50) of sera taken three weeks after boost to neutralize SARS-CoV-2. The dotted line represents LOD. The log-transformed data were analyzed by one-way ANOVA followed by Dunnett's multiple comparisons. *P = 0.0003. **b**, **c**, Lung (**b**) and nasal turbinate (**c**) viral titer at 2 dpi. The dotted line represents LOD. Undetected samples are plotted at half the LOD. The log-transformed data were analyzed as in **a**. In **b**, *$P \leq 0.0001$. In **c**, *P = 0.0360. **d**, Human primary airway epithelial cells were pretreated for 24 h with PEG-IFN-λ1, followed by infection with SARS-CoV-2. Infectious virus in apical washes from 48 h after infection was titrated. Remdesivir (RDV) was used as positive control. Data are representative of two independent experiments with samples from distinct human donors. **e**–**i**, One-year-old female BALB/c mice were subcutaneously treated with

vehicle or with 2 μg PEG-IFN-λ1 prophylactically or therapeutically and infected with SARS-CoV-2 MA. *n* = 5 per group per time point. **e**, Weight loss. The dotted line represents weight-loss criteria for humane euthanasia. Data were analyzed by mixed-effects analysis followed by Dunnett's multiple comparisons. In **b**, **P* ≤ 0.0001 (prophylactic, 2 dpi), 0.0128 (therapeutic, 2 dpi), 0.0042 (prophylactic, 4 dpi), 0.0037 (therapeutic, 4 dpi). **f**, **g**, Viral titers in the lung (**f**) and nasal turbinates (**g**) at 2 and 4 dpi. The dotted line represents LOD. The log-transformed data were analyzed by two-way ANOVA followed by Dunnett's multiple comparisons. **h**, **i**, Whole-body plethysmography assessing pulmonary function for PenH (**h**) and Rpef (**i**). Data were analyzed as in **e**. Data are mean ± s.e.m. In **h**, **P* = 0.0083 (prophylactic, 2 dpi), 0.0080 (therapeutic, 2 dpi), 0.0029 (prophylactic, 3 dpi), 0.0020 (therapeutic, 3 dpi), 0.0327 (therapeutic, 4 dpi). In **i**, **P* = 0.0442 (prophylactic, 1 dpi), 0.0033 (therapeutic, 1 dpi), 0.0048 (prophylactic, 2 dpi), 0.0118 (therapeutic, 3 dpi), 0.0259 (prophylactic, 4 dpi), 0.0247 (therapeutic, 4 dpi).

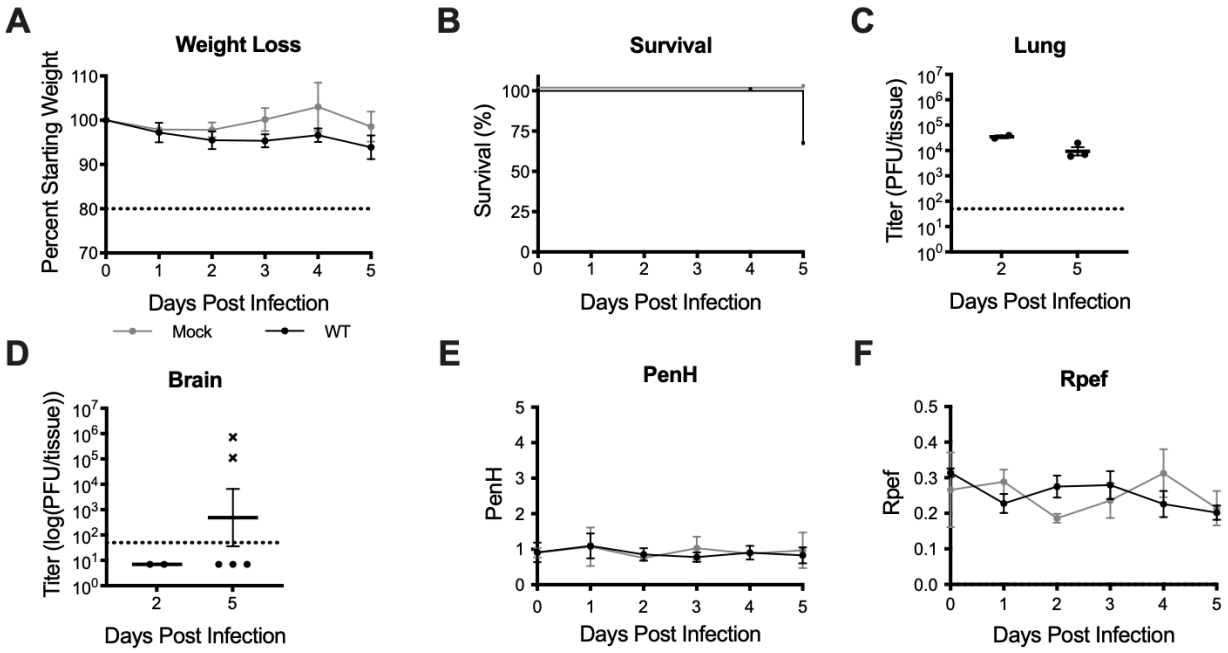

Figure 3.5. SARS-CoV-2 infection in Hfh4-hACE2 transgenic mice.

a–**f**, Male and female *Hfh4-hACE2* mice were infected with 10^5 PFU SARS-CoV-2 WT. **a**, Per cent starting weight. Dotted line represents weight-loss criteria for humane euthanasia. *n* = 2 mock and 5 SARS-CoV-2. **b**, Survival. **c**, **d**, Lung (**c**) and brain (**d**) viral titer. Dotted line represents LOD. Undetected samples are plotted at half the LOD. 'x' symbol indicates mice that succumbed to infection. 2 dpi: *n* = 2; 5 dpi: *n* = 5. **e**, **f**, Whole body plethysmography assessing pulmonary function for PenH (**e**) and Rpef (**f**).

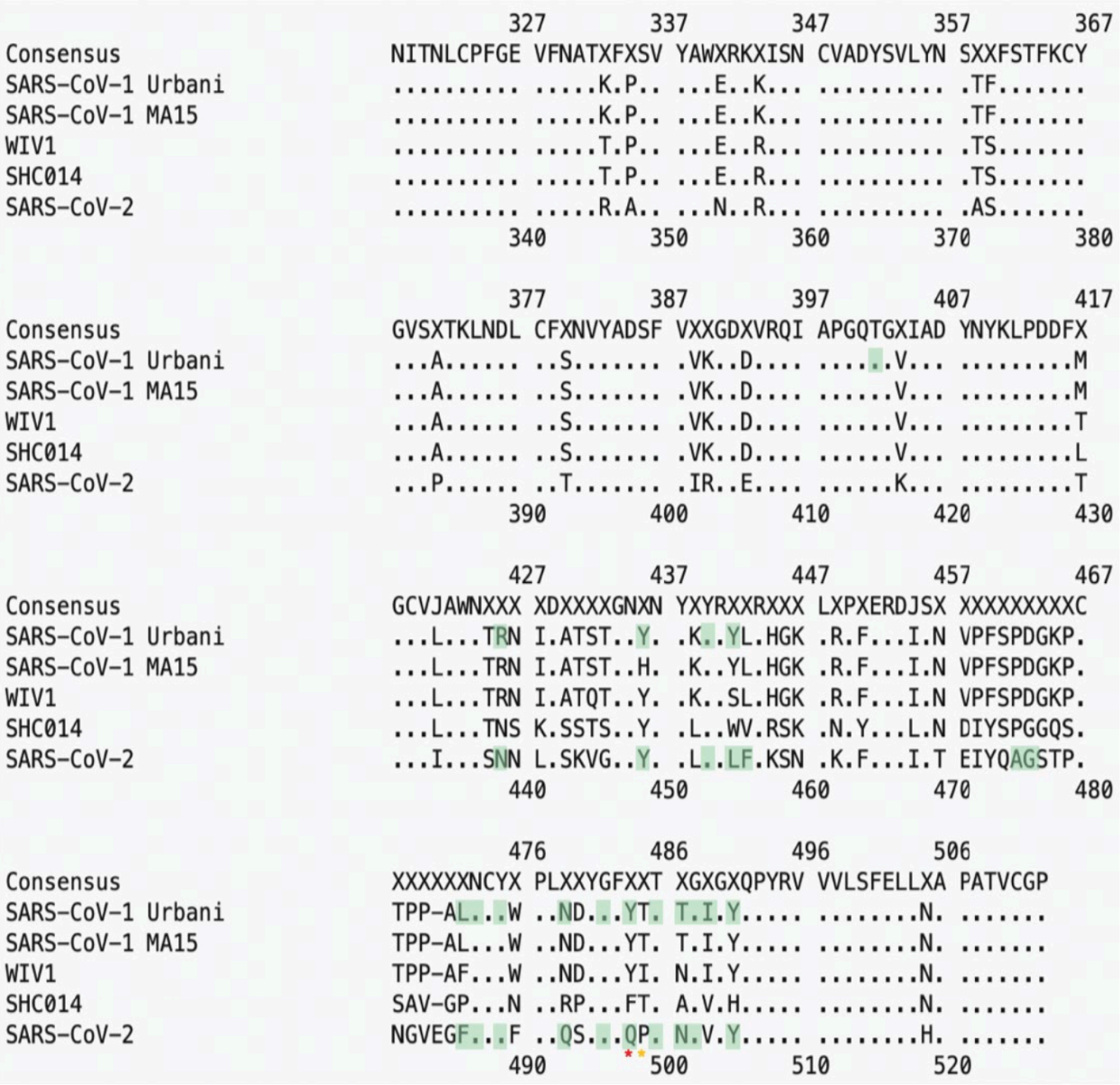

Figure 3.6. Group 2B coronavirus spike RBD alignment.

Amino acid positions are numbered above in reference to SARS-CoV-1, and below in reference to SARS-CoV-2. Green highlighted residues are hACE2 contacts as determined by published crystal structures.

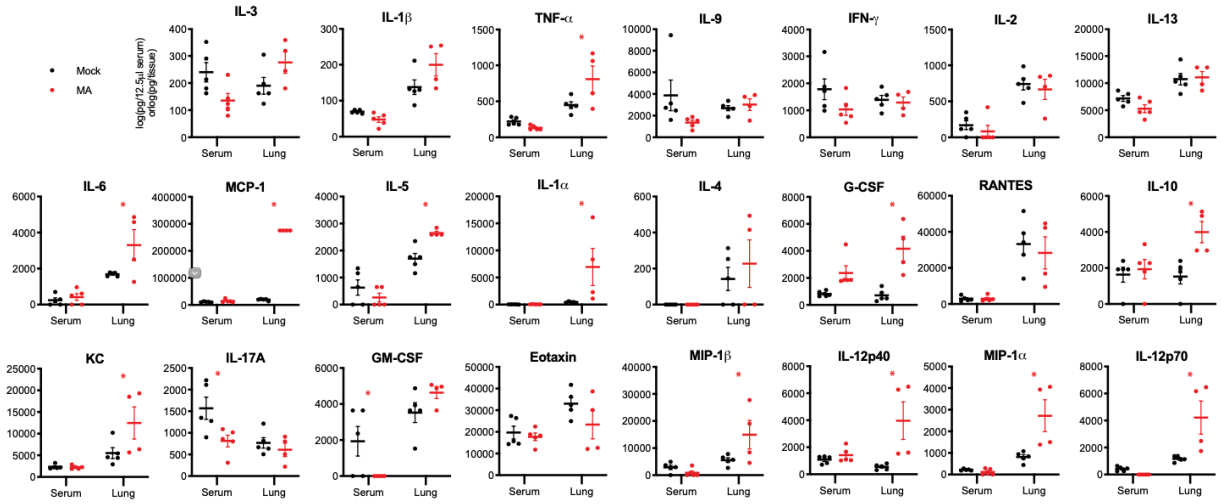

Figure 3.7. Cytokine analysis in SARS-CoV-2 MA infected 1-year-old BALB/c mice.

Cytokine and chemokine levels in serum and lung homogenates of 1-year-old female BALB/c mice from Figure 3.3 at 2 and 4 dpi. For each analyte, data analyzed by 2-way ANOVA followed by Sidak's multiple comparisons. '*' denotes P = 0.0155 (TNF-α), 0.0189 (IL-6), <0.0001 (MCP-1), 0.0115 (IL-5), 0.0127 (IL-1α), 0.0004 (G-CSF), 0.0070 (IL-10), 0.0243 (KC), 0.0152 (IL-17A), 0.0408 (GM-CSF), 0.0261 (MIP-1β), 0.0025 (IL-12p40), 0.0015 (MIP-1α), 0.0019 (IL-12p70).

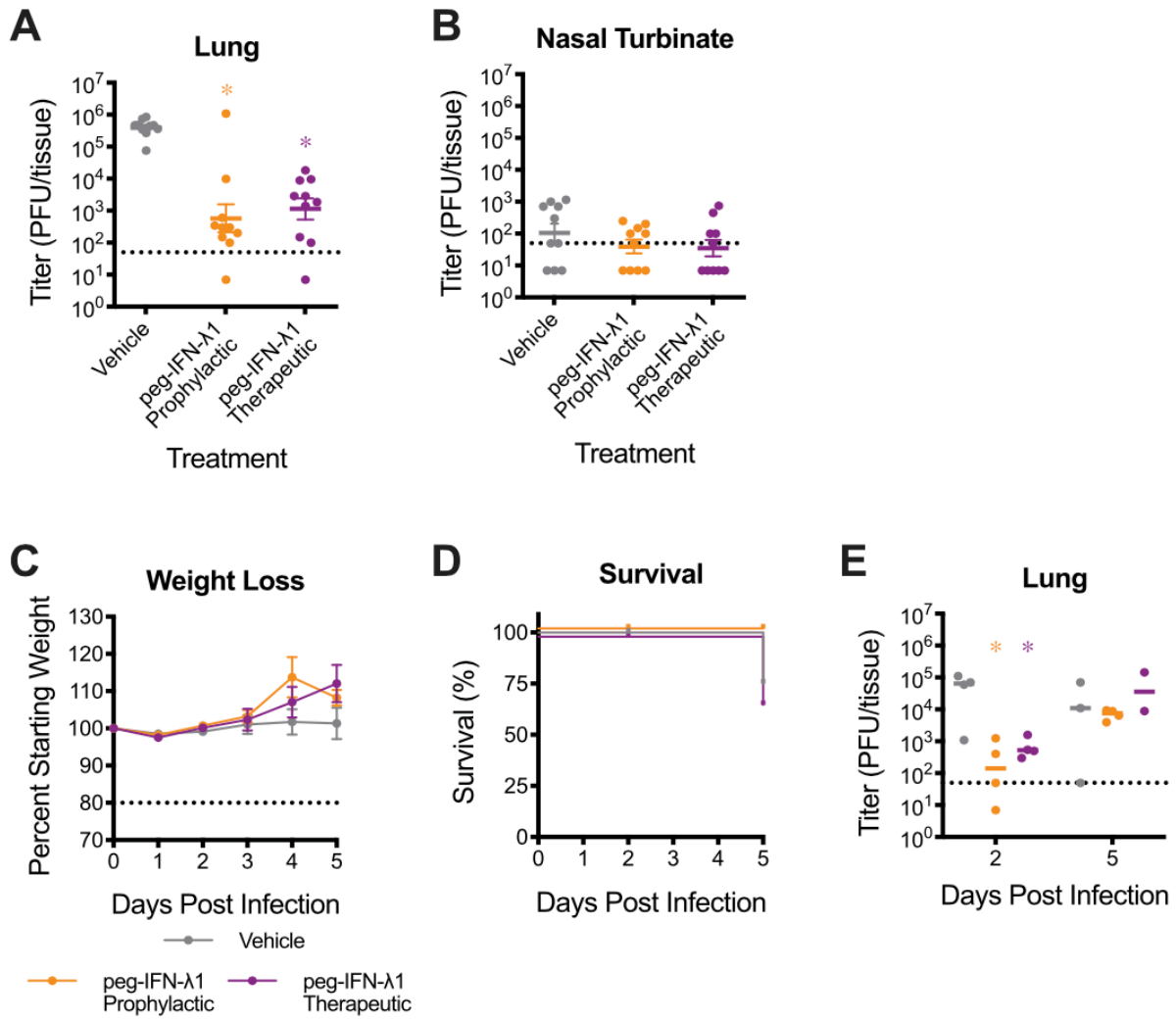

Figure 3.8. Evaluation of peg-IFN-λ1 against SARS-CoV-2 MA infection in young BALB/c and Hfh4-hACE2 mice.

a, **b**, Twelve-week-old female BALB/c mice were subcutaneously treated with vehicle or with 2μg peg-IFN-λ1 prophylactically or therapeutically and infected with SARS-CoV-2 MA. Viral titers in the lung (**a**) and nasal turbinates (**b**) at 2 dpi. *n* = 10 for each group, combined from two independent experiments. Dotted line represents LOD. Undetected samples plotted at half the LOD. log-transformed data analyzed by 1-way ANOVA followed by Holm–Sidak's multiple comparisons. In **a**, '*' denotes *P* = <0.0001 (prophylactic), <0.0001 (therapeutic). **c**–**e**, Four- to seven-week-old *Hfh4-hACE2* male and female mice were treated with peg-IFN-λ1 as done in **a**, **b**, and infected with 10^5 PFU SARS-CoV-2 WT. *n* = 8 vehicle; *n* = 10 prophylactic, *n* = 7 therapeutic. **c**, Per cent starting weight. Dotted line represents weight-loss criteria for humane euthanasia. Data analyzed by mixed effects analysis followed by Sidak's multiple comparisons. **d**, Survival. **e**, Lung viral titer at 2 and 5 dpi. 2 dpi: *n* = 4 vehicle, *n* = 4 prophylactic, *n* = 4 therapeutic: 5 dpi: *n* = 3 vehicle, *n* = 4 prophylactic, *n* = 2. Data analyzed by two-way ANOVA followed by Dunnett's multiple comparisons. '*' denotes *P* = 0.0037 (prophylactic, 2 dpi), 0.0365 (therapeutic, 2 dpi). All error bars represent standard error about the mean.

REFERENCES

1 Humeniuk, R. *et al.* Safety, Tolerability, and Pharmacokinetics of Remdesivir, An Antiviral for Treatment of COVID-19, in Healthy Subjects. *Clin Transl Sci* **13**, 896-906, doi:10.1111/cts.12840 (2020).

2 Corbett, K. S. *et al.* SARS-CoV-2 mRNA vaccine design enabled by prototype pathogen preparedness. *Nature* **586**, 567-571, doi:10.1038/s41586-020-2622-0 (2020).

3 Hassan, A. O. *et al.* A SARS-CoV-2 Infection Model in Mice Demonstrates Protection by Neutralizing Antibodies. *Cell* **182**, 744-753 e744, doi:10.1016/j.cell.2020.06.011 (2020).

4 Zhou, P. *et al.* A pneumonia outbreak associated with a new coronavirus of probable bat origin. *Nature* **579**, 270-273, doi:10.1038/s41586-020-2012-7 (2020).

5 Jiang, R. D. *et al.* Pathogenesis of SARS-CoV-2 in Transgenic Mice Expressing Human Angiotensin-Converting Enzyme 2. *Cell* **182**, 50-58 e58, doi:10.1016/j.cell.2020.05.027 (2020).

6 Bao, L. *et al.* The pathogenicity of SARS-CoV-2 in hACE2 transgenic mice. *Nature* **583**, 830-833, doi:10.1038/s41586-020-2312-y (2020).

7 Sun, S. H. *et al.* A Mouse Model of SARS-CoV-2 Infection and Pathogenesis. *Cell Host Microbe* **28**, 124-133 e124, doi:10.1016/j.chom.2020.05.020 (2020).

8 Sun, J. *et al.* Generation of a Broadly Useful Model for COVID-19 Pathogenesis, Vaccination, and Treatment. *Cell* **182**, 734-743 e735, doi:10.1016/j.cell.2020.06.010 (2020).

9 Israelow, B. *et al.* Mouse model of SARS-CoV-2 reveals inflammatory role of type I interferon signaling. *J Exp Med* **217**, doi:10.1084/jem.20201241 (2020).

10 Kim, Y. I. *et al.* Infection and Rapid Transmission of SARS-CoV-2 in Ferrets. *Cell Host Microbe* **27**, 704-709 e702, doi:10.1016/j.chom.2020.03.023 (2020).

11 Imai, M. *et al.* Syrian hamsters as a small animal model for SARS-CoV-2 infection and countermeasure development. *Proc Natl Acad Sci U S A* **117**, 16587-16595, doi:10.1073/pnas.2009799117 (2020).

12 Sia, S. F. *et al.* Pathogenesis and transmission of SARS-CoV-2 in golden hamsters. *Nature* **583**, 834-838, doi:10.1038/s41586-020-2342-5 (2020).

13 Rockx, B. *et al.* Comparative pathogenesis of COVID-19, MERS, and SARS in a nonhuman primate model. *Science* **368**, 1012-1015, doi:10.1126/science.abb7314 (2020).

14 Yu, P. *et al.* Age-related rhesus macaque models of COVID-19. *Animal Model Exp Med* **3**, 93-97, doi:10.1002/ame2.12108 (2020).

15 Munster, V. J. *et al.* Respiratory disease in rhesus macaques inoculated with SARS-CoV-2. *Nature* **585**, 268-272, doi:10.1038/s41586-020-2324-7 (2020).

16 Ostrowski, L. E., Hutchins, J. R., Zakel, K. & O'Neal, W. K. Targeting expression of a transgene to the airway surface epithelium using a ciliated cell-specific promoter. *Mol Ther* **8**, 637-645, doi:10.1016/s1525-0016(03)00221-1 (2003).

17 Menachery, V. D. *et al.* SARS-like WIV1-CoV poised for human emergence. *Proc Natl Acad Sci U S A* **113**, 3048-3053, doi:10.1073/pnas.1517719113 (2016).

18 Hou, Y. J. *et al.* SARS-CoV-2 Reverse Genetics Reveals a Variable Infection Gradient in the Respiratory Tract. *Cell* **182**, 429-446 e414, doi:10.1016/j.cell.2020.05.042 (2020).

19 Abdi, K. *et al.* Uncovering inherent cellular plasticity of multiciliated ependyma leading to ventricular wall transformation and hydrocephalus. *Nat Commun* **9**, 1655, doi:10.1038/s41467-018-03812-w (2018).

20 Menachery, V. D., Gralinski, L. E., Baric, R. S. & Ferris, M. T. New Metrics for Evaluating Viral Respiratory Pathogenesis. *PLOS ONE* **10**, e0131451, doi:10.1371/journal.pone.0131451 (2015).

21 Roberts, A. *et al.* A mouse-adapted SARS-coronavirus causes disease and mortality in BALB/c mice. *PLoS Pathog* **3**, e5, doi:10.1371/journal.ppat.0030005 (2007).

22 Menachery, V. D. *et al.* A SARS-like cluster of circulating bat coronaviruses shows potential for human emergence. *Nat Med* **21**, 1508-1513, doi:10.1038/nm.3985 (2015).

23 Wang, D. *et al.* Clinical Characteristics of 138 Hospitalized Patients With 2019 Novel Coronavirus-Infected Pneumonia in Wuhan, China. *JAMA* **323**, 1061-1069, doi:10.1001/jama.2020.1585 (2020).

24 de Wit, E., van Doremalen, N., Falzarano, D. & Munster, V. J. SARS and MERS: recent insights into emerging coronaviruses. *Nat Rev Microbiol* **14**, 523-534, doi:10.1038/nrmicro.2016.81 (2016).

25 Roberts, A. *et al.* Aged BALB/c mice as a model for increased severity of severe acute respiratory syndrome in elderly humans. *J Virol* **79**, 5833-5838, doi:10.1128/JVI.79.9.5833-5838.2005 (2005).

26 Kotenko, S. V. *et al.* IFN-lambdas mediate antiviral protection through a distinct class II cytokine receptor complex. *Nat Immunol* **4**, 69-77, doi:10.1038/ni875 (2003).

27 Sheppard, P. *et al.* IL-28, IL-29 and their class II cytokine receptor IL-28R. *Nat Immunol* **4**, 63-68, doi:10.1038/ni873 (2003).

28 Elazar, M. & Glenn, J. S. Emerging concepts for the treatment of hepatitis delta. *Curr Opin Virol* **24**, 55-59, doi:10.1016/j.coviro.2017.04.004 (2017).

29 Lan, J. *et al.* Structure of the SARS-CoV-2 spike receptor-binding domain bound to the ACE2 receptor. *Nature* **581**, 215-220, doi:10.1038/s41586-020-2180-5 (2020).

30 Shang, J. *et al.* Structural basis of receptor recognition by SARS-CoV-2. *Nature* **581**, 221-224, doi:10.1038/s41586-020-2179-y (2020).

31 Felgenhauer, U. *et al.* Inhibition of SARS-CoV-2 by type I and type III interferons. *J Biol Chem* **295**, 13958-13964, doi:10.1074/jbc.AC120.013788 (2020).

32 Muir, A. J. *et al.* A randomized phase 2b study of peginterferon lambda-1a for the treatment of chronic HCV infection. *J Hepatol* **61**, 1238-1246, doi:10.1016/j.jhep.2014.07.022 (2014).

33 Chan, H. L. Y. *et al.* Peginterferon lambda for the treatment of HBeAg-positive chronic hepatitis B: A randomized phase 2b study (LIRA-B). *J Hepatol* **64**, 1011-1019, doi:10.1016/j.jhep.2015.12.018 (2016).

34 Andreakos, E. & Tsiodras, S. COVID-19: lambda interferon against viral load and hyperinflammation. *EMBO Mol Med* **12**, e12465, doi:10.15252/emmm.202012465 (2020).

35 Feld, J. J. *et al.* Peginterferon lambda for the treatment of outpatients with COVID-19: a phase 2, placebo-controlled randomised trial. *The Lancet Respiratory Medicine* **9**, 498-510, doi:10.1016/s2213-2600(20)30566-x (2021).

36 Li, L. *et al.* IFN-lambda preferably inhibits PEDV infection of porcine intestinal epithelial cells compared with IFN-alpha. *Antiviral Res* **140**, 76-82, doi:10.1016/j.antiviral.2017.01.012 (2017).

37 Mordstein, M. *et al.* Lambda interferon renders epithelial cells of the respiratory and gastrointestinal tracts resistant to viral infections. *J Virol* **84**, 5670-5677, doi:10.1128/JVI.00272-10 (2010).

38 Rockx, B. *et al.* Escape from human monoclonal antibody neutralization affects in vitro and in vivo fitness of severe acute respiratory syndrome coronavirus. *J Infect Dis* **201**, 946-955, doi:10.1086/651022 (2010).

39 Sui, J. *et al.* Effects of human anti-spike protein receptor binding domain antibodies on severe acute respiratory syndrome coronavirus neutralization escape and fitness. *J Virol* **88**, 13769-13780, doi:10.1128/JVI.02232-14 (2014).

40 Rockx, B. *et al.* Structural basis for potent cross-neutralizing human monoclonal antibody protection against lethal human and zoonotic severe acute respiratory syndrome coronavirus challenge. *J Virol* **82**, 3220-3235, doi:10.1128/JVI.02377-07 (2008).

41 Zost, S. J. *et al.* Potently neutralizing and protective human antibodies against SARS-CoV-2. *Nature* **584**, 443-449, doi:10.1038/s41586-020-2548-6 (2020).

42 McCray, P. B., Jr. *et al.* Lethal infection of K18-hACE2 mice infected with severe acute respiratory syndrome coronavirus. *J Virol* **81**, 813-821, doi:10.1128/JVI.02012-06 (2007).

43 Li, F., Li, W., Farzan, M. & Harrison, S. C. Structure of SARS coronavirus spike receptor-binding domain complexed with receptor. *Science* **309**, 1864-1868, doi:10.1126/science.1116480 (2005).

44 Yount, B. *et al.* Reverse genetics with a full-length infectious cDNA of severe acute respiratory syndrome coronavirus. *Proc Natl Acad Sci U S A* **100**, 12995-13000, doi:10.1073/pnas.1735582100 (2003).

45 Scobey, T. *et al.* Reverse genetics with a full-length infectious cDNA of the Middle East respiratory syndrome coronavirus. *Proc Natl Acad Sci U S A* **110**, 16157-16162, doi:10.1073/pnas.1311542110 (2013).

46 Agnihothram, S. *et al.* Development of a Broadly Accessible Venezuelan Equine Encephalitis Virus Replicon Particle Vaccine Platform. *J Virol* **92**, doi:10.1128/JVI.00027-18 (2018).

47 Fulcher, M. L., Gabriel, S., Burns, K. A., Yankaskas, J. R. & Randell, S. H. Well-differentiated human airway epithelial cell cultures. *Methods Mol Med* **107**, 183-206, doi:10.1385/1-59259-861-7:183 (2005).

48 Davidson, S. *et al.* IFNlambda is a potent anti-influenza therapeutic without the inflammatory side effects of IFNalpha treatment. *EMBO Mol Med* **8**, 1099-1112, doi:10.15252/emmm.201606413 (2016).

CHAPTER 4 – A MOUSE-ADAPTED SARS-COV-2 INDUCES ACUTE LUNG INJURY AND MORTALITY IN STANDARD LABORATORY MICE[3]

4.1 Introduction

Zoonotic coronaviruses (CoVs) are responsible for three epidemics in the 21st century, including severe acute respiratory syndrome coronavirus (SARS-CoV) in 2003 and the ongoing Middle East respiratory syndrome coronavirus (MERS-CoV) since 2012. In December 2019, a third novel CoV designated SARS-CoV-2 emerged[1,2] and has resulted in a worldwide pandemic with over 25 million cases and over 850,000 deaths in over 220 countries[3]. SARS-CoV-2 infection results in a complex clinical syndrome, designated Coronavirus Disease 2019 (COVID-19), that causes a range of clinical symptoms from mild to a severe disease associated with acute lung injury (ALI) and the acute respiratory distress syndrome (ARDS)[4]. SARS-CoV-2 infection can also produce strokes, cardiac pathology, gastrointestinal disease, coagulopathy, and a hyperinflammatory shock syndrome[5-7]. The elderly, and those with underlying co-morbidities, are at increased risk of severe COVID-19[8] and death is most commonly linked to respiratory failure due to ARDS[9,10]. In fact, the mortality rate from COVID-19 ARDS approaches 40%– 50%, perhaps associated with a ‘‘cytokine storm’’ characterized by elevated levels of interferon (IFN)-γ, interleukin (IL)-18, transforming growth factor β (TGF-β), IL-6, IP-10, monocyte chemoattractant protein-1 (MCP-1), monokine-induced by IFN-γ (MIG), and IL-8[11].

---

[3]First published as: Leist, S.R.[**], Dinnon III, K.H.[**], Schafer, A., Tse, L.V., Okuda, K., Hou, Y.J., West, A., Edwards, C.E., Sanders, W., Fritch, E.J., et al. (2020). A Mouse-Adapted SARS-CoV-2 Induces Acute Lung Injury and Mortality in Standard Laboratory Mice. Cell 183, 1070-1085 e1012. 10.1016/j.cell.2020.09.050. [**]=co-first authors

SARS-CoV-2 uses the human angiotensin-converting enzyme 2 (hACE2) as a receptor for docking and entry into cells but is incapable of using the murine ortholog (mACE2) as a receptor[1,12]. To generate SARS-CoV-2 mouse models, several groups have developed transgenic mouse lines expressing hACE2, utilizing a variety of exogenous[13,14] or murine promoters[15], or by transduction using adenovirus[16,17] or adeno-associated virus vectors[18], to generate productive infections. Although each system has certain advantages (e.g., speed of development), infection in vector-mediated or transgenic over- expression models typically causes a mild alveolitis in the lung and/or progression to fatal encephalitis[19-22], rarely recapitulating the severe lung disease that is one of the hallmarks of COVID-19 in humans. As such, it is critical to develop models that use standard laboratory mice, reproduce age-dependent SARS- CoV-2 susceptibility, target nasal epithelia and alveolar pneumocytes, and develop the relevant pulmonary lesions of acute lung injury (including pneumonitis, edema, necrotic debris, and hyaline membrane formation) that are consistent with progression to ARDS. Such models, especially if available in standard laboratory mice, will accelerate studies of COVID-19 immune pathologies, the function of host genes in regulating disease progression, and will provide a high-throughput screening platform for evaluating antiviral drugs and vaccines.

In this study, we describe a lethal mouse model of mouse-adapted SARS-CoV-2 (defined as SARS-CoV-2 MA10) pathogenesis that recapitulates the age-related disease severity observed in humans, ALI/ARDS, and death in wild-type BALB/c mice. Like human infections, SARS-CoV-2 MA10 infection targets the conducting and distal airways, including airway epithelial cells and AT2 cells in the terminal bronchi and alveoli, and replicates in nasal olfactory epithelium sustentacular cells and Bowman's glands. The SARS-CoV-2 MA10 infection in BALB/c mice induces lung disease characterized by damaged airway epithelium, exfoliated cells in small airways, fibrin deposition, occasional hyaline membrane formation, pulmonary edema, surfactant expression loss, and congestion that can progress to ARDS, especially in aged animals. Many Th1 proinflammatory cytokines were elevated after infection, including IL-6. Interestingly, SARS-

CoV-2 MA10 infection of C57BL/6J mice caused a milder phenotype, whereas infection of immunodeficient type I and II interferon receptor double knockout C57BL/6J mice resulted in severe weight loss and morbidity. Notably, mice vaccinated with viral vector-delivered SARS-CoV-2 spike were protected from clinical disease and infection of the lung. The development of SARS-CoV-2 MA10 provides a much-needed standard laboratory mouse model that recapitulates the age- related severity spectrum and acute lung injury phenotype observed in human SARS-CoV-2 infections. It also provides a robust model to mechanistically address novel questions in COVID-19 immunity, pathogenesis, and vaccine and antiviral drug performance in wild-type and genetically modified standard laboratory mice.

4.2 Results

4.2.1 Adaptation of SARS-CoV-2 MA via Serial Passaging In Vivo

We previously developed a recombinant mouse adapted strain of SARS-CoV-2 (SARS-CoV-2 MA) capable of utilizing mACE2 for viral entry by remodeling the spike and receptor binding interface [23]. However, SARS-CoV-2 MA infection of wild-type young adult mice did not display the major clinical manifestations or hallmarks of ALI[23]. To improve the model, we used experimental evolution *in vivo* via serial passage of SARS-CoV-2 MA in the lungs of young adult BALB/cAnNHsd mice (herein referred to as ‘‘BALB/c’’ mice) every 2 days to select for more virulent strains[24]. With passage, we observed a decrease in body weight over time achieving greater than 10% body weight loss on 2 days post infection (dpi) by passage ten (P10) **(Figure 4.1A)**. We confirmed the virulence of the virus population generated at P10 using a plaque purified clonal isolate (SARS-CoV-2 MA10) from this passage in young adult BALB/c mice **(Figure 4.1B)**. Deep sequencing of mouse lung total RNA from the 10 passages, plaque purified SARS-CoV-2 MA10, and four additional plaque purified passage 10 viruses was performed to identify the

changes responsible for the increased pathogenicity and rare variants. In addition to the spike Q498Y/P499T substitutions engineered into the parental SARS-CoV-2 MA, SARS-CoV-2 MA10 included 5 additional nucleotide changes, all resulting in nonsynonymous coding changes **(Figures 4.1C–D; Table 4.1)**. These mutations emerged in an ordered fashion and included changes in nonstructural protein 4 (nsp4) (C9438T), nsp7 (A11847G), nsp8 (A12159G), spike (S; C23039A), and open reading frame 6 (ORF6; T27221C). Some sequence heterogeneity was observed across the plaque purified viruses, although SARS-CoV-2 MA10 had the fewest mutations and most represented the viral population found at passage 10 **(Table 4.1)**. The SARS CoV-2 MA10 maintained the ability to utilize non-human primate ACE2 and replicated and formed plaques in Vero E6 cells **(Figure 4.1E)**, consistent with utility for viral propagation and titration. Importantly, SARS-CoV-2 MA10 was also attenuated compared to wild-type SARS-CoV-2 (SARS-CoV-2 WT) in primary human bronchiolar epithelial cells (HBEs) **(Figure 4.1F)**, suggesting decreased fitness in human cells. Collectively, these observations led to the choice of SARS-CoV-2 MA10 for subsequent studies.

4.2.2 SARS-CoV-2 MA10 Causes Acute Lung Injury in Young BALB/c Mice

To gain insight into the dose-dependent pathogenic potential of SARS-CoV-2 MA10, we performed dose ranging studies in 10-week-old BALB/c mice infected with either PBS (mock), 10^5 plaque-forming unit (PFU) of the parental SARS-CoV-2 MA, or 10^2, 10^3, 10^4, and 10^5 PFU SARS-CoV-2 MA10. We observed a dose-dependent increase in morbidity and mortality over the course of 14 days with SARS-CoV-2 MA10 **(Figure 4.2A)**. Mortality rates of 20% and 60% were recorded for infection with 10^4 and 10^5 PFU, respectively. Notably, infection with 10^2 PFU of SARS- CoV-2 MA10 produced an increased weight loss as compared to 10^5 PFU infections with the parental SARS-CoV-2 MA strain, highlighting the increased pathogenicity gained through passaging. To best capture severe disease phenotypes without excessive mortality, we

proceeded with 10^4 PFU of SARS-CoV-2 MA10 as the standard infection dose for young adult BALB/c mice.

To characterize the pathogenesis of SARS-CoV-2 MA10 in young BALB/c mice, we examined the kinetics of disease in mice through 7 dpi using an intranasal inoculating dose of 10^4 PFU. SARS-CoV-2 MA10-infected mice rapidly lost weight and reached maximum weight loss at day 4 (losing 16% of starting weight) **(Figure 4.2B)**. At 5 dpi, the weight loss trajectories of infected mice diverged, with many mice recovering body weight juxtaposed to mice that continued to lose weight, collectively resulting in a ~15% mortality rate **(Figure 4.2C)**. At the time of necropsy, acute stage lung damage was noted grossly as firm, red, heavy lobes that were scored based on the extent of congestion-related discoloration[25] (indicative of edema and diffuse alveolar damage) that peaked at 4 dpi and remained high through 7 dpi **(Figure 4.2D)**. Virus replication in the lung peaked 1–2 dpi and was absent in most surviving mice by 7 dpi **(Figure 4.2E)**. Viral replication in the upper respiratory tract (measured by viral titer in the nasal cavity) remained high on 1–3 dpi but was non-detectable in most mice by 5 dpi **(Figure 4.2F)**.

To gain insight into the impact of infection on lung physiology, pulmonary function was measured over time via whole body plethysmography (WBP). As compared to control mice, infected mice exhibited a loss in pulmonary function as indicated by significant changes in PenH and Rpef, measures of airway obstruction, and EF50, a measurement of exhalation flow rate **(Figures 4.2G–2I)**.

Histopathologic analyses at 2, 4, and 7 dpi revealed early multifocal damage to conducting airway epithelia (including bronchioles) that corresponded to viral antigen staining, which was intense on 2 dpi, waned by 4 dpi, and was absent by 7 dpi **(Figure 4.2J)**. Often, bronchial damage progressed to segmental epithelial denudation with an accumulation of inflammatory cells, sloughed epithelial cells, cellular debris, fibrin deposition, and plasma proteins in the airway lumens. Later post-SARS-CoV-2 MA10 infection, airway epithelia became hyperplastic with regeneration. The distal alveolar ducts and sacs were markedly altered by infection, displaying

hallmarks of diffuse alveolar damage (DAD) and multifocal positive labeling of pneumocytes for viral antigen at early time points after infection. Histologic changes included hypercellular thickening of the alveolar septae caused by infiltrating immune cells, pneumocyte degeneration and necrosis, congestion of small vessels and capillaries, endothelial activation, increased neutrophils with extravasation, exudation of proteinaceous fluid and fibrin with occasional organization into hyaline membranes, and increased numbers of alveolar macrophages. Although later time points featured increased numbers of lymphocytes organizing around bronchioles, lymphocytic cuffing was not a prominent pathologic feature in comparison to findings induced by other respiratory viral pathogens. Importantly, the most severe, lingering damage over the time course was in the alveolar region.

The pathology of SARS-CoV-2 MA10-infected lungs was blindly quantified utilizing two metrics of ALI[26,27]. First, diffuse alveolar damage (DAD) was assessed based on the degree of cellular sloughing and necrosis. SARS-CoV-2 MA10 induced DAD as early as 2 dpi and was maintained through 7 dpi **(Figure 4.2J)**. Second, the American Thoracic Society (ATS) has generated a small animal model ALI scoring scheme that assesses neutrophil presence in the interstitium and alveolar space, hyaline membrane formation, protein accumulation, and alveolar septal thickening[27]. Consistent with DAD scores, ATS ALI scores were increased in SARS-CoV-2 MA10-infected mice at 2 dpi and increased through 7 dpi **(Figure 4.2K)**. Immunohistochemistry (IHC) staining for viral nucleocapsid revealed intense staining at 2 dpi and lack of staining by 7 dpi **(Figure 4.2L)**, consistent with the lung viral titer data **(Figure 4.2D)**. At 2 dpi, viral antigen was detected in conducting airway epithelia and in the alveoli, consistent with alveolar type II pneumocyte distribution patterns.

4.2.3 Increased Morbidity and Mortality in Old Mice after SARS-CoV-2 MA10 Infection

Because SARS-CoV-2 and other emerging human coronaviruses exhibit an age-dependent increase in disease severity, we investigated whether SARS-CoV-2 MA10 infection of

aged mice resulted in an increased disease severity. In comparison to young mice, 1-year-old mice were highly susceptible to SARS-CoV-2 MA10, with high morbidity and nearly 100% mortality when infected with 10^4 and 10^5 PFU **(Figure 4.3A)**. Although mice infected with 10^3 PFU rapidly lost weight with very few animals surviving, those infected with 10^2 PFU did not exhibit disease signs and all survived, suggesting a threshold of virus >10^2 PFU was necessary to cause significant disease in 1-year-old mice. Accordingly, we selected the lowest dose that caused severe disease (10^3 PFU) as the standard infection dose for 1-year-old mice. With this dose, the kinetics of weight loss were similar to young BALB/c mice infected with 10^4 PFU. However, unlike infected young adult mice, all aged mice continued to lose weight over time and ultimately lost 30% of their starting weight, succumbing to infection and/or reaching the criteria for humane euthanasia **(Figure 4.3B)**. Overall, we observed increased mortality starting on day 4 after infection with only ~15% survival by day 7 **(Figure 4.3C)**. Thus, data presented at late time points such as 6 or 7 dpi are biased toward rare survivors.

Gross pathological evaluations at necropsy revealed macroscopically detectable discoloration of lung tissue that achieved maximal severity on days 4 and 5 after infection **(Figure 4.3D)**. Virus replication in aged mice peaked 1 to 2 dpi (5.3 x 10^3 PFU/tissue and 1.2 x 10^7 PFU/tissue, respectively), values similar to young adult mice. In contrast with young adult mice, in which virus was cleared by 7 dpi, significant levels of infectious virus remained in the lungs of aged mice at later time points **(Figure 4.3E)**. Low levels of infectious virus were present in the serum at 2 dpi **(Figure 4.8A)**. Minimal virus was found in the heart, which may reflect residual virus from the serum, and virus was not detected in brain at the time of peak lung titer (2 dpi) **(Figure 4.8A)**. Viral protein was not detected in the heart, liver, small intestine, kidney, or spleen **(Figures 4.8B–F)**. Old mice also exhibited viral titers in the nasal cavity over the first 3 days of infection (peak on 3 dpi at 2 x 10^4 PFU/tissue), consistent with young adult mice **(Figure 4.3F)**. Infection with SARS-CoV-2 MA10 also disturbed lung function in aged mice in a similar, but more

prolonged, manner compared to young mice with significant changes in PenH, Rpef, and EF50 at 2–5 dpi **(Figures 4.3G–I)**.

Histological analyses revealed severe DAD and higher ATS ALI scores at later time points throughout the lung in 1-year-old mice **(Figures 4.3J–K)**, consistent with the more pronounced interstitial congestion, epithelial damage, immune cell infiltration, and edema in the older animals **(Figure 4.3L)**. Viral antigen was detected in small airways and alveolar regions at 2 and 4 dpi **(Figure 4.3L)**. Viral RNA was also detected in the olfactory epithelium at 2 dpi **(Figure 4.3M)**, concordant with nasal cavity viral titers **(Figure 4.3F)**. At 4 dpi, the olfactory epithelium was severely damaged, likely contributing to reduced nasal cavity viral titers, and infection had spread to the Bowman's gland in the submucosa **(Figure 4.3F)**.

Many viral diseases are associated with a systemic cytokine storm. We analyzed the chemokine and cytokine responses in the serum and lungs of 1-year-old BALB/c mice at 2 and 4 dpi **(Figures 4.9A–B)**. At 2 dpi, several proinflammatory cytokines were elevated in the lungs of SARS-CoV-2-infected mice, whereas few were elevated systemically in the serum. For instance, IL-6, IL-1α, IL-1β, TNF-α, MCP-1, and IFN-γ were highly elevated in the serum and/or lungs of infected mice, similar to reports in humans[11]. It remains uncertain as to whether these elevated cytokines contribute to severe disease outcomes after infection or simply reflect higher levels of viral replication.

4.2.4 Ameliorated Disease and No Mortality in C57BL/6J Mice after SARS-CoV-2 MA10 Infection

C57BL/6 is the most commonly used mouse strain and is the genetic background for the majority of genetically engineered mice[28]. Because host genetic background dependent differences in disease susceptibility have been described for many infectious diseases including SARS-CoV[29-33], we evaluated SARS-CoV-2 MA10 infection in young adult C57BL/6J mice. In comparison to BALB/c mice, 10-week-old C57BL/6J mice exhibited less severe disease and only

the two highest doses (10^4 and 10^5 PFU) were associated with significant weight loss, but no mortality after infection **(Figure 4.4A)**. Therefore, we performed a detailed analysis of the 10^4 PFU infectious dose over 7 days for a direct comparison between young BALB/c and C57BL/6J mice. After infection with 10^4 PFU, C57BL/6J mice exhibited a transient 10%–15% weight loss (peaked on 3 dpi and 4 dpi) **(Figure 4.4B)** without mortality **(Figure 4.4C)**. Gross congestion scores in lungs at the time of harvest never rose above a score of 1 (roughly 25% lung involvement) and declined from 3 dpi until 7 dpi **(Figure 4.4D)**. A clear peak in viral replication in the lungs was observed on 2 dpi (1.6×10^6 PFU/tissue) that was ~10-fold lower than peak titers observed in BALB/c mice. After 2 dpi, titers decreased steadily and were not detectable by 7 dpi **(Figure 4.4E)**. In addition, viral loads in the nasal cavity were relatively low through 3 dpi (2×10^3 to 1.2×10^4 PFU/tissue) and were undetectable by 4 dpi **(Figure 4.4F)**. Changes in lung function as measured by WBP were similar for the two mouse strains, but C57BL/6J mice exhibited restored lung function to near baseline levels by 5 dpi, whereas abnormalities in BALB/c mice persisted until 7 dpi **(Figures 4.4G–I)**. Similarly, the patterns of histologic changes were equivalent in C57BL/6J mice to young BALB/c mice **(Figure 4.4L)**, but the magnitudes of the acute lung injury scores were dramatically attenuated in C57BL/6J mice **(Figures 4.4J–K)**.

4.2.5 SARS-CoV-2 MA10 Cellular Tropism

To characterize the tissue and cellular tropism of SARS-CoV-2 MA10, BALB/c mouse nasal and lung tissues were probed for the SARS-CoV-2 viral nucleocapsid and tissue/cell type markers by RNA *in situ* hybridization (ISH) and immunohistochemistry (IHC). In the proximal conducting airways (e.g., trachea, bronchi), little, if any, SARS-CoV-2 MA10 infection was identified. However, robust viral infection was identified in terminal bronchioles that connect to the alveolar spaces **(Figures 4.5A–B)**. In the SARS-CoV-2 MA10-infected mouse terminal bronchiolar epithelial region, expression of *Scgb1a1*, which is a secretory club cell marker, largely disappeared whereas *Foxj1*, a ciliated cell marker, persisted. IHC identified SARS-CoV-2 MA10

nucleocapsid expression in non-ciliated cells with occasional colocalization with CCSP **(Figures 4.3L and 4.5C)**, suggesting that secretory club cells were infected by SARS-CoV-2 MA10 and subsequently lost *Scgb1a1* expression. This cellular tropism of SARS-CoV-2 MA10 is different in human airways, perhaps reflecting different cell levels for ACE2 expression between human versus mice (i.e., ciliated versus secretory club), respectively[34].

In alveoli, ISH studies of mock-infected mice identified the two major epithelial cell types, i.e., AT1 (*Ager* expressing) and AT2 (*Sftpc*, *Sftpb* expressing) cells **(Figures 4.5D and 4.5E)**. In SARS- CoV-2 MA10-infected mice, *Sftpc* and *Sftpb* expression characteristic of AT2 cells virtually disappeared, whereas *Ager* expression associated with AT1 cells persisted at 2 dpi. IHC identified occasional cells expressing a third AT2 cell marker (LAMP3) that also co-expressed the SARS-CoV-2 MA10 nucleocapsid **(Figure 4.3F)**. Collectively, the loss of surfactant protein transcripts, but not AGER, staining and colocalization of a third AT2 marker (LAMP3) with virus, argues for selective infection by SARS-CoV-2 MA10 of AT2 in the alveolus. The finding that SARS-CoV-2 MA10-infected AT2 cells suppressed expression of selective cell-type-specific genes (e.g., *Sftpc* and *Sftpb*) is consistent with findings in infected human AT2 cells *in vitro*[35].

The nasal cavity of the mouse is comprised of ~50% respiratory epithelium and 50% olfactory epithelium[36]. As noted above **(Figure 4.3M)**, SARS-CoV-2 MA10 RNA was detected in olfactory epithelium, as defined anatomically and by the olfactory sensory neuron marker (OSN) marker, *Uchl1* **(Figure 4.10)**. Notably, viral RNA was not detected in cells expressing *Uchl1*, indicating that SARS-CoV-2 MA10 likely infected sustentacular cells rather than OSNs. The selective olfactory infection by SARS-CoV-2 MA10 is likely associated with altered olfactory function commonly observed in subjects with COVID-19[37-39].

4.2.6 Interferon Signaling Is Protective in SARS-CoV-2 MA10 Infection

We next tested whether the pathogenic SARS-CoV-2 MA10 virus could be used with genetically deficient mice to elucidate aspects of underlying molecular pathways and networks

that regulate SARS-CoV-2 disease. IFN signaling plays an important role in controlling and regulating disease severity after infection with many viruses, including coronaviruses[18,40]. SARS-CoV-2 has also been reported to be sensitive to type I and III IFN in human cells *in vitro*[41,42] and mice *in vivo*[18,23]. Consequently, we infected C57BL/6J mice lacking the type I and II IFN receptors (IFNR DKO) and wild-type controls with 10^4 PFU of SARS-CoV-2 MA10. IFNR DKO mice were more susceptible to SARS-CoV-2 MA10 as indicated by the prolonged weight loss compared to wild-type mice **(Figure 4.6A)**. Animals were harvested on planned harvest days. At 4 dpi, SARS-CoV- 2 MA10 IFNR DKO mice displayed much higher congestion scores **(Figure 4.6B)**, which were associated with higher viral titers on 2 and 4 dpi in IFNR DKO mice **(Figure 4.6C)**. These data suggest that IFNs are important in limiting viral replication and assisting in virus clearance *in vivo*. Consistent with these data, lung function abnormalities were more pronounced and prolonged in infected IFNR DKO mice **(Figures 4.6C–E)**.

4.2.7 SARS-CoV-2 MA10 Allows Rapid Evaluation of Medical Counter Measurements

As previously shown for SARS-CoV-2 MA, mouse adapted viral strains allow for rapid testing of prevention and intervention strategies[23]. The SARS-CoV-2 MA10 murine model adds to measurements of viral load the ability to evaluate changes in clinical parameters (weight loss, lung function, and pathologic changes) and mortality[23]. Utilizing our previously described non-select BSL2 Venezuelan equine encephalitis viral replicon particle (VRP) system[23,43], 10-week-old young adult and 1-year-old (‘‘aged’’) BALB/c mice were immunized with 10^3 VRPs expressing SARS-CoV-2 WT spike (S), nucleocapsid (N), and GFP control, followed by a boost at 3 weeks, and challenged with SARS-CoV-2 MA10 4 weeks post boost (7 weeks post prime). Neutralization assays using nLuc expressing reporter virus revealed strongly neutralizing activity in the serum from mice at 3 weeks post boost from spike, but not serum from nucleocapsid or GFP vaccinated mice **(Figures 4.7A and 4.11A)**. Of note, older (1-year-old) animals exhibited significantly reduced neutralization titers as compared to 10-week-old animals, capturing age related vaccine

vulnerabilities often observed in human populations **(Figure 4.11B)**. Notably, polyclonal sera had similar neutralization titers for both SARS- CoV-2 and SARS-CoV-2 MA containing two of three receptor binding domain changes present in MA10, suggesting that the SARS-CoV-2 MA10 model can accurately be used to test vaccine efficacy **(Figure 4.11C)**. Only mice vaccinated with SARS-CoV-2 spike expressing VRPs exhibited disease protection as demonstrated by an absence of reductions in in body weight, protection from death **(Figures 4.7B–C, 4.11D–E)**, and total elimination of viral titers in the lower respiratory tract (lungs) **(Figures 4.7D and 4.11F)**. Only one old mouse had detectable lung titer, corresponding to the mouse with the lowest serum neutralization titer. Interestingly, viral titers were still detectable on 2 and 4 dpi after infection in the nasal cavity of immunized young and old mice **(Figures 4.7E and 4.11G)**, suggesting that mucosal immunity in the nasal cavity may be difficult to achieve by systemic immunization. Importantly, significant improvements in lung function were measured in both age groups in VRP-S vaccinated mice versus VRP-GFP or VRP-N controls **(Figures 4.7F–H and 4.11H–J)**.

4.3 Discussion

Mouse models of viral pathogenesis that faithfully recapitulate aspects of human COVID-19 are needed to better understand the underlying molecular mechanisms of disease and assess the performance of medical countermeasures. Herein, we used *in vivo* experimental evolution to select a mouse-adapted SARS-CoV-2 strain, designated SARS-CoV-2 MA10, capable of causing lethal disease in standard laboratory mice. Importantly, the pathologic findings of SARS-CoV-2 MA10 increased as a function of mouse age, mirroring age gradients observed in humans[9,10]. The cellular tropism of SARS-CoV-2 MA10 in the mouse respiratory tract generally reflects that reported in humans (e.g., tropism for AT2 cells and olfactory epithelia)[35]. Different from humans, SARS-CoV-2 MA10 infects the infected secretory (club) cells of the conducting airways of mice, versus ciliated cells in humans. The high cytokine expression levels measured in the lungs and to a lesser extent serum of aged animals are consistent with findings reported in humans with

ARDS[44,45]. Our data also demonstrated that IFN signaling played an important role in attenuating SARS-CoV-2 MA10 viral replication, disease morbidity, and mortality, suggesting that human genetic variation in IFN pathway genes may in part mediate the wide variation of clinical outcomes observed in human SARS-CoV-2 infections. Finally, we provided evidence for the practical application of this model to evaluate SARS-CoV-2 vaccine candidates, with VRP-S immunization protecting and significantly limiting viral growth and disease severity in the lung of young and aged mice.

The increased virulence of SARS-CoV-2 MA10 was associated with five mutations acquired through passage in mice. In contrast to SARS-CoV, which acquired nonsynonymous mutations in nsp5, nsp9, nsp13, S, and M when generating mouse adapted SARS-CoV MA15[24], the SARS-CoV-2 MA10 mouse adaptations reflected amino acid changes in nsp4, nsp7, nsp8, S, and ORF6. Like SARS-CoV MA15, the severity of SARS-CoV-2 MA10 infection was partially attenuated in C57BL/6J mice, providing evidence that host genetic variation in susceptibility and resistance alleles can alter the trajectory of disease in a model of moderate disease. Indeed, a similar intermediate disease phenotype with SARS-CoV MA15 infection in C57BL/6 mice revealed host genes that play protective or pathogenic roles in SARS-CoV disease severity[46-49].

With respect to the contribution of the 5 new mutations identified in SARS-CoV-2 MA10, two engineered (Q498Y, P499T) and one evolved (Q493K) amino acid change were noted in the S glycoprotein receptor binding domain, and the latter mutation is predicted to enhance interactions with mouse ACE2 receptor via interaction with residue N31. Other SARS-CoV-2 strains, which replicate but do not produce clinical signs of disease in mice, have RBD mutations at Q498H or R493K, respectively[50,51]. Like for the 2003 SARS-CoV mouse adapted strains[24,52], multiple mutational pathways exist to enhance virus adaptation to the mouse. The MA10 mutation in ORF6 is also interesting, because ORF6 acts as an IFN antagonist that blocks nuclear import of karyopherin 2 into the nucleus of the cell[53]. Previous studies in our lab demonstrated that deletion of ORF6 in SARS-CoV attenuated virus pathogenesis, allowing nuclear import of multiple

transcription factors and enhanced host defense expression patterns in immortalized human lung cells, Calu3[54]. Although speculative, these data suggest that the SARS-CoV-2 MA10 ORF6 mutation may enhance blockade of transcription factor nuclear import, resulting in dampened innate immune antiviral gene expression in the mouse. Finally, mutations were noted in nsp4, nsp7, and nsp8 that have known activities in endoplasmic reticulum and Golgi membrane reorganization to form viral replication factories, as scaffolds for replicase and RNA primase functions, and perhaps processivity activities, respectively[55]. Future mapping studies will determine the contribution of each change to viral pathogenesis and host expression patterns in young and aged mice.

Emerging CoVs like SARS-CoV, MERS-CoV, and SARS-CoV-2 primarily infect cells lining the upper and lower respiratory tract with damage that triggers the development of ALI, ARDS, and end stage severe lung disease. In humans, many COVID-19 patients exhibit varying degrees of acute injury to airway and alveolar epithelial cells, with resultant fibrin deposition, edema, and hyaline membrane formation. Subsequent hyperplasia of type II pneumocytes, organizing phases of diffuse alveolar damage, focal pulmonary microthrombi, and endothelialitis are also observed in patients[56-58]. Using established metrics to quantitate pathological features of ALI and ARDS in SARS-CoV[59] and MERS-CoV[25] mouse models, the lung pathology for SARS-CoV-2 MA10 was quantitated and demonstrated significant ALI and ARDS in an age- related disease gradient. The loss of surfactant protein B and C expression is also consistent with the development of ARDS in SARS-CoV2 MA10-infected mice. Surfactant protein B expression is absolutely required for postnatal lung function, lung compliance, and survival in surfactant protein B knockout mice[60,61], whereas lung structure and function in surfactant protein C null mice is normal. Future studies will need to address the real possibility that SARS-CoV-2 MA10 may cause a respiratory distress syndrome (RDS) phenotype primarily associated with surfactant deficiency and whether surfactant replacement therapy might reverse SARS-CoV-2 disease severity when administered early in the viral-dominated phase in animals[62,63]. Surfactant protein and RNA expressions are also reduced

in lethal SARS-CoV infection in mice, suggesting common mechanisms of respiratory distress across Sarbecoviruses[46].

The limited availability of transgenic mouse models that can be infected by SARS-CoV-2 has hindered testing of vaccines and therapeutics against this virus. Our data demonstrate that despite the three mutations in the S RBD, alphavirus VRP vaccination with wild-type full-length SARS-CoV-2 S elicited robust neutralization titers against wild-type and SARS-CoV-2 MA10 parental strains. Importantly, these neutralization titers completely protected against SARS-CoV-2 MA10 replication in most mice, which correlated with reduced clinical disease morbidity and mortality. Because aged human populations are most vulnerable to SARS-CoV-2, the use of aged BALB/c or C57BL/6J mice provides a robust measure of COVID-19 vaccine efficacy. It is noteworthy that several vaccines failed in aged mice challenged with the 2003 mouse-adapted SARS-CoV strain, associated with enhance viral infection-induced Th2 pathology[64,65]. Using alphavirus VRP vectors that drive strong neutralizing antibody responses and Th1 immune responses[43], enhanced disease phenotypes were not observed in SARS-CoV-2 MA10-infected aged animals, supporting the importance of vaccines that drive strong Th1 immunity and neutralizing titers to prevent deleterious immune outcomes after vaccination[66,67].

Notably, SARS-CoV-2 replicated efficiently in the nasal cavity of the mice, primarily targeting the olfactory epithelium, where sustentacular and Bowman's gland cells, but not olfactory neurons, express viral entry components, and support olfactory neuron function[68]. Unlike reports in hamsters, replication in mouse olfactory neurons was not evident[69]. Future studies will be needed to elucidate potential relationships between infection of sustentacular cells and chemosensory dysfunction in rodents. Because efficient SARS- CoV-2 transmission may well be associated with efficient high titer replication in the nasal cavity and oral pharynx, the SARS- CoV-2 MA10 model provides an important tool for evaluating vaccine and therapeutic performance in the upper respiratory tract. Our VRP vaccine platform provided limited protection in the nasal cavity of aged mice, suggesting an inability to prevent infection in mucosal as compared to

alveolar sites. Because S- IgA antibodies in the secretions of the upper respiratory tract and in saliva appear to result primarily from antigenic stimulation of organized lymphoid follicles of the local mucosa (e.g., pharyngeal, palatine, and lingual tonsils), these data suggest that intra-nasal vaccination may offer a strategy to protect from upper respiratory SARS-CoV-2 infection[70].

SARS-CoV-2 infection in hamsters results in moderate weight loss and lung pathology[71], whereas infections in primates typically produce minimal disease signs[72]. Both models provide important metrics for evaluating vaccines and therapeutics and identifying host expression signatures of infection. Although a variety of SARS-CoV-2 mouse models have been reported, these models may have more limited use for studies of alveolar disease pathogenesis. The SARS-CoV-2 MA10 model captures multiple aspects of the COVID-19 syndrome, including a spectrum of morbidity and mortality determined by host genetics and increasing age, and severe pathological features of ALI/ARDS, and corresponding defects in lung function. Accordingly, this model provides the global research community with a robust tool to elucidate the underlying host genetics and molecular mechanisms governing SARS-CoV-2 disease pathogenesis, host expression networks, and immunity after infection. Intermediate disease phenotypes in C57BL/6J mice also provide novel opportunities for using existing mutant mouse resources to determine the role of genes in protective or pathogenic disease outcomes as a function of age. Finally, the capacity to measure vaccine and therapeutic efficacy in high-throughput lethal mouse models of acute lung injury and ARDS may provide critical insights into therapeutic agent performance in the most vulnerable populations (e.g., the elderly and/ or in mouse models of the underlying co-morbidities) that contribute to COVID-19 severity.

4.4 Methods & Materials

4.4.1 Viruses and cells

The parental SARS-CoV-2 MA virus was derived from an infectious clone of SARS-CoV-2 and further genetically engineered to introduce Q498Y/P499T substitutions into the spike protein[23]. Passage 1 SARS-CoV-2 WT and MA stocks were grown using Vero E6 cells and titered via plaque assay. Briefly, serially diluted virus was added to a monolayer of Vero E6 cells and overlayed with media containing 0.8% agarose. After three days plaques were visualized via staining with Neutral Red dye and counted.

Vero E6 cells were cultured in Dulbecco's modified Eagle's medium (DMEM, GIBCO), 5% Fetal Clone II serum (Hyclone), and 1X antibiotic/antimycotic (GIBCO). For single step growth curves, cells were infected with a multiplicity of infection (MOI) of 0.5 for 1 hour. After removal of inoculum, cells were washed twice with PBS and 2mL of media added. At designated time points supernatant was harvested and stored at -80^{o}C until further analysis. Well differentiated primary human bronchiolar airway epithelial (HBE) cells were cultured in ALI media. In order to generate a growth curve, cells were infected with a MOI of 0.5 for 2 hours after which the inoculum was removed, cells were rinsed three times with PBS and replaced with media. At designated time points, HAEs were apically washed with 200 mL 1X PBS for 10 minutes and samples stored at 80^{o}C until further analysis.

Clonal isolate from P10 was plaque purified from a plaque assay of a P10-infected mouse lung homogenate via inoculation of Vero E6 cells with an agar stab, generating a passage 1 SARS-CoV-2 MA10 stock. A passage 2 stock was grown, and supernatant viral RNA was sequenced (described below). A larger passage 3 stock was grown, titered, and used for all subsequent experiments.

4.4.2 Sequencing (library preparation and SNP detection)

Viral RNA from clarified cell culture supernatant was isolated using TRIzol LS (*Invitrogen*) using a Direct-zol RNA Kit (*Zymo Research*) following manufacturers suggested protocol and quantified by NanoDrop (*ThermoFisher Scientific*). dsDNA was synthesized by random priming with Random Primer 9 (*New England BioLabs*) on 500-1000 ng of each isolate's RNA and reverse transcribed using Super Script II (Sigma-Aldrich) to make cDNA followed by second strand synthesis using NEBNext Ultra II Non-Directional RNA Second Strand Synthesis Module (*New England BioLabs*) following the manufacturer's suggested protocols. dsDNA was quantified using Qubit dsDNA HS Assay Kit (*ThermoFisher Scientific*). Libraries were prepared using Nextera XT DNA Library Preparation Kits (*Il- lumina*) and sequenced on a NovaSeq 6000 System (*Illumina*) with paired end reads (2 3 151). SARS-CoV-2 MA10 passage 2 reads were *de novo* assembled using CLC Genomics Workbench v12 (*QIAGEN*) to confirm initial viral sequence.

4.4.3 RNA in situ hybridization

RNA-ISH was performed on paraffin-embedded 4 μm tissue sections using the RNAscope Multiplex Fluorescent Assay v2, according to the manufacturer's instructions (Advanced Cell Diagnostics). Tissue sections were deparaffinized with xylene (2 changes 3 5 min) and 100% ethanol (2 changes 3 1 min), and then incubated with hydrogen peroxide for 10 min, followed by target retrieval in boiling water for 15 min, and incubation with Protease Plus (Advanced Cell Diagnostics) for 15 min at 40°C. Slides were hybridized with custom probes at 40°C for 2 hours, and signals were amplified according to the manufacturer's instructions. An Olympus VS200 fluorescent microscope and Olympus confocal microscope were utilized to capture the stained sections.

4.4.4 Immunohistochemistry

Immunohistochemical staining was performed on paraffin-embedded 4 μm tissue sections according to a protocol as previously described[73]. Briefly, paraffin-embedded sections were baked at 60°C for 2–4 hours, and deparaffinized with xylene. After rehydration, antigen retrieval was performed by boiling the slides in 0.1 M sodium citrate pH 6.0 (3 cycles with microwave settings: 100% power for 6.5 min, 60% for 6 min, and 60% for 6 min). After cooling and rinsing with distilled water, quenching of endogenous peroxidase was performed with 0.5% hydrogen peroxide in methanol for 15 min, slides washed in PBS, and blocked with 4% normal donkey serum, for an hour at RT. Primary antibodies were diluted in 4% normal donkey serum in PBST and incubated over night at 4 C. Species-matched gamma globulin was used as an isotype control at the same concentration as the primary antibody. Sections were washed in PBST and Species-matched secondary antibodies were applied for 60 min at RT. After washing in PBST, the Vector TrueVIEW Autofluorescence Quenching Kit (Vector laboratories) was used to reduce background staining, and glass coverslips were placed over tissue sections with the ProLong Gold Antifade Reagent with DAPI (Invitrogen). Coverslipped slides were scanned and digitized using an Olympus VS200 whole slide scanner microscope.

4.4.5 *In vivo* infection

BALB/cAnNHsd mice were obtained from Envigo (strain 047). C57BL/6J mice were obtained from the Jackson Laboratory (strain 000664). Type I and II interferon receptor double knock out (IFNR DKO) mice were originally obtained from the Whitmire laboratory and bred at the University of North Carolina at Chapel Hill. Anesthetized (ketamine/xylazine) mice were intranasally infected with 10^5 PFU SARS-CoV-2 MA and different doses of SARS-CoV-2 MA10 diluted in PBS where indicated. Clinical signs of disease (weight loss and lung function) were monitored daily. Lung function was assessed utilizing whole body plethysmography (WBP; DSI

Buxco respiratory solutions, DSI Inc.) by allowing mice to acclimate in WBP chambers for 30 minutes followed by 5 minutes of data recording as described previously[74]. Acquired data was analyzed using FinePointe software. Mice were euthanized by isoflurane overdose at indicated time points when samples for titer (caudal right lung lobe) and histopathological analyses (left lung lobe) were collected. All animals in this manuscript that are recorded as ‘‘dead’’ were either found dead in cage or were moribund and euthanized as they approached 70% of their starting body weight which is the defined human endpoint according to the respective animal protocol. Importantly, mice were randomized and assigned to specific harvest days before the start of the experiment. Lung viral titers were determined by plaque assay. Briefly, right caudal lung lobes were homogenized in 1mL PBS using glass beads and serial dilutions of the clarified lung homogenates were added to a monolayer of Vero E6 cells. After three days plaques were visualized via staining with Neutral Red dye and counted. The left lung lobe was stored in 10% phosphate buffered formalin for 7 days prior to removal from the BSL3 for processing. After paraffin embedding, sectioning, and staining histopathological scoring was performed.

4.4.6 Chemokine & Cytokine analysis

BioPlex Pro mouse cytokine 23-plex assay (Bio-Rad) was utilized to analyze chemokines and cytokines in serum and lung samples from 1-year-old BALB/c mice according to manufacturer’s protocol. 50 μL of clarified lung samples or 50 μL of 1:4 diluted serum samples were incubated with magnetic capture beads, washed, incubated with detection antibodies and SA-PE. Cytokines were recorded on a MAGPIX machine (Luminex) and quantitated via comparison to a standard curve. xPONENT software was used for data collection and analysis.

4.4.7 Histological analysis and antigen staining

Immediately after euthanasia, the left lung lobe was harvested and fixed by submersion in 10% phosphate buffered formalin for 7 days. Fixed tissues were routinely processed on a Leica

ASP 6025, embedded in paraffin (Leica Paraplast), and sectioned at 4μm thickness. Sequential sections were stained with hematoxylin and eosin (Richard Allan Scientific) and stained for SARS-CoV-2 nucleocapsid using a monoclonal anti-SARS-CoV nucleocapsid antibody (NB100-56576, Novus Biologicals) on the Ventana Discovery platform (Roche). Briefly, antigen retrieval was performed using Ventana's CC1 (pH 8.5), tissues were blocked, primary antibody diluted at 1:250 using Discovery Casein Diluent (760-219, Roche), ready-to use secondary antibody (Discovery OmniMap anti Rabbit HRP, 760-4311), followed by DAB development and Hematoxylin II staining. Pathology was evaluated and scored by a board-certified veterinary pathologist. Lung histopathology was blindly scored using three 600X fields per tissue as previously described. Briefly, three random fields of diseased tissue at 600X total magnification (60X objective x 10X eyepiece) were chosen and scored in a blinded manner for ALI and DAD histological scoring systems. For the ASL/ALI scoring system the following parameter were analyzed: (A) neutrophils in the alveolar space (none = 0, 1-5 cells = 1, > 5 cells = 2); (B) neutrophils in the interstitial space/septae (none = 0, 1-5 cells = 1, > 5 cells = 2); (C) hyaline membranes (none = 0, one membrane = 1; > 1 membrane = 2); (D) proteinaceous debris in air spaces (none = 0, one instance = 1, > 1 instance = 2); (E) alveolar septal thickening (> 2x mock thickness = 0, 2-4x mock thickness = 1, > 4x mock thickness = 2). Scores were calculated as followed: [(20 x A) + (14 x B) + (7 x C) + (7 x D) + (2 x E)] / 100. Final scores were obtained by averaging three fields per mouse. The defuse alveolar damage (DAD) scores were determined as followed: 1 = absence of cellular sloughing and necrosis; 2 = uncommon solitary cell sloughing and necrosis; 3 = multifocal (3 + foci) cellular sloughing and necrosis with uncommon septal wall hyalinization; 4 = multifocal (> 75% of field) cellular sloughing and necrosis with common and/or prominent hyaline membranes. The average of three fields determined the final DAD score per mouse. An Olympus BX43 light microscope was used to capture images at 200X magnification with a DP27 camera using cellSens Dimension software.

4.4.8 Vaccination and neutralization studies

Mice were vaccinated with Venezuelan equine encephalitis virus strain 3526 based replicon particles (VRPs) expressing SARS-CoV-2 spike (S), nucleocapsid (N), or GFP as control. VRPs were given via hind footpad injection at a dose of 10^3 in 10 mL. The same strategy was used to boost mice 3 weeks post prime and presence of neutralizing antibodies was confirmed in submandibular bleeds at the time of boost.

Authentic virus neutralization of sera from 3 weeks post boost using nanoLuciferase-expressing SARS-CoV-2 virus (SARS-CoV-2 nLuc), bearing wild-type spike protein, was performed as described with slight modification[23,35]. Briefly, Vero E6 cells were seeded at $2x10^4$ cells/well in a 96-well plate 24h before the assay. 100 PFU of SARS-CoV-2-nLuc virus were mixed with serial diluted sera at 1:1 ratio and incubated at 37C for 1h. An 8-point, 3-fold dilution curve was generated for each sample with starting concentration at 1:20. Virus and Ab mix was added to cells and incubated at 37 C + 5% CO_2 for 48h. Luciferase activities were measured by Nano-Glo Luciferase Assay System (Promega) following manufacturer protocol using SpectraMax M3 luminometer (Molecular Device). Percent inhibition and 50% inhibition concentration (IC_{50}) were calculated by the following equation: [1-(RLU with sample/ RLU with mock treatment)] x 100%. Fifty percent inhibition titer (IC_{50}) was calculated in GraphPad Prism 8.4.2 by fitting the data points using a sigmoidal dose-response (variable slope) curve.

Intranasal challenge of anesthetized (ketamine/xylazine) mice with 10^4 PFU SARS-CoV-2 MA10 was performed 4 weeks post boost. Changes in body weight and alterations in lung function parameters were recorded daily and mice were euthanized by isoflurane overdose for harvests on day 2 and day 4 after infection. Viral titers in lungs were analyzed via plaque assay.

4.4.9 Quantification and statistical analysis

Data visualization and analyses were performed using build-in functions of GraphPad Prism. Specific statistical tests, numbers of animals, and definitions of center, dispersion and precision measures are mentioned in respective figure legends. For the characterization of SARS-CoV-2 MA10 in young and old BALB/c as well as young C57BL/6 mice the following statistical tests were used: mixed effect analysis followed by Sidak's multiple comparisons was used to analyze weight loss and whole body plethysmography data; cell growth curves and cytokine / chemokine responses were analyzed by 2-factor ANOVA followed by Sidak's multiple correction; gross lung congestions scores, lung and nasal titers, as well as DAD and ATS / ALI scores were analyzed by 2-factor ANOVA followed by Sidak's multiple comparisons; survival rates were analyzed by log rank test. For the IFNR-DKO data the following statistical tests were used: weight loss data was analyzed using mixed effect analysis followed by Sidak's multiple comparisons; 2-factor ANOVA followed by Tukey's multiple comparisons was used for gross congestion scores and lung / nasal titer data; whole body plethysmography was analyzed via 2-factor ANOVA followed by Sidak's multiple comparisons. VRP mouse data was analyzed as followed: weight loss and whole body plethysmography data was analyzed via mixed effect analysis followed by Sidak's multiple comparisons; neutralization data was log transformed and analyzed via 1-factor ANOVA followed by Holm-Sidak's multiple comparison; lung / nasal titer data as well as whole body plethysmography was analyzed by 2-factor ANOVA followed by Dunnett's multiple comparisons; unpaired, two-tailed Student's t test was used for comparisons of serum IC_{50} values from 10-week and 1-year-old vaccinated mice; Comparison of serum IC_{50} values from 10-week-old spike vaccinated mice to neutralize SARS-CoV-2 WT versus SARS-CoV-2 MA was analyzed via Wilcoxon matched-pairs signed rank test.

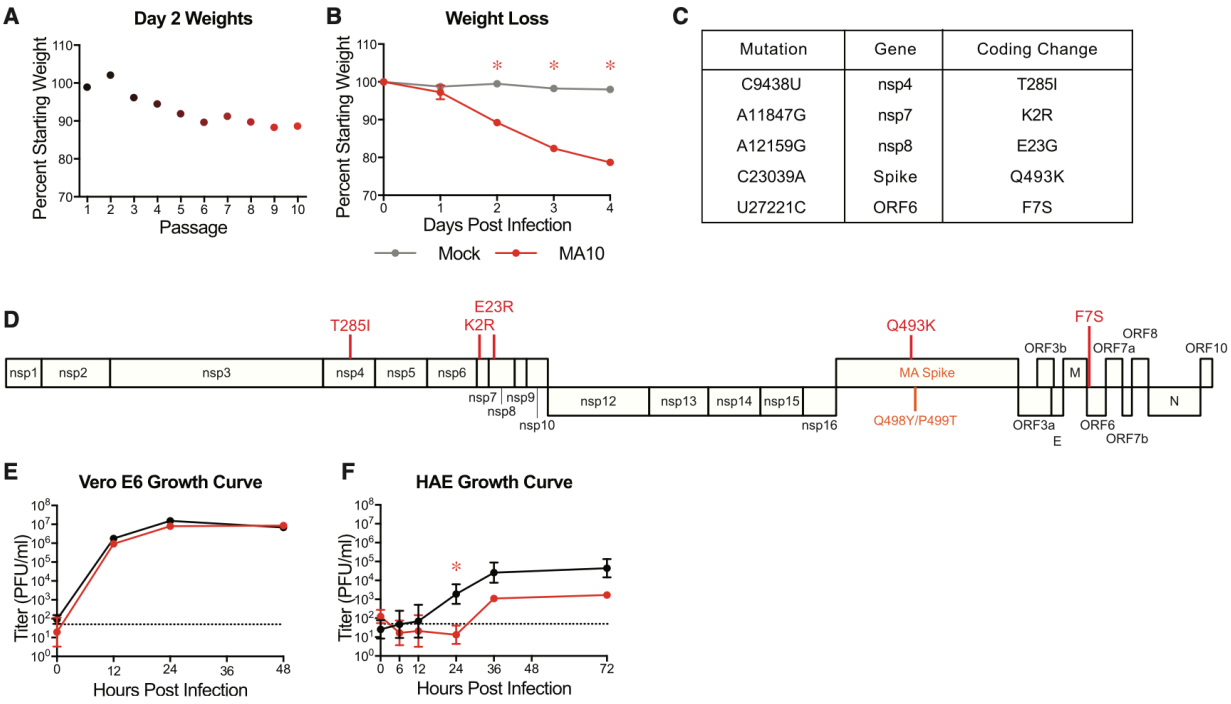

Mutation	Gene	Coding Change
C9438U	nsp4	T285I
A11847G	nsp7	K2R
A12159G	nsp8	E23G
C23039A	Spike	Q493K
U27221C	ORF6	F7S

Figure 4.1. SARS-CoV-2 MA Increases in Pathogenicity following Serial In Vivo Passaging in Mice.

(A) Percent starting weight at 2 dpi of mice throughout serial passage of SARS-CoV-2 MA10 in 10- to 12-week-old BALB/c mice infected with 10^5 PFU SARS- CoV-2 MA at passage 1, or blind titer for passages 2–10. (B) 10-week-old BALB/c mice were mock-infected with PBS or infected with 10^5 PFU of plaque-purified virus from passage 10 in (A), SARS-CoV-2 MA10, and monitored for weight loss. Data analyzed by mixed effects analysis followed by Sidak's multiple comparisons. (C) Table of mouse adaptations present in plaque purified SARS-CoV-2 MA10 relative to parental SARS-CoV-2 MA. WT, wild type; nsp, nonstructural protein; ORF, open reading frame. (D) Schematic of SARS-CoV-2 genome with locations of mouse adaptations from (C) shown. (E and F) Single step growth curve of SARS-CoV-2 WT and SARS-CoV-2 MA10 in Vero E6 cells (E) or differentiated primary human bronchiolar airway epithelial cells (HBE) (F). n = 3 for each group, sampled serially. Dotted line represents limit of detection. Log transformed data were analyzed by 2-factor ANOVA followed by Sidak's multiple corrections. Error bars represent SEM about the mean for (A) and (B) and SD about the mean for (E) and (F). *p < 0.05.

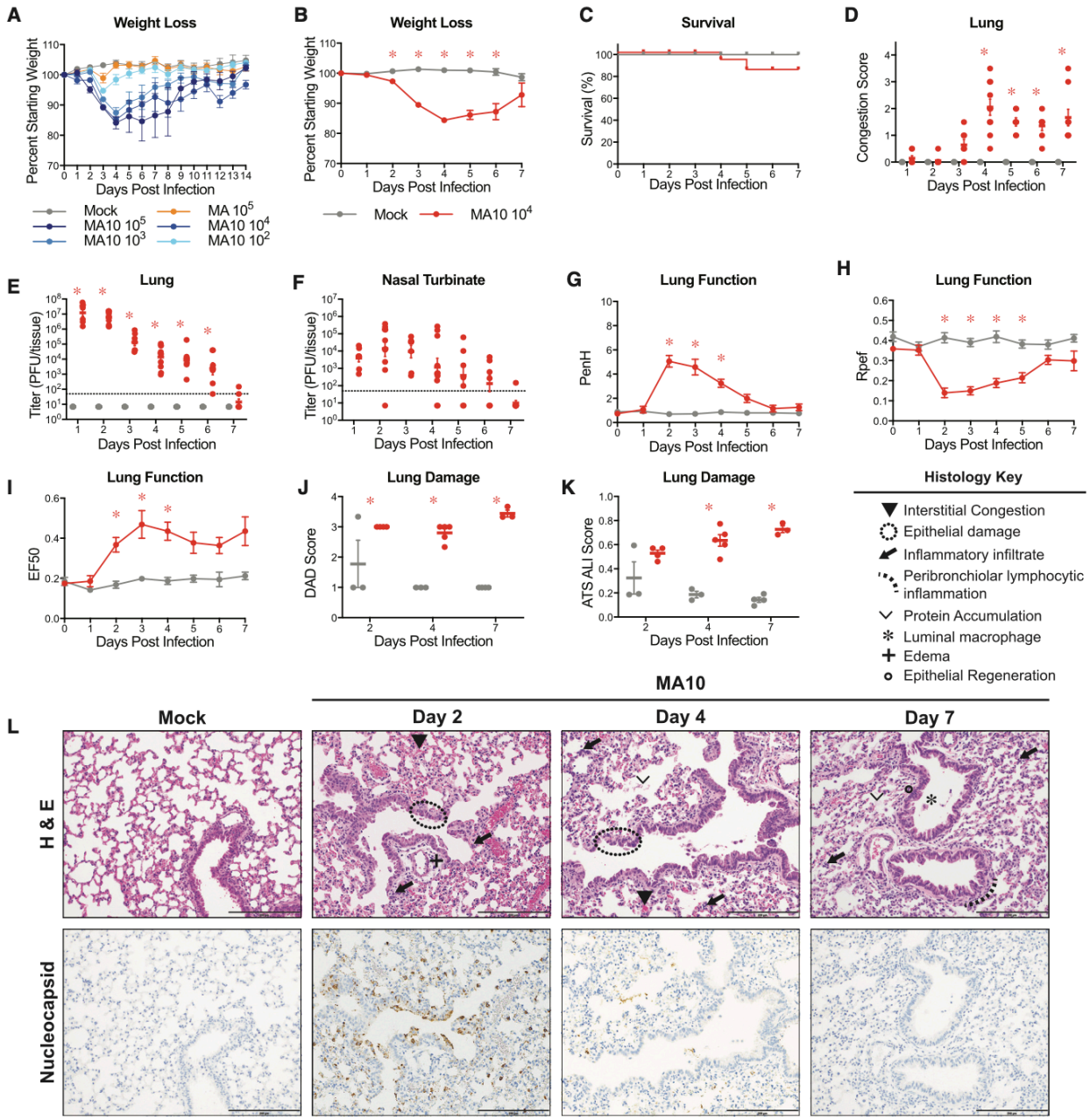

Figure 4.2. SARS-CoV-2 MA10 Causes Acute Lung Injury in Young Adult BALB/c Mice.

(A) 10-week-old female BALB/c mice (n = 5 per group) were mock-infected, infected with 10^5 PFU SARS-CoV-2 MA, or 10^2, 10^3, 10^4, and 10^5 PFU SARS-CoV- 2 MA10. (B–L) 10-week-old female BALB/c mice were mock-infected (n = 47) or infected with 10^4 PFU SARS-CoV-2 MA10 (n = 59). (B) Percent starting weight. Data analyzed by mixed effects analysis followed by Sidak's multiple comparisons. (C) Survival rate. (D) Gross lung congestion score. Data analyzed by 2-factor ANOVA followed by Sidak's multiple comparisons. (E)Viral lung titer (mock-infected:1dpi: n=6,2dpi: n=7,3dpi: n=6,4dpi: n=7,5dpi: n=6,6dpi: n=6,7dpi: n=9; SARS-CoV-2MA10-infected:1dpi: n=7,2 dpi: n = 10, 3 dpi: n = 7, 4 dpi: n = 10, 5 dpi: n = 7, 6 dpi: n = 7, 7 dpi: n = 9). Dotted line represents limit of detection. Undetected samples are plotted at half the limit of detection. Log transformed data analyzed as in (D). (F) Viral nasal cavity titer. Dotted line represents limit of detection. Undetected samples are plotted at half the limit of detection. (G–I)

Whole body plethysmography analysis of lung function parameters (10 mice per group at 0 dpi): PenH (G), Rpef (H), and EF50 (I). Data analyzed as in (B). (J and K) Blinded histopathological evaluation of lung damage using DAD scoring (J) and ATS ALI scoring (K) systems on days 2, 4, and 7 after mock or SARS- CoV-2 MA10 infection. Data analyzed as in (D). (L) Representative 2003 images of lungs from mock and SARS-CoV-2 MA10-infected mice from (J) and (K). H&E shown in the top panels. Bottom panels show immunohistochemistry (IHC) labeling against SARS-CoV-2 nucleocapsid, counterstained with hematoxylin. Scale bars represent 200 μm. All error bars represent SEM about the mean. *$p < 0.05$.

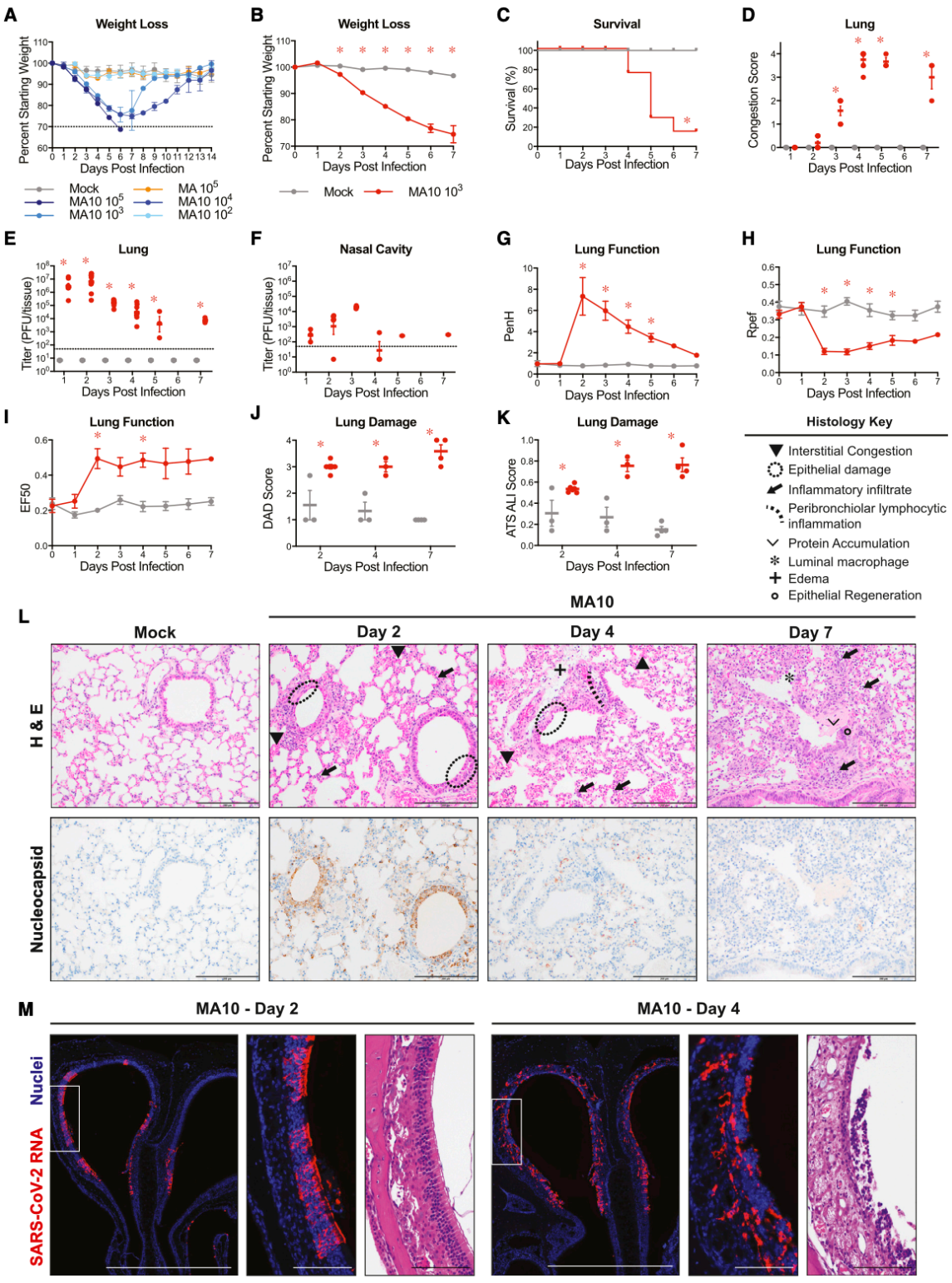

Figure 4.3. SARS-CoV-2 MA10 Disease Is Severely Exacerbated in Old Mice.

(A) 1-year old female BALB/c mice (n = 5 per group) were mock-infected (gray), infected with 10^5 PFU SARS-CoV-2 MA, or 10^2, 10^3, 10^4, and 10^5 PFU SARS-CoV- 2 MA10. Dotted line represents 70% starting body weight. (B–L) 1-year old female BALB/c mice were mock-infected (n = 51) or

infected with 10^3 PFU SARS-CoV-2 MA10 (n = 65). (B) Percent starting weight. Dotted line represents 70% starting body weight. Data analyzed by mixed effects analysis followed by Sidak's multiple comparisons. (C) Survival rate. Analyzed by log-rank test. (D) Gross lung congestion score. Data analyzed by 2-factor ANOVA followed by Sidak's multiple comparisons. (E) Lung viral titer (mock-infected: 1dpi: n=6, 2dpi, n=7; 3dpi, n=6; 4dpi, n=7; 5dpi, n=6; 6dpi, n=6; 7dpi, n=13; SARS-CoV-2MA10-infected:1dpi, n=6; 2 dpi, n=10; 3 dpi, n=7; 4 dpi, n=8; 5 dpi, n=1; 6 dpi, n=2; 7 dpi, n=3.) Dotted line represents limit of detection. Undetected samples are plotted at half the limit of detection. Log transformed data analyzed as in (D). (F) Viral nasal cavity titer. Dotted line represents limit of detection. Undetected samples are plotted at half the limit of detection. (G–I) Whole body plethysmography analysis of lung function parameters (10 mice per group at 0 dpi): PenH (G), Rpef (H), and EF50 (I). Data analyzed as in (B). (J and K) Blinded histopathological evaluation of lung damage using DAD scoring (J) and ATS ALI scoring (K) systems on days 2, 4, and 7 after mock or SARS- CoV-2 MA10 infection. Data analyzed as in (D). (L) Representative 2003 images of lungs from mock and SARS-CoV-2 MA10-infected mice from (J) and (K). H&E is shown in the top panels. Bottom panels show immunohistochemistry (IHC) labeling against SARS-CoV-2 nucleocapsid, counterstained with hematoxylin. Scale bars represent 200 mm. (M) Representative *in situ* hybridization images of viral RNA in nasal cavity from SARS-CoV-2 MA10-infected mice. Scale bar represents 100 μm. All error bars represent SEM about the mean. *$p < 0.05$.

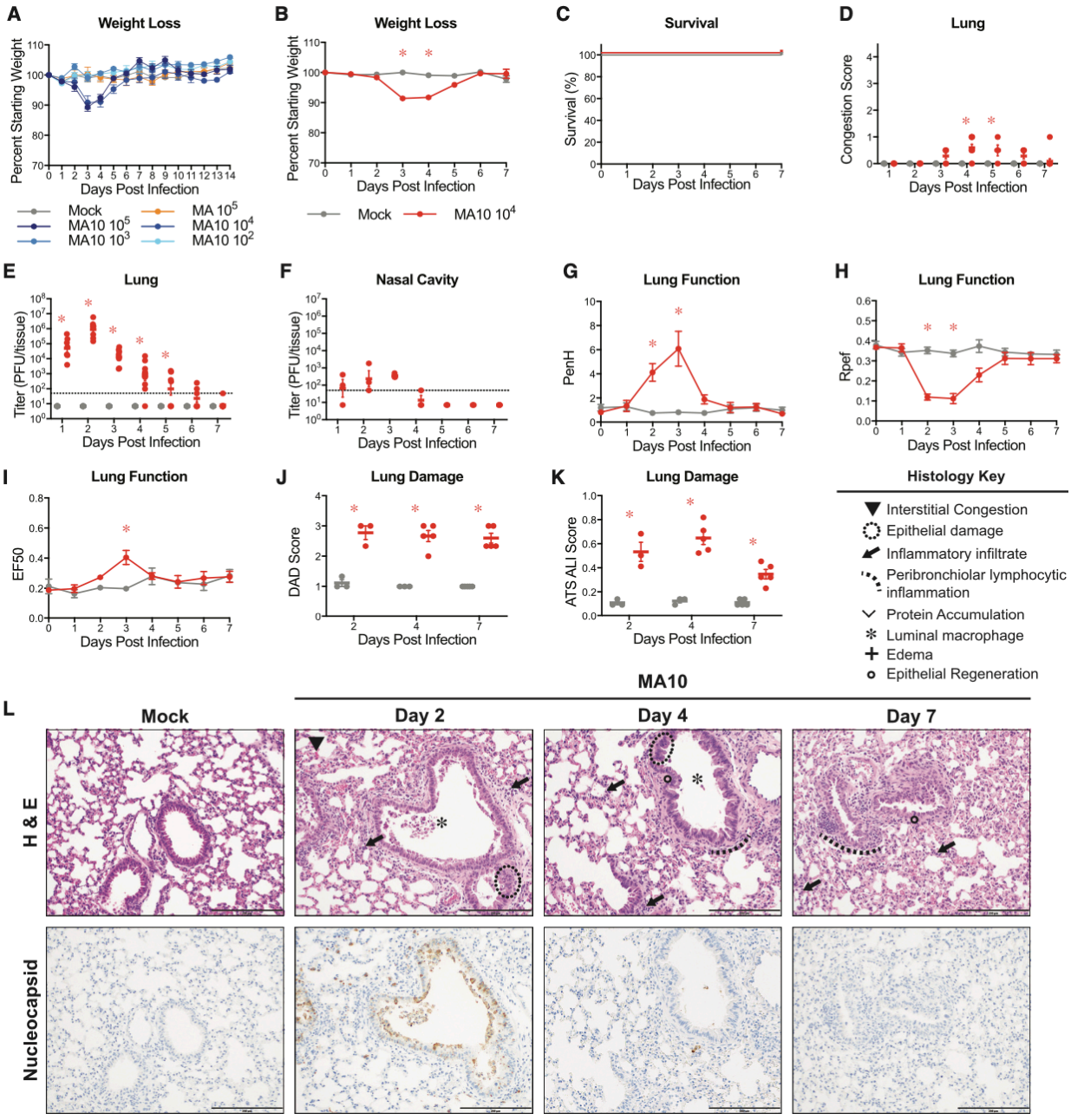

Figure 4.4. C57BL/6J Mice Display Less Severe Disease following SARS-CoV-2 MA10 Infection.

(A) 10-week-old female C57BL/6J mice (n = 5 per group) were mock-infected, infected with 10^5 PFU SARS-CoV-2 MA, or 10^2, 10^3, 10^4, and 10^5 PFU SARS-CoV- 2 MA10. (B–L) 10-week-old female BALB/c mice were mock-infected (n = 46) or infected with 10^4 PFU SARS-CoV-2 MA10 (n = 57). (B) Percent starting weight. Data analyzed by mixed effects analysis followed by Sidak's multiple comparisons. (C) Survival rate. (D) Gross lung congestion score. Data analyzed by 2-factor ANOVA followed by Sidak's multiple comparisons. (E) Viral lung titer of mice from (B) (mock-infected: 1 dpi, n = 6; 2 dpi, n = 7; 3 dpi, n = 5; 4 dpi, n = 7; 5 dpi, n = 6; 6 dpi, n = 6; 7 dpi, n = 8; SARS-CoV-2 MA10-infected: 1dpi, n=7; 2dpi,n=8; 3dpi,n=7; 4dpi,n=10; 5dpi,n=4; 6dpi,n=7; 7dpi,n=11). Dotted line represents limit of detection. Undetected samples are plotted at half the

limit of detection. Log transformed data analyzed as in (D). (F) Viral nasal cavity titer. Dotted line represents limit of detection. Undetected samples are plotted at half the limit of detection. Log transformed data analyzed as in (D). (G–I) Whole body plethysmography analysis of lung function parameters (10 mice per group at 0 dpi): PenH (G), Rpef (H), and EF50 (I). Data analyzed as in (B). (J and K) Blinded histopathological evaluation of lung damage using DAD scoring (J) and ATS ALI scoring (K) systems on days 2, 4, and 7 after mock or SARS- CoV-2 MA10 infection. Data analyzed as in (B). (L) Representative 2003 images of lungs from mock and SARS-CoV-2 MA10-infected mice from (J) and (K). H&E shown in the top panels. Bottom panels show immunohistochemistry (IHC) labeling against SARS-CoV-2 nucleocapsid, counterstained with hematoxylin. Scale bars represent 200 μm. Error bars represent SEM about the mean. *$p < 0.05$.

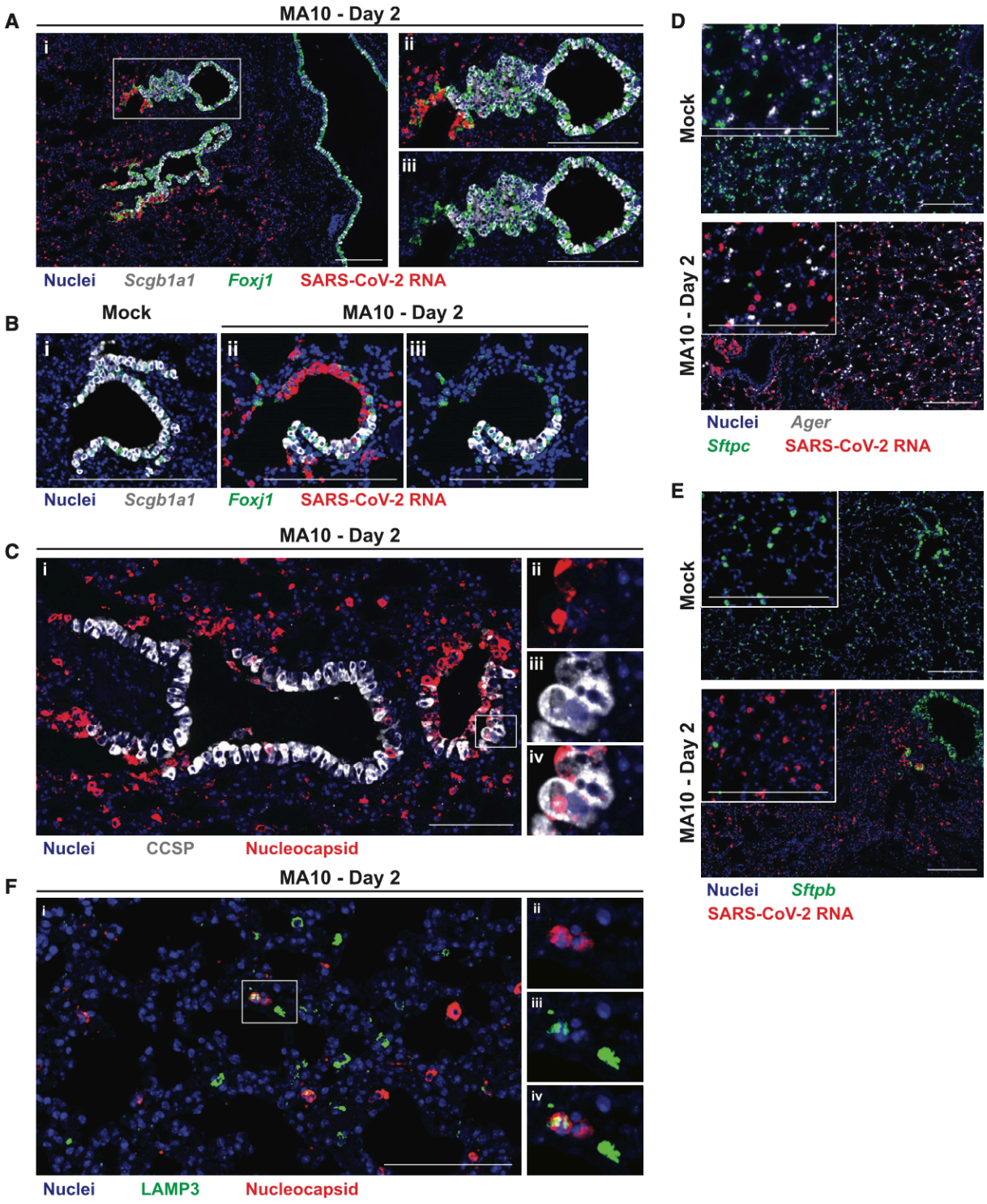

Figure 4.5. SARS-CoV-2 MA10 Infects Secretory Club Cells of the Lower Respiratory Tract and Type II Pneumocytes.

SARS-CoV-2 MA10 cellular tropism in the lung was assessed by RNA *in situ* hybridization (ISH) or immunohistochemistry (IHC) in mock or infected female 1-year- old BALB/c mice from Figure 4.3 at 2 dpi. (A) ISH of lower airway epithelium. *Scgb1a1* is a marker of secretory club cells. *Foxj1*

is a marker of ciliated cells. (A_{ii}–A_{iii}) are same inset field with or without SARS- CoV-2 RNA channel. (B) ISH of terminal bronchiole epithelium. (B_{ii}–B_{iii}) are same field with or without SARS-CoV-2 RNA channel. (C) IHC of terminal bronchiole epithelium. CCSP is a marker of secretory club cells. (C_{ii}–C_{iv}) are the same inset field as single color channels or merged (C_{iv}). (D and E) ISH of alveoli. *Ager* is a marker of type I pneumocytes. *Sftpc* and *Sftpb* are markers of type II pneumocytes. (E) IHC of alveoli. LAMP3 is a marker of type II pneumocytes. (E_{ii}–E_{iv}) are the same inset field as single color channels or merged (E_{iv}). Scale bars represent 200 μm.

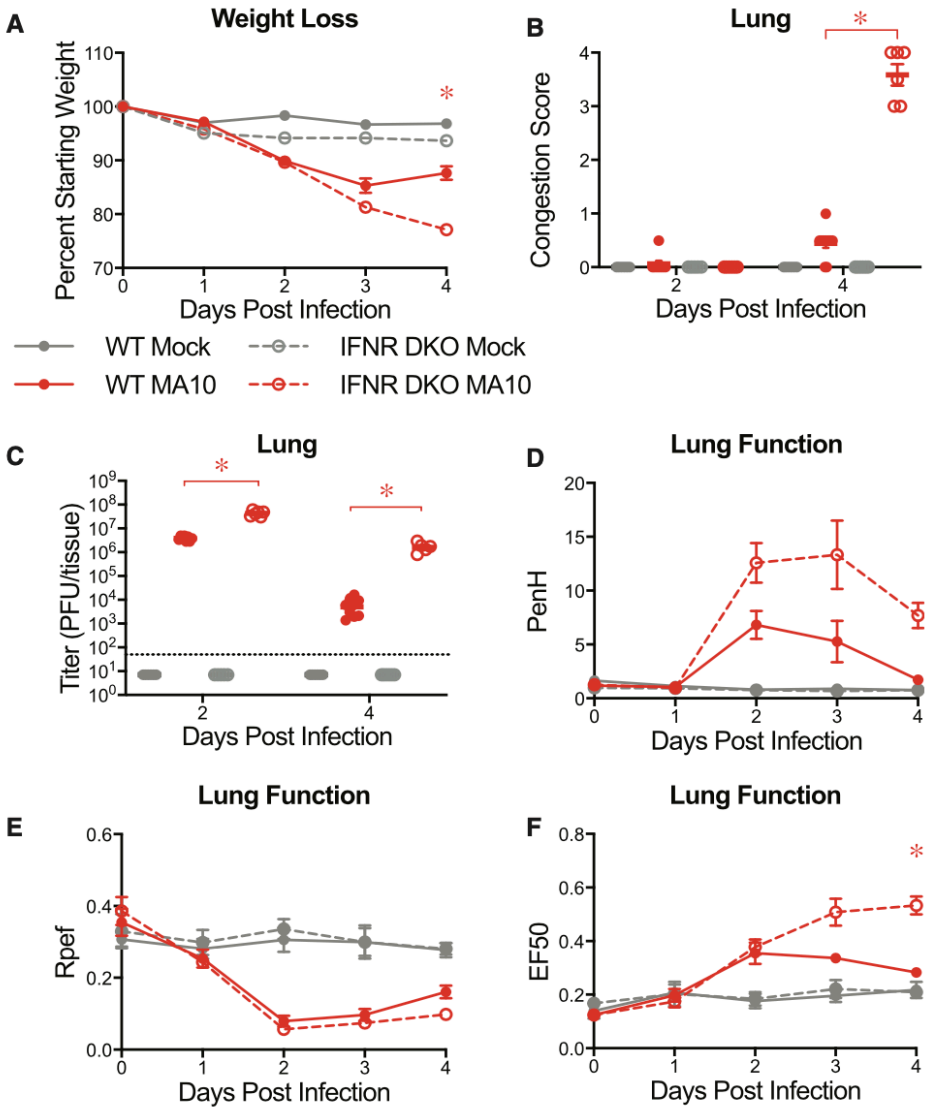

Figure 4.6. Interferon Signaling Deficient Mice Are More Susceptible to SARS-CoV- 2 MA10.

10-week-old male and female type I and II interferon receptor double knockout (IFNR DKO; n = 12 mock, n = 19 MA10) and wild-type (WT; n = 11 mock, n = 13 MA10) control mice were mock-infected or infected with 10^4 PFU SARS-CoV-2 MA10. (A) Percent starting weight. Data analyzed by mixed effects analysis followed by Sidak's multiple comparisons. Statistical comparisons shown between MA10-infected WT and MA10-infected IFNR DKO mice. (B) Gross lung congestion score of mice from (A). Data analyzed by 2-factor ANOVA followed by Tukey's multiple comparisons. (C) Viral lung titer of mice from (A) (mock-infected: 2 dpi, n = 6 WT and 5 IFNR DKO; 4 dpi, n = 6 WT and 6 IFNR DKO: SARS-CoV-2 MA10-infected: 2 dpi, n = 8 WT and 6 IFNR DKO; 4 dpi, n = 10 WT and 6 IFNR DKO). Dotted line represents limit of detection. Undetected samples are plotted at half the limit of detection. Log transformed data analyzed via 2-factor ANOVA followed by Tukey's multiple comparisons. (D–F) Whole body plethysmography analysis of lung function parameters (6 mice per group at 0 dpi): PenH (D), Rpef (E), and EF50 (F). Data analyzed using 2-factor ANOVA followed by Si- dak's multiple comparisons. Error bars represent SEM about the mean. *p < 0.05.

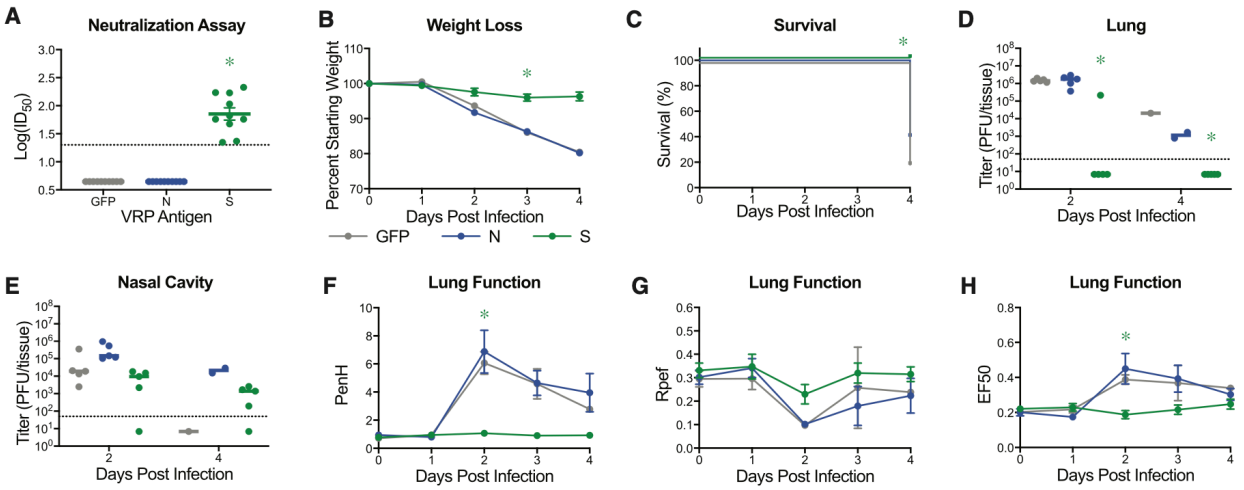

Figure 4.7. Virus Replicon Particle Delivered Spike Vaccination Protects Old Mice from SARS-CoV-2 MA10 Challenge.

1-year-old female BALB/c mice were vaccinated with 10^3 virus replicon particles (VRPs) expressing SARS-CoV-2 wild-type spike (S, n = 10), nucleocapsid (N, n = 10), or GFP (n = 10). Mice received a boost 3 weeks after prime immunization, and submandibular blood samples were collected for neutralization assays. All mice were challenged 4 weeks after the boost immunization. (A) Neutralization of SARS-CoV-2 WT by sera from vaccinated mice 3 weeks post boost. ID_{50}, inhibitory concentration necessary to achieve 50% virus neutralization. Dotted line represents limit of detection. Undetected samples are plotted at half the limit of detection. Log transformed data analyzed via 1-factor ANOVA followed by Holm-Sidak's multiple comparisons. (B) Percent starting weight. Data analyzed by mixed effects analysis followed by Sidak's multiple comparisons. (C) Survival rate. (D and E) Viral lung (D) and nasal cavity (E) titer of mice from (B). n = 5 for each group at each time point. Dotted line represents limit of detection. Undetected samples are plotted at half the limit of detection. Log transformed data analyzed via 2-factor ANOVA followed by Dunnett's multiple comparisons. (F–H) Whole body plethysmography analysis of lung function parameters (n = 5 mice per group at 0dpi): PenH (F), Rpef (G), and EF50 (H). Data analyzed as in (B). Error bars represent SEM about the mean. *$p < 0.05$.

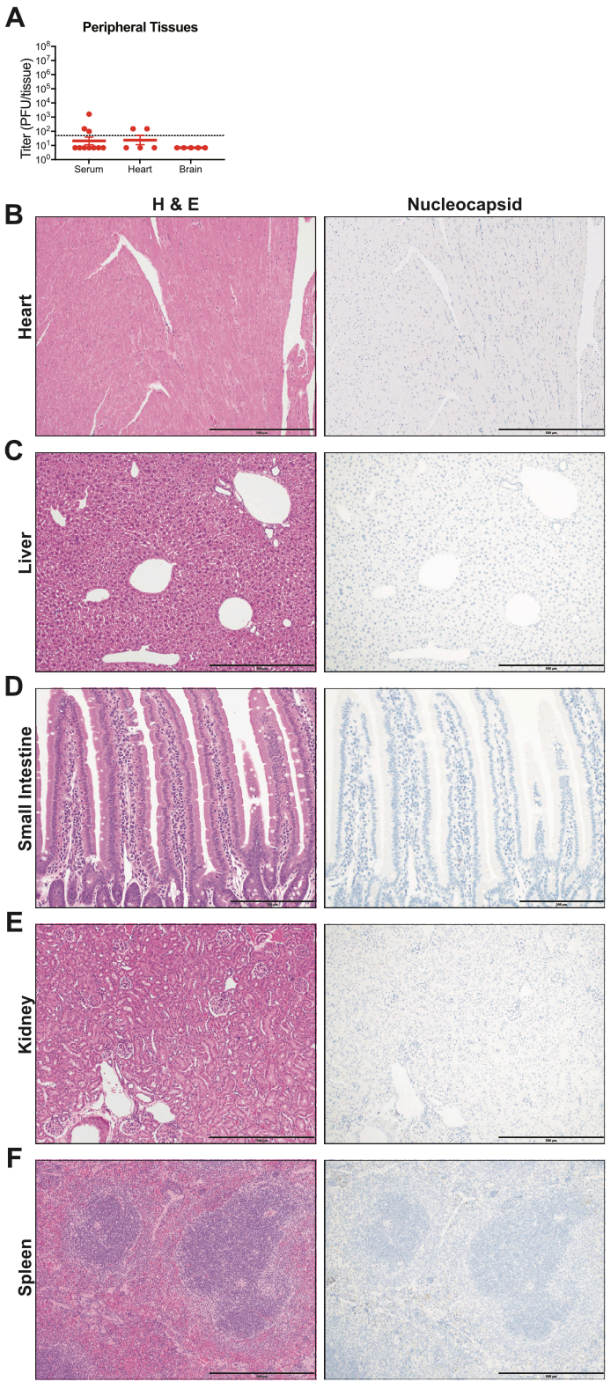

Figure 4.8. SARS-CoV-2 MA10 Does Not Replicate in Non-Respiratory Tract Tissues.

Analysis of non-respiratory tract tissues of SARS-CoV-2 MA10 infected 1-year-old female BALB/c mice at 2dpi from Figure 4.3. (A) Viral titer in serum, heart, and brain. Dotted line represents limit of detection. Undetected samples are plotted at half the limit of detection. (B-F) Representative hematoxylin & eosin (left) and IHC for viral nucleocapsid (right) images of heart (B), liver (C), small intestine (D), kidney (E), and spleen (F). Faint non-specific IHC staining in spleen is result of red blood cell metabolism in macrophages, not viral protein staining. (A, B, E, F) shown at 100X with scale bar representing 500 μm. (D) shown at 200X with scale bar representing 200 μm.

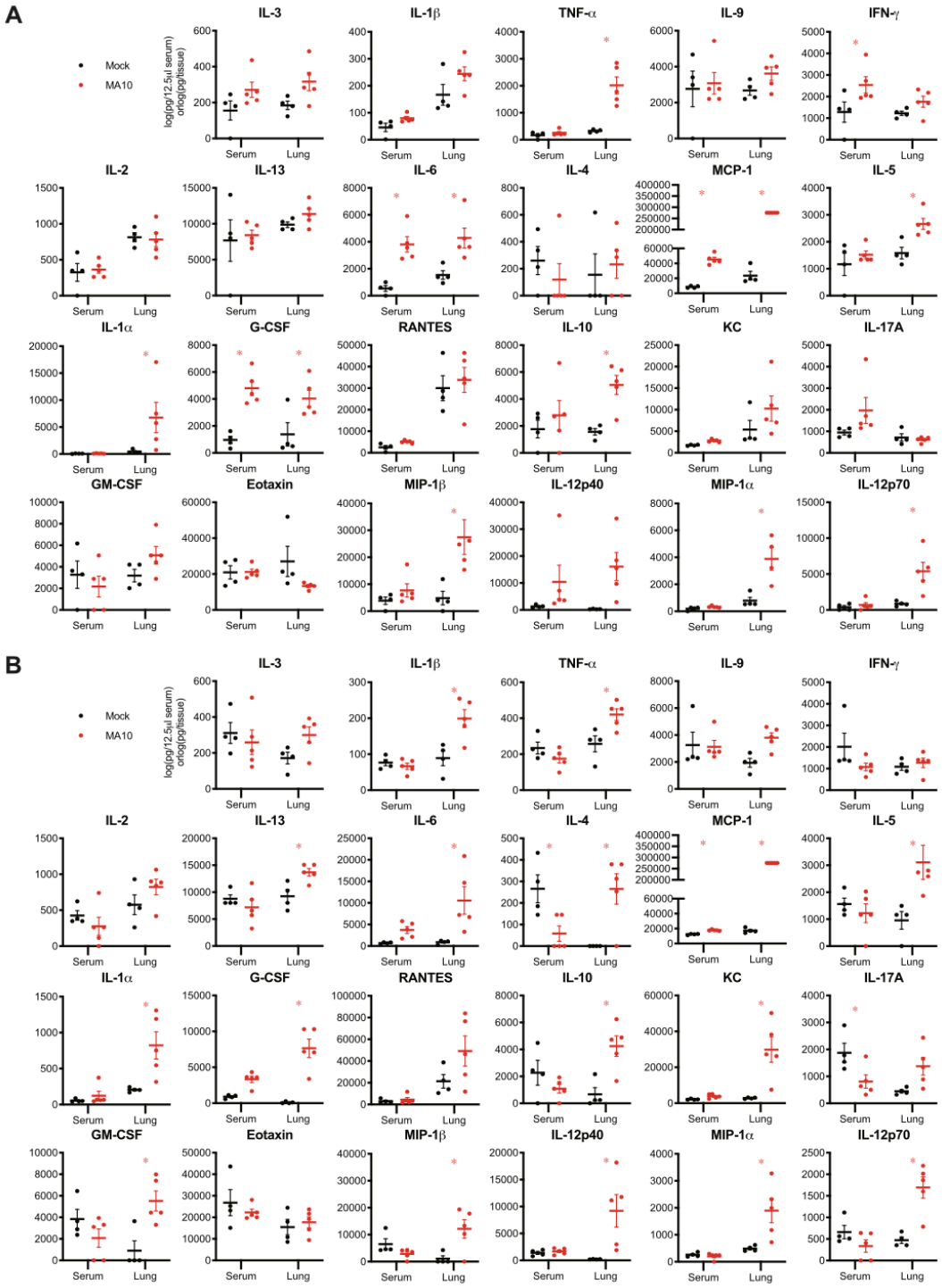

Figure 4.9. SARS-CoV-2 MA10 Induces Local and Systemic Cytokine and Chemokine Responses.

(A-B) Cytokine and chemokine analysis of mock or SARS-CoV-2 MA10 infected 1-year-old BALB/c mice from Figure 4.3. Serum and lung homogenate were assayed for 23 cytokines and chemokines at 2dpi (A) and 4dpi (B). n = 4 mock and 5 MA10 mice at each time point. Data analyzed by 2-factor ANOVA followed by Sidak's multiple comparisons. Asterisks represent $p < 0.05$.

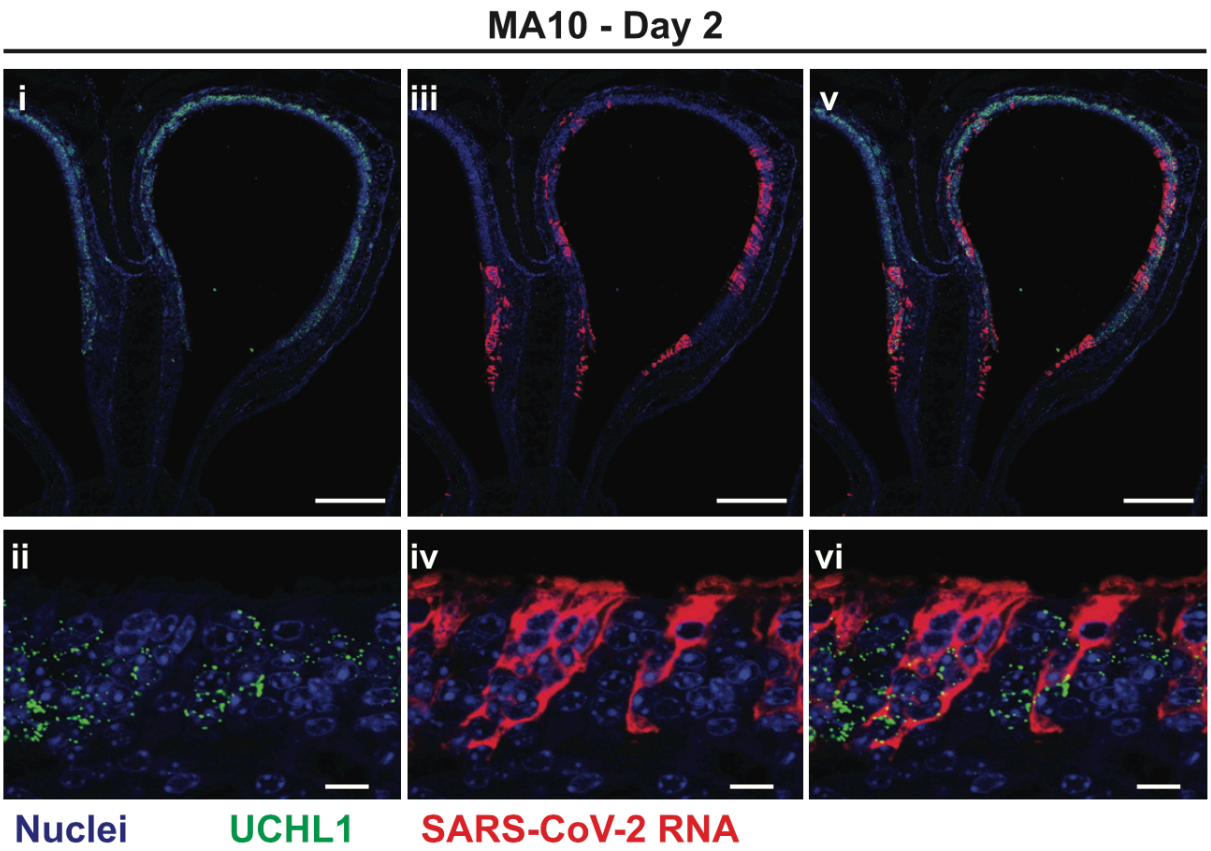

Figure 4.10. SARS-CoV-2 MA10 Infects the Nasal Olfactory Epithelium but Not Olfactory Sensory Neurons.

SARS-CoV-2 MA10 cellular tropism in the nasal cavity was assessed by RNA *in situ* hybridization (ISH) infected female 1-year-old BALB/c mice from Figure 4.3 at 2dpi. *Uchl1* is a marker of olfactory sensory neurons (OSNs). (i & iii and ii and iv) are single color channels shown merged in (v and vi). Scale bars represent 200 μm (i, iii, v) or 10 μm (ii, iv, vi).

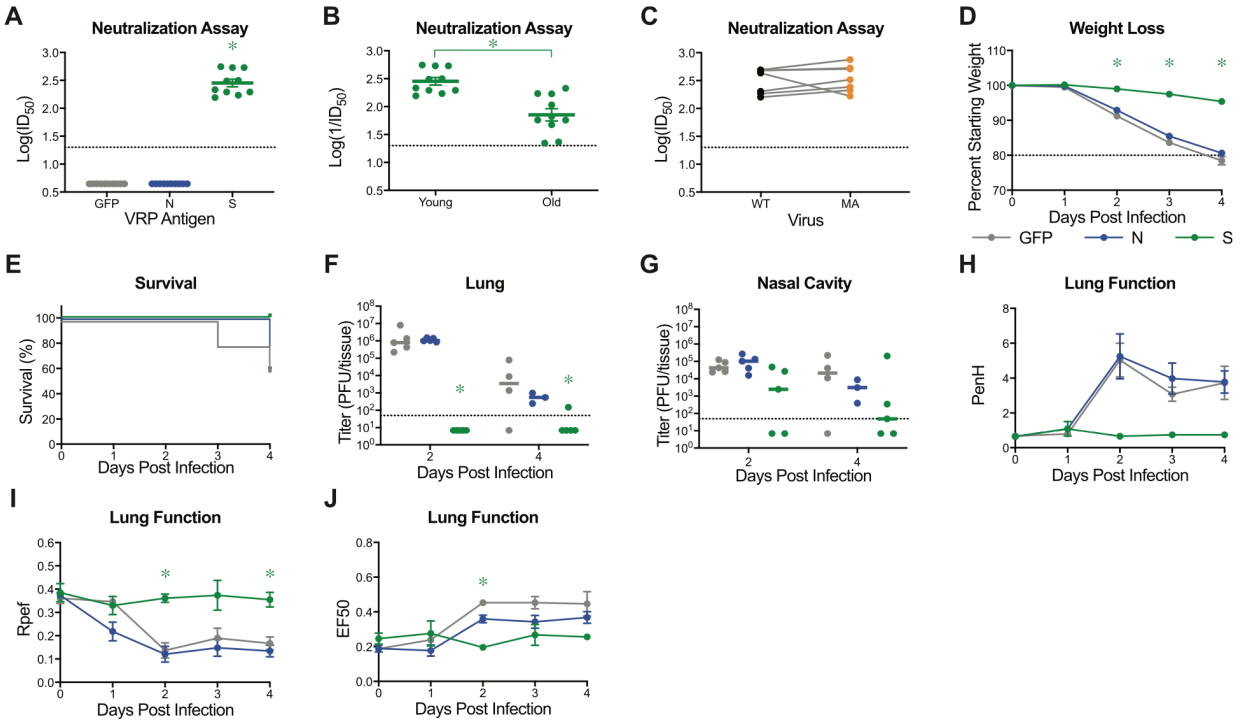

Figure 4.11. Virus Replicon Particle Delivered Spike Vaccination Protects Young Mice from SARS-CoV-2 MA10 Challenge.

10-week-old female BALB/c mice were vaccinated with 10^3 virus replicon particles (VRPs) expressing SARS-CoV-2 wild-type spike (S, n = 10), nucleocapsid (N, n = 10), or GFP (n = 10). Mice received a boost 3 weeks after prime immunization and submandibular blood samples were taken to be analyzed via neutralization assays. All mice were challenged 4 weeks after the boost immunization. (A) Neutralization of SARS-CoV-2 WT by sera from vaccinated mice 3 weeks post boost. ID_{50}: inhibitory concentration necessary to achieve 50% virus neutralization. Dotted line represents limit of detection. Undetected samples are plotted at half the limit of detection. Log transformed data analyzed via 1-factor ANOVA followed by Holm-Sidak's multiple comparisons. (B) Comparison of serum IC_{50} values from 10-week and 1-year-old spike vaccinated mice from Figure 4.6A. Dotted line represents limit of detection. Data analyzed by unpaired, two-tailed Student's t test. (C) Comparison of serum IC_{50} values from 10-week-old spike vaccinated mice to neutralize SARS-CoV-2 WT versus SARS-CoV-2 MA. Data analyzed by Wilcoxon matched-pairs signed rank test. Data not statistically significant. (D) Percent starting weight. Data analyzed by mixed effects analysis followed by Sidak's multiple comparisons. (E) Survival rate of mice from (D). (F-G) Viral lung (F) and nasal cavity (G) titer. n = 5 for each group at each time point. Dotted line represents limit of detection. Undetected samples are plotted at half the limit of detection. Log transformed data analyzed via 2-factor ANOVA followed by Dunnett's multiple comparisons. (G-I) Whole body plethysmography analysis of lung function parameters (n = 5 mice per group at 0dpi): PenH (G), Rpef (H), and EF50 (I). Data analyzed using 2-factor ANOVA followed by Dunnett's multiple comparisons. Error bars represent standard error of the mean about the mean. Asterisks represent $p < 0.05$.

Table 4.1. Frequency of mutations during mouse adaptation of SARS-CoV-2 MA.

			Bulk Mouse Passage										Plaque Purified				
Mutation	**Gene**	**Coding Change**	**1**	**2**	**3**	**4**	**5**	**6**	**7**	**8**	**9**	**10**	**Plaque 1**	**Plaque 2**	**Plaque 3**	**Plaque 4**	**MA10**
C9438T	nsp4	T285I	0.0%	0.0%	0.1%	1.9%	35.0%	64.9%	76.7%	85.5%	86.8%	86.4%	99.7%	0.1%	0.1%	99.7%	99.8%
G9479T	nsp4	G309C	0.3%	0.1%	0.2%	0.1%	0.3%	0.3%	0.4%	0.3%	0.4%	0.3%	0.1%	0.5%	98.7%	0.1%	0.1%
C9491T	nsp4	H313Y	0.5%	0.1%	0.4%	0.3%	3.2%	4.8%	5.9%	6.5%	7.5%	9.2%	0.1%	99.7%	0.0%	0.1%	0.0%
A11847G	nsp7	K2R	0.9%	17.7%	62.2%	86.9%	94.9%	96.3%	94.5%	90.6%	83.2%	70.2%	0.1%	0.1%	99.7%	99.8%	99.7%
A12159G	nsp8	E23G	1.0%	18.5%	64.4%	88.0%	95.4%	96.4%	94.7%	91.4%	84.5%	71.5%	0.1%	0.0%	99.8%	99.7%	99.7%
A12658G	nsp8	Silent	0.2%	0.5%	0.6%	1.1%	1.2%	2.0%	3.8%	7.2%	14.4%	28.2%	99.9%	99.9%	0.1%	0.1%	0.1%
A12678G	nsp8	K196R	0.1%	0.5%	0.7%	1.1%	1.3%	2.0%	3.9%	7.4%	14.8%	28.5%	99.9%	99.9%	0.1%	0.1%	0.1%
A12884G	nsp9	T67A	0.1%	0.6%	0.6%	1.2%	1.3%	1.9%	3.6%	6.6%	12.5%	26.4%	99.8%	99.6%	0.1%	0.2%	0.1%
A13003G	nsp9	Silent	0.2%	0.5%	0.7%	1.2%	1.4%	2.0%	3.7%	7.3%	14.3%	29.2%	99.8%	99.8%	0.1%	0.1%	0.1%
C23039A	Spike	Q493K	0.4%	5.2%	49.7%	88.1%	99.0%	99.8%	99.9%	99.9%	99.8%	99.8%	99.9%	99.9%	99.8%	99.8%	99.9%
T27221C	ORF6	F7S	0.4%	6.3%	49.8%	87.9%	98.4%	99.4%	99.5%	99.8%	99.4%	99.6%	99.9%	99.9%	99.8%	99.8%	99.9%
G28423A	Nucleocapsid	Silent	0.1%	0.0%	0.1%	0.1%	0.2%	0.1%	0.1%	0.1%	0.1%	0.1%	0.0%	0.1%	99.8%	0.0%	0.0%

REFERENCES

1 Zhou, P. *et al.* A pneumonia outbreak associated with a new coronavirus of probable bat origin. *Nature* **579**, 270-273, doi:10.1038/s41586-020-2012-7 (2020).

2 Zhu, N. *et al.* A Novel Coronavirus from Patients with Pneumonia in China, 2019. *N Engl J Med* **382**, 727-733, doi:10.1056/NEJMoa2001017 (2020).

3 Dong, E., Du, H. & Gardner, L. An interactive web-based dashboard to track COVID-19 in real time. *Lancet Infect Dis* **20**, 533-534, doi:10.1016/S1473-3099(20)30120-1 (2020).

4 Guan, W. J. *et al.* Clinical Characteristics of Coronavirus Disease 2019 in China. *N Engl J Med* **382**, 1708-1720, doi:10.1056/NEJMoa2002032 (2020).

5 Mao, R. *et al.* Manifestations and prognosis of gastrointestinal and liver involvement in patients with COVID-19: a systematic review and meta-analysis. *Lancet Gastroenterol Hepatol* **5**, 667-678, doi:10.1016/S2468-1253(20)30126-6 (2020).

6 Wichmann, D. *et al.* Autopsy Findings and Venous Thromboembolism in Patients With COVID-19: A Prospective Cohort Study. *Ann Intern Med* **173**, 268-277, doi:10.7326/M20-2003 (2020).

7 Cheung, E. W. *et al.* Multisystem Inflammatory Syndrome Related to COVID-19 in Previously Healthy Children and Adolescents in New York City. *JAMA* **324**, 294-296, doi:10.1001/jama.2020.10374 (2020).

8 Zhou, F. *et al.* Clinical course and risk factors for mortality of adult inpatients with COVID-19 in Wuhan, China: a retrospective cohort study. *Lancet* **395**, 1054-1062, doi:10.1016/S0140-6736(20)30566-3 (2020).

9 Rothan, H. A. & Byrareddy, S. N. The epidemiology and pathogenesis of coronavirus disease (COVID-19) outbreak. *J Autoimmun* **109**, 102433, doi:10.1016/j.jaut.2020.102433 (2020).

10 Li, X. & Ma, X. Acute respiratory failure in COVID-19: is it "typical" ARDS? *Crit Care* **24**, 198, doi:10.1186/s13054-020-02911-9 (2020).

11 Sinha, P., Matthay, M. A. & Calfee, C. S. Is a "Cytokine Storm" Relevant to COVID-19? *JAMA Intern Med* **180**, 1152-1154, doi:10.1001/jamainternmed.2020.3313 (2020).

12 Letko, M., Marzi, A. & Munster, V. Functional assessment of cell entry and receptor usage for SARS-CoV-2 and other lineage B betacoronaviruses. *Nature Microbiology* **5**, 562-569, doi:10.1038/s41564-020-0688-y (2020).

13 Jiang, R. D. *et al.* Pathogenesis of SARS-CoV-2 in Transgenic Mice Expressing Human Angiotensin-Converting Enzyme 2. *Cell* **182**, 50-58 e58, doi:10.1016/j.cell.2020.05.027 (2020).

14 Bao, L. *et al.* The pathogenicity of SARS-CoV-2 in hACE2 transgenic mice. *Nature* **583**, 830-833, doi:10.1038/s41586-020-2312-y (2020).

15 Sun, S. H. *et al.* A Mouse Model of SARS-CoV-2 Infection and Pathogenesis. *Cell Host Microbe* **28**, 124-133 e124, doi:10.1016/j.chom.2020.05.020 (2020).

16 Sun, J. *et al.* Generation of a Broadly Useful Model for COVID-19 Pathogenesis, Vaccination, and Treatment. *Cell* **182**, 734-743 e735, doi:10.1016/j.cell.2020.06.010 (2020).

17 Hassan, A. O. *et al.* A SARS-CoV-2 Infection Model in Mice Demonstrates Protection by Neutralizing Antibodies. *Cell* **182**, 744-753 e744, doi:10.1016/j.cell.2020.06.011 (2020).

18 Israelow, B. *et al.* Mouse model of SARS-CoV-2 reveals inflammatory role of type I interferon signaling. *J Exp Med* **217**, doi:10.1084/jem.20201241 (2020).

19 Menachery, V. D. *et al.* SARS-like WIV1-CoV poised for human emergence. *Proc Natl Acad Sci U S A* **113**, 3048-3053, doi:10.1073/pnas.1517719113 (2016).

20 McCray, P. B., Jr. *et al.* Lethal infection of K18-hACE2 mice infected with severe acute respiratory syndrome coronavirus. *J Virol* **81**, 813-821, doi:10.1128/JVI.02012-06 (2007).

21 Butler, N., Pewe, L., Trandem, K. & Perlman, S. Murine encephalitis caused by HCoV-OC43, a human coronavirus with broad species specificity, is partly immune-mediated. *Virology* **347**, 410-421, doi:10.1016/j.virol.2005.11.044 (2006).

22 Jacomy, H., Fragoso, G., Almazan, G., Mushynski, W. E. & Talbot, P. J. Human coronavirus OC43 infection induces chronic encephalitis leading to disabilities in BALB/C mice. *Virology* **349**, 335-346, doi:10.1016/j.virol.2006.01.049 (2006).

23 Dinnon, K. H., 3rd *et al.* A mouse-adapted model of SARS-CoV-2 to test COVID-19 countermeasures. *Nature* **586**, 560-566, doi:10.1038/s41586-020-2708-8 (2020).

24 Roberts, A. *et al.* A mouse-adapted SARS-coronavirus causes disease and mortality in BALB/c mice. *PLoS Pathog* **3**, e5, doi:10.1371/journal.ppat.0030005 (2007).

25 Sheahan, T. P. *et al.* Comparative therapeutic efficacy of remdesivir and combination lopinavir, ritonavir, and interferon beta against MERS-CoV. *Nat Commun* **11**, 222, doi:10.1038/s41467-019-13940-6 (2020).

26 Schmidt, M. E. *et al.* Memory CD8 T cells mediate severe immunopathology following respiratory syncytial virus infection. *PLoS Pathog* **14**, e1006810, doi:10.1371/journal.ppat.1006810 (2018).

27 Matute-Bello, G. *et al.* An official American Thoracic Society workshop report: features and measurements of experimental acute lung injury in animals. *Am J Respir Cell Mol Biol* **44**, 725-738, doi:10.1165/rcmb.2009-0210ST (2011).

28 Bryant, C. D. The blessings and curses of C57BL/6 substrains in mouse genetic studies. *Ann N Y Acad Sci* **1245**, 31-33, doi:10.1111/j.1749-6632.2011.06325.x (2011).

29 Noll, K. E. *et al.* Complex Genetic Architecture Underlies Regulation of Influenza-A-Virus-Specific Antibody Responses in the Collaborative Cross. *Cell Rep* **31**, 107587, doi:10.1016/j.celrep.2020.107587 (2020).

30 Rasmussen, A. L. *et al.* Host genetic diversity enables Ebola hemorrhagic fever pathogenesis and resistance. *Science* **346**, 987-991, doi:10.1126/science.1259595 (2014).

31 Gralinski, L. E. *et al.* Genome Wide Identification of SARS-CoV Susceptibility Loci Using the Collaborative Cross. *PLoS Genet* **11**, e1005504, doi:10.1371/journal.pgen.1005504 (2015).

32 Graham, J. B. *et al.* Genetic diversity in the collaborative cross model recapitulates human West Nile virus disease outcomes. *mBio* **6**, e00493-00415, doi:10.1128/mBio.00493-15 (2015).

33 Manet, C. *et al.* Genetic Diversity of Collaborative Cross Mice Controls Viral Replication, Clinical Severity, and Brain Pathology Induced by Zika Virus Infection, Independently of Oas1b. *J Virol* **94**, doi:10.1128/JVI.01034-19 (2020).

34 Zhang, H. *et al.* Expression of the SARS-CoV-2 ACE2 Receptor in the Human Airway Epithelium. *Am J Respir Crit Care Med* **202**, 219-229, doi:10.1164/rccm.202003-0541OC (2020).

35 Hou, Y. J. *et al.* SARS-CoV-2 Reverse Genetics Reveals a Variable Infection Gradient in the Respiratory Tract. *Cell* **182**, 429-446 e414, doi:10.1016/j.cell.2020.05.042 (2020).

36 Chamanza, R. & Wright, J. A. A Review of the Comparative Anatomy, Histology, Physiology and Pathology of the Nasal Cavity of Rats, Mice, Dogs and Non-human Primates. Relevance to Inhalation Toxicology and Human Health Risk Assessment. *J Comp Pathol* **153**, 287-314, doi:10.1016/j.jcpa.2015.08.009 (2015).

37 Wolfel, R. *et al.* Virological assessment of hospitalized patients with COVID-2019. *Nature* **581**, 465-469, doi:10.1038/s41586-020-2196-x (2020).

38 Lechien, J. R. *et al.* Olfactory and gustatory dysfunctions as a clinical presentation of mild-to-moderate forms of the coronavirus disease (COVID-19): a multicenter European study. *Eur Arch Otorhinolaryngol* **277**, 2251-2261, doi:10.1007/s00405-020-05965-1 (2020).

39 Spinato, G. *et al.* Alterations in Smell or Taste in Mildly Symptomatic Outpatients With SARS-CoV-2 Infection. *JAMA* **323**, 2089-2090, doi:10.1001/jama.2020.6771 (2020).

40 Mesev, E. V., LeDesma, R. A. & Ploss, A. Decoding type I and III interferon signalling during viral infection. *Nat Microbiol* **4**, 914-924, doi:10.1038/s41564-019-0421-x (2019).

41 Felgenhauer, U. *et al.* Inhibition of SARS-CoV-2 by type I and type III interferons. *J Biol Chem* **295**, 13958-13964, doi:10.1074/jbc.AC120.013788 (2020).

42 Vanderheiden, A. *et al.* Type I and Type III Interferons Restrict SARS-CoV-2 Infection of Human Airway Epithelial Cultures. *J Virol* **94**, doi:10.1128/JVI.00985-20 (2020).

43 Agnihothram, S. *et al.* Development of a Broadly Accessible Venezuelan Equine Encephalitis Virus Replicon Particle Vaccine Platform. *J Virol* **92**, doi:10.1128/JVI.00027-18 (2018).

44 Song, P., Li, W., Xie, J., Hou, Y. & You, C. Cytokine storm induced by SARS-CoV-2. *Clin Chim Acta* **509**, 280-287, doi:10.1016/j.cca.2020.06.017 (2020).

45 Costela-Ruiz, V. J., Illescas-Montes, R., Puerta-Puerta, J. M., Ruiz, C. & Melguizo-Rodriguez, L. SARS-CoV-2 infection: The role of cytokines in COVID-19 disease. *Cytokine Growth Factor Rev* **54**, 62-75, doi:10.1016/j.cytogfr.2020.06.001 (2020).

46 Gralinski, L. E. *et al.* Mechanisms of severe acute respiratory syndrome coronavirus-induced acute lung injury. *mBio* **4**, doi:10.1128/mBio.00271-13 (2013).

47 Totura, A. L. *et al.* Toll-Like Receptor 3 Signaling via TRIF Contributes to a Protective Innate Immune Response to Severe Acute Respiratory Syndrome Coronavirus Infection. *mBio* **6**, e00638-00615, doi:10.1128/mBio.00638-15 (2015).

48 Sheahan, T. *et al.* MyD88 is required for protection from lethal infection with a mouse-adapted SARS-CoV. *PLoS Pathog* **4**, e1000240, doi:10.1371/journal.ppat.1000240 (2008).

49 Channappanavar, R. *et al.* Dysregulated Type I Interferon and Inflammatory Monocyte-Macrophage Responses Cause Lethal Pneumonia in SARS-CoV-Infected Mice. *Cell Host Microbe* **19**, 181-193, doi:10.1016/j.chom.2016.01.007 (2016).

50 Wang, J. *et al.* Mouse-adapted SARS-CoV-2 replicates efficiently in the upper and lower respiratory tract of BALB/c and C57BL/6J mice. *Protein Cell* **11**, 776-782, doi:10.1007/s13238-020-00767-x (2020).

51 Gu, H. *et al.* Adaptation of SARS-CoV-2 in BALB/c mice for testing vaccine efficacy. *Science* **369**, 1603-1607, doi:10.1126/science.abc4730 (2020).

52 Frieman, M. *et al.* Molecular determinants of severe acute respiratory syndrome coronavirus pathogenesis and virulence in young and aged mouse models of human disease. *J Virol* **86**, 884-897, doi:10.1128/JVI.05957-11 (2012).

53 Frieman, M. *et al.* Severe acute respiratory syndrome coronavirus ORF6 antagonizes STAT1 function by sequestering nuclear import factors on the rough endoplasmic reticulum/Golgi membrane. *J Virol* **81**, 9812-9824, doi:10.1128/JVI.01012-07 (2007).

54 Sims, A. C. *et al.* Release of severe acute respiratory syndrome coronavirus nuclear import block enhances host transcription in human lung cells. *J Virol* **87**, 3885-3902, doi:10.1128/JVI.02520-12 (2013).

55 Fehr, A. R. & Perlman, S. Coronaviruses: an overview of their replication and pathogenesis. *Methods Mol Biol* **1282**, 1-23, doi:10.1007/978-1-4939-2438-7_1 (2015).

56 Ackermann, M. *et al.* Pulmonary Vascular Endothelialitis, Thrombosis, and Angiogenesis in Covid-19. *N Engl J Med* **383**, 120-128, doi:10.1056/NEJMoa2015432 (2020).

57 Bradley, B. T. *et al.* Histopathology and ultrastructural findings of fatal COVID-19 infections in Washington State: a case series. *Lancet* **396**, 320-332, doi:10.1016/S0140-6736(20)31305-2 (2020).

58 Tian, S. *et al.* Pathological study of the 2019 novel coronavirus disease (COVID-19) through postmortem core biopsies. *Mod Pathol* **33**, 1007-1014, doi:10.1038/s41379-020-0536-x (2020).

59 Sheahan, T. P. *et al.* An orally bioavailable broad-spectrum antiviral inhibits SARS-CoV-2 in human airway epithelial cell cultures and multiple coronaviruses in mice. *Sci Transl Med* **12**, doi:10.1126/scitranslmed.abb5883 (2020).

60 Clark, J. C. *et al.* Decreased lung compliance and air trapping in heterozygous SP-B-deficient mice. *Am J Respir Cell Mol Biol* **16**, 46-52, doi:10.1165/ajrcmb.16.1.8998078 (1997).

61 Weaver, T. E. & Conkright, J. J. Function of surfactant proteins B and C. *Annu Rev Physiol* **63**, 555-578, doi:10.1146/annurev.physiol.63.1.555 (2001).

62 Stevens, T. P. & Sinkin, R. A. Surfactant replacement therapy. *Chest* **131**, 1577-1582, doi:10.1378/chest.06-2371 (2007).

63 Koumbourlis, A. C. & Motoyama, E. K. Lung Mechanics in COVID-19 Resemble Respiratory Distress Syndrome, Not Acute Respiratory Distress Syndrome: Could Surfactant Be a Treatment? *Am J Respir Crit Care Med* **202**, 624-626, doi:10.1164/rccm.202004-1471LE (2020).

64 Sheahan, T. *et al.* Successful vaccination strategies that protect aged mice from lethal challenge from influenza virus and heterologous severe acute respiratory syndrome coronavirus. *J Virol* **85**, 217-230, doi:10.1128/JVI.01805-10 (2011).

65 Tseng, C. T. *et al.* Immunization with SARS coronavirus vaccines leads to pulmonary immunopathology on challenge with the SARS virus. *PLoS One* **7**, e35421, doi:10.1371/journal.pone.0035421 (2012).

66 Bolles, M. *et al.* A double-inactivated severe acute respiratory syndrome coronavirus vaccine provides incomplete protection in mice and induces increased eosinophilic

proinflammatory pulmonary response upon challenge. *J Virol* **85**, 12201-12215, doi:10.1128/JVI.06048-11 (2011).

67 Corbett, K. S. *et al.* SARS-CoV-2 mRNA vaccine design enabled by prototype pathogen preparedness. *Nature* **586**, 567-571, doi:10.1038/s41586-020-2622-0 (2020).

68 Gupta, K. *et al.* The Cellular basis of loss of smell in 2019-nCoV-infected individuals. *Brief Bioinform* **22**, 873-881, doi:10.1093/bib/bbaa168 (2021).

69 Zhang, A. J. *et al.* SARS-CoV-2 infects and damages the mature and immature olfactory sensory neurons of hamsters. *Clin Infect Dis*, doi:10.1093/cid/ciaa995 (2020).

70 Quiding-Jarbrink, M., Granstrom, G., Nordstrom, I., Holmgren, J. & Czerkinsky, C. Induction of compartmentalized B-cell responses in human tonsils. *Infect Immun* **63**, 853-857, doi:10.1128/iai.63.3.853-857.1995 (1995).

71 Sia, S. F. *et al.* Pathogenesis and transmission of SARS-CoV-2 in golden hamsters. *Nature* **583**, 834-838, doi:10.1038/s41586-020-2342-5 (2020).

72 Rockx, B. *et al.* Comparative pathogenesis of COVID-19, MERS, and SARS in a nonhuman primate model. *Science* **368**, 1012-1015, doi:10.1126/science.abb7314 (2020).

73 Okuda, K. *et al.* Localization of Secretory Mucins MUC5AC and MUC5B in Normal/Healthy Human Airways. *Am J Respir Crit Care Med* **199**, 715-727, doi:10.1164/rccm.201804-0734OC (2019).

74 Menachery, V. D., Gralinski, L. E., Baric, R. S. & Ferris, M. T. New Metrics for Evaluating Viral Respiratory Pathogenesis. *PLOS ONE* **10**, e0131451, doi:10.1371/journal.pone.0131451 (2015).

CHAPTER 5 – SPATIAL TRANSCRIPTIONAL PROFILING OF CHRONIC PULMONARY FIBROSIS IN A MOUSE-ADAPTED MODEL OF SARS-COV-2 INFECTION

5.1 Introduction

Severe acute respiratory syndrome coronavirus 2 (SARS-CoV-2) was identified as the causative agent for COVID-19[1], and rapid human-to-human transmission led to worldwide spread and a devastating pandemic[2]. Even though hundreds of millions of people have been infected with SARS-CoV-2[3], the rapid development of antivirals, antibody therapies, and improved critical care strategies has aided in keeping the acute case fatality rate low. However, survivors of emerging coronavirus infections, like the 2003 SARS-CoV, the 2012 MERS-CoV and the 2020 SARS-CoV-2 strains, report post-acute fibrotic lung sequelae long after the acute phase of infection[4-6]. Moreover, major risk factors for severe COVID-19 and idiopathic pulmonary fibrosis (IPF) are shared, like increasing age, male sex, and certain comorbidities. About 40% of COVID-19 patients develop acute respiratory distress syndrome (ARDS), another shared risk factor for the development of long-term fibrotic lung disease[7]. Currently, 30-50% of the asymptomatic as well as symptomatic COVID-19 acute infection survivors report 'long COVID' or 'post-acute sequelae after SARS-CoV-2 infection' (PASC), including dyspnea, fatigue, chest pain and effects on cognitive functions, and chronic lung diseases[8-11]. Given these numbers, strategies are needed to prevent second waves of late-onset disease mortality associated with COVID-19 induced pulmonary fibrosis, a potential consequence of this terrible pandemic.

Hit-and-run virus infections have long been recognized as potential cofactors in the development of chronic organ diseases[12,13]. COVID-19 is currently characterized as a biphasic disease that includes: 1) an acute phase dominated by SARS-CoV-2 viral infection; and 2) a repair

phase dominated by host immunologic and reparative processes. Studies describing human autopsy samples highlight severe disease manifestations in people who succumbed to COVID-19[14,15], usually after clearance of the virus from the lungs and/or other organ systems; therefore, a clear understanding of the early programming and expression alterations is lacking. Additionally, autopsy samples represent patients who have died to COVID-19 complications, and likely differ greatly from those who survive infection. The lungs from these individuals exhibit broad features of an organizing pneumonia, with characteristic loss of alveolar architecture, dense cellularity, myofibroblast proliferation, and collagen deposition[7,16-21]. Notably, the mechanisms describing the development of non-viral chronic organizing pneumonias and/or pulmonary fibrosis are not well understood, providing only partial roadmaps to understanding this emerging third disease stage of COVID-19 infection in the lung and the potential treatment options that are needed for improved human health[22].

Understanding chronic lung manifestations of PASC will require longitudinal tissue samples excised or at the time of transplantation for post-COVID-19 lung disease. In parallel, small animal models of COVID-19, like use of SARS-CoV-2 MA10 in mice, are available that cause ARDS, phenocopy the severe age-related disease manifestations associated with acute infection, and target sustentacular cells of the olfactory epithelium, ciliated and club cells in the airway epithelium, and AT2 cells in the alveoli[23]. To date, animal models that successfully recapitulate PASC chronic disease phenotypes in the lung have not been reported, hampering a detailed understanding of the mechanistic and reparative processes. Time ordered, cross species, comparative studies of the expression and disease manifestations after SARS-CoV-2 clearance are desperately needed to identify early disease markers of severe late-stage disease, identify the dysregulated pathways as well as reparative pathways associated with early onset of pulmonary fibrosis, and the performance of intervention strategies to prevent chronic disease onset and progression and to reverse end stage fibrotic disease outcomes in patients. Despite the development of small molecule inhibitors and therapeutic antibodies that appear somewhat

effective in treating early COVID-19 infections, strategies to intervene after acute virus infection is limited by an absence of precise descriptions of the post-sequelae immunopathologic and repair mechanisms involved in the entire spectrum of long-term disease symptoms.

In this study, we aimed to elucidate the patterns and mechanisms mediating the long-term pulmonary consequences of SARS-CoV-2 infection. Employing a mouse model of SARS-CoV-2 infection that recapitulates the acute phase of human disease, we examined the long-term manifestation of lung disease in surviving young and aged mice utilizing multiple complementary approaches, including histologic studies supplemented with immunohistochemistry (IHC) and CT scan studies. Digital spatial profiling and RNA *in situ* hybridization (ISH) validation studies were utilized to identify the transcriptional profiles of diseased and healthy tissue during the acute and chronic phases of disease to gain insights into disease mechanisms. Our data reveal early pulmonary fibrosis disease signatures and fibrotic lesions that become more organized over time in young and aged mice infected with SARS-CoV-2 MA10. Comparative spatial profiling reveals concordant signatures of persistent alveolar disease, a shifting population of AT2 intermediates including ‘pre-alveolar type-1 transitional cell state’ (PATS) and ‘damage-associated transient progenitors’ (DATPs) cells, coupled to a striking upregulation of pro-fibrotic markers such as smooth muscle actin, type 1 collagens, fibronectin, complement, and frank fibrosis as revealed by Picrosirius red staining. SARS-CoV-2 MA10 infection in standard laboratory mice not only provides opportunities to study the role of host genes in early pulmonary fibrosis disease onset and progression but allows for the evaluation of countermeasures designed to prevent, attenuate, or reverse chronic lung disease outcomes after SARS-CoV2 acute infection.

5.2 Results

5.2.1 SARS-CoV-2 MA10 infection causes chronic inflammation and fibrosis in aged BALB/c mice

As observed in humans, aged (1-year-old) animals were significantly more susceptible to acute SARS-CoV-2 pulmonary disease than young adult (10-week-old) mice[23]. To induce severe acute disease without excessive mortality, 1-year-old female BALB/c mice were infected with 10^3 PFU of mouse-adapted SARS-CoV-2 MA10, intranasally. Acute SARS-CoV-2 MA10 infection resulted in rapid and significant decrease in body weight over 7 days compared to PBS infected (mock) mice, with a maximal weight loss of 18% at 6-7 days post infection (dpi) **(Figure 5.1A)**. These results replicated those observed previously during the acute phase (4 dpi) of infection[23], and the overall survival frequency (75%) allowed us to monitor mice for up to 60d post infection (dpi) to assess long-term pulmonary effects of the initial infection. Surviving mice clinically recovered and slowly regained most of their body weight by 15 (95%) and 30 dpi (100%). Notably, 25% of MA10 infected mice did not recover from infection and were either found dead or reached criteria for humane euthanasia at 4-10 dpi **(Figure 5.1B)**.

Mice were necropsied at days 2, 7, 15, 30, and 60dpi to determine lung viral titer and collect lung specimens for histopathological analyses. Peak viral titers occurred on 2 dpi (~10^7 PFU/lobe). Thereafter, virus titers waned with higher variation noted at 7 dpi (ranging from 10^3 to 10^6 PFU/lobe), and by 15 dpi, surviving mice had cleared virus from their lungs **(Figure 5.1C)**. Pulmonary function was assessed via whole body plethysmography (WBP), utilizing PenH and Rpef as measures of airway obstruction and EF50 as a measure of expiratory flow rate. Significant changes on 2 dpi (PenH and Rpef) and on 7 dpi (PenH, Rpef, and EF50) were observed, consistent with virus-induced decrements in pulmonary function **(Figure 5.1D-F)**.

By histopathologic analyses, there was acute lung injury on days 4 and 7 post infection. At 15, 30, and 60 dpi, mice exhibited heterogeneous regions of healthy tissue vs regions with prolonged injury **(Figure 5.1G)**. At 15, 30 and 60 dpi, the bronchiolar epithelium was repaired morphologically. However, heterogeneous regions in the subpleural alveolar space exhibited dense cellularity and prolonged loss of alveolar architecture. These dense lesions were characterized by an accumulation of immune cells, smooth muscle actin (SMA) positive myofibroblasts, and collagen deposition, characteristic of an organizing pneumonia and fibrosis **(Figure 5.1G-I)**.

Given the striking age-related disease phenotypes noted in humans, younger, 10-week-old, mice were also infected with 10-fold more SARS-CoV-2 MA10 virus (10^4 PFU). These animals exhibited a similar clinical disease, e.g., weight loss, survival, and respiratory dysfunction as 1-year-old animals, but cleared infectious virus by 7 dpi **(Figure 5.2A-F)**. Like old mice, younger mice developed subpleural cellular/fibrotic lesions, but these were less severe **(Figure 5.2G)**.

In old and young animals, whole lung and serum cytokine and chemokine analyses revealed robust immune responses at 2 and 7 dpi, but by 15 dpi all cytokine profiles were restored to baseline levels, concordant with clinical phenotypes and clearance of infectious virus **(Figure 5.3)**. Collectively, these data demonstrate that mice that survived SARS-CoV-2 MA10 infection developed features of chronic organizing pneumonia and pulmonary fibrosis as reported in human patients.

5.2.2 Spatial and temporal alteration in host transcriptional profiles in response to SARS-CoV-2 infection.

To characterize host transcriptional pathways involved in the processes of acute lung injury and subsequent impaired alveolar epithelial regeneration and persistent organizing pneumonia/fibrosis following SARS-CoV-2 MA10 infection, we employed GeoMx Digital Spatial Profiling (DSP) to survey nearly 20,000 mouse transcript targets per interrogated regions of

interest **(Figure 5.4A)**. Since SARS-CoV-2 MA10 efficiently infects alveolar type 2 (AT2) cells in the alveoli and secretory club cells in terminal bronchiolar epithelia[23], we focused on those two compartments as regions of interests (ROIs) **(Figure 5.4B)**. The alveoli are lined by two epithelial cell types, alveolar type 1 (AT1) cells and AT2 cells, the latter produce surfactants to maintain lung compliance and serve as progenitor cells, capable of self-renewal as well as differentiation into AT1 cells[24-27]. Club cells also provide secretory surfactants and serve as progenitor cells for ciliated and secretory epithelial and suggested to also be involved in alveolar repair[28-30]. Following data quality control and normalization, the GeoMx DSP technique was used to perform multiplexed high-resolution spatial whole transcriptomic profiling of a total of 60 alveolar and 36 distal airway epithelial tissue ROIs from mock or SARS-CoV-2 MA10-infected mice at acute (2 dpi) and later (15 and 30 dpi) time points after infection **(Figure 5.4C)**. Disease regions were selected as ROIs based on SARS-CoV-2 MA10 RNA positive cells at early time points and consolidated and disorganized morphological microstructures in serial hematoxylin and eosin (H&E) stained slides at late time points. Since all distal airway epithelia in SARS-CoV-2 MA10-infected mice were morphologically intact at late time points, they were defined as healthy.

Principal components analysis (PCA) clustered disease ROIs in SARS-CoV-2-infected mice at 2 dpi separately from the other ROIs in both distal airway and alveolar epithelial regions **(Figure 5.4D-E)**. In alveolar ROIs, while healthy alveolar ROIs were tightly clustered regardless of time point or presence of infection, the diseased alveolar ROIs in SARS-CoV-2-infected mice at 15 and 30 dpi were also clustered together but significantly distinct from either healthy alveolar ROIs or disease alveolar ROIs at 2 dpi clusters **(Figure 5.4D)**. This finding suggests persistent alterations of host transcriptome evolved over time in morphologically diseased alveolar regions. In contrast, distal airway ROIs from mock and SARS-CoV-2-infected mice at day 15 and 30 except for one outlier clustered together, suggesting full recovery from airway epithelial damage caused by SARS-CoV-MA10 infection after 15 dpi **(Figure 5.4E).** These data were consistent with morphologically repaired distal airway epithelia, or cells that were never infected or damaged, in

SARS-CoV-2-infected mice at day 15 and 30. Importantly, ROIs that were classified as healthy tissue transcriptionally resembled tissue from mock infected animals **(Figure 5.4E)**.

5.2.3 Dynamic innate host responses to acute-phase mouse-adapted SARS-CoV-2 MA10 infection.

To gain insights into acute host responses to SARS-CoV-2 infection, we first focused on transcriptional pathways at early time points following SARS-CoV-2 MA10 infection. Supervised hierarchical clustering of all ROIs studied was performed, using differentially expressed genes (DEGs) between diseased airway or alveolar ROIs at 2 dpi versus healthy airway or alveolar ROIs in mock mice, respectively (**Figure 5.5**). These heatmaps revealed distinct transcriptomic profiling of disease ROIs in SARS-CoV-2 MA10-infected mice at 2 dpi compared to other ROIs in both airway and alveolar regions, reflecting dynamic host transcriptional responses to acute phase SARS-CoV-2 MA10 infection (**Figure 5.5A, B**). DEG analysis demonstrated enrichment of common interferon-stimulated genes (ISGs) in diseased airway and alveolar ROIs in SARS-CoV-2 MA10-infected mice at 2 dpi (**Figure 5.6A-B**), supported by gene ontology analyses revealing enrichment of genes involved in interferon signaling (**Figure 5.5C**). Upregulated ISGs in SARS-CoV-2 MA10-infected mice at 2 dpi are consistent with ISGs that were reported to be upregulated in Calu-3 cells by coronavirus infection (**Figure 5.6C-E**)[31,32], suggesting that common antiviral pathways are activated in human and mouse lung cells. By 15 and 30 dpi, ISG expression returned to mock infected levels, consistent with clearance of infectious virus in the lung **(Figure 5.1C)**.

Next, the epithelial tropism and damage caused by SARS-CoV-2 MA10 infection was investigated. Cell types that were infected by SARS-CoV-2 in the distal airway and alveolar epithelium in SARS-CoV-2 MA10-infected mice at 1 dpi were characterized by RNA in situ hybridization (RNA-ISH). Consistent with our prior studies, SARS-CoV-2 MA10 RNA was identified in *Scgb1a1*+ secretory club cells and *Sftpc*+ AT2 cells in the distal airway epithelium

and alveoli, respectively (**Figure 5.6F-G**). GeoMx DSP data demonstrated loss of club (*Scgb1a1*) and AT2 (*Sftpc*) cell marker expression in SARS-CoV-2 MA10-infected mice at 2 dpi and restoration to normal levels by 15 dpi (**Figure 5.6H, I**), consistent with RNA-ISH quantification data (**Figure 5.7**). The loss of *Scgb1a1* and surfactant protein genes is consistent with reported human COVID-19 autopsy data [33]. It is notable that ciliated (*FoxJ1*) and AT1 (*Ager*) cell markers were not affected by SARS-CoV-2 MA10 infection, suggesting a selective SARS-CoV-2 MA10 cellular tropism for airway club and AT2 cells (**Figure 5.6F-I, 5.7**).

5.2.4 Alveolar epithelial damage and regeneration following SARS-CoV-2 infection.

Infection of AT2 cells can result in cell death or transition into an intermediate cell that may or may not be "frozen" in transition and unable to generate new AT2 and AT1 cells. A unique AT2 cell to AT1 cell transitional alveolar epithelial cell following alveolar inflammation has been characterized as "damage-associated transient progenitors (DATP)"[34] or "pre-AT1 transitional state cells (PATS)"[35] (DATP/PATS hereafter). Incomplete transition from AT2 to AT1 cells, with an accumulation of transitional (DATP/PATS) cells, was identified in human IPF lungs[35] and in human COVID-19 postmortem lungs[36,37], suggesting an association of a persistent alveolar epithelial transitional cell state and prolonged epithelial damage/repair. We identified three distinct DATP/PATS signature gene clusters that were enriched in alveolar disease ROIs, depending on time after infection (**Figure 5.8**). The first gene cluster (*Cdkn1a/Krt8/Timp1*) was enriched in disease ROIs at 2 dpi and decreased by 15 dpi, suggesting these genes may play a role in AT2 cell trans-differentiation into DATP/PATS cells. The second gene cluster exhibited increased expression levels (*Hif1a/Cxcl16/Csrp1*) at 2 dpi that persisted through 30 dpi. The persistent increase in *Cxcl16* and *HIF1a* expression levels in disease ROIs in both acute and chronic phases suggests their contribution to organizing pneumonia/fibrosis, consistent with previous reports[36,38]. The third gene cluster, including *Basp1/Trp53/Mif*, exhibited an increase in expression levels in disease ROIs only at later time points. This cluster includes genes associated with p53 signaling

pathway, including *Trp53*/*Ccnd1*/*Bax*, suggesting an association of p53 signaling with pulmonary fibrosis in our mouse model of SARS-CoV-2 infection. Importantly, DATP/PATS cell fate has been shown to be transcriptionally regulated by p53 pathways[35]. An enrichment of p53 signaling was also found in COVID-19 autopsy lungs, suggesting late phase COVID-19 in humans and our mouse adapted model of SARS-CoV-2 infection share common pathways in the development and persistence of an organizing pneumonia/pulmonary fibrosis phenotype.

5.2.5 Organizing pneumonia/fibrosis as a chronic manifestation of SARS-CoV-2 MA10-infected mice.

In diseased ROIs at 15 and 30 dpi, several genes involved in adaptive immune signaling and extracellular matrix deposition are highly upregulated, suggesting a would repair or profibrotic environment **(Figure 5.9A-B)**. Recent human COVID-19 autopsy studies identified abundant interstitial pro-fibrotic monocyte-derived macrophages in organizing pneumonia regions, which are characterized by increased expression of *Spp1*, *Ilrn*, *Mmp9*, also features of macrophages in human IPF[39]. GeoMx analyses identified features associated with the profibrotic IPF macrophage archetype[40] in disease alveolar ROIs at 15 and 30 dpi, including *Spp1* and *Sparc* expression (**Figure 5.9C**). RNA-ISH confirmed a persistent increase in *Spp1* expression in SARS-CoV-2 MA10-infected mice after 7 dpi (**Figure 5.9J-L**). These chronic organizing pneumonia/fibrotic manifestations are consistent with deconvolution into major cell type compositions from GeoMx DSP data which demonstrated an increase in interstitial fibroblast and macrophage populations in disease alveolar ROIs at later time points (**Figure 5.10**).

Finally, we sought to characterize spatial transcriptomic profiling in subpleural fibrotic regions at later time points post SARS-CoV-2 MA10 infection. Unsupervised hierarchical clustering of alveolar ROIs (**Figure 5.5**), as well as PCA analysis (**Figure 5.4B**), demonstrated distinct transcriptomic profiling in diseased alveolar ROIs at 15 and 30 dpi. An enrichment in genes was identified that is reported to be associated with human IPF lung tissue[40], including *Col1a1*,

Fbn1, and *Fn1* (**Figure 5.9A-D, G**). Immunohistochemistry and RNA-ISH confirmed increased expression levels of Col1a1 protein and *Fn1* transcript in the subpleural pro-fibrotic alveolar regions at 15 and 30 dpi, respectively (**Figure 5.9E, F, H, and I**). These data suggest that common pathways are activated in response to virus-induced damage in mouse models of SARS-CoV-2 infection sequelae and human IPF. The underlying origin of human IPF remains to be determined, but alveolar epithelial cell injury is a likely trigger that releases TGF-β1, a central pro-fibrotic growth factor driving lung parenchymal fibrosis. GeoMx DSP data exhibited a trend of *Tgfb1* upregulation in alveolar disease ROIs at 15 and 30 dpi compared to healthy ROIs (**Figure 5.11**). Importantly, *Tgfb1* transcript was highly expressed in alveolar fibrotic regions in SARS-CoV-2 MA10-infected mice at 30 dpi with its expression being most enriched in the enhanced accumulation of CD8+ lymphocytes. This observation is consistent with previous reports that describe the relationship between TGF-β1 pathway-mediated exaggerated local accumulation of CD8+ tissue-resident memory T cells and pulmonary fibrosis in human IPF and mouse models of viral pneumonia sequelae[41,42], suggesting common pathways are activated to develop pulmonary fibrosis in human pulmonary interstitial diseases and our mouse models of SARS-CoV-2 infection sequelae.

5.2.6 Complement pathway is active in profibrotic pulmonary lesions

In addition to ISG and fibrosis-associated genes, DSP analysis revealed differential activation of several complement genes following SARS-CoV-2 MA10 infection. Complement has been shown to play a pathological role in the acute phase of SARS-CoV infection [43] and complement blockade antibody therapies have been beneficial in mouse models of MERS-CoV infection[44]. At 2 dpi, *C3*/*C4b*/*C1ra* expression levels were elevated and remained elevated through 30 dpi **(Figure 5.12A-C)**. *C3* expression was confirmed by RNA-ISH and remained elevated only in disorganized subpleural profibrotic regions at later time points **(Figure 5.12D)**. At 15 and 30 dpi, *C1q* subunit genes of the classical complement pathway were also highly elevated **(Figure**

5.12A-C). While circulating serum C1q is produced by Kupffer cells of the liver, locally produced C1q can be generated by several myeloid derived cell types, including macrophages and dendritic cells, as well as fibroblasts[45]. In addition to direct pathogen-targeting effects, C1q has been shown to induce anti-inflammatory cytokine production in M2 macrophages, promoting clearance of cellular debris and tissue repair. Together with previous reports, these findings demonstrate an acute activation of *C3* that may contribute to SARS-CoV-2 MA10 pathogenesis and later, *C1q* activation that may promote tissue repair.

5.3 Discussion

Acute viral infections are risk factors for the development of chronic inflammatory lung diseases like pulmonary fibrosis and asthma[46]. SARS-CoV-2 is the causative agent of COVID-19 and was first identified in late 2019 in Wuhan, China[1]. Since then, the virus has spread at an unprecedented speed and efficiency, causing high morbidity and mortality[3] as well as huge economic losses, globally. Due to social mitigation measures and the rapid development of prevention and intervention strategies, newly reported cases are decreasing in the US but most of the world population remains at extreme risk[47]. Another growing concern is the expanding number of reports from different countries on patients presenting long-term sequelae weeks to months after asymptomatic and symptomatic infections[8,16,48-52]. Typical symptoms include dyspnea, fatigue, chest tightness and interference with neurocognitive functions[8-10], now described as ‘post-acute sequelae of SARS-CoV-2 infection’ (PASC). Currently, there are no specific treatment options for PASC and due to the wide variety of manifestations, multidisciplinary collaborations are needed.

SARS-CoV-2 infection can cause ALI and ARDS in human. We have developed a mouse-adapted model of SARS-CoV-2 (SARS-CoV-2 MA10) that causes ALI and ARDS in aged BALB/c mice[23]. While SARS-CoV-2 MA10-induced ARDS-surviving mice were able to clear virus and

recover body weights and pulmonary function by 15 dpi, acute infection elicited an upregulation of a variety of profibrotic cytokines IL-1β, TNF-α, GM-CSF, IL-33, and IL-17A. Surviving animals developed persistent organizing pneumonia with early-stage pulmonary fibrotic features, characterized by abnormally repairing AT2 cells, lymphoid cell accumulation, and interstitial collagen deposition identified by Picrosirius red and α-SMA staining in subpleural regions (**Figure 5.1**). Importantly, these cellular and fibrotic features are also evident in late stage COVID-19 patients[53]. The severity of pulmonary fibrosis post SARS-CoV infection in human subjects correlates with duration and severity of the initial viral infection and patient age[54]. Similar associations between the severity of acute phase disease and organizing pneumonia/pulmonary fibrosis were observed in young versus old mice in our mouse-adapted SARS-CoV-2 model, suggesting that while all ages harbor some degree of risk, the aged are most vulnerable (**Figure 5.2).**

Our previous studies demonstrated that SARS-CoV-2 MA10 exhibits a tissue tropism for distal airway epithelia and alveoli in the lung. The loss of club cell (*Scgb1a1*) and AT2 cell (*Sftpc*) marker expression in each region, respectively, is consistent with a SARS-CoV-2 cellular tropism for club and AT2 cells in distal airway and alveoli, respectively. This prediction was directly confirmed by RNA-ISH on SARS-CoV-2 MA10-infected mice at 1 dpi, showing co-localization of SARS-CoV-2 RNA and *Scgb1a1* or *Sftpc* with preserved expression of ciliated (*Foxj1*) and AT1 (*Ager*) cell markers in the absence of SARS-CoV-2 RNA **(Figures 5.6, 5.7)**. After the significant loss of club and AT2 cell signature genes during the acute phase, their expression levels were completely restored by 15 dpi **(Figure 5.7)**. While SARS-CoV-2 MA10-infected distal airway epithelium, in general, appeared morphologically intact after 15 dpi, alveolar regions damaged by SARS-CoV-2 MA10 infection developed organizing pneumonia/fibrotic changes despite complete recovery of *Sftpc* expression, but not other AT1 markers after 15 dpi. The failure of alveolar regions to repair after viral infection may reflect either or both: 1) a failure to generate a pool of competent repairing cells; or 2) destruction of lung architecture. Since AT2 cells normally serve

as progenitor cells for AT1 cells in the alveolar epithelium, high intensity of SARS-CoV-2 MA10 infections that led to loss of a competent progenitor pool, i.e., AT2 cells, that limited the capacity to replenish AT2 cells and/or replenish a loss of AT1 cells.

The failure to repair alveolar structures has long-term consequences for lung structure/function. For example, if the failure of AT2 cells to replenish AT2/AT1 cells reflects more than a simple loss via cell death of AT2 cells, i.e., accumulation of defective (DATP/PATS) transitional cells, then persistent inflammation may result. This notion is buttressed by the observation that DATP/PATS cells were detected at d2 and persisted through d30 pi (**Figure 5.8**). There are likely interactions between DATP/PATS cells, macrophages, and lymphocytes that also perpetuate the pro-inflammatory, organizing pneumonia state. At later time points, while some lung tissue morphologically resembles healthy tissue, distal subpleural regions dominated by fibrotic markers, e.g., smooth muscle actin and collagen, emerged. These pro-fibrotic lesions transcriptionally exhibit adaptive immune, complement, hypoxia, fibrotic, and extracellular matrix pathways **(Figures 5.5, 5.9, 5.11, 5.12)**. It is likely that these regions reflect escape from the chronic pro-inflammatory state and heal into a fibrotic scar. The consequences of such a resolution are verse for reduction of inflammation but adverse for lung function.

A similar spectrum of pathologies has been observed in human autopsy studies and related to single cell responses by scRNAseq and spatial transcriptomics. In human single cell data, SARS-CoV-2-induced loss of AT2 cells is also associated with an overall reduction of AT2 and AT1 cell numbers and an accumulation of damage-associated transient progenitors (DATP) and pre-AT1 transitional state cells (PATS) cells. The inability of these DATP/PATS cells to properly differentiate into AT1 and AT2 cells in the more distal, subpleural lung may cause continued local hypoxia and decreased surfactant levels causing prolonged damage in these regions of the human lung. Importantly, the fibrotic pathways identified in mice are also upregulated in COVID-19 autopsy samples[18,33,37].

Human organizing pneumonias and interstitial fibrosis are multifactorial diseases influenced by age, genetic predisposition, and environmental components among others and can be triggered by factors such as viral infections[55]. Our model provides novel opportunities not only to study the molecular mechanisms and underlying pathways of COVID-19 long-term sequelae but also to study the influence of known fibrosis co-factors on progression and outcome after SARS-CoV-2 infection. While the focus in 2020 was heavily on the development of efficient and successful prevention and intervention strategies against the acute phase viral disease, there remains a need to find effective options for the prevention and treatment of long-term system-wide COVID-19 sequelae. The requirement in human clinical trials for observation intervals of ~1 year in length to assess therapeutic benefit of organizing pneumonia/anti-fibrotic agents emphasizes the utility of animal models to study the long-term pulmonary effects of COVID-19[22,56]. The murine model described in this study offers ideal conditions for investigation of such strategies with the benefit of an accelerated timeline including the possibility for longitudinal sampling of statistically significant amounts of individuals in controlled experimental settings.

We observed heterogeneous spatial and temporal histopathologic changes in diseased regions of tissue during acute and chronic phases of disease. The acute phase of infection was defined by robust but heterogeneous infection of bronchiolar club cells and AT2 cells throughout the lung. After viral clearance, some regions of the lung resolved to a normal lung architecture. Other regions evolved into a fibrosis-dominated phenotype. Finally, major areas of the lung exhibited a persistent organizing pneumonia phenotype characterized by distorted alveolar architecture, DATP alveolar cells with failed proliferative/hyperinflammatory features, lymphatic infiltration, and pro-fibrotic interstitial changes.

5.4 Material and Methods

5.4.1 Ethics and Biosafety

The generation and use of SARS-CoV-2 MA10 was approved for use under BSL3 conditions by the University of North Carolina at Chapel Hill Institutional Review Board (UNC-CH IBC) and by a Potential Pandemic Pathogen Care and Oversight committee at the National Institute of Allergy and Infectious Diseases (NIAID). All animal work was approved by Institutional Animal Care and Use Committee at University of North Carolina at Chapel Hill according to guidelines outlined by the Association for the Assessment and Accreditation of Laboratory Animal Care and the US Department of Agriculture. All work was performed with approved standard operating procedures and safety conditions for SARS-CoV-2. Our institutional BSL3 facilities have been designed to conform to the safety requirements recommended by Biosafety in Microbiological and Biomedical Laboratories (BMBL), the US Department of Health and Human Services, the Public Health Service, the Centers for Disease Control and Prevention (CDC), and the National Institutes of Health (NIH). Laboratory safety plans have been approved, and the facility has been approved for use by the UNC Department of Environmental Health and Safety (EHS) and the CDC.

5.4.2 Viruses and cells

SARS-CoV-2 MA10 was generated and cultured as previously described[23]. A large working stock of SARS-CoV-2 MA10 was generated by passaging the plaque purified clonal isolate sequentially on Vero E6 cells (passage 3, SARS-CoV-2 P3). SARS-CoV-2 MA10 P3 was used for all *in vivo* experiments.

Vero E6 cells were cultured in Dulbecco's modified Eagle's medium (DMEM, Gibco) with the addition of 5% Fetal Clone II serum (Hyclone) and 1X antibiotic/antimycotic (Gibco). Working stock titers were determined via plaque assay by adding serially diluted virus to Vero E6 cell

monolayers. After incubation, monolayers were overlayed with media containing 0.8% agarose. After 72 hours, Neutral Red dye was used to visualize plaques.

5.4.3 In vivo infection

All BALB/c mice used in this study were purchased from Envigo (BALB/cAnNHsd; strain 047) and housed at the University of North Carolina at Chapel Hill throughout the experiment. For intranasal infection, mice were anesthetized using a mixture of ketamine and xylazine. 10^4 plaque forming units (PFU) or 10^3 PFU of SARS-CoV-2 MA10 diluted in PBS were used for inoculation of young (10 week) and old (12 months) BALB/c mice. Weight loss and morbidity were monitored daily as clinical signs of disease whereas lung function was assessed at indicated timepoints using whole body plethysmography (WBP; DSI Buxco respiratory solutions, DSI Inc.). Lung function data was acquired as previously described by allowing mice to acclimate in WBP chambers for 30 min and a data acquisition time of 5 min[57]. Data was analyzed using FinePointe software.

At indicated harvest timepoints, randomly assigned animals were euthanized by an overdose of isoflurane and samples for analyses of titer (caudal right lung lobe) and histopathology (left lung lobe) were collected. Animals recorded as “dead” on non-harvest days were either found dead in cage or were approaching 70% of their starting body weight which resembles the criteria for humane euthanasia defined by respective animal protocols.

Viral load in lungs were determined by plaque assay for which caudal right lung lobes were homogenized in 1mL of PBS and glass beads, monolayers of Vero E6 cells inoculated, and 72 hours after incubation stained with Neutral Red dye for visualization of plaques. For histopathological analyses left lung lobes were stored in 10% phosphate buffered formalin for at least 7 days before transferring out of the BSL3 for further processing.

5.4.4 Chemokine & Cytokine analysis

Chemokine and cytokine profiles of serum and lung samples were assessed using Immune Monitoring 48-plex mouse ProcartaPlex™ Panel kits. Briefly, 50μL of either a 1:4 dilution of serum or 50μL undiluted clarified lung homogenate were incubated with magnetic capture beads following manufacturers protocol. After washing, 96-well plates containing samples and magnetic beads were incubated with detection antibodies and SA-PE. Results were obtained using a MAGPIX machine (Luminex) and quantification was achieved by comparing to a standard curve in xPONENT software.

5.4.5 RNA *in situ* hybridization and quantification

RNA-ISH was performed on paraffin-embedded 5 μm tissue sections using the RNAscope Multiplex Fluorescent Assay v2 or RNAscope 2.5 HD Reagent Kit according to the manufacturer's instructions (Advanced Cell Diagnostics). Briefly, tissue sections were deparaffinized with xylene and 100% ethanol twice for 5 min and 1 min, respectively, incubated with hydrogen peroxide for 10 min and in boiling water for 15 min, and then incubated with Protease Plus (Advanced Cell Diagnostics) for 15 min at 40°C. Slides were hybridized with custom probes at 40°C for 2 h, and signals were amplified according to the manufacturer's instructions. Stained sections were scanned and digitized by using an Olympus VS200 fluorescent microscope. Images were imported into Visiopharm Software® (version 2020.09.0.8195) for quantification. Lung tissue and probe signals for targeted genes were quantified using a customized analysis protocol package to 1) detect lung tissue using a decision forest classifier, 2) detect the probe signal based on the intensity of the signal in the channel corresponding to the relevant probe. All slides were analysed under the same conditions. Results were expressed as the area of the probe relative to total lung tissue area.

5.4.6 Immunohistochemistry

Chromogenic Immunohistochemistry (IHC) was performed on paraffin-embedded lung tissues that were sectioned at 5 microns. This IHC was carried out using the Leica Bond III Autostainer system. Slides were dewaxed in Bond Dewax solution and hydrated in Bond Wash solution. Heat induced antigen retrieval was performed for 20 min at 100ºC in Bond-Epitope Retrieval solution 2, pH-9.0. After pretreatment, slides were incubated with primary antibody **(Table 5.1)** for 1h followed with Novolink Polymer secondary antibody. Antibody detection with 3,3'-diaminobenzidine (DAB) was performed using the Bond Intense R detection system. Stained slides were dehydrated and coverslipped with Cytoseal 60. A control slide containing positive and negative control tissues were included for this run.

Slides were imaged with An Olympus VS200 whole slide scanner microscope or Keyence BZ-X800 microscope was used for scanning and digitalization of whole slides. Photomicrographs were captured on an Olympus BX43 light microscope at indicated magnification with a DP27 camera using cellSens Entry software.

5.4.7 GeoMx Digital Spatial Profiling

5 µm-thick FFPE sections were prepared using the RNAscope & DSP combined slide prep protocol from Nanostring Technologies. Prior to imaging, tissue morphology was visualized by IHC for CD45 and RNAscope for SARS-CoV-2 RNA. DNA was visualized with 500nM. Mouse Whole Transcriptome Atlas probes targeting over 19,000 targets were hybridized, and slides were washed twice in fresh 2X SSC then loaded on the GeoMx™ Digital Spatial Profiler (DSP) [58]. In brief, entire slides were imaged at 20x magnification and 6-10 regions of interest (ROI) were selected per sample. ROIs were chosen based serial hematoxylin and eosin stained sections and morphology markers (DNA/CD45 IHC/SARS-CoV-2 RNA) by a veterinary pathologist (S.A.M.). The GeoMx then exposed ROIs to 385 nm light (UV) releasing the indexing oligos and collecting them with a microcapillary. Indexing oligos were then deposited in a 96-well plate for subsequent

processing. The indexing oligos were dried down overnight and resuspended in 10 µL of DEPC-treated water.

Sequencing libraries were generated by PCR from the photo-released indexing oligos and ROI-specific Illumina adapter sequences and unique i5 and i7 sample indices were added. Each PCR reaction used 4 µL of indexing oligos, 1 µL of indexing PCR primers, 2 µL of Nanostring 5X PCR Master Mix, and 3 µL PCR-grade water. Thermocycling conditions were 37°C for 30 min, 50°C for 10 min, 95°C for 3 min; 18 cycles of 95°C for 15sec, 65°C for 1min, 68°C for 30 sec; and 68°C 5 min. PCR reactions were pooled and purified twice using AMPure XP beads (Beckman Coulter, A63881) according to manufacturer's protocol. Pooled libraries were sequenced at 2×75 base pairs and with the single-index workflow on an Illumina NovaSeq.

5.4.8 Analysis of GeoMx transcriptomic data

Raw count and 3rd quantile (Q3) normalized count data of target genes from ROIs were provided by the vendor, which were used as input to downstream analyses. Q3 normalized data were used for principal component analysis (PCA) using the R package and visualized using factoextra package. Raw count data were used for differential expression analysis using the Bioconductor R package, variancePartition[59], with transformation of raw counts by voom method[60]. The dream function from variancePartition allows fitting of mixed-effect models to account for ROIs obtained from the same animal, and assay slides as random-effect factors. Cell type decomposition from raw count data were performed using the R package, BisqueRNA[61], and the mouse lung reference single-cell data set[62]. Pre-ranked gene set enrichment analysis (GSEA) was performed using the Bioconductor R package, fgsea[63], with gene set collections obtained from Gene Ontology Biological Process[64], and Reactome pathways[65]. Various plots and hierarchical clustering heatmaps were generated using the R package, ggplot2[66] and ComplexHeatmap[67].

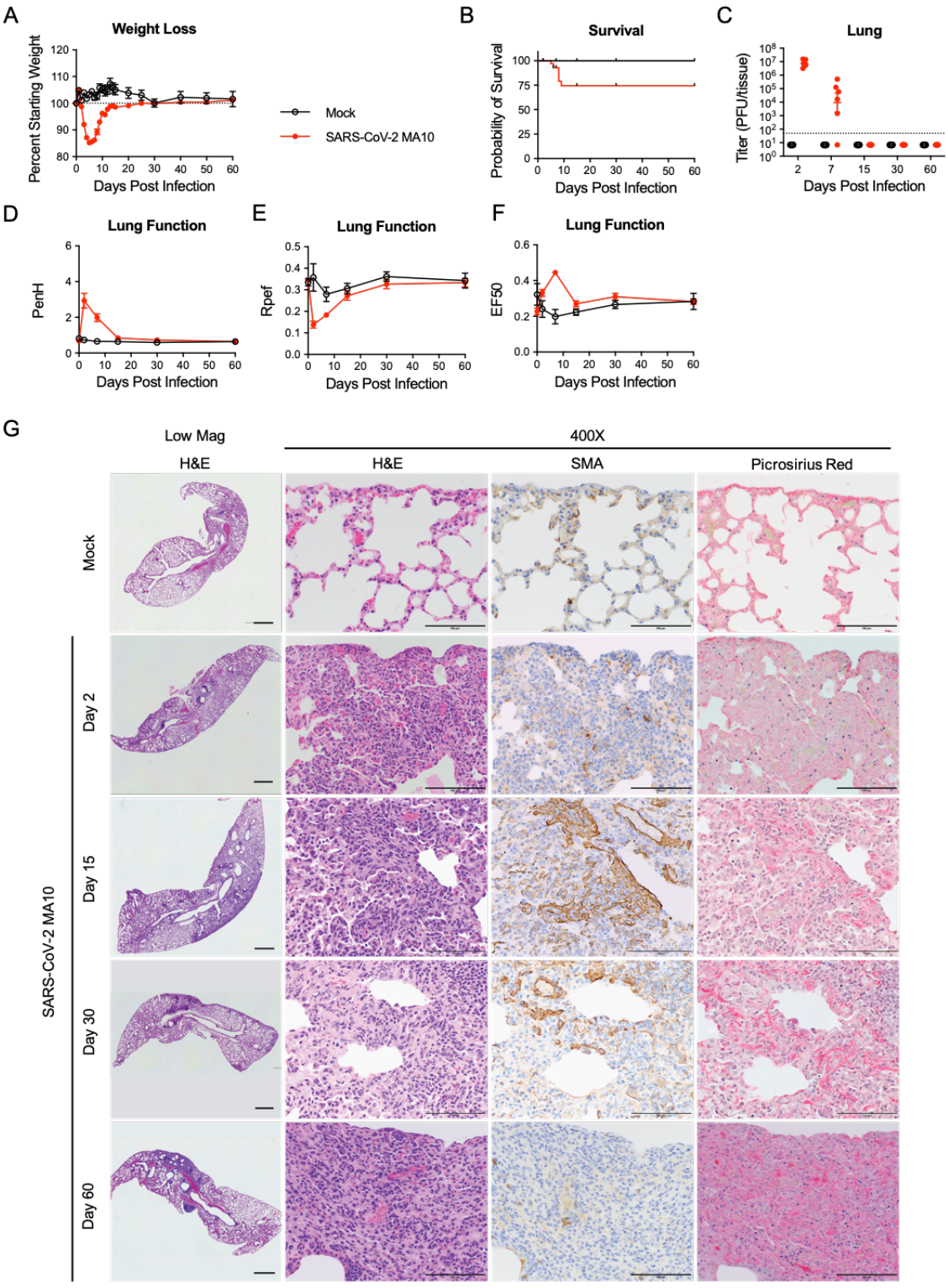

Figure 5.1. SARS-CoV-2 MA10 infection causes lung damage in aged surviving mice.

1-year-old female BALB/c mice were infected with 10^3 PFU SARS-CoV-2 MA10 or PBS and monitored for (A) percent starting weight and (B) survival. Infectious virus lung titers were assayed at indicated time points. Dotted line represents limit of detection. Undetected samples are plotted

at half the limit of detection. (D-F) Lung function was assessed by whole body plethysmography for (D) PenH, (E) Rpef, and (F) EF50. (G) Histopathological analysis of lungs at indicated time points. H&E: hematoxylin and eosin. SMA: immunohistochemistry for smooth muscle actin. Picrosirius Red directly stains collagen fibers. Image scale bars represents 1000 μm for low magnification and 100 μm for 200X images.

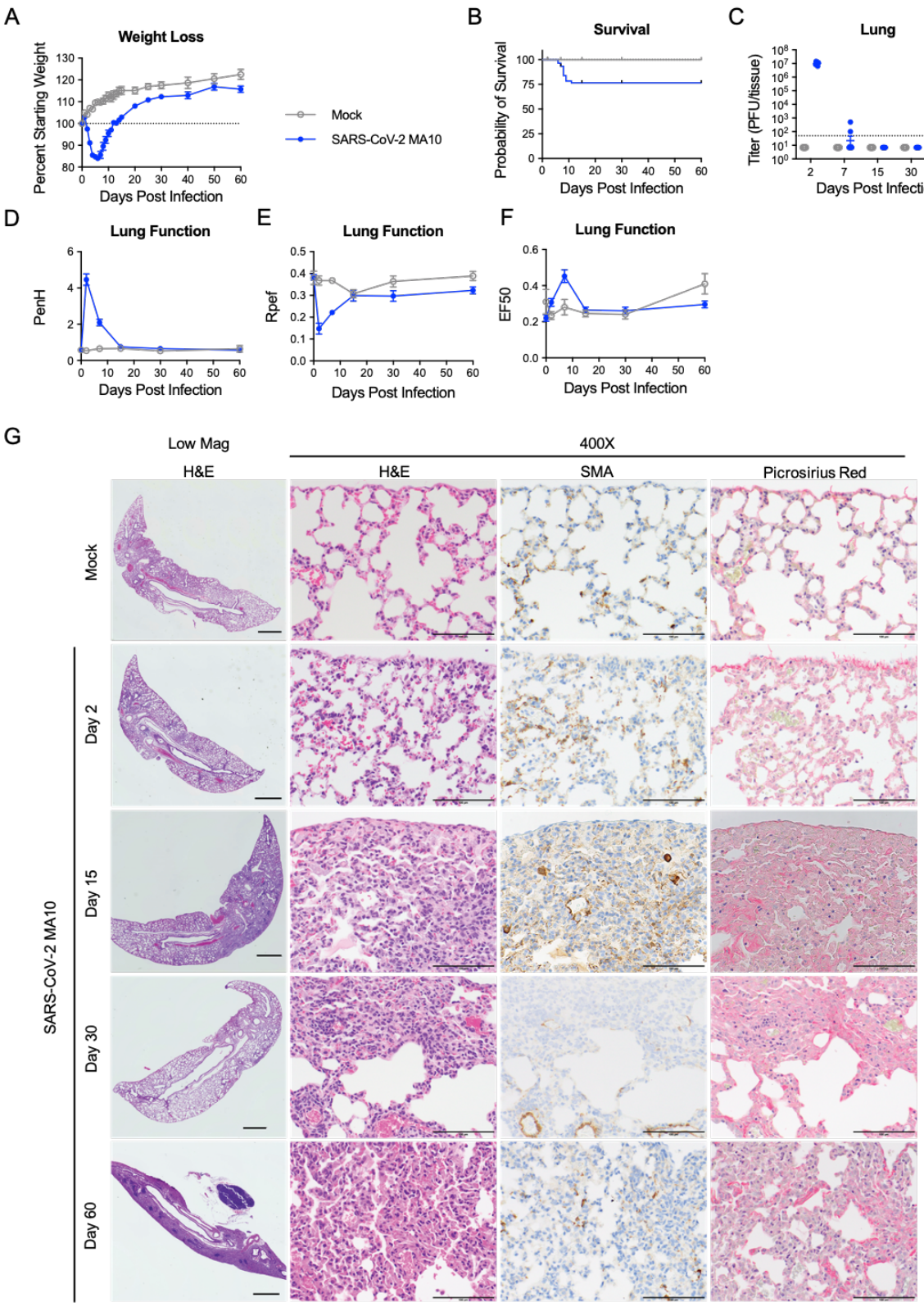

Figure 5.2. SARS-CoV-2 MA10 infection causes lung damage in young surviving mice.

1-year-old female BALB/c mice were infected with 10^3 PFU SARS-CoV-2 MA10 or PBS and monitored for (A) percent starting weight and (B) survival. Infectious virus lung titers were assayed

at indicated time points. Dotted line represents limit of detection. Undetected samples are plotted at half the limit of detection. (D-F) Lung function was assessed by whole body plethysmography for (D) PenH, (E) Rpef, and (F) EF50. (G) Histopathological analysis of lungs at indicated time points. H&E: hematoxylin and eosin. SMA: immunohistochemistry for smooth muscle actin. Picrosirius Red directly stains collagen fibers. Image scale bars represents 1000 μm for low magnification and 100 μm for 200X images.

A

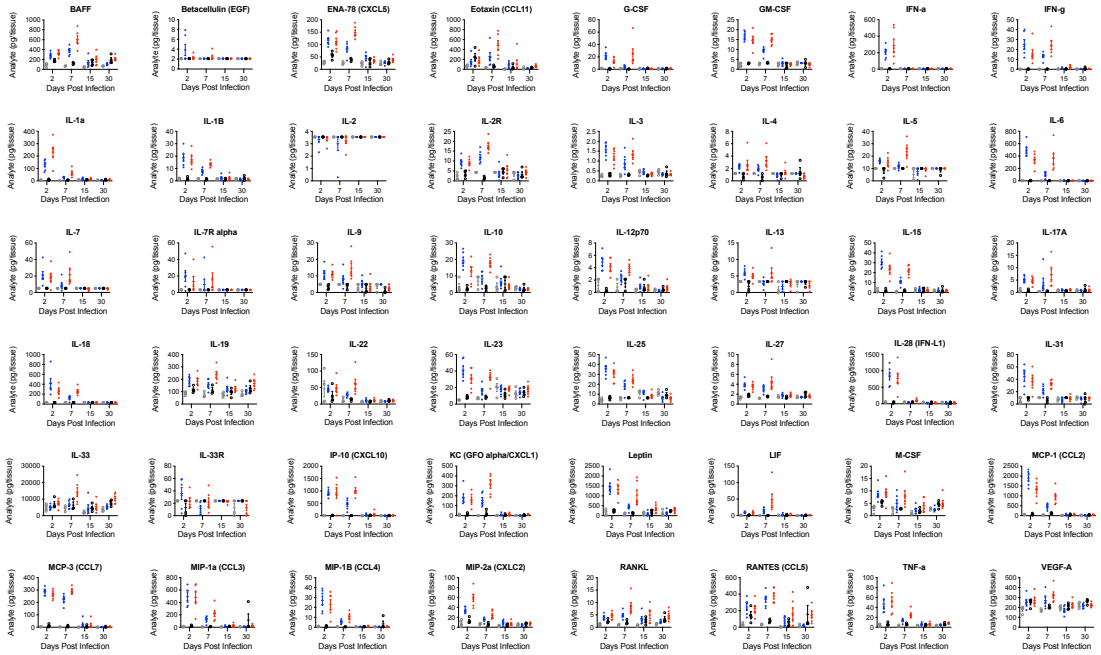

B

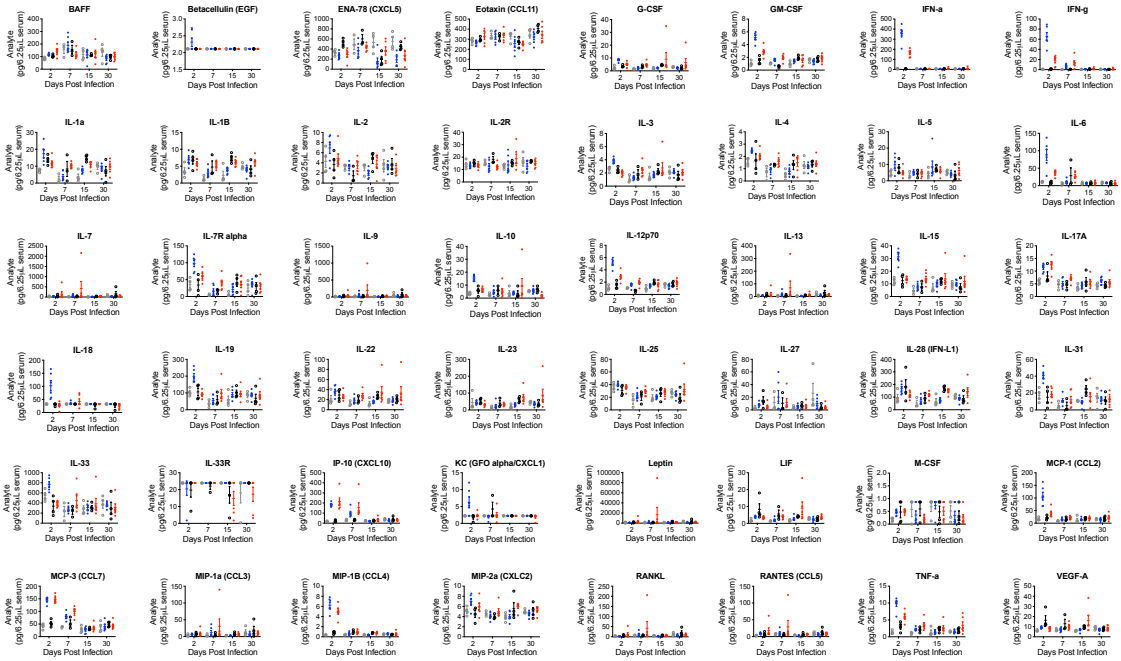

Figure 5.3 SARS-CoV-2 MA10 induces local and systemic cytokine and chemokine responses.

Cytokine and chemokine analysis of mock or SARS-CoV-2 MA10 infected 1-year-old BALB/c (A) and 10-week-old (B) mice from Figures 1 and S1. Serum and lung homogenate were assayed for 48 cytokines and chemokines at indicated time points.

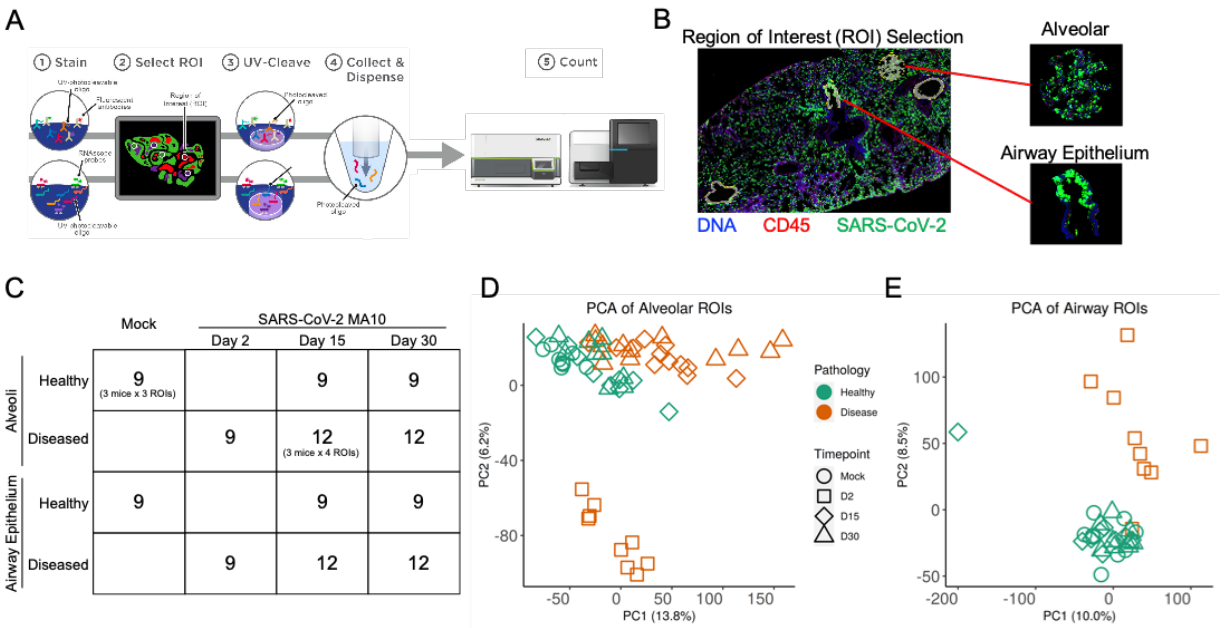

Figure 5.4. Transcriptional digital spatial profiling reveals unique signatures in diseased tissue compartments.

(A) Overview of NanoString Technologies' GeoMx digital spatial profiling platform. (B) Example of region of interest (ROI) selection from a day 2 post SARS-CoV-2 MA10 lung. ROIs were selected from alveolar and epithelial compartments, based on presence of infected cells as indicated by positive SARS-CoV-2 RNA staining, $CD45^{+}$ immune cells, and tissue morphology on serial H&E sections. Tissue was determined to be healthy or diseased based on serial H&E sections. (C) A table summarizing numbers of ROI from each tissue compartment, disease state, and time point. Each time point includes 3 independent mouse samples. (D-E) Principal component analysis (PCA) plot of alveolar (D) and epithelial (E) ROIs.

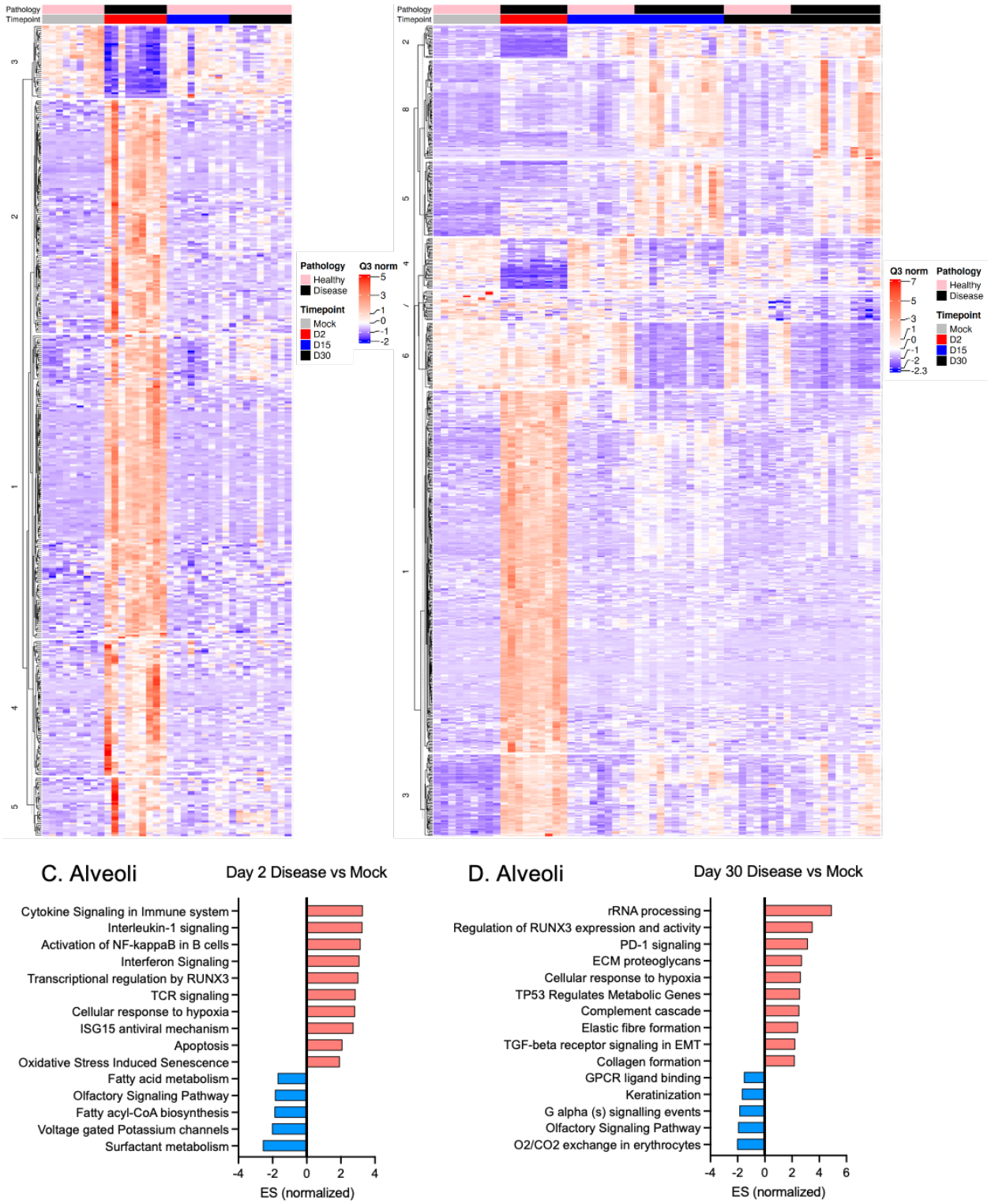

Figure 5.5. DSP reveals distinct transcriptional pathway changes during acute and late stages of SARS-CoV-2 disease.

(A-B) Heatmaps of DEGs in epithelial ROIs across all time points in (A) epithelial and (B) alveolar tissue compartments. (C-D) Pathway enrichment analysis of most up- and down-regulated genes in diseased alveolar ROIs at (C) day 2 and (D) 30 post SARS-CoV-2 MA10 infection.

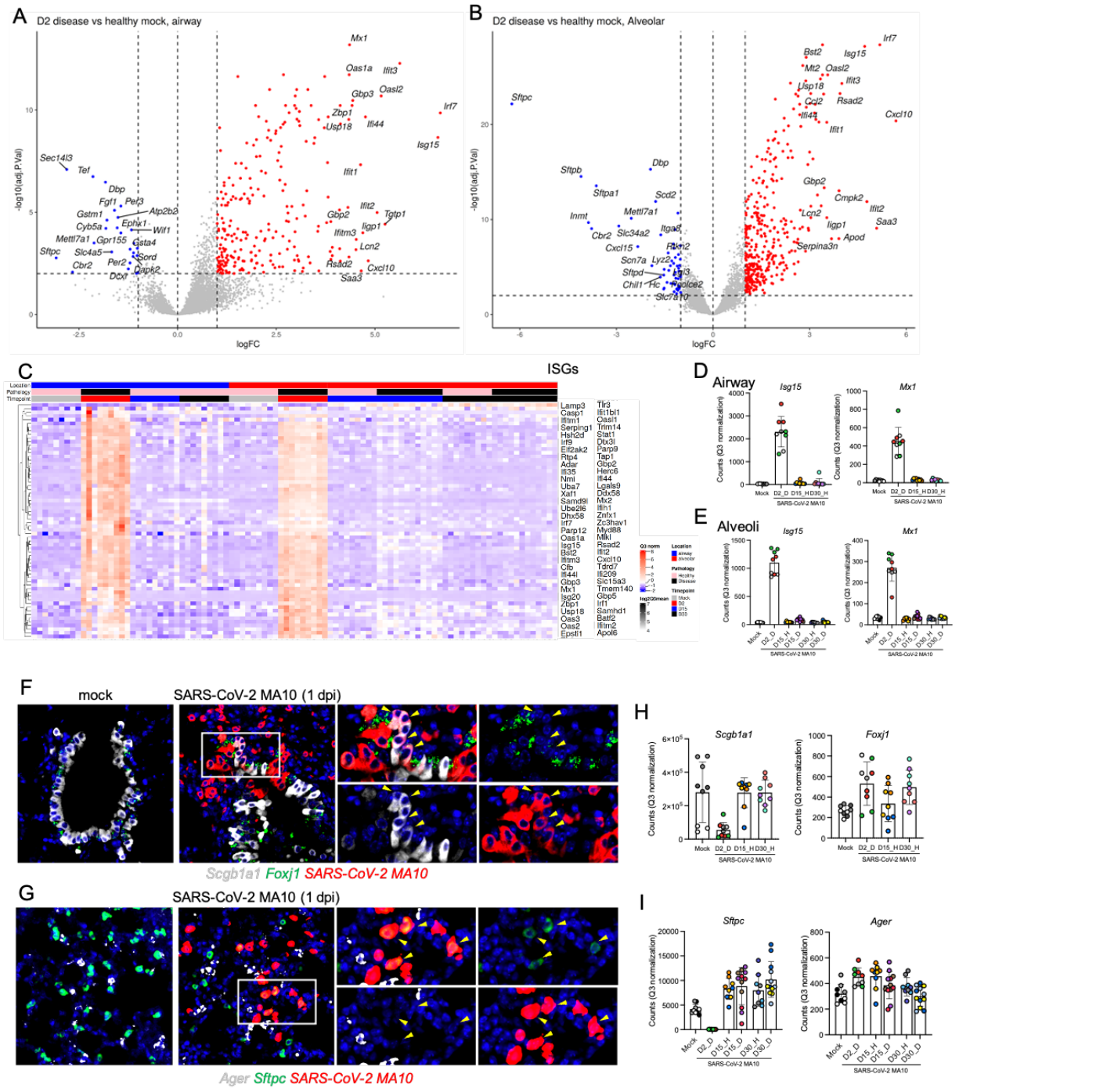

Figure 5.6. DPS reveals antiviral transcriptional changes and loss of lung cell type identity early during SARS-CoV-2 infection.

(A-B) Volcano plot of differentially expressed genes (DEGs) in SARS-CoV-2 MA10 infection healthy (A) epithelial and (B) alveolar ROIs compared to mock infected mice at day 2 post infection. Red and Blue dots represent statistically significantly differentially expressed genes with a fold change of greater than 2-fold compared to mock ROIs. (C) Heatmap of select interferon stimulated genes (ISGs) in alveolar and epithelial ROIs at day 2 post infection. (D-E) Select ISG counts from Q3 normalized DSP data in (D) epithelial and (E) alveolar ROIs. (F-G) RNA *in situ*

hybridization for markers of (F) epithelial and (G) alveolar cell populations. (H-I) Select cell type marker counts from Q3 normalized DSP data in (D) epithelial and (E) alveolar ROIs.

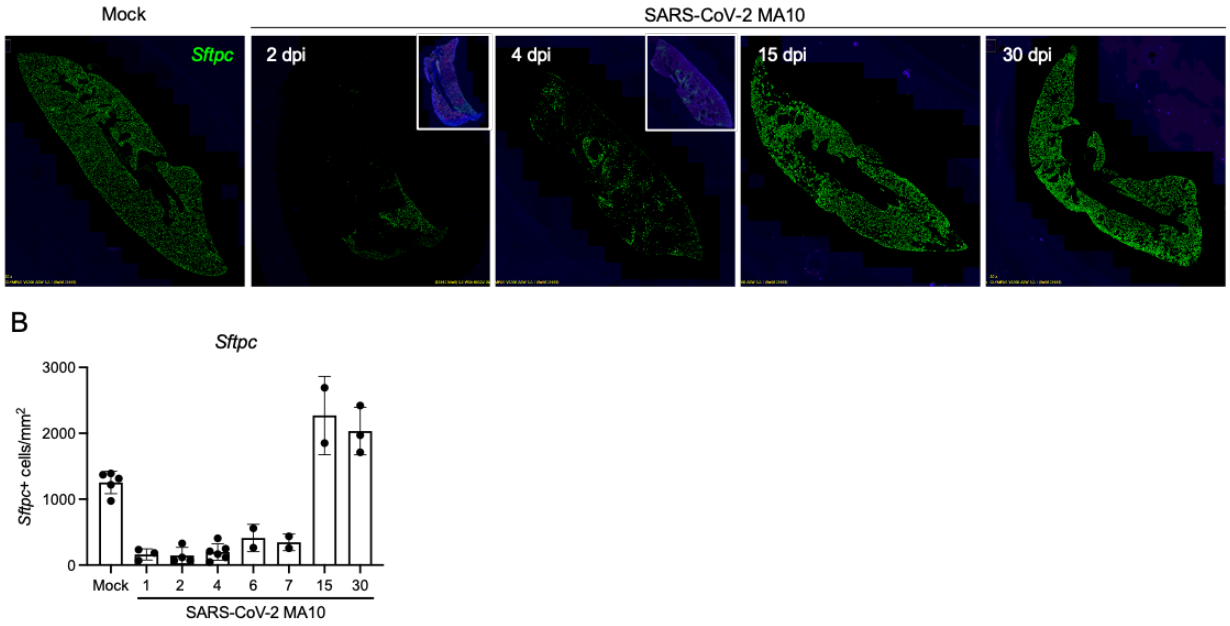

Figure 5.7. SARS-CoV-2 MA10 induces transient loss of ATII cells.

(A) RNA *in situ* hybridization for *Sftpc* at indicated timepoints. (B) RNA ISH quantification of *Sftpc*$^{+}$ cells.

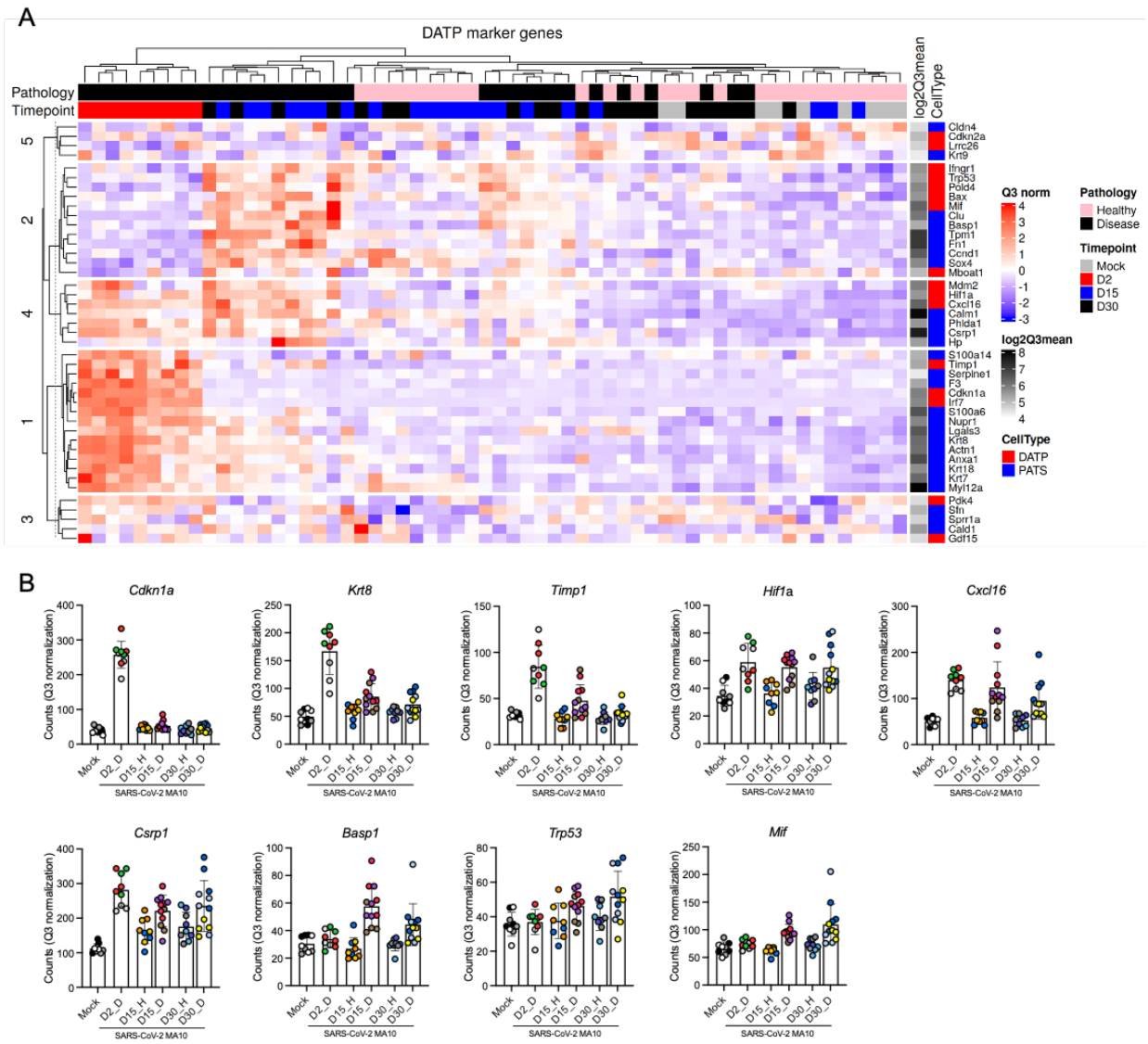

Figure 5.8. DATP/PATS cell genes are upregulated following SARS-CoV-2 MA10 infection.

(A) Heatmap of DATP and PATS associated genes from human idiopathic pulmonary fibrosis and COVID-19 patients in alveolar ROIs. (B) Select DATP/PATS marker counts from Q3 normalized DSP data. (C) RNA ISH and quantification (D) for *Cdkn1a* at indicated time points.

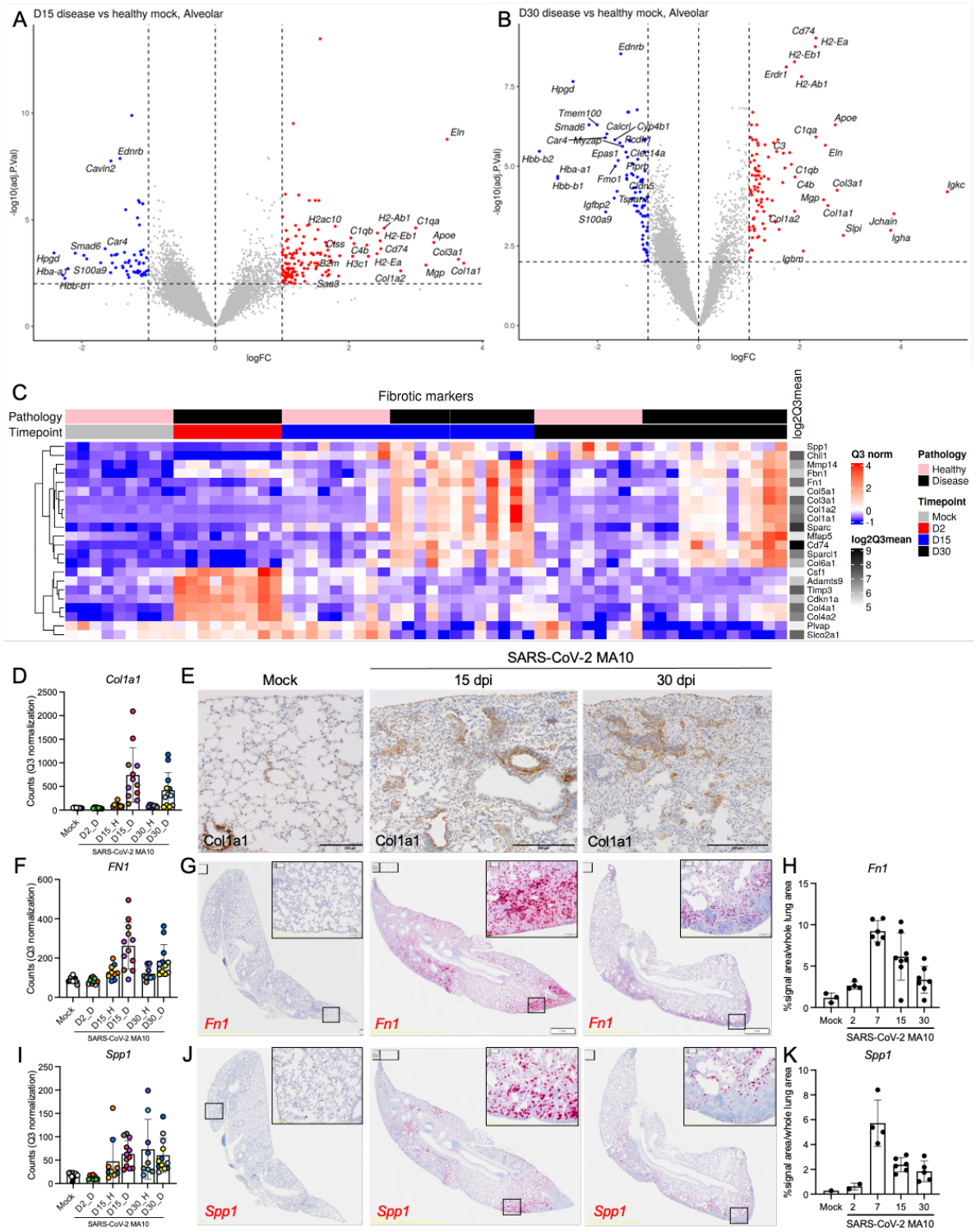

Figure 5.9. SARS-CoV-2 MA10 infection induces profibrotic gene expression at late time points.

(A-B) Volcano plots of DEGs in diseased alveolar ROIs at (A) day 15 and (B) 30 post SARS-CoV-2 MA10 infection compared to mock. Most differentially regulated genes labeled. (C) Heatmap of select fibrosis related genes from human idiopathic pulmonary fibrosis. (D) Q3 normalized DSP

counts for *Col1a1*. (E) IHC for COL1A1. (F) Quantification of COL1A1 IHC. (F) Q3 normalized DSP counts for *Col1a1*. (H) RNA ISH for *Fn1*. (I) Quantification of *Fn1* RNA ISH. (J) Q3 normalized DSP counts for *Spp1*. (K) RNA ISH for *Spp1*. (L) Quantification of *Spp1* RNA ISH.

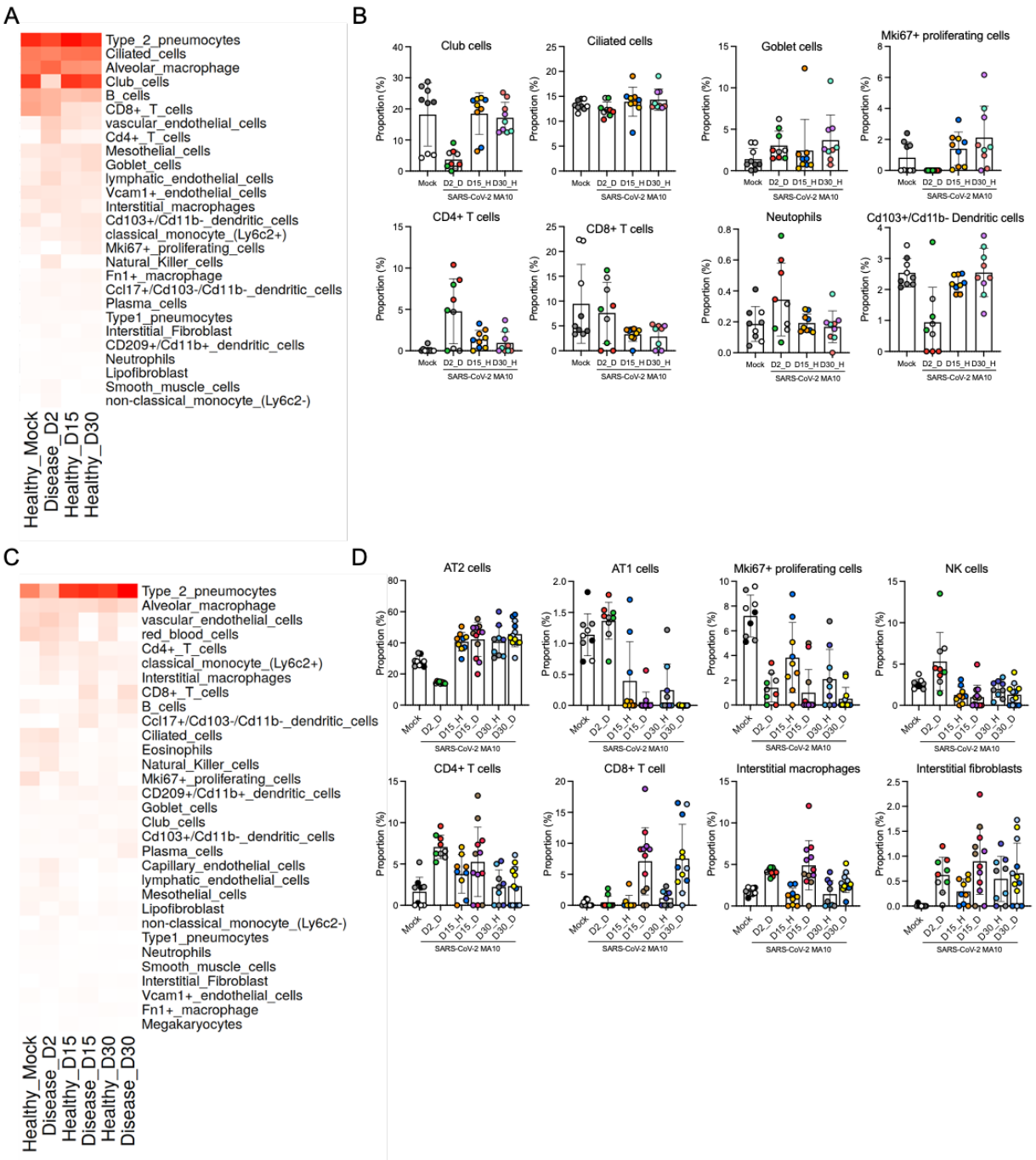

Figure 5.10. Cell type deconvolution of DSP data reveals cell type frequency changes following SARS-CoV-2 MA10 infection.

(A) Heatmap of cell type proportions in epithelial ROIs based on deconvolution of DSP data. (B) Proportions of individual cell types in epithelial ROIs. (C) Heatmap of cell type proportions in alveolar ROIs based on deconvolution of DSP data. (D) Proportions of individual cell types in alveolar ROIs.

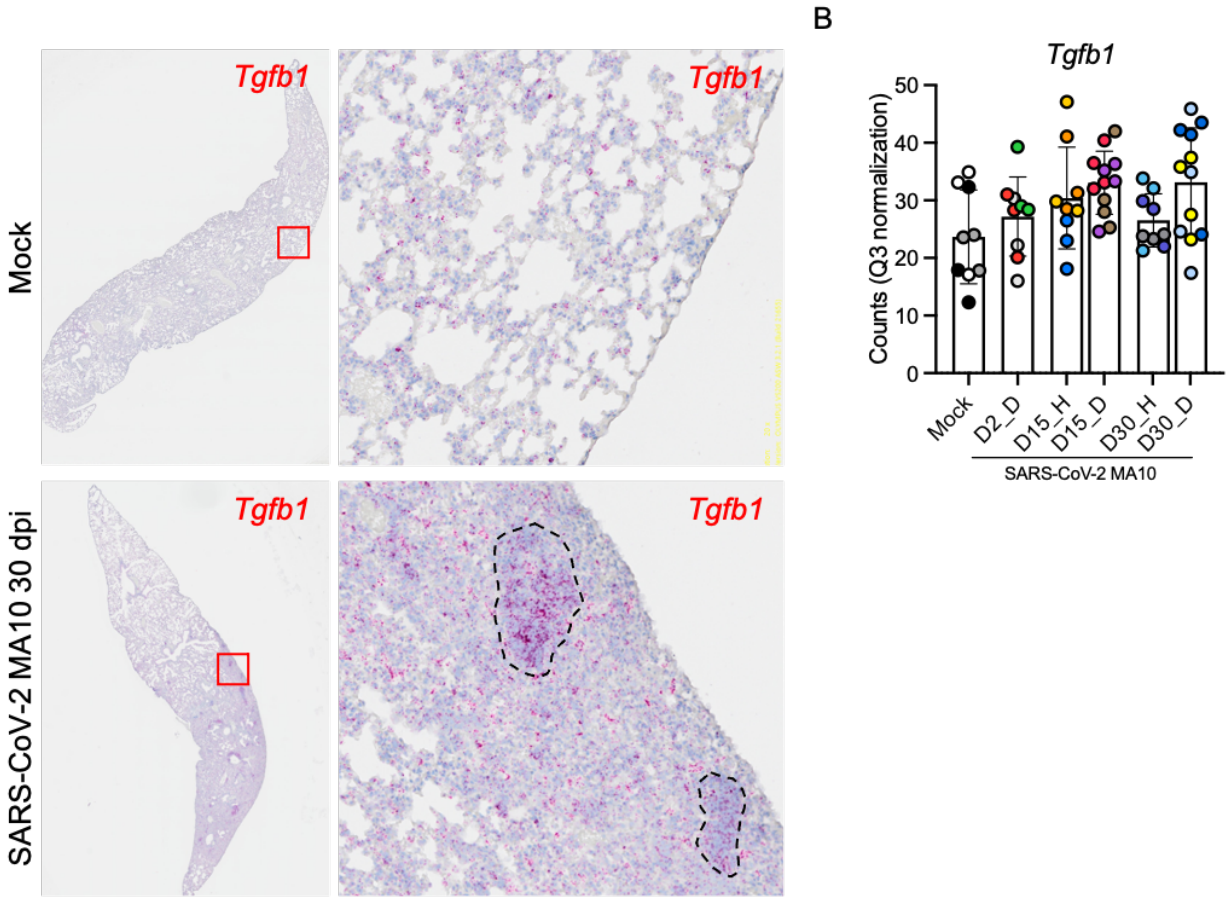

Figure 5.11. TGF-β1 is upregulated in tertiary lymphoid structures in diseased lung tissue.

(A) RNA ISH and (B) quantification of *TGF-β1* expression at indicated timepoints.

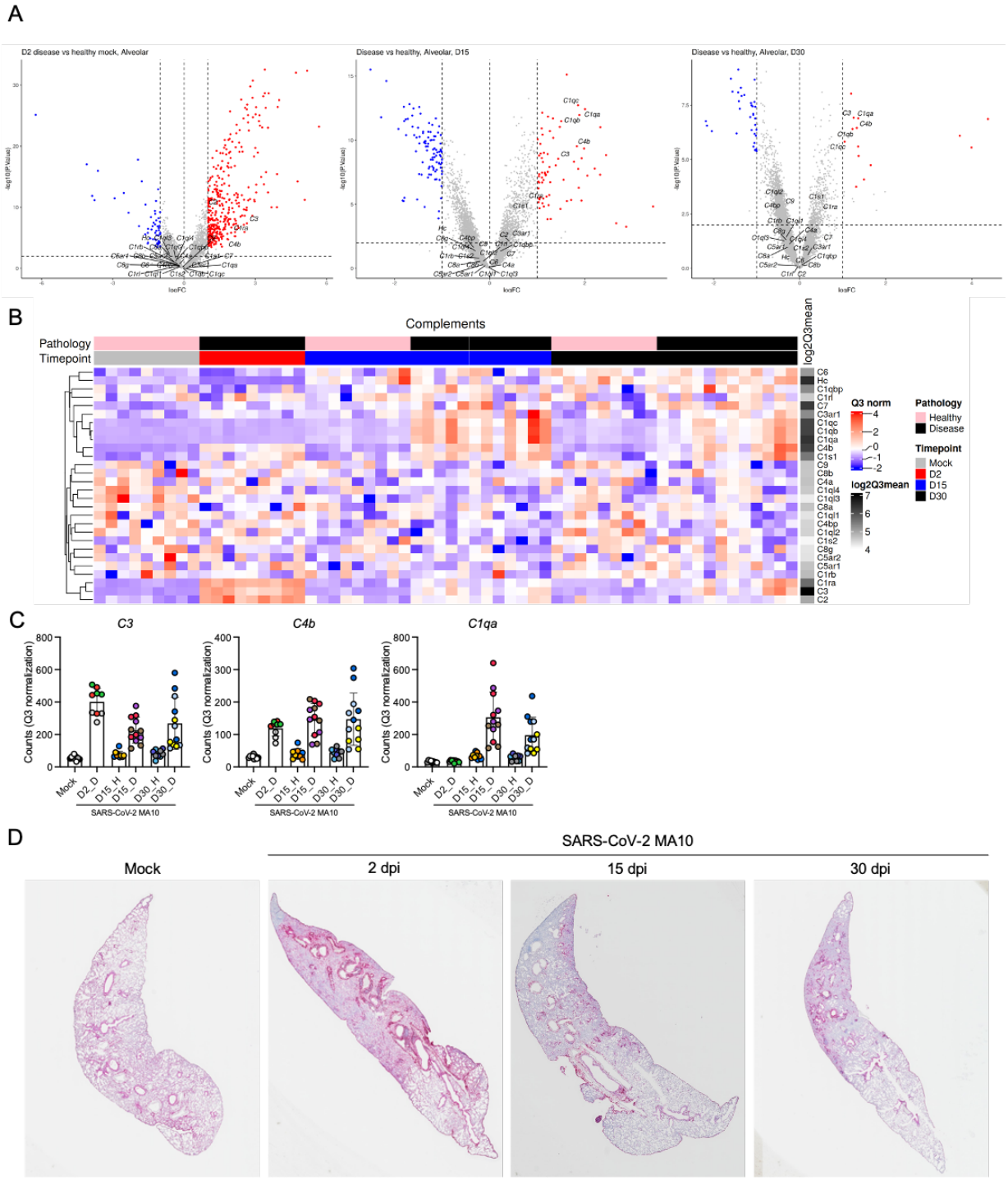

Figure 5.12. Complement cascade is activated during both acute and chronic SARS-CoV-2 MA10 disease.

(A-C) Volcano plots of DEGs in diseased alveolar ROIs at (A) day 2, (B) 15, and (C) 30 post SARS-CoV-2 MA10 infection compared to mock. Complement pathway genes labeled. (D) Heatmap of complement pathway genes. (E) Q3 normalized DSP counts for select complement genes. (F) RNA ISH for *C3* at indicated time points. (G) IHC for C3 deposition at indicated time points.

REFERENCES

1 Zhou, P. *et al.* A pneumonia outbreak associated with a new coronavirus of probable bat origin. *Nature* **579**, 270-273, doi:10.1038/s41586-020-2012-7 (2020).

2 Whitworth, J. COVID-19: a fast evolving pandemic. *Trans R Soc Trop Med Hyg* **114**, 241-248, doi:10.1093/trstmh/traa025 (2020).

3 Dong, E., Du, H. & Gardner, L. An interactive web-based dashboard to track COVID-19 in real time. *Lancet Infect Dis* **20**, 533-534, doi:10.1016/S1473-3099(20)30120-1 (2020).

4 Ahmed, H. *et al.* Long-term clinical outcomes in survivors of severe acute respiratory syndrome and Middle East respiratory syndrome coronavirus outbreaks after hospitalisation or ICU admission: A systematic review and meta-analysis. *J Rehabil Med* **52**, jrm00063, doi:10.2340/16501977-2694 (2020).

5 Hui, D. S. *et al.* Impact of severe acute respiratory syndrome (SARS) on pulmonary function, functional capacity and quality of life in a cohort of survivors. *Thorax* **60**, 401-409, doi:10.1136/thx.2004.030205 (2005).

6 Lam, M. H. *et al.* Mental morbidities and chronic fatigue in severe acute respiratory syndrome survivors: long-term follow-up. *Arch Intern Med* **169**, 2142-2147, doi:10.1001/archinternmed.2009.384 (2009).

7 Bari, E. *et al.* Mesenchymal Stromal Cell Secretome for Post-COVID-19 Pulmonary Fibrosis: A New Therapy to Treat the Long-Term Lung Sequelae? *Cells* **10**, doi:10.3390/cells10051203 (2021).

8 Carfi, A., Bernabei, R., Landi, F. & Gemelli Against, C.-P.-A. C. S. G. Persistent Symptoms in Patients After Acute COVID-19. *JAMA* **324**, 603-605, doi:10.1001/jama.2020.12603 (2020).

9 Tenforde, M. W. *et al.* Symptom Duration and Risk Factors for Delayed Return to Usual Health Among Outpatients with COVID-19 in a Multistate Health Care Systems Network - United States, March-June 2020. *MMWR Morb Mortal Wkly Rep* **69**, 993-998, doi:10.15585/mmwr.mm6930e1 (2020).

10 Huang, C. *et al.* 6-month consequences of COVID-19 in patients discharged from hospital: a cohort study. *Lancet* **397**, 220-232, doi:10.1016/S0140-6736(20)32656-8 (2021).

11 Nalbandian, A. *et al.* Post-acute COVID-19 syndrome. *Nature Medicine* **27**, 601-615, doi:10.1038/s41591-021-01283-z (2021).

12 Rouse, B. T. & Sehrawat, S. Immunity and immunopathology to viruses: what decides the outcome? *Nature Reviews Immunology* **10**, 514-526, doi:10.1038/nri2802 (2010).

13 Hilleman, M. R. Strategies and mechanisms for host and pathogen survival in acute and persistent viral infections. *Proceedings of the National Academy of Sciences* **101**, 14560-14566, doi:10.1073/pnas.0404758101 (2004).

14 Carsana, L. *et al.* Pulmonary post-mortem findings in a series of COVID-19 cases from northern Italy: a two-centre descriptive study. *Lancet Infect Dis* **20**, 1135-1140, doi:10.1016/S1473-3099(20)30434-5 (2020).

15 Nienhold, R. *et al.* Two distinct immunopathological profiles in autopsy lungs of COVID-19. *Nat Commun* **11**, 5086, doi:10.1038/s41467-020-18854-2 (2020).

16 Jacobs, L. G. *et al.* Persistence of symptoms and quality of life at 35 days after hospitalization for COVID-19 infection. *PLoS One* **15**, e0243882, doi:10.1371/journal.pone.0243882 (2020).

17 Tian, S. *et al.* Pathological study of the 2019 novel coronavirus disease (COVID-19) through postmortem core biopsies. *Mod Pathol* **33**, 1007-1014, doi:10.1038/s41379-020-0536-x (2020).

18 Rendeiro, A. F. *et al.* The spatial landscape of lung pathology during COVID-19 progression. *Nature* **593**, 564-569, doi:10.1038/s41586-021-03475-6 (2021).

19 Ye, Z., Zhang, Y., Wang, Y., Huang, Z. & Song, B. Chest CT manifestations of new coronavirus disease 2019 (COVID-19): a pictorial review. *European Radiology* **30**, 4381-4389, doi:10.1007/s00330-020-06801-0 (2020).

20 Tale, S. *et al.* Post-COVID-19 pneumonia pulmonary fibrosis. *QJM: An International Journal of Medicine* **113**, 837-838, doi:10.1093/qjmed/hcaa255 (2020).

21 Spagnolo, P. *et al.* Pulmonary fibrosis secondary to COVID-19: a call to arms? *The Lancet Respiratory Medicine* **8**, 750-752, doi:10.1016/s2213-2600(20)30222-8 (2020).

22 George, P. M., Wells, A. U. & Jenkins, R. G. Pulmonary fibrosis and COVID-19: the potential role for antifibrotic therapy. *Lancet Respir Med* **8**, 807-815, doi:10.1016/S2213-2600(20)30225-3 (2020).

23 Leist, S. R. *et al.* A Mouse-Adapted SARS-CoV-2 Induces Acute Lung Injury and Mortality in Standard Laboratory Mice. *Cell* **183**, 1070-1085 e1012, doi:10.1016/j.cell.2020.09.050 (2020).

24 Barkauskas, C. E. *et al.* Type 2 alveolar cells are stem cells in adult lung. *Journal of Clinical Investigation* **123**, 3025-3036, doi:10.1172/jci68782 (2013).

25 Evans, M. J., Cabral, L. J., Stephens, R. J. & Freeman, G. Transformation of alveolar Type 2 cells to Type 1 cells following exposure to NO2. *Experimental and Molecular Pathology* **22**, 142-150, doi:10.1016/0014-4800(75)90059-3 (1975).

26 Zacharias, W. J. *et al.* Regeneration of the lung alveolus by an evolutionarily conserved epithelial progenitor. *Nature* **555**, 251-255, doi:10.1038/nature25786 (2018).

27 Nabhan, A. N., Brownfield, D. G., Harbury, P. B., Krasnow, M. A. & Desai, T. J. Single-cell Wnt signaling niches maintain stemness of alveolar type 2 cells. *Science* **359**, 1118-1123, doi:10.1126/science.aam6603 (2018).

28 Kathiriya, J. J., Brumwell, A. N., Jackson, J. R., Tang, X. & Chapman, H. A. Distinct Airway Epithelial Stem Cells Hide among Club Cells but Mobilize to Promote Alveolar Regeneration. *Cell Stem Cell* **26**, 346-358.e344, doi:10.1016/j.stem.2019.12.014 (2020).

29 Chen, H. *et al.* Airway Epithelial Progenitors Are Region Specific and Show Differential Responses to Bleomycin-Induced Lung Injury. *STEM CELLS* **30**, 1948-1960, doi:10.1002/stem.1150 (2012).

30 Vaughan, A. E. *et al.* Lineage-negative progenitors mobilize to regenerate lung epithelium after major injury. *Nature* **517**, 621-625, doi:10.1038/nature14112 (2015).

31 Menachery, V. D. *et al.* Pathogenic influenza viruses and coronaviruses utilize similar and contrasting approaches to control interferon-stimulated gene responses. *mBio* **5**, e01174-01114, doi:10.1128/mBio.01174-14 (2014).

32 Menachery, V. D. *et al.* MERS-CoV and H5N1 influenza virus antagonize antigen presentation by altering the epigenetic landscape. *Proc Natl Acad Sci U S A* **115**, E1012-E1021, doi:10.1073/pnas.1706928115 (2018).

33 Desai, N. *et al.* Temporal and spatial heterogeneity of host response to SARS-CoV-2 pulmonary infection. *Nature communications* **11**, 6319, doi:10.1038/s41467-020-20139-7 (2020).

34 Choi, J. *et al.* Inflammatory Signals Induce AT2 Cell-Derived Damage-Associated Transient Progenitors that Mediate Alveolar Regeneration. *Cell Stem Cell* **27**, 366-382.e367, doi:10.1016/j.stem.2020.06.020 (2020).

35 Kobayashi, Y. *et al.* Persistence of a regeneration-associated, transitional alveolar epithelial cell state in pulmonary fibrosis. *Nature Cell Biology* **22**, 934-946, doi:10.1038/s41556-020-0542-8 (2020).

36 Melms, J. C. *et al.* A molecular single-cell lung atlas of lethal COVID-19. *Nature*, doi:10.1038/s41586-021-03569-1 (2021).

37 Delorey, T. M. *et al.* COVID-19 tissue atlases reveal SARS-CoV-2 pathology and cellular targets. *Nature*, doi:10.1038/s41586-021-03570-8 (2021).

38 Besnard, V. *et al.* Identification of periplakin as a major regulator of lung injury and repair in mice. *JCI Insight* **3**, doi:10.1172/jci.insight.90163 (2018).

39 Morse, C. *et al.* Proliferating SPP1/MERTK-expressing macrophages in idiopathic pulmonary fibrosis. *European Respiratory Journal* **54**, 1802441, doi:10.1183/13993003.02441-2018 (2019).

40 Adams, T. S. *et al.* Single-cell RNA-seq reveals ectopic and aberrant lung-resident cell populations in idiopathic pulmonary fibrosis. *Science Advances* **6**, eaba1983, doi:10.1126/sciadv.aba1983 (2020).

41 Wang, Z. *et al.* PD-1^{hi} CD8⁺ resident memory T cells balance immunity and fibrotic sequelae. *Science Immunology* **4**, eaaw1217, doi:10.1126/sciimmunol.aaw1217 (2019).

42 Goplen, N. P. *et al.* Tissue-resident CD8(+) T cells drive age-associated chronic lung sequelae after viral pneumonia. *Sci Immunol* **5**, doi:10.1126/sciimmunol.abc4557 (2020).

43 Gralinski, L. E. *et al.* Complement Activation Contributes to Severe Acute Respiratory Syndrome Coronavirus Pathogenesis. *mBio* **9**, doi:10.1128/mBio.01753-18 (2018).

44 Jiang, Y. *et al.* Blockade of the C5a-C5aR axis alleviates lung damage in hDPP4-transgenic mice infected with MERS-CoV. *Emerg Microbes Infect* **7**, 77, doi:10.1038/s41426-018-0063-8 (2018).

45 Thielens, N. M., Tedesco, F., Bohlson, S. S., Gaboriaud, C. & Tenner, A. J. C1q: A fresh look upon an old molecule. *Mol Immunol* **89**, 73-83, doi:10.1016/j.molimm.2017.05.025 (2017).

46 Sheng, G. *et al.* Viral Infection Increases the Risk of Idiopathic Pulmonary Fibrosis: A Meta-Analysis. *Chest* **157**, 1175-1187, doi:10.1016/j.chest.2019.10.032 (2020).

47 Mesa-Vieira, C., Botero-Rodriguez, F., Padilla-Munoz, A., Franco, O. H. & Gomez-Restrepo, C. The Dark Side of the Moon: Global challenges in the distribution of vaccines and implementation of vaccination plans against COVID-19. *Maturitas*, doi:10.1016/j.maturitas.2021.05.003 (2021).

48 Chopra, V., Flanders, S. A., O'Malley, M., Malani, A. N. & Prescott, H. C. Sixty-Day Outcomes Among Patients Hospitalized With COVID-19. *Ann Intern Med* **174**, 576-578, doi:10.7326/M20-5661 (2021).

49 Carvalho-Schneider, C. *et al.* Follow-up of adults with noncritical COVID-19 two months after symptom onset. *Clin Microbiol Infect* **27**, 258-263, doi:10.1016/j.cmi.2020.09.052 (2021).

50 Arnold, D. T. *et al.* Patient outcomes after hospitalisation with COVID-19 and implications for follow-up: results from a prospective UK cohort. *Thorax*, doi:10.1136/thoraxjnl-2020-216086 (2020).

51 Moreno-Perez, O. *et al.* Post-acute COVID-19 syndrome. Incidence and risk factors: A Mediterranean cohort study. *J Infect* **82**, 378-383, doi:10.1016/j.jinf.2021.01.004 (2021).

52 Halpin, S. J. *et al.* Postdischarge symptoms and rehabilitation needs in survivors of COVID-19 infection: A cross-sectional evaluation. *J Med Virol* **93**, 1013-1022, doi:10.1002/jmv.26368 (2021).

53 John, A. E., Joseph, C., Jenkins, G. & Tatler, A. L. COVID-19 and pulmonary fibrosis: A potential role for lung epithelial cells and fibroblasts. *Immunol Rev*, doi:10.1111/imr.12977 (2021).

54 Zuo, W., Zhao, X. & Chen, Y.-G. 247-258 (Springer Berlin Heidelberg, 2010).

55 Naik, P. K. & Moore, B. B. Viral infection and aging as cofactors for the development of pulmonary fibrosis. *Expert Rev Respir Med* **4**, 759-771, doi:10.1586/ers.10.73 (2010).

56 Wells, A. U. *et al.* Nintedanib in patients with progressive fibrosing interstitial lung diseases—subgroup analyses by interstitial lung disease diagnosis in the INBUILD trial: a randomised, double-blind, placebo-controlled, parallel-group trial. *The Lancet Respiratory Medicine* **8**, 453-460, doi:10.1016/s2213-2600(20)30036-9 (2020).

57 Menachery, V. D., Gralinski, L. E., Baric, R. S. & Ferris, M. T. New Metrics for Evaluating Viral Respiratory Pathogenesis. *PLOS ONE* **10**, e0131451, doi:10.1371/journal.pone.0131451 (2015).

58 Merritt, C. R. *et al.* Multiplex digital spatial profiling of proteins and RNA in fixed tissue. *Nature Biotechnology* **38**, 586-599, doi:10.1038/s41587-020-0472-9 (2020).

59 Hoffman, G. E. & Roussos, P. Dream: powerful differential expression analysis for repeated measures designs. *Bioinformatics* **37**, 192-201, doi:10.1093/bioinformatics/btaa687 (2021).

60 Law, C. W., Chen, Y., Shi, W. & Smyth, G. K. voom: Precision weights unlock linear model analysis tools for RNA-seq read counts. *Genome Biol* **15**, R29, doi:10.1186/gb-2014-15-2-r29 (2014).

61 Jew, B. *et al.* Accurate estimation of cell composition in bulk expression through robust integration of single-cell information. *Nature Communications* **11**, doi:10.1038/s41467-020-15816-6 (2020).

62 Angelidis, I. *et al.* An atlas of the aging lung mapped by single cell transcriptomics and deep tissue proteomics. *Nat Commun* **10**, 963, doi:10.1038/s41467-019-08831-9 (2019).

63 Korotkevich, G. *et al. Fast gene set enrichment analysis* (Cold Spring Harbor Laboratory, 2016).

64 Carbon, S. *et al.* The Gene Ontology resource: enriching a GOld mine. *Nucleic Acids Research* **49**, D325-D334, doi:10.1093/nar/gkaa1113 (2021).

65 Jassal, B. *et al.* The reactome pathway knowledgebase. *Nucleic Acids Res* **48**, D498-D503, doi:10.1093/nar/gkz1031 (2020).

66 Wickham, H. in *Use R!,* 1 online resource (XVI, 260 pages 232 illustrations, 140 illustrations in color (Springer International Publishing : Imprint: Springer,, Cham, 2016).

67 Gu, Z., Eils, R. & Schlesner, M. Complex heatmaps reveal patterns and correlations in multidimensional genomic data. *Bioinformatics* **32**, 2847-2849, doi:10.1093/bioinformatics/btw313 (2016).

CHAPTER 6 – CONCLUSIONS

6.1 Determinants of emergent coronaviruses

Over the past two decades, the vast increase in coronavirus surveillance has resulted in an extremely large number of deposited virus sequences[1-6]. These sequences provide a glimpse of the size of the reservoir of possible zoonotic coronavirus pathogens, but experimentally testing these virus sequences for ability to infect human cells is a laborious and expensive process. Complete synthesis of a full virus genome is dependent on high quality of the deposited sequence, including proper 5'- and 3'-UTRs. However, due to the highly redundant host antagonism functions and independent RNA replicase complex encoded by the uniquely large coronavirus genomes, once viral RNA can be delivered to the cytoplasm of cells either by native infection or by direct delivery of RNA to the cell by transfection or electroporation, it is often able to replicate and produce progeny virus[7]. However, this progeny virus may not be able to spread in culture due to incompatibilities of the virus spike protein and the ability to enter a particular host species cell.

Traditionally, the compatibility of a given coronavirus spike to enter a cell was thought to be restricted by binding to a host receptor. Previous studies using chimeric SARS-CoV viruses expressing the spike proteins of bat viruses WIV1 or SHC014 showed that these spike proteins are sufficient for infection of human primary lung epithelial cells without adaptation, suggesting these viruses are capable of emerging into humans, but it remained unclear if the remaining viral genes are capable of replicating efficiently in human cells[8,9]. Further studies using full-length reconstituted WIV1 and SHC014 viruses reveals that they can replicate in primary human cells as efficiently as SARS-CoV. These studies highlighted that zoonotic SARS-CoV-like viruses are poised for human emergence, possibly without adaptation[8,9]. However, similar studies for MERS-

CoV-like viruses were lacking. HKU4 and HKU5 are bat MERS-CoV-like viruses that are ~60% identical to MERS-CoV across their genomes and represent distant ancestors of MERS-CoV[10,11]. Biochemical assays showed that the HKU4 spike, but not HKU5, can bind the human MERS-CoV receptor, DPP4[12,13]. However, attempts to recover full-length HKU4 and HKU5 viruses in our laboratory have been unsuccessful. More recently, a closer relative of MERS-CoV, PDF-2180, was identified in bats in Uganda. PDF-2180 is ~80% similar to MERS-CoV across the genome, but only 64% identical in the S1 subunit of the spike[14]. Chimeric MERS-CoV expressing the PDF-2180 spike could replicate in primate cells electroporated with viral RNA but could not spread in culture or be passaged onto new cell cultures, including primary human airway cells[14]. This led to the initial conclusion that the PDF-2180 spike is not capable of emergence into humans.

In Chapter 2 of this dissertation, we show that the inability of PDF-2180 spike to mediate entry into human cells is not due to inability to bind a human receptor, but instead is due to lack of proteolytic processing of the spike protein in human cells. This proteolytic processing could be complemented by use of exogenous trypsin, similar to techniques required for culturing of porcine enteric CoVs. The PDF-2180 spike did not allow entry into continuous human lung cell lines or primary human airway epithelial cells, but did allow entry into human liver cells (Huh7) and intestinal cells (Caco-2). We additionally show that PDF-2180 spike does not require DPP4 as a receptor, suggesting that MERS-CoV-like viruses may emerge into humans utilizing receptors other than DPP4. Furthermore, we show that use of exogenous trypsin could facilitate recovery of full-length HKU5 virus and allow for replication in primate cells. We also experimentally validated with live virus that HKU5 does not require DPP4 as a receptor, as predicted by pseudotyped virus assays[13].

We know that proteolytic processing of the spike at the S1/S2 junction is required for conformational changes necessary for membrane fusion; however, it was under appreciated that host proteases may serve as an additional barrier to host range expansion. Our work describing the protease restriction of PDF-2180 and HKU5 emphasize the necessity of host protease

compatibility in coronavirus host range expansion. Subsequent work by others using a large panel of all SARS-CoV-like spike protein sequences found three clades of spike proteins based on their ability to utilize human and bat ACE2 as receptors, and whether they were dependent on exogenous trypsin treatment[15]. Since the emergence of SARS-CoV-2 and the identification of many more animal reservoir CoVs, we expect many of these viruses are capable of entering human cells, likely resolving additional clade distinctions for ACE2 usage and protease compatibility. Further analysis of cleavage of endemic, emergent, and pre-emergent CoVs by specific cellular proteases such as cathepsins, TMPRSS2, and furin from humans and animal hosts will greatly aid in our ability to screen reservoir viruses for patterns that predict risk for human emergence[16].

6.2 Importance of SARS-CoV-2 mouse models

The emergence and rapid spread of SARS-CoV-2 revealed the need for rapid scientific and medical advances to develop medical countermeasures. Animal models are critical in preclinical development of medical countermeasures. While SARS-CoV-2 can infect several animal species including non-human primate (NHP)[17-19], hamster[20,21], ferret[22], early SARS-CoV-2 isolates were unable to infect mice. Laboratory mice are one of the most common, cheapest, and convenient animal models with numerous tools and reagents available to study. There are multiple strategies to develop mouse models for viruses unable to utilize murine orthologues of the human receptors: 1) use transgenic mice expressing the human receptor, 2) transduce mice using viral vectors to ectopically express the human receptor, 3) alter the virus to utilize the murine receptor.

Following the SARS-CoV epidemic, several groups generated transgenic mice expressing human ACE2 under varying promoters[9,23-27]. These mice allow for replication of SARS-CoV and SARS-CoV-2, but develop varying amounts of clinical disease, and often ultimately succumb due to encephalitis, which is not representative of human disease. These transgenic mice are limited

in availability and restricted to a single genetic background, making studies to understand host genetic diversity of genetic knockouts difficult or impossible. Other groups developed adenovirus (AdV) or adeno-associated virus (AAV) viral vectors to deliver expression of human ACE2[28-30]. These systems allow for rapid transduction of commercially available or specific knockout mice for subsequent SARS-CoV-2 infection and study. However, one limitation of these virus vectored platforms is that the vector itself induces an immune response that may alter the responses to SARS-CoV-2 infection. Both transgenic and viral vectored human ACE2 models also may create differences in cellular tropism in mice compared to humans due to the promoters or viral vectors chosen.

Upon the initial observation that SARS-CoV-2 could not utilize murine ACE2 as a receptor, we rapidly employed our expertise derived from years of working with other coronavirus mouse models and reverse genetics to generate a mouse-adapted strain of SARS-CoV-2[31-34]. In Chapter 3 of this dissertation, we engineered two amino acid substitutions in the RBD predicted to restore critical interactions between the SARS-CoV-2 RBD and mouse ACE2[25]. This mouse-adapted virus, SARS-CoV-2 MA, is able to replicate to high titers in wildtype BALB/c mice but causes only minor respiratory disease. The lack of severe disease is not surprising as clinical isolates of SARS-CoV also do not cause major disease in standard laboratory mice. However, this SARS-CoV-2 model can still rapidly be employed for testing of medical countermeasures using viral replication as the predominant feature. In Chapter 4 of this dissertation, we developed a more clinically relevant, highly pathogenic mouse model, we employed serial *in vivo* passage of SARS-CoV-2 MA to generate a virus that acquires additional mutations that increase fitness in mice, SARS-CoV-2 MA10[35]. SARS-CoV-2 MA10 replicates to higher titers in the lungs compared to SARS-CoV-2 MA and persists longer. Additionally, SARS-CoV-2 MA10 causes severe respiratory illness in young mice of multiple genetic backgrounds and recapitulates the age-related exacerbation seen in human COVID-19 patients. The SARS-CoV-2 MA10 model also robustly replicates many aspects of human COVID-19 disease.

In addition to the utility of SARS-CoV-2 MA and MA10 for understanding COVID-19 and SARS-CoV-2 pathogenesis, these models were utilized for preclinical testing of several medical countermeasures including monoclonal antibodies[36-43], pegylated interferon lambda[25], antivirals[44], and vaccines including Moderna's mRNA-1273[25,35,45-50]. SARS-CoV-2 MA10 was the first highly pathogenic, widely tractable mouse model available and has been shared with numerous laboratories and reagent repositories.

6.3 Adaptation of SARS-CoV-2 in mice

SARS-CoV-2 MA10 accumulated five additional mutations located nonstructural protein 4 (nsp4), nsp7, nsp8, spike, and open reading frame 6 (ORF6). nsp4, along with nsp6, reorganizes host intracellular membranes to form double membrane vesicles (DMVs) that form viral RNA replication complexes protected from surveillance of host innate immune sensors[51]. It is not unreasonable to predict that nsp4 interacts directly with host proteins to reorganize intracellular membranes, and thus adaptation of nsp4 to new hosts is important for increasing viral fitness in those hosts. nsp7 and nsp8 are known to both directly interact with the viral RNA-dependent RNA polymerase, increasing processivity[52-54]. It is unknown if nsp7 and nsp8 interact with host proteins, but adaptations of these viral proteins in mice suggests they may interact with host proteins to mediate viral RNA replication. It is unsurprising to see further adaptation of the viral spike protein during passage as the spike protein undergoes rapid change during mouse adaptation of SARS-CoV and MERS-CoV and adaptation of SARS-CoV-2 in humans throughout the COVID-19 pandemic[32,55-61]. The introduced and acquired changes to the spike protein in SARS-CoV-2 MA and SARS-CoV-2 MA10 are all in the RBD and involved in direct contact to ACE2, highlighting the importance of receptor binding affinity. Finally, ORF6 is known to dampen the host innate immune system by preventing nuclear import of transcription factors[62,63]. Mouse adaptation of ORF6 may augment the ability to antagonize the murine innate immune system. The different

mutations that arise between mouse adaptation of SARS-CoV and SARS-CoV-2 may serve similar functions or illustrate multiple paths for adaptation to new host species.

These five mutations arose during serial *in vivo* passage in three consecutive steps: firstly, the spike and ORF6 mutations arise, followed by nsp7 and nsp8, then finally nsp4[35]. Due to genetic linkage of the spike/ORF6 and nsp7/nsp8 mutations, it is possible that one adaptation from each pair is beneficial and selected for during *in vivo* passaging. Testing of individual mouse-adaptations using reverse genetics will be important in determining the effects of each on SARS-CoV-2 MA10 pathogenesis. Since the development of our SARS-CoV-2 MA and MA10 models, other groups have also reported pathogenic mouse-adapted strains of SARS-CoV-2[64-68]. These other models cause similar disease in mice, but each mouse-adapted virus developed a combination of similar and unique mutations. Further comparison and analysis of these mouse-models may elucidate convergent and divergent mechanisms of coronavirus host adaptation. Furthermore, identification of genetic loci that rapidly undergo host adaptation can inform zoonotic reservoir surveillance for identification of high-risk pre-emergent coronaviruses as these loci may encode proteins with strong selective pressure in new hosts.

6.4 Utilizing SARS-CoV-2 MA10 pathogenesis to understand COVID-19

Despite several effective vaccines for SARS-CoV-2, global vaccine availability and hesitancy contribute to ongoing spread of the pandemic worldwide. In addition to the burden caused by acute infections, nearly 50% of COVID-19 survivors describe long term sequelae, a condition termed ‘long COVID’, or ‘post-acute sequelae of SARS-CoV-2’ (PASC)[69-72]. The pathological mechanisms of both acute and chronic sequelae are poorly understood and highly variable between individuals. PASC has been reported in 30-50% of COVID-19 survivors, with varying sequelae that lower the quality of life[69-72]. Computed tomography (CT) imaging of COVID-19 survivors reveals ground glass opacities in roughly 50% of patients at 6 months post clearance

of acute symptoms[71], highlighting the prevalence of pulmonary damage long after infection. It remains unclear how long these sequelae will affect survivors.

Our current understanding of human COVID-19 lung pathobiology is limited to autopsy samples that are only representative of the most severe and terminal cases and do provide details of the temporal changes within each patient[73-77]. A strong advantage of using animal models is the ability to control disease severity by altering virus dose, animal age, and host genetics. Mice in particular allow for large sample sizes, reproducibility, and sampling of tissues across progression of disease.

SARS-CoV-2 MA10 infects AT2 cells of the mouse lung and causes a decrease in surfactant expression, as observed in humans[35]. Surfactants are necessary for maintaining plasticity of the lung for efficient alveolar expansion and gas exchange[78,79]. Loss of AT2 cell function likely contributes to decreased respiratory function through loss of lung plasticity. Additionally, during ALI and ARDS, immune pathological mechanisms lead to breakdown of AT1 cellular barriers, which account for over 90% of the surface area of the alveoli, resulting in edema in the lungs. During lung injury repair, AT2 cells serve as progenitor cells for repopulation of both AT1 and AT2 cells. AT2 cells undergo differentiation into transitional DATP/PATS cells that then undergo redifferentiation into AT1 and AT2 cells[80,81]. In human IPF and COVID-19, and our SARS-CoV-2 MA10 model, DATP/PATS cells accumulate and seem to be locked in this transitional state without the ability to properly redifferentiate into necessary AT1 and AT2 cells[82,83]. An alternative mechanism of alveolar cell repopulation is through transdifferentiation of terminal bronchiolar epithelial cells into AT1 and AT2 cells. While total AT2 cells are recovered by D30 post SARS-CoV-2 MA10 infection, fibrotic lesions continue to lack proper AT2 cell distribution and alveolar architecture. Subpleural and distal localization of pulmonary fibrotic lesions in SARS-CoV-2 MA10 infected mice may be due to the combination of the inability of DATP/PATS cells to properly differentiate into AT1 and AT2 cells and being located too far from terminal bronchial for repopulation by transdifferentiation of epithelial cells. Use of lineage trace mice to label alveolar

and bronchial epithelial cells prior to infection will allow for testing of if restored AT2 cell populations are derived from prior AT2 or bronchial epithelial cells. Additionally, use of Cre recombinase-expressing SARS-CoV-2 MA10 virus will be important in defining if infected AT2 cells are cleared, either intrinsically or by immune cells, or if a subset of AT2 cells survive infection and transition to DATP/PATS cells and subsequent AT1 and AT2 cells.

PASC has many shared features with human IPF, including retention of DATP/PATS cells, collagen deposition, and general disruption of lung architecture. IPF is currently a poorly understood disease characterized by progressive scarring and stiffening of the lungs, with poor prognosis and few options for clinical intervention[84]. Lung transplant may be required in some cases but is not available for all patients. Currently, there are no treatments to reverse IPF, but two drugs are available to slow the progression of IPF: pirfenidone and nintedanib[85]. Due to the long-term progression of IPF, diagnoses often occur after severe disease progression has already occurred. It is unclear if pirfenidone and nintedanib treatment at earlier stages of IPF can have even greater effect. Similarly, it is unknown if these anti-fibrotic drugs could be beneficial to COVID-19 patients. Additionally, it is unknown if use of antiviral interventions such as monoclonal antibodies or direct acting antivirals during the acute phase of infection can prevent PASC development. Our SARS-CoV-2 MA10 mouse model provides a system to study interventions to prevent or dampen PASC symptoms.

Altogether, our collective understanding of pre-emergent and emergent coronaviruses has allowed for rapid development of *in vitro* and *in vivo* model systems to respond rapidly to the COVID-19 pandemic. The work presented in this dissertation has provided critical models and approaches for coronavirus preparedness and response. These mouse models will continue to elucidate mechanisms of COVID-19 pathogenesis and allow preclinical development of current and future coronavirus medical countermeasures.

REFERENCES

1 Li, W. Bats Are Natural Reservoirs of SARS-Like Coronaviruses. *Science* **310**, 676-679, doi:10.1126/science.1118391 (2005).

2 Hu, B. *et al.* Discovery of a rich gene pool of bat SARS-related coronaviruses provides new insights into the origin of SARS coronavirus. *PLOS Pathogens* **13**, e1006698, doi:10.1371/journal.ppat.1006698 (2017).

3 Ge, X. Y. *et al.* Isolation and characterization of a bat SARS-like coronavirus that uses the ACE2 receptor. *Nature* **503**, 535-538, doi:10.1038/nature12711 (2013).

4 Latinne, A. *et al. Origin and cross-species transmission of bat coronaviruses in China* (Cold Spring Harbor Laboratory, 2020).

5 Fan, Y., Zhao, K., Shi, Z.-L. & Zhou, P. Bat Coronaviruses in China. *Viruses* **11**, 210, doi:10.3390/v11030210 (2019).

6 Anthony, S. J. *et al.* Global patterns in coronavirus diversity. *Virus Evolution* **3**, doi:10.1093/ve/vex012 (2017).

7 Kasuga, Y., Zhu, B., Jang, K.-J. & Yoo, J.-S. Innate immune sensing of coronavirus and viral evasion strategies. *Experimental & Molecular Medicine* **53**, 723-736, doi:10.1038/s12276-021-00602-1 (2021).

8 Menachery, V. D. *et al.* A SARS-like cluster of circulating bat coronaviruses shows potential for human emergence. *Nat Med* **21**, 1508-1513, doi:10.1038/nm.3985 (2015).

9 Menachery, V. D. *et al.* SARS-like WIV1-CoV poised for human emergence. *Proc Natl Acad Sci U S A* **113**, 3048-3053, doi:10.1073/pnas.1517719113 (2016).

10 Lau, S. K. *et al.* Genetic characterization of Betacoronavirus lineage C viruses in bats reveals marked sequence divergence in the spike protein of pipistrellus bat coronavirus HKU5 in Japanese pipistrelle: implications for the origin of the novel Middle East respiratory syndrome coronavirus. *J Virol* **87**, 8638-8650, doi:10.1128/JVI.01055-13 (2013).

11 Annan, A. *et al.* Human Betacoronavirus 2c EMC/2012–related Viruses in Bats, Ghana and Europe. *Emerging Infectious Diseases* **19**, 456-459, doi:10.3201/eid1903.121503 (2013).

12 Wang, Q. *et al.* Bat Origins of MERS-CoV Supported by Bat Coronavirus HKU4 Usage of Human Receptor CD26. *Cell Host & Microbe* **16**, 328-337, doi:10.1016/j.chom.2014.08.009 (2014).

13 Yang, Y. *et al.* Receptor usage and cell entry of bat coronavirus HKU4 provide insight into bat-to-human transmission of MERS coronavirus. *Proc Natl Acad Sci U S A* **111**, 12516-12521, doi:10.1073/pnas.1405889111 (2014).

14 Anthony, S. J. *et al.* Further Evidence for Bats as the Evolutionary Source of Middle East Respiratory Syndrome Coronavirus. *mBio* **8**, doi:10.1128/mBio.00373-17 (2017).

15 Letko, M., Marzi, A. & Munster, V. Functional assessment of cell entry and receptor usage for SARS-CoV-2 and other lineage B betacoronaviruses. *Nature Microbiology* **5**, 562-569, doi:10.1038/s41564-020-0688-y (2020).

16 Shulla, A. *et al.* A Transmembrane Serine Protease Is Linked to the Severe Acute Respiratory Syndrome Coronavirus Receptor and Activates Virus Entry. *Journal of Virology* **85**, 873-882, doi:10.1128/jvi.02062-10 (2011).

17 Rockx, B. *et al.* Comparative pathogenesis of COVID-19, MERS, and SARS in a nonhuman primate model. *Science* **368**, 1012-1015, doi:10.1126/science.abb7314 (2020).

18 Yu, P. *et al.* Age-related rhesus macaque models of COVID-19. *Animal Model Exp Med* **3**, 93-97, doi:10.1002/ame2.12108 (2020).

19 Munster, V. J. *et al.* Respiratory disease in rhesus macaques inoculated with SARS-CoV-2. *Nature* **585**, 268-272, doi:10.1038/s41586-020-2324-7 (2020).

20 Imai, M. *et al.* Syrian hamsters as a small animal model for SARS-CoV-2 infection and countermeasure development. *Proc Natl Acad Sci U S A* **117**, 16587-16595, doi:10.1073/pnas.2009799117 (2020).

21 Sia, S. F. *et al.* Pathogenesis and transmission of SARS-CoV-2 in golden hamsters. *Nature* **583**, 834-838, doi:10.1038/s41586-020-2342-5 (2020).

22 Kim, Y. I. *et al.* Infection and Rapid Transmission of SARS-CoV-2 in Ferrets. *Cell Host Microbe* **27**, 704-709 e702, doi:10.1016/j.chom.2020.03.023 (2020).

23 Sun, S. H. *et al.* A Mouse Model of SARS-CoV-2 Infection and Pathogenesis. *Cell Host Microbe* **28**, 124-133 e124, doi:10.1016/j.chom.2020.05.020 (2020).

24 Bao, L. *et al.* The pathogenicity of SARS-CoV-2 in hACE2 transgenic mice. *Nature* **583**, 830-833, doi:10.1038/s41586-020-2312-y (2020).

25 Dinnon, K. H., 3rd *et al.* A mouse-adapted model of SARS-CoV-2 to test COVID-19 countermeasures. *Nature* **586**, 560-566, doi:10.1038/s41586-020-2708-8 (2020).

26 Zheng, J. *et al.* COVID-19 treatments and pathogenesis including anosmia in K18-hACE2 mice. *Nature* **589**, 603-607, doi:10.1038/s41586-020-2943-z (2021).

27 Yinda, C. K. *et al.* K18-hACE2 mice develop respiratory disease resembling severe COVID-19. *PLOS Pathogens* **17**, e1009195, doi:10.1371/journal.ppat.1009195 (2021).

28 Sun, J. *et al.* Generation of a Broadly Useful Model for COVID-19 Pathogenesis, Vaccination, and Treatment. *Cell* **182**, 734-743 e735, doi:10.1016/j.cell.2020.06.010 (2020).

29 Israelow, B. *et al.* Mouse model of SARS-CoV-2 reveals inflammatory role of type I interferon signaling. *J Exp Med* **217**, doi:10.1084/jem.20201241 (2020).

30 Hassan, A. O. *et al.* A SARS-CoV-2 Infection Model in Mice Demonstrates Protection by Neutralizing Antibodies. *Cell* **182**, 744-753 e744, doi:10.1016/j.cell.2020.06.011 (2020).

31 Hou, Y. J. *et al.* SARS-CoV-2 Reverse Genetics Reveals a Variable Infection Gradient in the Respiratory Tract. *Cell* **182**, 429-446 e414, doi:10.1016/j.cell.2020.05.042 (2020).

32 Roberts, A. *et al.* A mouse-adapted SARS-coronavirus causes disease and mortality in BALB/c mice. *PLoS Pathog* **3**, e5, doi:10.1371/journal.ppat.0030005 (2007).

33 Scobey, T. *et al.* Reverse genetics with a full-length infectious cDNA of the Middle East respiratory syndrome coronavirus. *Proc Natl Acad Sci U S A* **110**, 16157-16162, doi:10.1073/pnas.1311542110 (2013).

34 Yount, B. *et al.* Reverse genetics with a full-length infectious cDNA of severe acute respiratory syndrome coronavirus. *Proc Natl Acad Sci U S A* **100**, 12995-13000, doi:10.1073/pnas.1735582100 (2003).

35 Leist, S. R. *et al.* A Mouse-Adapted SARS-CoV-2 Induces Acute Lung Injury and Mortality in Standard Laboratory Mice. *Cell* **183**, 1070-1085 e1012, doi:10.1016/j.cell.2020.09.050 (2020).

36 Martinez, D. R. *et al. A broadly neutralizing antibody protects against SARS-CoV, pre-emergent bat CoVs, and SARS-CoV-2 variants in mice* (Cold Spring Harbor Laboratory, 2021).

37 Li, D. *et al. The functions of SARS-CoV-2 neutralizing and infection-enhancing antibodies in vitro and in mice and nonhuman primates* (Cold Spring Harbor Laboratory, 2021).

38 Li, W. *et al.* Rapid identification of a human antibody with high prophylactic and therapeutic efficacy in three animal models of SARS-CoV-2 infection. *Proceedings of the National Academy of Sciences* **117**, 29832-29838, doi:10.1073/pnas.2010197117 (2020).

39 Li, W. *et al.* High Potency of a Bivalent Human VH Domain in SARS-CoV-2 Animal Models. *Cell* **183**, 429-441.e416, doi:10.1016/j.cell.2020.09.007 (2020).

40 Schäfer, A. *et al.* Antibody potency, effector function, and combinations in protection and therapy for SARS-CoV-2 infection in vivo. *Journal of Experimental Medicine* **218**, doi:10.1084/jem.20201993 (2021).

41 Shiakolas, A. R. *et al.* Cross-reactive coronavirus antibodies with diverse epitope specificities and Fc effector functions. *Cell Reports Medicine*, 100313, doi:10.1016/j.xcrm.2021.100313 (2021).

42 Zost, S. J. *et al.* Potently neutralizing and protective human antibodies against SARS-CoV-2. *Nature* **584**, 443-449, doi:10.1038/s41586-020-2548-6 (2020).

43 Rappazzo, C. G. *et al.* Broad and potent activity against SARS-like viruses by an engineered human monoclonal antibody. *Science* **371**, 823-829, doi:10.1126/science.abf4830 (2021).

44 Martinez, D. R. *et al.* Early therapy with remdesivir and antibody combinations improves COVID-19 disease in mice. *bioRxiv*, doi:10.1101/2021.01.27.428478 (2021).

45 Corbett, K. S. *et al.* SARS-CoV-2 mRNA vaccine design enabled by prototype pathogen preparedness. *Nature* **586**, 567-571, doi:10.1038/s41586-020-2622-0 (2020).

46 Hörner, C. *et al.* A highly immunogenic and effective measles virus-based Th1-biased COVID-19 vaccine. *Proceedings of the National Academy of Sciences* **117**, 32657-32666, doi:10.1073/pnas.2014468117 (2020).

47 Sun, W. *et al.* Newcastle disease virus (NDV) expressing the spike protein of SARS-CoV-2 as a live virus vaccine candidate. *EBioMedicine* **62**, 103132, doi:10.1016/j.ebiom.2020.103132 (2020).

48 Sun, W. *et al.* A Newcastle Disease Virus (NDV) Expressing a Membrane-Anchored Spike as a Cost-Effective Inactivated SARS-CoV-2 Vaccine. *Vaccines* **8**, 771, doi:10.3390/vaccines8040771 (2020).

49 Tostanoski, L. H. *et al. Protective efficacy of rhesus adenovirus COVID-19 vaccines against mouse-adapted SARS-CoV-2* (Cold Spring Harbor Laboratory, 2021).

50 Walls, A. C. *et al.* Elicitation of Potent Neutralizing Antibody Responses by Designed Protein Nanoparticle Vaccines for SARS-CoV-2. *Cell* **183**, 1367-1382.e1317, doi:10.1016/j.cell.2020.10.043 (2020).

51 Fehr, A. R. & Perlman, S. Coronaviruses: an overview of their replication and pathogenesis. *Methods Mol Biol* **1282**, 1-23, doi:10.1007/978-1-4939-2438-7_1 (2015).

52 Kirchdoerfer, R. N. & Ward, A. B. Structure of the SARS-CoV nsp12 polymerase bound to nsp7 and nsp8 co-factors. *Nature Communications* **10**, doi:10.1038/s41467-019-10280-3 (2019).

53 Bera, S. C. *et al. The nucleotide addition cycle of the SARS-CoV-2 polymerase* (Cold Spring Harbor Laboratory, 2021).

54 Reshamwala, S. M. S., Likhite, V., Degani, M. S., Deb, S. S. & Noronha, S. B. Mutations in SARS-CoV-2 nsp7 and nsp8 proteins and their predicted impact on replication/transcription complex structure. *Journal of Medical Virology* **93**, 4616-4619, doi:10.1002/jmv.26791 (2021).

55 Greaney, A. J. *et al.* Complete Mapping of Mutations to the SARS-CoV-2 Spike Receptor-Binding Domain that Escape Antibody Recognition. *Cell Host & Microbe* **29**, 44-57.e49, doi:10.1016/j.chom.2020.11.007 (2021).

56 Starr, T. N. *et al.* Deep Mutational Scanning of SARS-CoV-2 Receptor Binding Domain Reveals Constraints on Folding and ACE2 Binding. *Cell* **182**, 1295-1310.e1220, doi:10.1016/j.cell.2020.08.012 (2020).

57 Harvey, W. T. *et al.* SARS-CoV-2 variants, spike mutations and immune escape. *Nature Reviews Microbiology* **19**, 409-424, doi:10.1038/s41579-021-00573-0 (2021).

58 Holmes, K. V. STRUCTURAL BIOLOGY: Adaptation of SARS Coronavirus to Humans. *Science* **309**, 1822-1823, doi:10.1126/science.1118817 (2005).

59 Douglas, M. G., Kocher, J. F., Scobey, T., Baric, R. S. & Cockrell, A. S. Adaptive evolution influences the infectious dose of MERS-CoV necessary to achieve severe respiratory disease. *Virology* **517**, 98-107, doi:10.1016/j.virol.2017.12.006 (2018).

60 Cockrell, A. S. *et al.* A mouse model for MERS coronavirus-induced acute respiratory distress syndrome. *Nature Microbiology* **2**, 16226, doi:10.1038/nmicrobiol.2016.226 (2017).

61 Li, K. *et al.* Mouse-adapted MERS coronavirus causes lethal lung disease in human DPP4 knockin mice. *Proc Natl Acad Sci U S A* **114**, E3119-E3128, doi:10.1073/pnas.1619109114 (2017).

62 Frieman, M. *et al.* Severe acute respiratory syndrome coronavirus ORF6 antagonizes STAT1 function by sequestering nuclear import factors on the rough endoplasmic reticulum/Golgi membrane. *J Virol* **81**, 9812-9824, doi:10.1128/JVI.01012-07 (2007).

63 Sims, A. C. *et al.* Release of severe acute respiratory syndrome coronavirus nuclear import block enhances host transcription in human lung cells. *J Virol* **87**, 3885-3902, doi:10.1128/JVI.02520-12 (2013).

64 Roy Wong, L.-Y. *et al. Eicosanoid signaling as a therapeutic target in middle-aged mice with severe COVID-19* (Cold Spring Harbor Laboratory, 2021).

65 Muruato, A. *et al. Mouse Adapted SARS-CoV-2 protects animals from lethal SARS-CoV challenge* (Cold Spring Harbor Laboratory, 2021).

66 Rathnasinghe, R. *et al. The N501Y mutation in SARS-CoV-2 spike leads to morbidity in obese and aged mice and is neutralized by convalescent and post-vaccination human sera* (Cold Spring Harbor Laboratory, 2021).

67 Gu, H. *et al.* Adaptation of SARS-CoV-2 in BALB/c mice for testing vaccine efficacy. *Science* **369**, 1603-1607, doi:10.1126/science.abc4730 (2020).

68 Wang, J. *et al.* Mouse-adapted SARS-CoV-2 replicates efficiently in the upper and lower respiratory tract of BALB/c and C57BL/6J mice. *Protein Cell* **11**, 776-782, doi:10.1007/s13238-020-00767-x (2020).

69 Carfi, A., Bernabei, R., Landi, F. & Gemelli Against, C.-P.-A. C. S. G. Persistent Symptoms in Patients After Acute COVID-19. *JAMA* **324**, 603-605, doi:10.1001/jama.2020.12603 (2020).

70 Tenforde, M. W. *et al.* Symptom Duration and Risk Factors for Delayed Return to Usual Health Among Outpatients with COVID-19 in a Multistate Health Care Systems Network - United States, March-June 2020. *MMWR Morb Mortal Wkly Rep* **69**, 993-998, doi:10.15585/mmwr.mm6930e1 (2020).

71 Huang, C. *et al.* 6-month consequences of COVID-19 in patients discharged from hospital: a cohort study. *Lancet* **397**, 220-232, doi:10.1016/S0140-6736(20)32656-8 (2021).

72 Nalbandian, A. *et al.* Post-acute COVID-19 syndrome. *Nature Medicine* **27**, 601-615, doi:10.1038/s41591-021-01283-z (2021).

73 Rendeiro, A. F. *et al.* The spatial landscape of lung pathology during COVID-19 progression. *Nature* **593**, 564-569, doi:10.1038/s41586-021-03475-6 (2021).

74 Delorey, T. M. *et al.* COVID-19 tissue atlases reveal SARS-CoV-2 pathology and cellular targets. *Nature*, doi:10.1038/s41586-021-03570-8 (2021).

75 Ackermann, M. *et al.* Pulmonary Vascular Endothelialitis, Thrombosis, and Angiogenesis in Covid-19. *N Engl J Med* **383**, 120-128, doi:10.1056/NEJMoa2015432 (2020).

76 Bradley, B. T. *et al.* Histopathology and ultrastructural findings of fatal COVID-19 infections in Washington State: a case series. *Lancet* **396**, 320-332, doi:10.1016/S0140-6736(20)31305-2 (2020).

77 Tian, S. *et al.* Pathological study of the 2019 novel coronavirus disease (COVID-19) through postmortem core biopsies. *Mod Pathol* **33**, 1007-1014, doi:10.1038/s41379-020-0536-x (2020).

78 Stevens, T. P. & Sinkin, R. A. Surfactant replacement therapy. *Chest* **131**, 1577-1582, doi:10.1378/chest.06-2371 (2007).

79 Weaver, T. E. & Conkright, J. J. Function of surfactant proteins B and C. *Annu Rev Physiol* **63**, 555-578, doi:10.1146/annurev.physiol.63.1.555 (2001).

80 Choi, J. *et al.* Inflammatory Signals Induce AT2 Cell-Derived Damage-Associated Transient Progenitors that Mediate Alveolar Regeneration. *Cell Stem Cell* **27**, 366-382.e367, doi:10.1016/j.stem.2020.06.020 (2020).

81 Kobayashi, Y. *et al.* Persistence of a regeneration-associated, transitional alveolar epithelial cell state in pulmonary fibrosis. *Nature Cell Biology* **22**, 934-946, doi:10.1038/s41556-020-0542-8 (2020).

82 Melms, J. C. *et al.* A molecular single-cell lung atlas of lethal COVID-19. *Nature* **595**, 114-119, doi:10.1038/s41586-021-03569-1 (2021).

83 Ting, C. *et al. Fatal COVID-19 ARDS associated with incomplete AEC1 differentiation from the transitional state without senescence or fibrosis* (Cold Spring Harbor Laboratory, 2021).

84 Martinez, F. J. *et al.* Idiopathic pulmonary fibrosis. *Nature Reviews Disease Primers* **3**, 17074, doi:10.1038/nrdp.2017.74 (2017).

85 Wells, A. U. *et al.* Nintedanib in patients with progressive fibrosing interstitial lung diseases—subgroup analyses by interstitial lung disease diagnosis in the INBUILD trial: a randomised, double-blind, placebo-controlled, parallel-group trial. *The Lancet Respiratory Medicine* **8**, 453-460, doi:10.1016/s2213-2600(20)30036-9 (2020).

APPENDIX

In addition to my research detailed in this dissertation, I contributed to the following studies during my graduate work:

In collaboration with Emily N. Gallichotte, we performed and published a pair of studies characterizing the role of the Zika virus envelope protein in virion stability and pathogenesis.

Gallichotte, E.N.*, **Dinnon III, K.H.***, Lim, X., Ng, T., Lim, E.X.Y., Menachery, V.D., Lok, S., Baric, R.S. CD-Loop Extension in Zika Virus Envelope Protein Key for Stability and Pathogenesis. *The Journal of Infectious Diseases* 216, no. 10 (05 2017): 1196–1204.

Dinnon III, K.H.*, Gallichotte, E.N.*, Fritch, E.J., Menachery, V.D., Baric, R.S. Shortening of Zika Virus CD-Loop Reduces Neurovirulence While Preserving Antigenicity. *PLoS Neglected Tropical Diseases* 13, no. 3 (2019): e0007212.

In collaboration with Simon Anthony, W. Ian Lipkin, and the PREDICT program, we identified and characterized MERS-CoV-like PDF-2180 as an ancestor of MERS-CoV. I performed experiments for the following publication.

Anthony, S.J., Menachery, V.D., Goldstein, T., Ssebide, B., Mbabazi, R., Navarrete-Macias, I., Liang, E., Wells, H., Hicks, A., Petrosov, A., Byarugaba, D.K., Debbink, K., **Dinnon III, K.H.**, Scobey, T., Randell, S.H., Yount, B.L., Cranfield, M., Johnson, C.K., Baric, R.S., Lipkin, W.I., Mazet, J.A.K. Further Evidence for Bats as the Evolutionary Source of Middle East Respiratory Syndrome Coronavirus. MBio 8, no. 2 (04 2017).

In collaboration with numerous other scientists from around the world, I assisted in testing of COVID-19 medical countermeasures including several preclinical vaccine candidates. For these publications, I contributed a combination of reagent generation, experimental design, performed experiments, and data analysis.

Sheahan, T.P., Sims, A.C., Zhou, S., Graham, R.L., Pruijssers, A.J., Agostini, M.L., Leist, S.R., Schäfer, A., **Dinnon III, K.H.**, Stevens, L.J., Chappel, J.D., Lu, X., Hughes, T.M., George, A.S., Hill, C.S., Montgomery, S.A., Brown, A.J., Bluemling, G.R., Natchus, M.G., Saindane, M., Kolykhalov, A.A., Painter, G., Harcourt, J., Tamin, A., Thornburg, N.J., Swanstrom, R., Denison, M.R., Baric, R.S. An Orally Bioavailable Broad-Spectrum Antiviral Inhibits SARS-CoV-2 in Human

Airway Epithelial Cell Cultures and Multiple Coronaviruses in Mice. Science Translational Medicine 12, no. 541 (29 2020).

Pruijssers, A.J., George, A.S., Schäfer, A., Leist, S.R., Gralinski, L.E., **Dinnon III, K.H.**, Yount, B.L., Agostini, M.L., Stevens, L.J., Chappel, J.D., Lu, X., Hughes, T.M., Gully, K., Martinez, D.R., Brown, A.J., Graham, R.L., Perry, J.K., Du Pont, V., Pitts, J., Ma, B., Babusis, D., Murakami, E., Feng, J.Y., Bilello, J.P., Porter, D.P., Cihlar, T., Baric, R.S., Denison, M.R., Sheahan, T.P. Remdesivir Inhibits SARS-CoV-2 in Human Lung Cells and Chimeric SARS-CoV Expressing the SARS-CoV-2 RNA Polymerase in Mice. Cell Reports 32, no. 3 (21 2020): 107940.

Corbett, K.S., Edwards, D.K., Leist, S.R., Abiona, O.M., Boyoglu-Barnum, S., Gillespie, R.A., Himansu, S., Schäfer, A., Ziwawo, C.T., DiPiazza, A.T., **Dinnon III, K.H.**, Elbashir, S.M., Shaw, C.A., Woods, A., Fritch, E.J., Martinez, D.R., Bock, K.W., Minai, M., Nagata, B.M, Hutchinson, G.B., Wu, K., Henry, C., Bahl, K., Garcia-Dominguez, D., Ma, L., Renzi, I., Kong, W., Schmidt, S.D., Wang, L., Zhang, Y., Phung, E., Chang, L.A., Loomis, R.J., Altaras, N.E., Narayanan, E., Metkar, M.,m Presnyak, V., Liu, C., Louder, M.K., Shi, W., Leung, K., Yang, E.S., West, A., Gully, K.L., Stevens, L.J., Wang, N., Wrapp, D., Doria-Rose, N.A., Stewart-Jones, G., Bennett, H., Alvarado, G.S., Nason, M.C., Ruckwardt, T.J., McLellan, J.S., Denison, M.R., Chappel, J.D., Moore, I.N., Morabito, K.M., Mascola, J.R., Baric, R.S., Carfi, A., Graham, B.S. SARS-CoV-2 MRNA Vaccine Design Enabled by Prototype Pathogen Preparedness. *Nature* 586, no. 7830 (2020): 567–71.

Walls, A.C., Fiala, B., Schäfer, A., Wrenn, S., Pham, M.N., Murphy, M., Tse, L.V., Shehata, L., O'Connor, M.A., Chen, C., Navarro, M.J., Miranda, M.C., Pettie, D., Ravichandran R., Kraft, J.C., Ogohara, C., Palser, A., Chalk, S., Lee, E., Guerriero, K., Kepl, E., Chow, C.M., Sydeman, C., Hodge, E.A., Brown, B., Fuller, J.T., **Dinnon III, K.H.**, Gralinski, L.E., Leist, S.R., Gully, K.L., Lewis, T.B., Guttman, K., Chu, H.Y., Lee, K.K., Fuller, D.H., Baric, R.S., Kellam, P., Carter, L., Pepper, M., Sheahan, T.P., Veesler, D., King, N.P. Elicitation of Potent Neutralizing Antibody Responses by Designed Protein Nanoparticle Vaccines for SARS-CoV-2. *Cell*, October 31, 2020.

Sun, W., Leist, S.R., McCroskery, S., Liu, Y., Slamanig, S., Oliva, J., Amanat, F., Schäfer, S., **Dinnon III, K.H.**, García-Sastre, A., Krammer, F., Baric, R.S., Palese, P. Newcastle disease virus (NDV) expressing the spike protein of SARS-CoV-2 as a live virus vaccine candidate. *EBioMedicine* (2020).

Hömer, C., Schürmann, C., Auste, A., Ebenig, A., Muraleedharan, S., **Dinnon III, K.H.**, Scholz, T., Herrmann, M., Schneirle, B.S., Baric, R.S., Mühleback, M.D. A Highly Immunogenic and Effective Measles Virus-based Th1-biased COVID-19 Vaccine. *PNAS* (2020).

Sun, W., McCroskery, S., Liu, W.C., Leist, S.R., Liu, Y., Albrecht, R.A., Slamanig, S., Oliva, J., Amanat, F., Schäfer, A., **Dinnon III, K.H.**, Innis, B.L., García-Sastre, A., Kramer, F., Baric, R.S., Palese, P. A Newcastle Disease Virus (NDV) expressing a membrane-anchored spike as a cost-effective inactivated SARS-CoV-2 vaccine. *Vaccines* (Dec 2020).

Wahl, A., Gralinski, L.E., Johnson, C.E., Yao, W., Kavarova, M., **Dinnon III, K.H.**, Liu, H., Madden, V.J., Krzystek, H.M., De, C., White, K.K., Gully, K.L., Schäfer, A., Zaman, T., Leist, S.R., Grant, P.O., Bluemling, G.R., Kolykhalov, A.A., Natchus, M.G., Askin, F.B., Painter, G., Browne, E.P., Jones, C.D., Pickles, R.J., Baric, R.S., Garcia, J.V. SARS-CoV-2 infection is effectively treated and prevented by EIDD-2801. *Nature* (2021).

Routhu, N.K., Cheedarla, N., Bollimpelli, V.S., Gangadhara, S., Edara, V.V., Lai, L., Sahoo, A., Shiferaw, A., Styles, T.M., Floyd, K., Fischinger, S., Atyeo, C., Shin, S.A., Gumber, S., Kirejczyk, S., Dinnon III, K.H., Shi, P., Menachery, V.D., Tomai, M., Fox, C.B., Alter, G., Vanderford, T.H.,

Gralinski, L., Suthar, M.S., Amara, R.R. SARS-CoV-2 RBD trimer protein adjuvanted with Alum-3M-052 protects from SARS-CoV-2 infection and immune pathology in the lung. *Nature Communications* (2021).